1997

Flux Corrected Method: An accurate approach to fluid flow modeling

Sutikno Wirogo
Iowa State University

INFORMATION TO USERS

This manuscript has been reproduced from the microfilm master. UMI films the text directly from the original or copy submitted. Thus, some thesis and dissertation copies are in typewriter face, while others may be from any type of computer printer.

The quality of this reproduction is dependent upon the quality of the copy submitted. Broken or indistinct print, colored or poor quality illustrations and photographs, print bleedthrough, substandard margins, and improper alignment can adversely affect reproduction.

In the unlikely event that the author did not send UMI a complete manuscript and there are missing pages, these will be noted. Also, if unauthorized copyright material had to be removed, a note will indicate the deletion.

Oversize materials (e.g., maps, drawings, charts) are reproduced by sectioning the original, beginning at the upper left-hand corner and continuing from left to right in equal sections with small overlaps. Each original is also photographed in one exposure and is included in reduced form at the back of the book.

Photographs included in the original manuscript have been reproduced xerographically in this copy. Higher quality 6" x 9" black and white photographic prints are available for any photographs or illustrations appearing in this copy for an additional charge. Contact UMI directly to order.

UMI

A Bell & Howell Information Company
300 North Zeeb Road, Ann Arbor MI 48106-1346 USA
313/761-4700 800/521-0600

Flux Corrected Method:
An accurate approach to fluid flow modeling

by

Sutikno Wirogo

A dissertation submitted to the graduate faculty

in partial fulfillment of the requirements for the degree of

DOCTOR OF PHILOSOPHY

Major: Aerospace Engineering

Major Professor: Ganesh Rajagopalan

Iowa State University

Ames, Iowa

1997

Graduate College
Iowa State University

This is to certify that the Doctoral dissertation of

Sutikno Wirogo

has met the dissertation requirements of Iowa State University

Signature was redacted for privacy.

Major Professor

Signature was redacted for privacy.

For the Major Program

Signature was redacted for privacy.

For the Graduate College

TABLE OF CONTENTS

LIST OF TABLES

LIST OF FIGURES

NOMENCLATURE

(x, y)	Two-dimensional Cartesian coordinates
t	Time variable
u	x-direction velocity component
v	y-direction velocity component
V	Velocity
P	Pressure
ρ	Density
μ	Viscosity
ν	Kinematic viscosity
Re	Reynolds number
ϕ	General flow dependent variable
Γ	Diffusion parameter present in the general transport equation
P_e	Local grid Reynolds number
S	Source present in the multi-dimensional transport equation
S_{cd}	One-dimensional convection-diffusion source
F	Convection flux
D	Diffusion flux
J	Total-flux expression

ACKNOWLEDGEMENTS

I would like to express my deepest and foremost gratitude to the Lord God Almighty whose unfailing love and guidance has enabled me to complete my studies. Many thanks and deep gratitude are due to my major professor, Dr. R. G. Rajagopalan, for his guidance and encouragement throughout my graduate studies. Thanks are also due to the members and research review committee, Dr. J.M. Vogel, Dr. A.K. Mitra, Dr. T.J. McDaniel, and Dr. P.E. Sacks.

I am deeply indebted to my parents for their continued moral and financial support. This degree is certainly achieved with them and for them. Special gratitude is due to my girl friend, Susien Sugeng, whose love and patience sustained me in all the difficult times experienced. I also wish to express my gratitude to my sisters and all of my family members for their support and prayers.

I would also like to thank Dr. A.J. Zori for his friendship and cheerful encouragement. His technical and nontechnical suggestions are deeply appreciated. Thanks are also due to the other members of my research group, S. Ochs and Michael Maresca. Thanks to J.H. Miller for helpful technical discussions. Last but not least, I would like to thank the Indonesian Christian Fellowship in Ames. Their encouragement, prayers, and fellowship have brightened my years here in Ames, Iowa.

Local computing support for this work was provided by the Iowa State University Computational Center and the AEEM department.

1 INTRODUCTION

1.1 Convection and Diffusion Transport Mechanisms

The conservation equation governing the physical behavior of a fluid flow dependent variable (flow property) can always be cast into a general transport equation consisting of unsteady, convection transport, gradient-diffusion transport, and source term. Since flow properties are transported by means of convection and diffusion, numerical modeling of fluid flow deals with the modeling of the two transport terms in the governing conservation equation. An important physical fact in the convection transport is that the flow property is convected in the strongest sense in the direction of the convecting velocity. In other words, the role of the convecting velocity is to sweep the influence of that property downstream in its direction. A larger convecting velocity means that the upstream information has a greater influence on the distribution of the flow property at a point along the direction of that convecting velocity. This physical fact should be appropriately taken into account in the modeling of the convection term. Meanwhile, the effect of diffusion is to disperse/diffuse the influence of the flow variable in all directions.

It has been the case that the diffusion term is more straightforward to model. High convection and low diffusion mean that the distribution of the flow variable is more 'one-dimensional' along the streamlines of the flow with less variation in the cross-wise directions. Low convection and high diffusion mean that the transport of the flow variable is less characterized by dominant directions but is more diffused. When both convection and diffusion have dominant roles in establishing the distribution of the de-

pendent variable, as in the case of recirculating flows, it is expected that the transport of the flow variable is significant in the cross-wise directions normal to the streamlines of the flow. This latter flow situation underscores the importance of maintaining comparable accuracy in the differencing of both the convection and diffusion terms since it is only in very specialized flow problems that either convection or diffusion is the dominant transport throughout the flow domain. Moreover, a successful approach to the modeling of fluid flow must also reflect a balance/interdependence between the two transport mechanisms in the considered multi-dimensional realm. In a domain discretized by a structured mesh, it is important to realize that accurate modeling of the convection and diffusion terms in a certain coordinate direction must take into account the effects of the cross-wise convection and diffusion.

The governing conservation equation also explicitly states the dependence of the convection and diffusion transports on the unsteady term and source term in order to maintain the overall conservation of the dependent variable. This particular dependence is often overlooked, or in many cases, is only indirectly taken into consideration in the approximation of the convection and diffusion flux (total-flux) at the control-volume interfaces. In a paper introducing the Skew Upwind Differencing Scheme (SUDS) [1], Raithby addressed the fact that SUDS and its variants have not considered the complete effect of transient and source terms and thus are not suitable for problems with a large transient gradient and/or a large source. In a more recent paper, Leonard [2] also explicitly stated that significant numerical diffusion may result if the effect of the transient and source terms are not taken into account appropriately.

1.2 Previous Approaches in the Modeling of Convection and Diffusion

1.2.1 Central-Difference

In the early period of CFD, classical central-difference appeared to offer a logical and natural approach to the approximation of the dependent variable (convection) and its derivative (diffusion) at the interfaces. In this formulation, both the dependent variable and its derivative at an interface in a given coordinate direction are approximated by using a piecewise linear profile (of the dependent variable) involving two neighboring points. Central-difference formulation is the natural outcome of a Taylor-series formulation and can be shown to have second-order formal accuracy. This formulation gives fairly accurate solutions for a class of low Reynolds number problems under specific conditions. However, Roache [3], Leonard [4], Patankar [5], and many other researchers have shown in great detail that central-differencing may lead to unphysical oscillatory behavior for an implicit solution or to disastrous non-convergence in an explicit computation in regions where convection strongly dominates diffusion. Patankar has shown that in the case of central-difference formulation, when the Peclet number (local grid Reynolds number) exceeds the value of two, violation of the positive coefficient rule [5] (and thus violation of the Scarborough criterion) becomes possible with consequent unstable numerical iteration. For this reason, all the early attempts to solve convection-dominated problems by the central-difference scheme were limited to low Reynolds number flows. Although theoretically it is possible to keep the Peclet number below two by refining the grid, this approach is neither economical nor practical. Previous work by Khosla and Rubin [6], and more recent work by Ghia [7], Hayase [8], and Leonard [2] have shown that it is possible to write the central-difference formulation in a form similar to the so called 'deferred-correction method'. In this form, the value of the dependent variable at

an interface is approximated by an upwind value plus a correction term. Significantly enhanced stability has been observed when the central-difference scheme is written in this form.

Higher order central-difference schemes involving wider stencils have been developed and tested with some success. While it is true that the formal order of accuracy is higher using this strategy, the oscillatory and stability problems of the classical second-order scheme are retained. Leonard [4] showed that in the case of central-differencing methods (of any order), there is no convective feedback sensitivity, so that under high convection conditions (large Peclet number), stability problems and numerical oscillations are likely to occur.

In recent years, the so called High Order Essentially Non-Oscillatory schemes (ENO) [9] have been introduced in an attempt to reduce the oscillation and stability problems inherent in classical central-difference schemes. These schemes were originally designed for compressible flow and in general for hyperbolic conservation law but have recently been applied to incompressible Navier-Stokes equations. It was concluded that when it is either impossible or too costly to fully resolve the flow, ENO can be used on a coarse grid to obtain at least some partial information about the flow.

1.2.2 Upwind Scheme

Central-difference formulation is second-order accurate in both convection and diffusion. For a low Peclet number, the piecewise linear variation of the dependent variable is generally acceptable. In this condition, both the upstream and downstream values exert linear influence on the interface value. However, for high convection flow, this approximation is less than physical. For a high Peclet number flow, it is known that the upstream value has more influence on the interface variable than the downstream value. Numerical instabilities can be traced to the non-consideration of this physics in the convection modeling.

The first-order upwind scheme is an attempt to remedy this deficiency in the convection modeling. The interface variable is approximated solely by using the immediate upstream value (thus earning the name 'donor-cell technique' [10]) while central-difference is used to evaluate the first derivative. Thus, it is first-order representation for the convection and second-order representation for the diffusion. The resulting scheme removes the oscillatory and stability problems associated with the central-difference scheme and gives acceptable solutions when it is convection that is mainly responsible for establishing the streamwise distribution of the dependent variable [4]. However, if the Peclet number (based on grid dimension in the flow direction) is less than or equal to five in magnitude (Peclet number restriction), and additionally, if the flow is significantly oblique to the grid, large numerical diffusion is observed. This makes the first-order upwind scheme highly unsuitable for the modeling of recirculating flows. The diffusive nature of the first-order upwind scheme can be understood by a reference to the one-dimensional convection-diffusion process outlined by Patankar [5]. It is known that for low Peclet numbers, the variation of the dependent variable is largely linear between the two neighboring values (a concept captured correctly by the central-difference scheme). Neglecting the downstream information is certainly non-physical for this low convection flow.

In an attempt to reduce the presence of large numerical diffusion inherent in the first-order upwind scheme, a second-order upwind scheme (original idea traced to Price et al. [11]) has been proposed which uses one more node in the upwind direction for evaluating the convective term. There are many variants of the second-order upwind scheme for estimating the mass flux across the interface of a computational cell, with the common theme that the value of the dependent variable at a local node is connected to two upstream values rather than just one, while central-difference is used to evaluate the diffusion term. This scheme can be shown to have second-order accuracy in both the convection and diffusion terms. Many researchers have investigated this scheme over the

years, but the findings are not necessarily consistent among the different studies. Atial et al. [12] have used this scheme to study the lid-driven cavity flow and the problem of impinging jet on a normal flat plate in conjunction with the streamfunction vorticity approach. Wilkes and Thompson [13] have applied this scheme in the numerical study of laminar and turbulent flow in sudden expansions and contractions. Shyy and Correa [14] have used this scheme for the laminar lid-driven cavity problem. These researchers have concluded that for the evaluated test problems, second-order upwind schemes have been shown to give less numerical diffusion and thus a better accuracy than their first-order predecessor. On the other hand, Vanka [15] found that second-order upwind schemes do not yield satisfactory performance, both in terms of numerical accuracy and computational stability, in solving the two-dimensional lid-driven cavity flows for a range of Reynolds numbers. These conflicting findings prompted a more systematic and thorough study of this scheme by Shyy [16]. The different variants of second-order upwind schemes were investigated for the two-dimensional lid-driven cavity problem. It has been concluded that even though all the variants of this scheme have formal second-order accuracy, they all have different characteristics. It has been found that the scheme which performs the best is the one which conforms most closely to the principles of finite-volume formulation and is strictly conservative.

It should be noted that the dependence of convection and diffusion processes on the transient and source terms has not been addressed in the formulation of classical upwind schemes. It was not until the introduction of the QUICKEST scheme by Leonard that the transient term was taken into account.

1.2.3 Skew Upwind Differencing Scheme

The Skew Upwind Differencing Scheme (SUDS) of Raithby [1] has also been suggested as an improved alternative to the first-order upwind scheme. As mentioned earlier, the first-order upwind scheme is known to produce unacceptably large numerical diffusion

when the flow is oblique to the grid, rendering the scheme too expensive for recirculating flow problems. This is because the first-order upwind approximation of the dependent variable at the interface in a given coordinate direction is satisfactory only when the flow is aligned to the grid. When the flow is skewed to the grid, the component-wise upwind direction does not follow the 'true' direction of the convecting velocity, resulting in significant numerical diffusion. The idea behind SUDS is to use the first-order upwind scheme applied along the skewed streamline passing through the interface to be evaluated. The upwinding is then used in a vector sense rather than component-wise along the coordinate directions. As in the previous case of an upwind scheme, central-difference is used to approximate the diffusion term. This scheme has been shown to significantly reduce numerical diffusion which arises when the flow cuts across the grid at a large angle. This is expected since theoretically it is in direct agreement with the observed physics of the flow. However, the 'Peclet number restriction' associated with the first-order upwind scheme is not removed. A slightly more complicated yet more accurate variant of SUDS is also proposed by Raithby. This scheme is called Skew Upwind Weighted Differencing Scheme (SUWDS), and as its name suggests, downstream information is taken into consideration in the differencing stencil, thus removing the restriction on the grid Peclet number. In his paper, Raithby also noted that the effects of transient and source terms have not yet been considered, and thus the scheme may produce numerical diffusion in the presence of high transient gradient and source term, as is the case with the previous upwind formulation.

1.2.4 Third Order Upstream Weighted Scheme (QUICK)

Not long after the publication of Raithby's Skew Upwind differencing scheme, Leonard introduced a different approach in the modeling of the convection term [4], called the QUICK (Quadratic Upstream Interpolation for Convective Kinematics) scheme. Over the years, the QUICK scheme has proven to be highly successful in solving a wide variety

of convection-diffusion problems. The main motivation behind the development of the QUICK scheme is to investigate the possibility of constructing an 'interpolation scheme' (for the dependent variable and its derivative at an interface) which simultaneously possesses good accuracy and the directional properties associated with stable convective sensitivity. The formulation of the differencing stencil at an interface is illustrated in Figure 1.1.

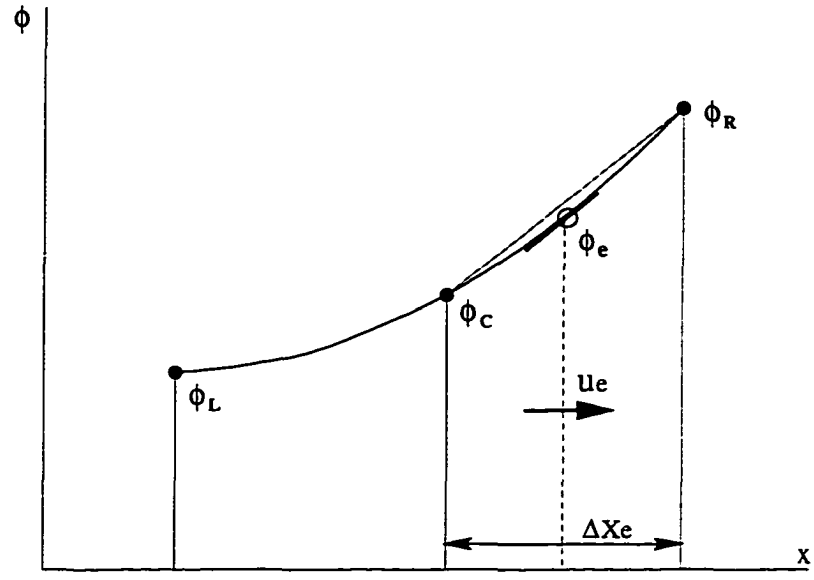

Figure 1.1 QUICK three node parabolic profile.

Assuming that u_e is positive, the interface dependent variable can be written as:

$$\begin{aligned} \phi_e &= -\frac{1}{4}\phi_L + \frac{1}{4}\phi_C + \frac{5}{8}\phi_R \qquad u_e > 0 \\ &= \frac{1}{2}(\phi_C + \phi_R) - \frac{1}{8}(\phi_L - 2\phi_C + \phi_R)\,, \end{aligned} \tag{1.1}$$

for an equally spaced grid. The dependent variable at an interface is approximated by constructing a parabola using two adjacent neighboring nodes and one more node in the upstream direction. It should be noted that this approximation can also be interpreted as a linear interpolation (involving two neighboring nodes) corrected by a term proportional to the upstream curvature. Using the geometric property of parabolas that the slope

halfway between two points is equal to that of the chord joining the points, the gradient at the interface is given by:

$$\frac{\partial \phi}{\partial x} = \frac{\phi_R - \phi_C}{\Delta X_e}, \tag{1.2}$$

which is identical to the central-difference formula. Leonard has shown that this procedure has greater formal accuracy than the central-difference scheme but retains the basic stable convective sensitivity property that is characteristic of upstream weighted schemes. Moreover, since the downstream information is taken into account, the Peclet number restriction associated with the first-order upwind scheme is removed. Soon after Leonard's publication of the QUICK scheme, several researchers (Leschziner [17], Han et al. [18], Pollard and Siu [19], Freitas et al. [20], Perng and Street [21], Hayase et al. [8]) addressed the implementational details and testing of the scheme in two- and three-dimensional flows more complex than those originally inspected by Leonard. Higher order results using this scheme have been consistently reported for a wide range of flow problems. Besides its upwind characteristics, another reason that the QUICK scheme is able to capture the effects of source and cross-wise transports relatively well is the wider stencil involved. The presence of both source and cross-wise transport indirectly influences the value of the dependent variable at the interface by changing the node values used in the construction of the parabolic profile. In other words, a better mathematical profile is used to take into consideration the effects of source and cross-wise transport.

High order upwind-weighted methods are potentially quite stable. But because of the wide-stencil involved, care is needed when applying traditional tridiagonal matrix-solver techniques. Simply casting the outlying values into the source term can evidently lead to slow convergence or even divergence. Among the various QUICK schemes developed over the years, the 'Consistent QUICK' formulation by Hayase et al. [8] seems to posses the best convergence property. Systematic study of the performance of the various QUICK schemes applied to the two-dimensional lid-driven cavity problem by Hayase

clearly shows that while the converged solutions of the schemes are identical since they are all derived from Leonard's formulation, their respective stability characteristics show different behaviors. It is noted in this study that the particular formulation by Pollard and Siu [19] consistently requires more iterations for the range of the Reynolds numbers investigated. Hayase's formulation requires that the finite-difference approximation of the profile of the dependent variable at the interface satisfy Patankar's well-known 'Four Rules', ensuring stable convergence. Adherence to these convergent rules dictates that the value of the interface variable be written as the sum of a first-order upwind estimation and a correction term. The correction term is deferred or lagged from the previous values and is eventually lumped into the source term. This method is often referred to as the 'Deferred Correction' method and has been proven to enhance stability.

Another inherent difficulty with the high-order upwind scheme is the formulation of the scheme for the cells adjacent to the wall. Depending on the flow direction, the scheme may require a value outside the calculation domain. Leonard's subsequent paper [22] gave the modification of the QUICK scheme for the cells near the boundary. However, because a third-order boundary-treatment sometimes causes instabilities, a second-order boundary is often used to avoid potential stability problems. Hayase's formulation shows that Leonard's third-order boundary formulation can also be written as the sum of the upwind evaluation plus the correction term, consistent with his proposed QUICK scheme. The main motivation for retaining third-order boundary treatment is to preserve the continuity of the third-order truncation error throughout the computational domain. As shown by Hayase, the use of a lower order boundary in conjunction with the higher order scheme has been proven to degrade the overall accuracy of the solution. This is especially true in elliptic problems.

It is known that the high order upwind scheme has the tendency to generate unphysical overshoots near sharp transitions. This means that a typical step-like profile which should be sharp and monotonic will be computed with an overshoot on one side

or the other, or both. This is particularly true with the QUICK scheme. In his recent paper [2], Leonard proposed the use of a flux limiter to curb possible overshoots. In the first strategy, the Universal Limiter for Tight Resolution and Accuracy (ULTRA) ([23] and [24]) is used with the QUICK scheme. In the second strategy, a combination of the ULTRA method and Leonard's Simple High Accuracy Resolution Program (SHARP) is also proposed. It was concluded that while the ULTRA-QUICK strategy eliminates the overshoot problems (for the test case considered), numerical diffusion is also introduced to some extent. On the other hand, the ULTRA-SHARP strategy has been shown to eliminate the overshoot without introducing additional numerical diffusion.

Modification of the QUICK scheme for unsteady flows is known as the QUICKEST scheme [4]. Initial testing of the QUICKEST on the simulation of the complex hydrodynamics and salinity transport of a large estuary by Leonard showed that the QUICKEST scheme does not introduce any appreciable numerical diffusion for highly unsteady problems. However, since its introduction, there have not been many published results for the application of this scheme to a wide range of unsteady problems.

1.2.5 Exponential Difference Scheme (EDS)

The past two decades have witnessed the popularity of this class of schemes which is often referred to as the Exponential Differencing Scheme (EDS). The first variant of these schemes is called the exponential scheme, developed by Allen and Southwell [25]. The exponential scheme models the convection-diffusion transport process by focusing on each grid-wise component of that process. That is, the dependent variable and its derivative at the interface in a given coordinate direction are approximated by using the exact solution of the one-dimensional, constant-coefficients, and source free convection-diffusion equation along that coordinate direction, resulting in an exponential profile. Since the present work relies heavily on an understanding of the EDS, a detailed discussion of its advantages and disadvantages is presented.

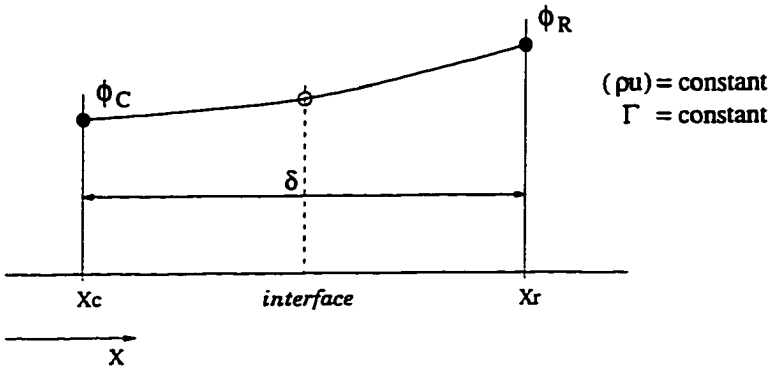

Figure 1.2 One-dimensional convection-diffusion profile.

With the aid of Figure 1.2, the convection-diffusion transport in the x-direction is modelled by solving:

$$\frac{\partial}{\partial x}\left((\rho u)\phi - \Gamma\frac{\partial \phi}{\partial x}\right) = \frac{\partial}{\partial x}J_x = 0 \ , \tag{1.3}$$

where (ρu)=*constant* and (Γ=*constant*) across the cell considered. This means that the x-direction total-flux (J_x) is always constant across that cell, and its analytic expression, subject to known boundary conditions ϕ_{i-1} and ϕ_i, is given by:

$$J_x = \frac{\Gamma}{\delta}(B\phi_{i-1} - A\phi_i) = constant \ , \tag{1.4}$$

where A and B are a function of the Peclet number only and are given by:

$$\begin{aligned} A &= \frac{P_e}{e^{P_e} - 1} \\ B &= A + P_e \\ P_e &= \frac{(\rho u)\delta}{\Gamma} = Peclet\ number \ . \end{aligned} \tag{1.5}$$

The dependence of the total-flux on the Peclet number is shown in Figure 1.3.

Over the years, motivated by the relatively expensive exponential calculations involved, several researchers have independently developed variants of the exponential scheme. The most notable of these convection-diffusion methods are the hybrid scheme of Spalding [26] (also known as the high lateral flux modification) and the Power Law

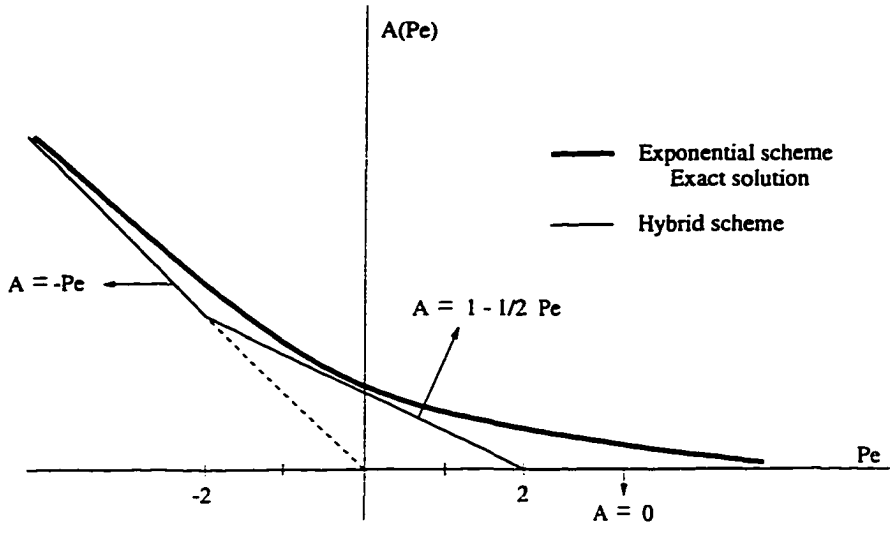

Figure 1.3 Variation of A(P_e) as a function of P_e

scheme of Patankar [5]. The hybrid scheme tries to approximate the exponential function $A(P_e)$ by using a three-line piecewise approximation to the exact curve. It should be noted that the hybrid scheme is identical to the central-difference scheme for a Peclet number range of $-2 < P_e < 2$, and outside this range, it reduces to the upwind scheme in which the diffusion has been set equal to zero. It has been discussed previously that the second-order central-difference scheme is stable for $|P_e| < 2$ but is potentially unstable for a higher Peclet number. On the other hand, the upwind scheme performs better for a higher Peclet number but is diffusive for a low Peclet number case. Hence, as its name suggests, the hybrid scheme is a combination of the central and upwind schemes, using the better option between the two schemes for each Peclet number case. A better approximation to the exact curve is given by the Power Law scheme. The Power Law expression is not particularly expensive to compute but provides an extremely good representation of the exponential behavior. For this reason, a reference to the exponential scheme will be used interchangebly with the Power Law scheme.

The exponential Differencing Scheme started to gain popularity with the introduction

of the SIMPLE solver [5]. The combination of these procedures resulted in the so-called TEACH code [27] developed at Imperial College, giving a robust, general purpose elliptic equation solver suitable for solving steady-state Navier-Stokes equations and the associated heat and mass transfer problems. In the past decade, hybrid and Power Law schemes have been widely used for solving a wide class of problems. Their popularity stems from good convective stability and 'relatively accurate' solutions (compared with the first-order upwind scheme).

However, in the intervening period, researchers have also shown that for a high-frequency transient, multidimensional transport process with a significant source, EDS results in solutions which are marred by unacceptably large numerical diffusion. Many researchers, including Huang [28], Patel [29], and Leonard [2], have shown that, as is the case with the first-order upwind scheme, the numerical solution of the EDS scheme for general flow problems can be significantly inaccurate for coarse grids. Considerable grid refinement may be needed to produce acceptable results. Careful observation of the characteristics of EDS shows that EDS can be considered to be a variant of the first-order upstream weighted scheme with the weighting coefficients obtained from solving a one-dimensional, source free convection-diffusion equation. These weighting coefficients are such that when the Peclet number is relatively small (i.e. $|P_e|< 2$), both the upstream and downstream nodes have 'linear' influence on the interface profile. However, as the Peclet number increases in magnitude, the influence of the upstream node grows in significance while the effect of the downstream node diminishes. Thus, the inherent diffusive characteristic of the first-order upwind scheme is also shared to some extent by EDS (and first order upwind schemes in general). Leonard has shown that for large Peclet numbers, EDS is equivalent to first-order upwinding for the convection with physical diffusion neglected [2], which results in the introduction of numerical diffusion in the cross-wise direction. However, perhaps the most serious misapplication of EDS is to multidimensional problems involving high-speed flow oblique or skewed

to the grid [2]. In this case, more than one component of the grid Reynolds number (Peclet number) is large at any given control-volume. Thus, the components of the convection-diffusion process in each coordinate direction have 'equal' influence on the values of the dependent variable at the interface. Recall that for a given coordinate direction, EDS approximates the dependent variable and its derivative at the interface by solving the one-dimensional, source free convection-diffusion equation in that direction. Thus, the influence of the cross-wise components of the convection-diffusion process is neglected. Cross-wise transports only influence the interface profile indirectly by changing the values of the dependent variables at the two nodes surrounding the interface. This simplification means that EDS is most effective for solving flow situations which are steady and quasi-one-dimensional (dominant streamwise transport), provided that the convecting velocity is nearly aligned with one of the grid coordinate directions.

1.2.6 Locally Analytic Differencing Scheme (LOADS)

At about the same time Patankar introduced the Power Law scheme, an extension to the exponential scheme, named LOADS, which takes into account the multidimensionality of the flow, was introduced by Raithby [30]. LOADS realizes that unless a sufficiently fine grid is used, the use of a conventional locally exact one-dimensional solution (i.e. exponential scheme) cannot be expected to give accurate solutions for strongly multidimensional problems, such as when the flow is skewed to the grid. A locally one-dimensional solution can be a viable approximation only if the lateral transport and source terms are taken into account in the determination of the one-dimensional profile. This can be done by rewriting the conservation equation (equation 1.8 to be given later) as a one-dimensional convection-diffusion process in a grid direction with the rest of the terms combined as one source term. An analytical expression is then used to approximate the exponential solution of the modified one-dimensional transport process. Referring to the stencil used previously to explain the QUICK profile (Figure 1.1), the

value of the dependent variable at interface e is given by:

$$\phi_e = \phi_C + \frac{1}{2}(\phi_R - \phi_C)\frac{(1-0.1Pe_e)^5}{(1-0.05Pe_e)^5} + \frac{1}{2}\frac{k_x}{(\rho u)_e}\Delta X_e \left[1 - \frac{(1-0.1Pe_e)^5}{(1-0.05Pe_e)^5}\right] . \quad 0 \le Pe_e \le 10 , \tag{1.6}$$

$$= \phi_c + \frac{1}{2}\frac{k_x}{(\rho u)_e}\Delta X_e . \qquad Pe_e > 10 , \tag{1.7}$$

where k_x is the combined source for the one-dimensional equation and is evaluated using the numerical solution currently available. Huang et al. [28] showed that for nearly linear problems, LOADS is clearly more accurate than the Power Law scheme. However, for highly non-linear problems (such as high Reynolds number lid-driven cavity flow), LOADS failed to converge in most of the cases considered. Huang also mentioned that convergence for the non-linear problems might be possible if the unsteady term is retained in the momentum equations. However, this renders the scheme less attractive due to the computational time needed in the time marching process. Convergence for the lid-driven cavity problems is indeed achieved by retaining the unsteady term, as shown by Patel et al. [29]. However, it was also concluded that for the test problems considered, the performance of LOADS, even though it is superior to the Power Law scheme, is not competitive when compared with the QUICK scheme.

1.2.7 Flux Spline Scheme

The realization of the shortcomings of the Power Law scheme also motivated the development of the Flux Spline scheme by Varejao [31]. It was finally determined that the constant total-flux approximation across the control-volume cell is inadequate in flow regions with large cross-flow transport. To better capture the physics of the flow, total-flux should be allowed to vary to express the presence of cross-wise transport and source. The Flux Spline scheme attempts to model these facts by using a linear total-flux variation along a coordinate direction within the considered control-volume. Total-flux at the interface is expressed as the sum of a constant value obtained using the lower

order Power Law scheme plus an extra term. It is then clear that the extra term is intended as the means by which source and flow multidimensionality are captured.

The Flux Spline scheme has been applied to several two- and three-dimensional flow problems [32] and was reported to be more accurate than the Power Law scheme. To get the same level of accuracy, the Flux Spline scheme requires a fewer number of grid points. However, little research has been reported on the use of flux-spline on a wide variety of problems.

QUICK and Flux spline schemes represent a further step in the realization that a successful approach to the modeling of convection and diffusion processes must take into account the presence of the cross-wise transport, the source, and the unsteady term. Failure to account for these three factors could result in the generation of unwanted numerical diffusion and/or numerical instabilities.

1.3 Modeling of Convection Diffusion Problem

The general transport equation which governs the physical behavior of the dependent variable ϕ in two-dimensions is given by:

$$\frac{\partial(\rho\phi)}{\partial t} + \frac{\partial}{\partial x}\left((\rho u)\phi - \Gamma\frac{\partial\phi}{\partial x}\right) + \frac{\partial}{\partial y}\left((\rho v)\phi - \Gamma\frac{\partial\phi}{\partial y}\right) = S \tag{1.8}$$

It should be noted that the convection and diffusion processes have been represented component-wise in each coordinate direction. Observation of the above equation confirms the previous qualitative conclusion that the convection-diffusion process in one coordinate direction is directly balanced by the unsteady term, source term, and transport processes in the remaining coordinate directions. Thus, smaller y-direction transport can mean larger x-direction transport and vice versa. The influence of the unsteady term and source also works in the same way.

The first step in the discretization process is to integrate equation 1.8 over time and over the considered control-volume cell given in Figure 1.4. Then, an approximation

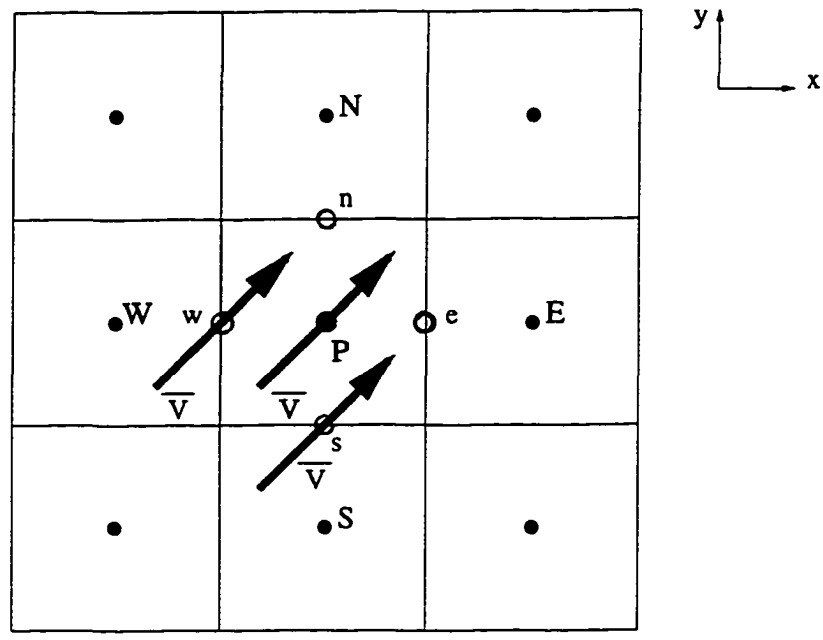

Figure 1.4 Two-dimensional discretized domain.

should be devised to represent the total-fluxes at both the x- and y-interfaces. This requires the formulation of the dependent variable and its derivative at an interface in terms of the values at the neighboring nodes. Different schemes use different stencils (number of nodes) and different weighting factors for each node used.

There are two different ways in which the unsteady, source, and cross-wise transports (the remaining terms) affect the approximation of the interface total-flux. First, a typical two-node approximation of the dependent variable (or its derivative) at interface e (refer to Figure 1.4) will use the values of the dependent variable at nodes P and E. Thus the effect of the remaining terms 'indirectly' influences the interface value by changing the values at nodes P and E when the transport equation is integrated and solved over the cells containing those two nodes. This is inherent in every scheme, and it is obvious that the use of more nodes means greater influence on the interface profile. Secondly, the remaining terms can influence the interface value 'directly' by including those effects

directly in the profile approximation. The potential of the latter approach should be immediately apparent.

1.3.1 High Convection Flow Oblique to the Grid

Accurate modeling of complex flows is at best difficult. Most flow problems involve situations where the flow has more than one dominant direction throughout the region of interest. Therefore, it is very difficult, if not impossible, to have a grid structure which is mostly aligned to the streamlines of the flow. Regardless of the type of grid chosen, there will always be regions where the flow is significantly oblique or skewed to the grid.

It is often stated that flows oblique to the grid may cause significant numerical diffusion if the numerical scheme is not properly formulated. The following discussion attempts to clarify both the characteristics of flow oblique to the grid and the way in which the previously discussed schemes handle this situation.

First, it is helpful to state the following observation:

> *In the convection transport of variable ϕ, the scalar ϕ at a given location will be convected in the direction of the convecting velocity $\vec{V}$ at that location. The larger the magnitude of the convecting velocity, the greater is the influence of the upstream value on the downstream distribution.*

This observation is then used as a guide to study the various approximations of the value of ϕ_b given below.

Case A Approximating ϕ_b by a linear interpolation of ϕ_e and ϕ_f is accurate when $|\vec{V}|$ is of moderate value. But for larger P_e, this approximation may result in overshoots or undershoots since linear profile does not take into account the direction of the flow. This approximation is used by the central-difference scheme and has second-order truncation error.

Case B Approximating ϕ_b by ϕ_e (first-order truncation error) has some virtues, but it does not take into account the aforementioned observation properly if θ is

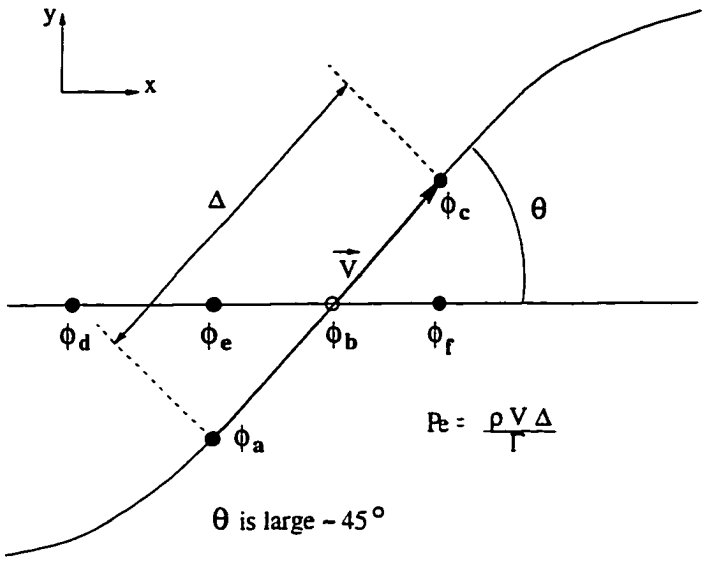

Figure 1.5 Diagram for possible approximation of ϕ_b.

large. This approximation is acceptable only if $\vec{V}$ is nearly aligned with X. and the approximation is more accurate with larger $|\vec{V}|$ (P_e restriction). This is the approach of the first-order upwind scheme.

Case C Approximating ϕ_b by a linear profile using ϕ_d and ϕ_e (second-order truncation error) improves the accuracy considerably when compared to **Case B**. However, the shortcomings of **Case B** are also shared to some extent. This approach is used by the second-order upwind scheme.

Case D Approximating ϕ_b by ϕ_a takes into account the above observation better than **Case B**, but still has the first-order truncation error and Peclet number restriction. If ϕ_c is also used, then the Peclet number restriction is removed. A slight stencil modification of this approach is used by the Skew Upwind and Skew Upwind Weighted schemes.

Case E Approximating ϕ_b by a parabolic profile using ϕ_d, ϕ_e, and ϕ_f can be shown

to have a third-order truncation error. Since approximate downstream information is considered, the Peclet number restriction is removed. This approximation is theoretically better than any of the previous approximations and is known as the QUICK scheme as discussed previously. The basic idea of this scheme is to use a stencil which recognizes both the upwind and more elliptic nature of the flow (depending on the P_e) and fits a polynomial profile appropriate to the stencil used.

The exponential scheme uses the same stencil employed by the central-difference scheme, but instead of using linear-interpolation, a first-order upwind biased profile obtained by solving a one-dimensional, source free convection-diffusion equation is used. It is therefore a better approximation than the first-order upwind scheme, but is still very diffusive if the flow is skewed to the grid.

Mathematically, high convection flow oblique to the grid means that the convection in the other coordinate directions (refer to equation 1.8) are large and should be accounted for in the approximation of the convection and diffusion processes in all the coordinate directions considered. The failure of the first-order upwind scheme to recognize this results in the generation of unacceptably large numerical diffusion for flows oblique to the grid.

1.3.2 High Cross-flow Gradient

A high cross-flow gradient means that there is a steep variation in the dependent variable in the cross-wise grid directions. Mathematically, referring to equation 1.8, this means that the first-derivative term of the total-flux (diffusion term) is large in one or all grid directions, depending on how the flow angles with the grid. If the flow is mostly aligned with a grid direction, then the approximation of the dependent variable along that direction should take into account the rate of variation of that variable in

the mutually perpendicular grid directions. If the flow is skewed to the grid, then the formulation in each direction should take into account the variation rate in the other normal directions.

1.3.3 Unsteady and Source Influence

It is clear from equation 1.8 that unsteady and source terms directly influence the convection and diffusion transports of ϕ. If the conservation of the dependent variable is to be properly maintained, then both terms must be considered in the modeling of the convection and diffusion terms. This is especially important for solving high gradient transient problems and for modeling of the effects of rotating bodies through source term additions, such as a rotating helicopter rotor [33].

1.3.4 Previous Approaches to the Overall Balance Principle

In conclusion, in the pursuit of a stable, highly accurate scheme for general flow problems, the modeling of convection and diffusion transports in a grid direction should properly reflect a balance of the overall conservation of the dependent variable. Among the different mainstream approaches considered thus far, only the Locally Analytic Differencing Scheme (LOADS) by Raithby comes close to applying this overall conservation idea. Unfortunately, an improper approach in the implementation of this concept leads to disastrous non-convergence of LOADS for many non-linear problems. A distinctly different and widely popular approach is to realize the upwind nature of the flow for a higher Peclet number and its more elliptic characteristics for a lower Peclet number. Thus, at a given interface, it is logical to use more than one node in the upstream direction while using fewer (though at least one) nodes in the downstream direction. This wider stencil also shows a greater ability to capture cross-wise transport and source. This is the approach used by the other schemes discussed previously. The most success-

ful scheme to date from this family is the QUICK scheme, which uses a parabolic profile fitted to two upstream and one downstream nodes.

1.4 Current Work: Flux Corrected Method

The Flux Corrected Method (FCM), introduced in this work, attempts to model the convection and diffusion processes at an interface along a grid direction by conserving the whole transport equation. This is done by solving a one-dimensional convection-diffusion equation with a source. The unsteady, cross-wise transport, and source terms are all lumped together with the original source to form one new source used in the one-dimensional equation. Thus, the unsteady multi-dimensional problem is treated as a steady, source driven, one-dimensional problem. FCM is a straightforward extension of the Power Law scheme since all the correction terms fall conveniently into the source of the discretized equation.

FCM has been tested on two- and three-dimensional standard test problems involving high convection flows oblique to the grid and high frequency transient problems. In all the cases considered, FCM has consistently given very accurate results without the need to use an excessively fine grid. Qualitative comparisons using the published results in the literature show that FCM is at least as accurate as the well-known QUICK scheme. Limited comparison with the spectral method has shown that FCM performs very competitively.

Detailed development of this research is presented in the following chapters. **Chapter 2** introduces the governing conservation equations, the discretization process, the FCM approach for modeling the convection-diffusion transport, and the modified SIMPLER algorithm. **Chapter 3** presents the possible choices of the convection-diffusion sources and the combined effects of those possible sources on the solution accuracy. In **Chapter 4**, the detailed development of the general pressure boundary implementation

is presented. **Chapter 5** presents the verification of FCM using two standard test problems commonly used in CFD. Finally, in **Chapter 6**, the conclusions drawn from this research and recommendations for future research in FCM development are suggested.

2 THEORETICAL FORMULATION AND SOLUTION PROCEDURE

2.1 Governing Equations

The mass, momentum, and energy conservation equations applied to a fluid passing through an infinitesimal, fixed control-volume can be written in divergence form as:

Continuity Equation:

$$\frac{\partial \rho}{\partial t} + \nabla \bullet (\rho \mathbf{V}) = \mathbf{0} \ , \tag{2.1}$$

Momentum Equation:

$$\frac{\partial}{\partial t}(\rho \mathbf{V}) + \nabla \bullet (\rho \mathbf{V}\mathbf{V}) = \rho \mathbf{f} + \nabla \bullet \tilde{\prod}_{ij} \ , \tag{2.2}$$

where $\rho \mathbf{f}$ is the body force per unit volume and $\nabla \bullet \tilde{\prod}_{ij}$ is the surface force per unit volume due to external forces on the fluid element. The stress tensor $\tilde{\prod}_{ij}$ consists of both the normal and shearing viscous stresses and its divergence is given by:

$$\nabla \bullet \tilde{\prod}_{ij} = -\nabla P - \nabla(\nabla \bullet \tilde{I}) + \nabla \bullet \tilde{\tau} \ . \tag{2.3}$$

The second term $\nabla(\nabla \bullet \tilde{I})$ vanishes for orthogonal coordinate systems and hence can be neglected in the current formulation.

For Newtonian fluid, the stress at a point is linearly proportional to the rate of strain of the fluid, and the shear component of the stress tensor is given by:

$$\tilde{\tau} = \mu \left[\nabla \mathbf{V} + (\nabla \mathbf{V})^T - \frac{2}{3} \nabla \bullet \mathbf{V} \tilde{I} \right] \ . \tag{2.4}$$

Energy Equation:

$$\frac{\partial E_t}{\partial t} + \nabla \bullet (E_t \mathbf{V}) = \frac{\partial Q}{\partial t} - \nabla \bullet \mathbf{q} + \rho \mathbf{f} \bullet \mathbf{V} + \nabla \bullet (\tilde{\prod}_{ij} \bullet \mathbf{V}) \tag{2.5}$$

In three-dimensional flow, the vector momentum equation consists of three scalar momentum conservation equations corresponding to the three coordinate directions. Thus, together with the continuity and energy equations, there are a total of five equations in six unknowns (three velocity components, density(ρ), enthalpy(h), and temperature(T)). A closure equation is then needed to make the above system of equations deterministic. This final link is provided by the equation of state given in the general form:

$$P = P(\rho, T) \ . \tag{2.6}$$

The mass, momentum, and energy conservation equations (equations 2.1, 2.2, and 2.5) are often called the Navier-Stokes equations, and together with the equation of state, are sufficient to model the most general flow situations, whether steady or unsteady, incompressible or compressible, and laminar or turbulent.

It is obvious that the correct pressure field must satisfy the momentum equation to obtain the velocity field. What is not directly obvious is that the correct pressure field (together with the correct velocity and temperature field) must also satisfy the continuity equation. Pressure affects mass conservation by means of the equation of state through the density and time-dependent density term in the continuity equation. For incompressible flow, density is assumed to be constant throughout the flow-field. Therefore, the time-dependent density term can be dropped from the continuity equation. In addition, if temperature is assumed to be constant, then both the energy equation and the equation of state are not needed. Continuity and momentum equations thus give four equations which can be solved for the three velocity components and pressure. The scope of the present work focuses on the development of an accurate formulation for solving the incompressible Navier-Stokes equations.

2.2 Methods for Solving Incompressible Flow Equations

Even though the complexity due to the coupling of the energy equation (through the equation of state) to the mass and momentum conservation equations no longer exists, solving the incompressible Navier-Stokes equations does not prove to be much simpler than solving the compressible counterparts. The real difficulty in solving the incompressible flow equations lies in the methodology used to determine the pressure field during the iterative process. The pressure gradient forms a part of the source term of the momentum equation. Given a pressure field, there is no particular difficulty in solving the momentum equation for the velocity field. However, there is no obvious equation for obtaining the pressure field. Moreover, there no longer exists a 'direct' means by which pressure can affect mass conservation and vice versa. The pressure field is only 'indirectly' specified through the continuity equation. When the correct pressure field is used to solve the momentum equations, the resulting velocity field also satisfies the mass conservation.

For two-dimensional situations, it is possible to eliminate the pressure terms by cross-differencing and then substituting the two components of the momentum equation. Using the definition of streamfunction (for steady and two-dimensions) and vorticity. the resulting combined equation is transformed into what is often referred to as the vorticity-transport equation. Similarly, the continuity equation can also be expressed in terms of the streamfunction. The resulting two equations can then be solved for the two dependent variables (streamfunction and vorticity). Upon convergence of the iterative process, pressure can be obtained separately by solving a Poisson equation. This approach is known as the vorticity/streamfunction method, and its wide usage has been limited to two-dimensional flow problems only.

Another approach used for solving the incompressible Navier-Stokes equations is known as the primitive variable formulation, wherein the primitive variables $\mathbf{V}$ and P

are directly solved. A method based on the primitive variable technique is the artificial compressibility method which was first proposed by Chorin [34]. This method was originally formulated for steady flows and has recently been extended to time-accurate solutions by Kwak et al. [35] and Merkle and Athavale [36]. In this method, a pseudo-time derivative of pressure is added to the continuity equation, and this provides the coupling between the velocity and the pressure field. At a given time level, the equations are advanced in pseudo-time by subiterations until a divergent-free velocity field is obtained at the next time level.

The most common primitive variable approach is introduced by Harlow and Welch [37]. This method tries to provide the velocity-pressure coupling by using an iterative procedure which alternately solves for the velocity field and pressure field. Given an initial pressure distribution, the momentum equation is solved to determine the velocity field. This velocity field does not necessarily satisfy the continuity equation (unless the correct pressure field is used) and thus needs to be corrected to preserve mass conservation. This is done via a correction to the pressure field by solving the Poisson equation for pressure, which is derived from the mass conservation equation. The subiteration is continued until convergence is achieved for that time level. A popular derivative of this method is the SIMPLER scheme of Patankar [5].

2.3 Conservation Equations in Cartesian Coordinates

For simplicity of development, the governing incompressible flow equations are expressed in two-dimensional Cartesian coordinates:

Continuity Equation:

$$\frac{\partial}{\partial x}(\rho u) + \frac{\partial}{\partial y}(\rho v) = 0 \,, \tag{2.7}$$

X-momentum Equation:

$$\frac{\partial}{\partial t}(\rho u) + \frac{\partial}{\partial x}((\rho u)u) + \frac{\partial}{\partial y}((\rho v)u) = \frac{\partial}{\partial x}\left(\mu\frac{\partial u}{\partial x}\right) + \frac{\partial}{\partial y}\left(\mu\frac{\partial u}{\partial y}\right) - \frac{\partial P}{\partial x} . \tag{2.8}$$

Y-momentum Equation:

$$\frac{\partial}{\partial t}(\rho v) + \frac{\partial}{\partial x}((\rho u)v) + \frac{\partial}{\partial y}((\rho v)v) = \frac{\partial}{\partial x}\left(\mu\frac{\partial v}{\partial x}\right) + \frac{\partial}{\partial y}\left(\mu\frac{\partial v}{\partial y}\right) - \frac{\partial P}{\partial y} . \tag{2.9}$$

It should also be noted that body forces have been neglected in the momentum equations.

These conservation equations can also be written as:

Continuity Equation:

$$\frac{\partial F_x}{\partial x} + \frac{\partial F_y}{\partial y} = 0 , \tag{2.10}$$

where

$$F_x = \rho u \tag{2.11}$$

$$: \quad x-direction\ flow-flux ,$$

$$F_y = \rho v \tag{2.12}$$

$$: \quad y-direction\ flow-flux ,$$

X-momentum Equation:

$$\frac{\partial}{\partial t}(\rho u) + \frac{\partial}{\partial x}(J_{xx}) + \frac{\partial}{\partial y}(J_{yx}) = -\frac{\partial P}{\partial x} , \tag{2.13}$$

where

$$J_{xx} = (\rho u)u - \mu\frac{\partial u}{\partial x} \tag{2.14}$$

$$: \quad x-momentum\ x-direction\ total-flux ,$$

$$: \quad x-momentum\ directional\ total-flux ,$$

$$J_{yx} = (\rho v)u - \mu\frac{\partial u}{\partial y} \tag{2.15}$$

$$: \quad x-momentum\ y-direction\ total-flux ,$$

$$: \quad x-momentum\ non-directional\ total-flux ,$$

Y-momentum Equation:

$$\frac{\partial}{\partial t}(\rho v) + \frac{\partial}{\partial x}(J_{xy}) + \frac{\partial}{\partial y}(J_{yy}) = -\frac{\partial P}{\partial y} \tag{2.16}$$

where

$$J_{xy} = (\rho u)v - \mu\frac{\partial v}{\partial x} \tag{2.17}$$

$$: \; y\text{-}momentum\ x\text{-}direction\ total\text{-}flux\ .$$

$$: \; y\text{-}momentum\ non\text{-}directional\ total\text{-}flux\ .$$

$$J_{yy} = (\rho v)v - \mu\frac{\partial v}{\partial y} \tag{2.18}$$

$$: \; y\text{-}momentum\ y\text{-}direction\ total\text{-}flux\ .$$

$$: \; y\text{-}momentum\ directional\ total\text{-}flux\ ,$$

Note that the second subscript indicates which momentum equation the total-flux belongs to. and the first subscript, when used in conjunction with the second subscript. indicates whether it is directional or non-directional. Careful observation of the x- and y-momentum equations (equations 2.8 and 2.9) shows that the scalar momentum equation in a given coordinate direction is basically a transport equation for the velocity component in that coordinate direction. Both equations also posses similar form and thus can be written in a generic differential transport equation. It can also be shown that other conservation principles can always be written in the same generic form. For this reason, a generic scalar differential transport equation will be used to represent the flow conservation principles. This will avoid unnecessary repetition and allows the development of a numerical scheme for any general conservation variable. If the dependent variable is denoted by ϕ, the general transport equation is given by:

$$\frac{\partial}{\partial t}(\rho\phi) + \nabla \bullet (\rho\mathbf{V}\phi) = \nabla \bullet (\Gamma\nabla\phi) + S\ , \tag{2.19}$$

where Γ is the diffusion coefficient and S is the source term. The quantities Γ and S are specific to a particular meaning of ϕ. The four terms in the general transport equation are

the unsteady, convection, gradient driven diffusion, and source terms. Not all diffusion fluxes are governed by the gradient of the relevant variable. However, whatever cannot be cast into this 'nominal' diffusion term can always be expressed as part of the source term. In Cartesian coordinates, equation 2.19 will take the form:

$$\frac{\partial}{\partial t}(\rho\phi) + \frac{\partial}{\partial x}((\rho u)\phi) + \frac{\partial}{\partial y}((\rho v)\phi) = \frac{\partial}{\partial x}\left(\Gamma\frac{\partial\phi}{\partial x}\right) + \frac{\partial}{\partial y}\left(\Gamma\frac{\partial\phi}{\partial y}\right) + S\ , \tag{2.20}$$

which is the same as equation 1.8. The corresponding conservation form is given by:

$$\frac{\partial}{\partial t}(\rho\phi) + \frac{\partial}{\partial x}(J_x) + \frac{\partial}{\partial y}(J_y) = S\ , \tag{2.21}$$

where

$$J_x = (\rho u)\phi - \Gamma\frac{\partial\phi}{\partial x} \tag{2.22}$$

$$: \quad x\text{-}direction\ total\text{-}flux\ ,$$

$$J_y = (\rho v)\phi - \Gamma\frac{\partial\phi}{\partial y} \tag{2.23}$$

$$: \quad y\text{-}direction\ total\text{-}flux\ .$$

Note that in the conservation form, the convection and diffusion terms in a coordinate direction are grouped together to form the total-flux in that direction. This is an important property which will be used in the subsequent development of this work.

2.4 Integral Balance of Conservation Equations

2.4.1 Control Volume Approach

Equation 2.21 implies a continuous distribution of the dependent variable ϕ over an arbitrary domain. In the real, finite world, the domain of interest must be divided into smaller, non-overlapping subdomains (control-volumes) over each of which the conservation principle is applied. For the scheme to be consistent, it is important to impose the condition that the flux leaving a portion of the boundary enclosing a control-volume is the

same as the flux entering the adjacent control-volume sharing that same boundary portion. Moreover, the summation of the total influx and outflux of all the control-volumes must reflect the overall conservation of ϕ applied over the whole domain considered. This control-volume approach for discretizing the governing equations ensures that the final discretized equation conserves the dependent variable locally and globally and thus will help suppress any production of non-physical sources or sinks which are not part of the original differential equation.

2.4.2 Time Integration

Time variation of a general variable ϕ is given by a generalized formula

$$\int_t^{t+\Delta t} \phi \, dt = f\phi + (1-f)\phi^o \ , \tag{2.24}$$

where ϕ^o is the value at time t, and ϕ is the value at time $t + \Delta t$. For the rest of this work, a variable with the superscript ^{o} represents a variable at the old timestep, and a variable without the superscript ^{o} represents a variable at the new timestep.

For certain specific values of the weighting factor f, the discretization equation reduces to one of the well-known schemes for parabolic differential equations. In particular, f=0 leads to an explicit scheme, f=0.5 leads to the Crank-Nicholson scheme, and f=1 leads to a fully implicit scheme.

2.4.3 Integral Balance of Continuity Equation

Integrating the mass conservation equation (equation 2.10) over the two-dimensional control-volume (Figure 2.1) results in the following mass integral balance:

$$\int_s^n \int_w^e \frac{\partial}{\partial x} F_x \, dxdy + \int_w^e \int_s^n \frac{\partial}{\partial y} F_y \, dydx = 0 \ , \tag{2.25}$$

where the order of the integration is chosen according to the flux direction. Evaluation of the integrals yields the discretized continuity equation:

$$F_{x-e}^{intg} - F_{x-w}^{intg} + F_{y-n}^{intg} - F_{y-s}^{intg} = 0 \ , \tag{2.26}$$

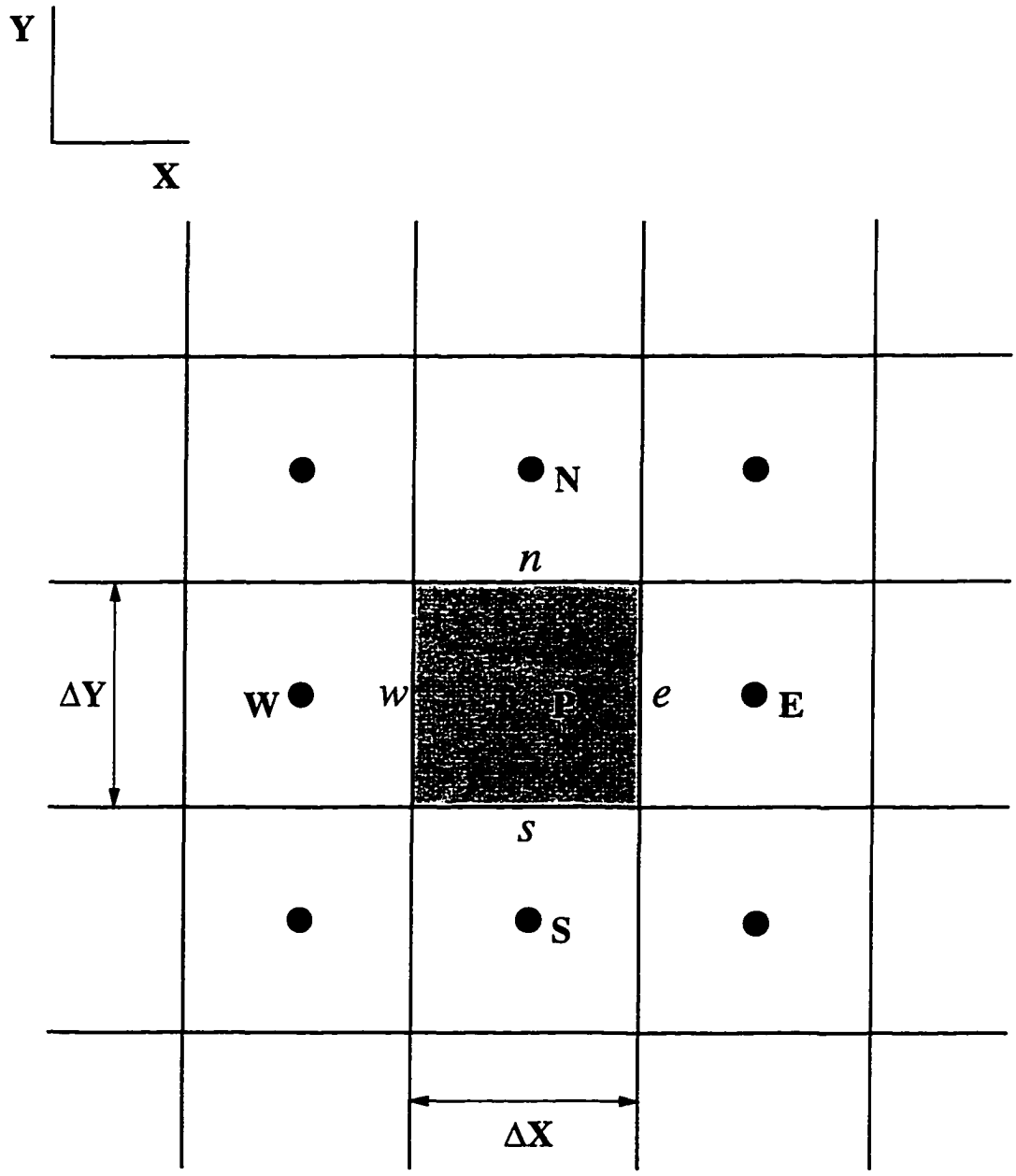

Figure 2.1 Two-dimensional X-Y control-volume

where

$$F^{intg}_{x-e,w} = \int_s^n F_{x-e,w}\, dy = F_{x-e,w}\, \Delta y \tag{2.27}$$

$$: \; integrated\ x-direction\ flow-flux\ at\ interface\ e,w\ ,$$

$$F^{intg}_{y-n,s} = \int_w^e F_{y-n,s}\, dx = F_{y-n,s}\, \Delta x \tag{2.28}$$

$$: \; integrated\ y-direction\ flow-flux\ at\ interface\ n,s\ .$$

The expressions for the flow-flux in the x- and y-directions are given in equations 2.11 and 2.12.

2.4.4 Integral Balance of General Transport Equation

Similarly, the general transport equation (equation 2.21) is integrated over the control volume (Figure 2.1) and over the time interval from t to $t + \Delta t$. Assuming that the grid point value of ϕ (grid point P) prevails throughout the control-volume, the following discretized equation is obtained:

$$\frac{\left[(\rho\phi)_p - (\rho\phi)^o_p\right]\Delta x\Delta y\Delta z}{\Delta t} +$$

$$f(J^{intg}_{x-e} - J^{intg}_{x-w} + J^{intg}_{y-n} - J^{intg}_{y-s}) +$$

$$(1-f)(J^{o\ intg}_{x-e} - J^{o\ intg}_{x-w} + J^{o\ intg}_{y-n} - J^{o\ intg}_{y-s}) =$$

$$fS^{intg} + (1-f)S^{o\ intg}\ , \tag{2.29}$$

where

$$J^{intg}_{x-e,w} = \int_s^n J_{x-e,w}\, dy = J_{x-e,w}\, \Delta y \tag{2.30}$$

$$: \; integrated\ x-direction\ total-flux\ at\ interface\ e,w\ ,$$

$$J^{intg}_{y-n,s} = \int_w^e J_{y-n,s}\, dx = J_{y-n,s}\, \Delta x \qquad (2.31)$$

$$: \quad integrated\ y-direction\ total-flux\ at\ interface\ n,s\ ,$$

$$S^{intg} = \int_s^n \int_w^e S\, dxdy = S\Delta x\Delta y\ .$$

The expressions for the total-flux in the x- and y-directions are given in equations 2.22 and 2.23. The next step toward the formulation of the discretized form of the transport equation is to decide how to evaluate the total-fluxes at the control-volume faces.

2.5 Modeling of the Convection and Diffusion Transport

2.5.1 Review of Basic Qualitative Characteristics

The expression for the total-flux in a coordinate direction consists of the convection and diffusion transport terms in that direction. For convenience, the equation for the total-flux in the x-direction (equation 2.22) is repeated below:

$$J_x = (\rho u)\phi - \Gamma \frac{\partial \phi}{\partial x} \qquad (2.32)$$

where

$$(\rho u)\phi \ : \ Convection\ flux\ ,$$

$$\Gamma \frac{\partial \phi}{\partial x} \ : \ Diffusion\ flux\ .$$

Throughout the first chapter, the nature of convection and diffusion processes has been discussed rather extensively. However, a short summary of the qualitative characteristics of both transport mechanisms is helpful in the development of a physically consistent and accurate numerical scheme.

Convection transports the dependent variable in the direction of the velocity. The larger the magnitude of the velocity, the more prominent is the influence of the upstream

information. With the help of Spalding's concept of one-way and two-way coordinates, it can be said that convection exhibits more of a one-way nature in the presence of a large flow-rate. On the other hand, diffusion always has two-way influences. It is true that when the flow-rate is large, convection overpowers diffusion and thus makes the space coordinates nearly one-way. Unfortunately, most practical flow situations have a dominant one-way nature in certain regions and a strong two-way influence in other regions. Emphasizing one or the other in the modeling of the transport terms will result in a numerical scheme which is inferior in other situations. The differences in the modeling of the convection and diffusion fluxes at the control-volume faces contributes to the different characteristics and accuracy of the various schemes in existence.

2.5.2 Steady One-dimensional Convection Diffusion with Source

A convenient way to model the profile of the dependent variable ϕ and its derivative at a control-volume face in a given coordinate direction is to use the steady, one-dimensional, convection-diffusion equation given by:

$$\frac{\partial}{\partial X}(J_X) = \frac{\partial}{\partial X}\left((\rho u)\phi - \Gamma\frac{\partial \phi}{\partial X}\right) = S_{cd}\ , \quad 0 \leq X \leq L\ , \tag{2.33}$$

where

$$(\rho u) = constant\ , \tag{2.34}$$

$$\Gamma = constant\ , \tag{2.35}$$

$$S_{cd} = constant\ . \tag{2.36}$$

The corresponding domain of interest is given in Figure 2.2 and the boundary conditions are defined by equations 2.37 and 2.38.

$$\phi = \phi_o \ \ at\ X = 0\ , \tag{2.37}$$

$$\phi = \phi_L \ \ at\ X = L\ . \tag{2.38}$$

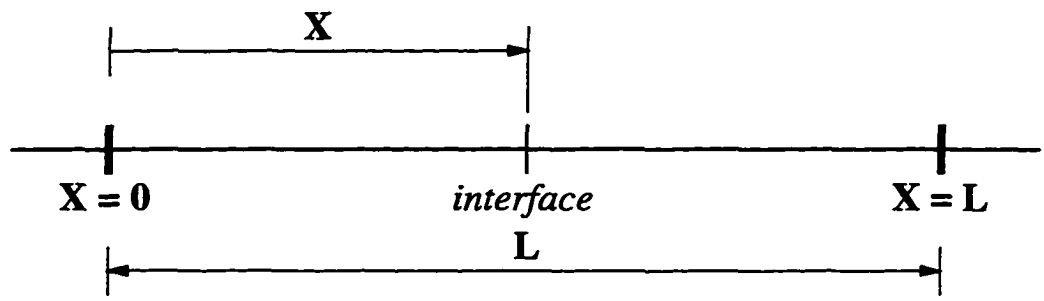

Figure 2.2 Domain for one-dimensional convection-diffusion equation.

At this point, it is important to define the convection strength (F), the diffusion strength (D), and the Peclet number (local grid Reynolds number), which is the ratio of the strengths of convection and diffusion.

$$F = (\rho u) , \tag{2.39}$$

$$D = \frac{\Gamma}{L} , \tag{2.40}$$

$$P_e = \frac{(\rho u)L}{\Gamma} = \frac{F}{D} . \tag{2.41}$$

Equation 2.33 can be rewritten as:

$$\Gamma \frac{\partial^2 \phi}{\partial X^2} - (\rho u)\frac{\partial \phi}{\partial X} = -S_{cd} . \tag{2.42}$$

Equation 2.42 is a one-dimensional, steady, second-order, constant-coefficients, non-homogeneous ODE which can be solved using any of the available standard methods. The general solution is composed of two parts, namely, the homogeneous and the particular solutions. The characteristic equation and characteristic roots of the differential equation are given by:

$$\begin{aligned} \Gamma\lambda^2 - (\rho u)\lambda &= 0 \\ \lambda[\Gamma\lambda - (\rho u)] &= 0 \end{aligned} \tag{2.43}$$

and

$$\lambda_1 = 0 , \tag{2.44}$$

$$\lambda_2 = \frac{(\rho u)}{\Gamma} . \tag{2.45}$$

The homogeneous solution is obtained as:

$$\phi_H(X) = e^{P_e(X/L)} , \tag{2.46}$$

and the particular solution is given by:

$$\phi_P(X) = \frac{S_{cd}X}{(\rho u)} . \tag{2.47}$$

The sum of the homogeneous and particular solutions gives the general solution:

$$\phi(X) = \phi_H(X) + \phi_P(X) \tag{2.48}$$

$$= C_1 \, e^{P_e(X/L)} + \frac{S_{cd}X}{(\rho u)} + C_2 . \tag{2.49}$$

Applying the left and right boundary conditions (equations 2.37 and 2.38) results in the following expressions for the constants C_1 and C_2:

$$C_1 = \frac{(\phi_L - \phi_o) - (S_{cd}L)/(\rho u)}{e^{P_e} - 1} , \tag{2.50}$$

$$C_2 = \frac{\phi_o e^{P_e} - \phi_L + (S_{cd}L)/(\rho u)}{e^{P_e} - 1} . \tag{2.51}$$

Substituting the above constants into equation 2.49 results in the profile of the dependent variable ϕ as a function of the interface distance X:

$$\phi(X) = \phi_o + \left[\frac{e^{P_e(X/L)} - 1}{e^{P_e} - 1}\right](\phi_L - \phi_o) + \phi_s(X) , \tag{2.52}$$

where

$$\phi_s(X) = -\left(\frac{S_{cd}L}{(\rho u)}\right)\left[\frac{e^{P_e(X/L)} - 1}{e^{P_e} - 1}\right] + \left(\frac{S_{cd}}{(\rho u)}\right)X . \tag{2.53}$$

Note that $\phi_s(X)$ is the correction to the homogeneous solution due to the presence of source S_{cd}. If S_{cd} is set to zero, then $\phi_s(X)$ vanishes, and $\phi(X)$ recovers the exponential scheme for one-dimensional, convection-diffusion, without source [5].

The profile of the first derivative of ϕ can then be obtained as:

$$\frac{\partial \phi}{\partial X} = \left(\frac{P_e}{L}\right)\left[\frac{e^{P_e(X/L)}}{e^{P_e}-1}\right](\phi_L - \phi_o) + \frac{\partial \phi_s}{\partial X}\ , \tag{2.54}$$

where

$$\frac{\partial \phi_s}{\partial X} = -\left(\frac{S_{cd}L}{\Gamma}\right)\left[\frac{e^{P_e(X/L)}}{e^{P_e}-1}\right] + \frac{S_{cd}}{(\rho u)}\ . \tag{2.55}$$

Again, vanishing S_{cd} means that the source-induced first-derivative term becomes zero. and only the homogeneous term remains.

To better understand the nature of the profile of ϕ obtained from solving the convection-diffusion equation considered previously, two complementing cases are investigated. In the first case, the effect of source S_{cd} is neglected and the homogeneous solution of ϕ along X is plotted for different values of the Peclet number (Figure 2.3).

It is observed that the profile of ϕ is far from linear except for small values of $|P_e|$. For small $|P_e|$ (small convection and/or large diffusion), the influences of ϕ_o and ϕ_L on the middle interface value are equally dominant. For large $|P_e|$ (large convection and/or small diffusion), the interface value is predominantly influenced by the upstream value. This is consistent with the physics. The role of the boundary conditions, in this case, is to establish a difference in the boundary ϕ values so that the effect of different Peclet numbers can be established.

In the second case, the boundary values are set to equal value, leaving only the source induced part of the general solution. As expected, both the Peclet number and the source level have a profound influence on the profile of ϕ. The effect of varying the Peclet number while fixing S_{cd} is given in Figure 2.4. For a given source level, as $|P_e|$ increases, the peak of the profile decreases in magnitude and is shifted more toward the downstream direction. Recall that the upstream and downstream are defined relative to the flow direction. Maximum peak occurs at P_e=0. Thus it can be concluded that maximum correction to the homogeneous profile happens at the middle of the domain for small values of the Peclet number. The plot of the percentage of the ratio of peak value

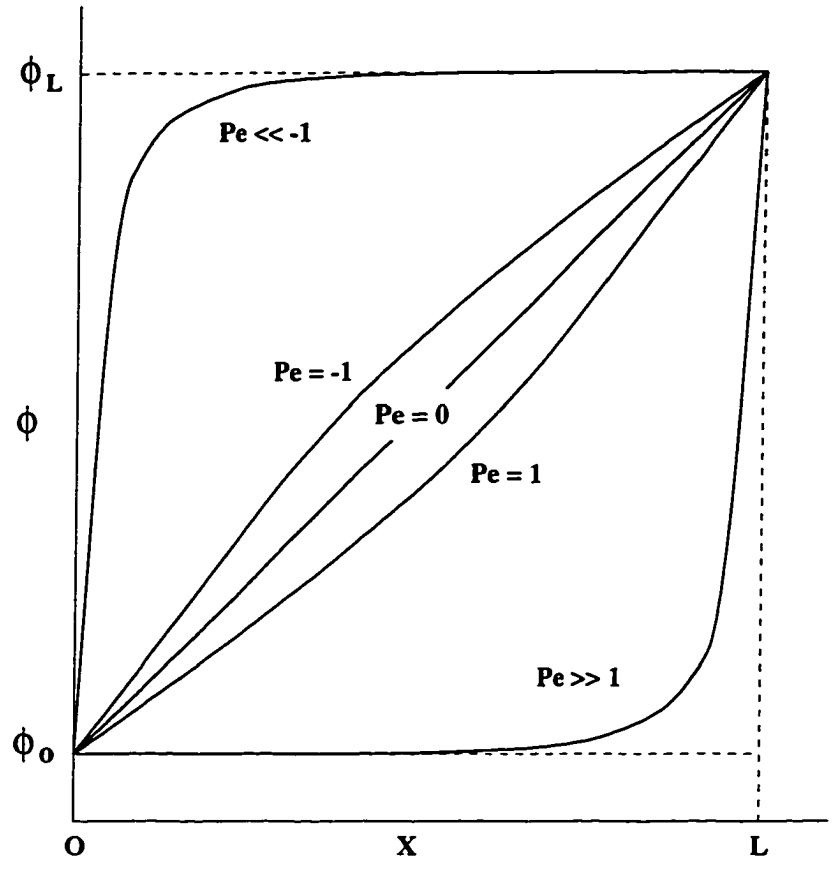

Figure 2.3 Profile of ϕ with S_{cd}=0 and different Peclet numbers.

at a given Peclet number to the maximum peak value as the Peclet number increases is given in Figure 2.5. The curve is identical for different source levels. This plot reveals that the correction is significant until $|P_e| \approx 20$. At higher $|P_e|$, the curve is very slowly assymptoting to 0 as $P_e \rightarrow \infty$. In essence, this says that for a very high convection flow aligned to a grid direction, the homogeneous solution is nearly sufficient to model the interface value of ϕ. Recall that this is the ideal condition for the application of the Power Law scheme.

The profile of the particular solution as the Peclet number is fixed and the source level is varied is given in Figure 2.6. It is observed that for a given Peclet number, different source levels give different peak values but the same peak location. In this analysis, all

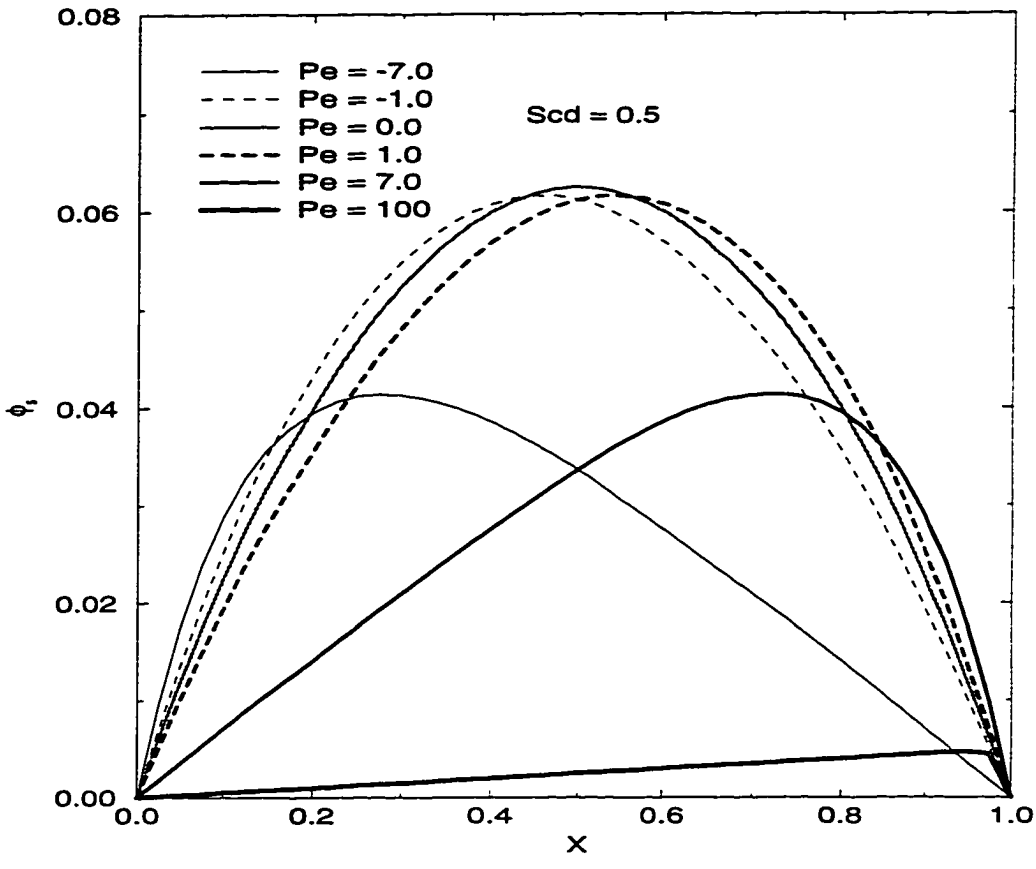

Figure 2.4 Profile of ϕ with $S_{cd} = 0.5$ and different $|P_e|$.

source is assumed to be positive, and a negative source only means a negative correction profile to the homogeneous solution.

In the general case of a non-zero source and nonequal left and right boundary conditions, the combined homogeneous and particular solutions, each with its own characteristics, gives the exact profile of ϕ along X.

Attention will now be focused on finding the expression of the total-flux variation along X. First, the expressions for the dependent variable ϕ and its derivative (equation 2.52 and equation 2.54) can be written as:

$$\phi(X) = [\alpha(X)\phi_o + (1 - \alpha(X))\phi_L] + \phi_s(X) \ , \tag{2.56}$$

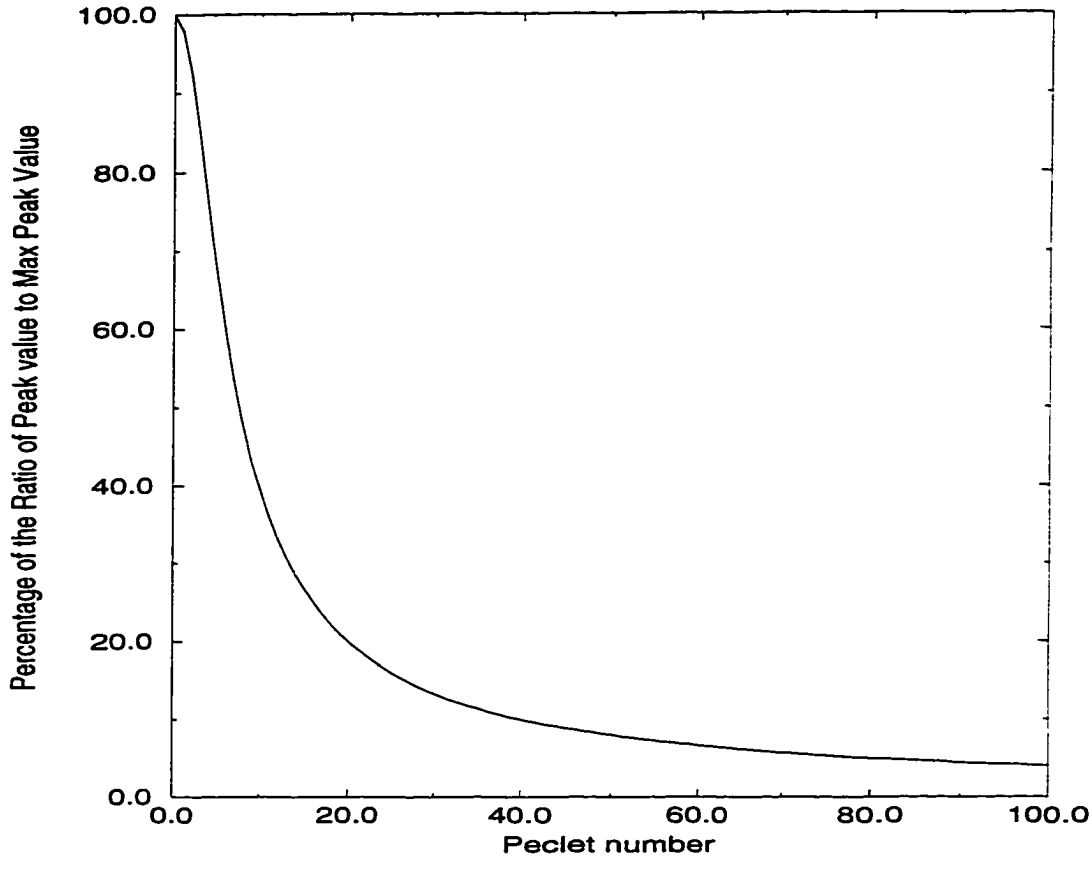

Figure 2.5 Middle interface value of ϕ as function of $|P_e|$.

where

$$\alpha(X) = \frac{e^{P_e} - e^{P_e(X/L)}}{e^{P_e} - 1}\,, \tag{2.57}$$

and

$$\frac{\partial \phi}{\partial X}(X) = \beta(X)(\phi_L - \phi_o) + \frac{\partial \phi_s}{\partial X}\,, \tag{2.58}$$

where

$$\beta(X) = \left(\frac{(\rho u)}{\Gamma}\right)\left[\frac{e^{P_e(X/L)}}{e^{P_e} - 1}\right]\,. \tag{2.59}$$

An intermediate variable J_x^* will now be defined as:

$$\begin{aligned} J_x^*(X) &= \frac{J_x(X)}{D} = J_x(X)\left(\frac{L}{\Gamma}\right) \\ &= \left((\rho u)\phi(X) - \Gamma\frac{\partial \phi}{\partial x}(X)\right)\left(\frac{L}{\Gamma}\right) \end{aligned} \tag{2.60}$$

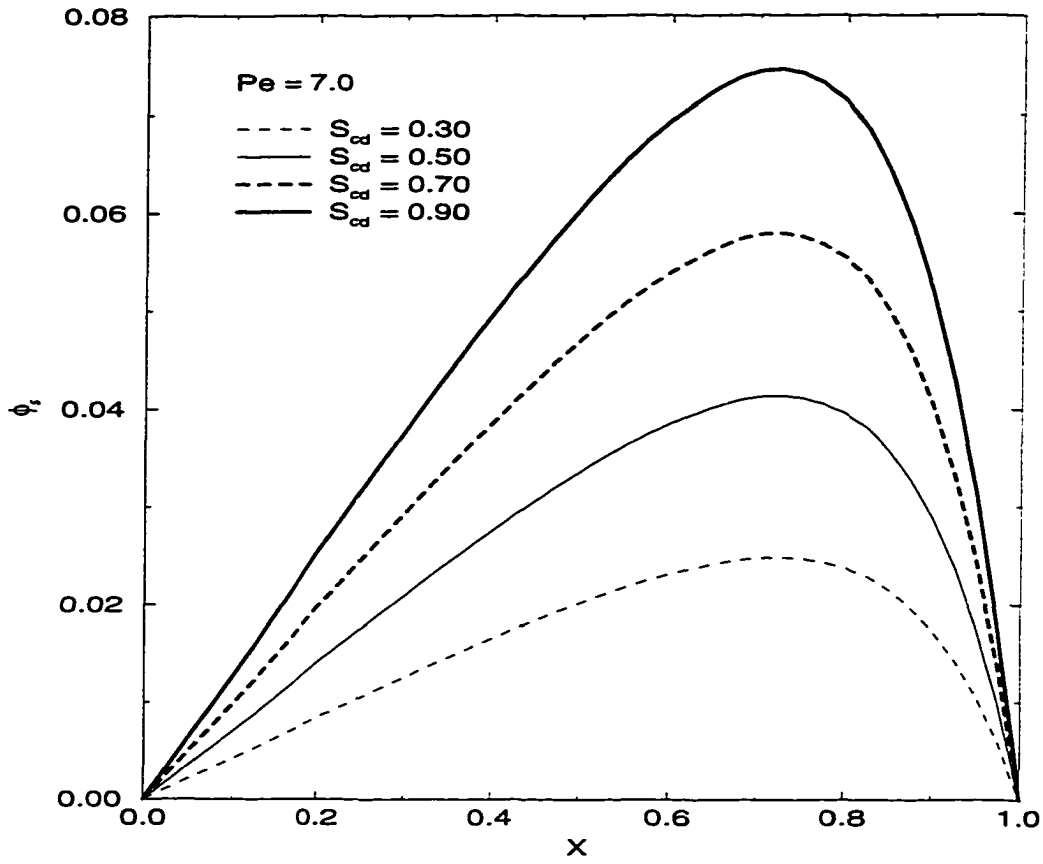

Figure 2.6 Profile of ϕ with fixed $|P_e|$ and different S_{cd}.

$$= P_e\phi(X) - L\frac{\partial\phi}{\partial X}(X) .$$

Substituting equation 2.56 and 2.58 into the above equation results in:

$$J_x^*(X) = [B(P_e)\phi_o - A(P_e)\phi_L] + Js_x^* , \tag{2.61}$$

where

$$A(P_e) = \frac{P_e}{e^{P_e} - 1} , \tag{2.62}$$

$$B(P_e) = \frac{P_e e^{P_e}}{e^{P_e} - 1} , \tag{2.63}$$

and

$$Js_x^* = P_e\phi_s(X) - L\frac{\partial\phi_s}{\partial X}(X) . \tag{2.64}$$

The term involving $A(P_e)$ and $B(P_e)$ on the right-hand side of equation 2.61 (within the [ ]) is the constant total-flux term and is identical to the one obtained by Patankar [5] by solving the one-dimensional convection-diffusion equation without a source:

$$\frac{\partial J_x}{\partial X} = S_{cd} = 0 \ . \tag{2.65}$$

On the other hand, Js_x^* results from the presence of a source in the convection-diffusion equation and can be understood as the correction to the homogeneous constant flux profile.

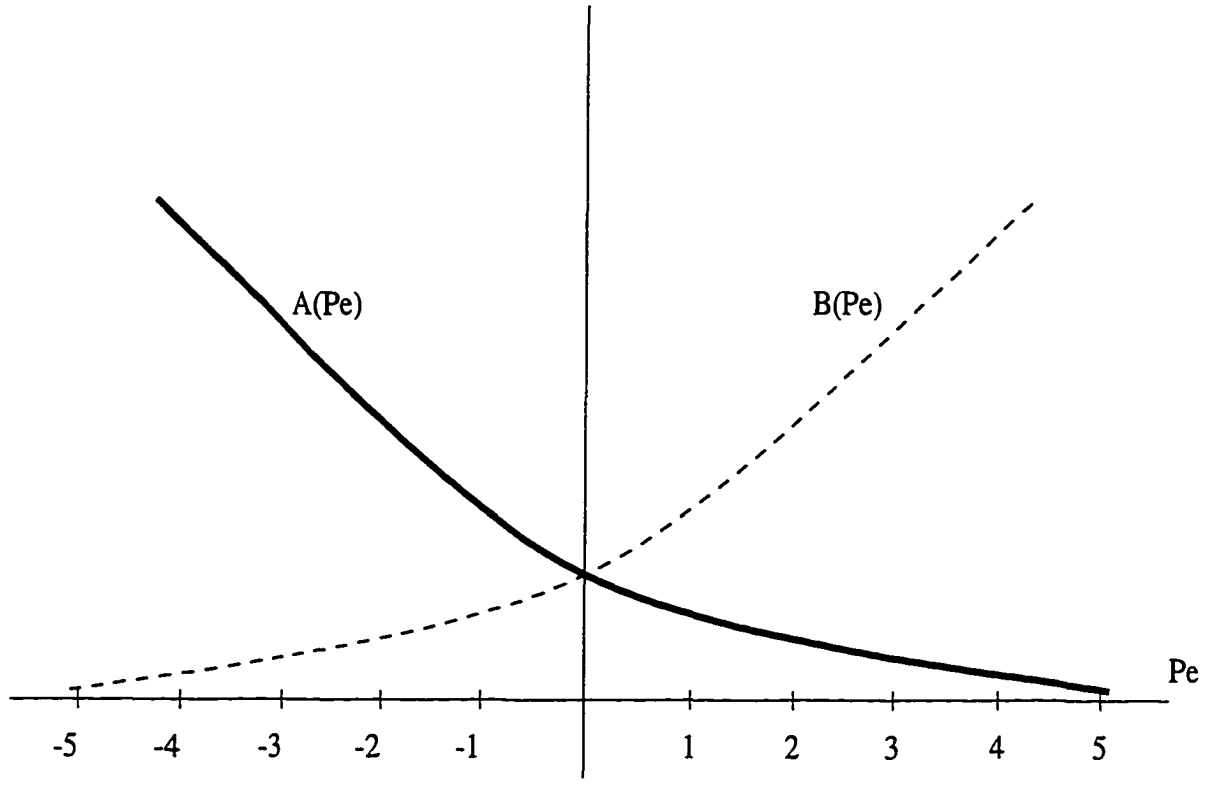

Figure 2.7 Variation of $A(P_e)$ and $B(P_e)$ as function of P_e.

The variation of $A(P_e)$ and $B(P_e)$ as a function of the Peclet number is given in Figure 2.7. Patankar also showed that $A(P_e)$ and $B(P_e)$ posses certain mathematical characteristics. First, subracting $A(P_e)$ from $B(P_e)$ results in:

$$B(P_e) = A(P_e) + P_e \,. \tag{2.66}$$

Secondly, careful observation of Figure 2.7 shows that there exists a certain kind of symmetry between the two curves. Rotating the vertical axis such that P_e becomes $-P_e$ will result in the two functions interchanging their roles. Thus, $A(P_e)$ and $B(P_e)$ must be related by:

$$A(-P_e) = B(P_e) \,, \tag{2.67}$$

$$B(-P_e) = A(P_e) \,. \tag{2.68}$$

Consequently, $A(P_e)$ and $B(P_e)$ can be rewritten as:

$$A(P_e) = A(|P_e|) + [\![-P_e, 0]\!] \,, \tag{2.69}$$

$$B(P_e) = A(|P_e|) + [\![P_e, 0]\!] \,. \tag{2.70}$$

Substituting equation 2.66 into equation 2.61 and then using equation 2.69 gives the following equation:

$$J_x^*(X) = P_e\phi_o + \{A(|P_e|) + [\![-P_e, 0]\!]\}(\phi_o - \phi_L) + Js_x^* \,, \tag{2.71}$$

where $[\![\ ,\ ,\ ]\!]$ means the largest of the quantities contained within it. Similarly, using equations 2.66, 2.61, and 2.70 results in the second equation for $J_x^*(X)$:

$$J_x^*(X) = P_e\phi_L + \{A(|P_e|) + [\![P_e, 0]\!]\}(\phi_o - \phi_L) + Js_x^* \,. \tag{2.72}$$

It can be easily verified that equation 2.71 and equation 2.72 are identical. The purpose of writing $J_x^*(X)$ in these two forms will be evident in the section to follow.

Attention will now be focused on the $Js_x^*(X)$. Substituting equation 2.53 and equation 2.55 into equation 2.64 yields:

$$\begin{aligned} Js_x^*(X) &= -\left(\frac{L^2}{\Gamma}S_{cd}\right)\left[\frac{e^{P_e(X/L)}-1}{e^{P_e}-1}\right]+\frac{XL}{\Gamma}S_{cd}+ \\ &\quad \left(\frac{L^2}{\Gamma}S_{cd}\right)\left[\frac{e^{P_e(X/L)}}{e^{P_e}-1}\right]-\frac{L}{(\rho u)}S_{cd}\left(\frac{\Gamma}{L}\times\frac{L}{\Gamma}\right) \\ &= \left(\frac{L^2}{\Gamma}S_{cd}\right)\left[\frac{1}{e^{P_e}-1}\right]+\frac{XL}{\Gamma}S_{cd}-\left(\frac{L^2}{\Gamma}S_{cd}\right)\times\frac{1}{P_e} \\ &= \left(\frac{L^2}{\Gamma}S_{cd}\right)\left[\frac{1}{e^{P_e}-1}-\frac{1}{P_e}\right]+\frac{XL}{\Gamma}S_{cd} \\ &= \frac{L}{\Gamma}[LQ(P_e)+X]S_{cd}\ , \end{aligned} \tag{2.73}$$

where Q is a function of the Peclet number only and is given by:

$$Q(P_e)=\frac{P_e-e^{P_e}+1}{Pe^{P_e}-P_e}\ . \tag{2.74}$$

Note that $Q(P_e)$ is singular for P_e=0; however, taking the limit as $P_e\to 0$, yields $Q(P_e)\to-\frac{1}{2}$.

Finally, using equations 2.71, 2.72, and 2.73, the expression for the total-flux profile can be written as:

$$J_x(X)=J_x^*(X)D=J_x^*\left(\frac{\Gamma}{L}\right)$$

$$=F\phi_o+\{DA(|P_e|)+[\![-F,0]\!]\}(\phi_o-\phi_L)+Js_x(X) \tag{2.75}$$

$$=F\phi_L+\{DA(|P_e|)+[\![F,0]\!]\}(\phi_o-\phi_L)+Js_x(X)\ , \tag{2.76}$$

where

$$Js_x(X)=[LQ(P_e)+X]S_{cd}\ . \tag{2.77}$$

An important observation concerning the above equation is that the total-flux at a given X-location now consists of a term which multiplies the difference in the boundary values of ϕ. Note that the total-flux correction $Js_x(X)$ is directly driven by the strength of the source and is not monotonous but varies across the domain considered. Again, in the absence of a source, the total-flux correction vanishes and the total-flux profile

J_x becomes a constant profile resulting from solving the convection-diffusion equation without a source.

2.6 Flux Corrected Method: Application of Steady One-dimensional Convection Diffusion with Source to Two- and Three-dimensional Transport Modeling

2.6.1 Discretization of General Transport Equation

Recall the general conservation equation given previously in equation 2.20:

$$\frac{\partial(\rho\phi)}{\partial t} + \frac{\partial}{\partial x}\left((\rho u)\phi - \Gamma\frac{\partial\phi}{\partial x}\right) + \frac{\partial}{\partial y}\left((\rho v)\phi - \Gamma\frac{\partial\phi}{\partial y}\right) = S\ , \tag{2.78}$$

$$\frac{\partial(\rho\phi)}{\partial t} + \frac{\partial}{\partial x}(J_x) + \frac{\partial}{\partial y}(J_y) = S\ . \tag{2.79}$$

The above equation represents a conservation of the dependent variable ϕ with terms representing the unsteady term, x-direction transport (convection and diffusion), y-direction transport, and a source. An increase or decrease in one or more of these four terms will result in changes in the other terms such that the overall balance of equation 2.78 is still maintained. Integration of equation 2.79 over time and over a two-dimensional control-volume (Figure 2.1) is given in equation 2.29 and is quoted here for convenience:

$$\frac{\left[(\rho\phi)_p - (\rho\phi)_p^o\right]\Delta x\Delta y}{\Delta t} +$$

$$f(J_{x-e}^{intg} - J_{x-w}^{intg} + J_{y-n}^{intg} - J_{y-s}^{intg}) +$$

$$(1-f)(J_{x-e}^{o\ intg} - J_{x-w}^{o\ intg} + J_{y-n}^{o\ intg} - J_{y-s}^{o\ intg}) =$$

$$fS^{intg} + (1-f)S^{o\ intg}\ . \tag{2.80}$$

Having decided on how to model the convection-diffusion transport, it is now possible to take the next step toward the formulation of the discretized equation, which is to

express the total-flux at a control-volume face in a coordinate direction in terms of the neighboring ϕ values in that direction. Consider for example the w-interface in Figure 2.1. Flux Corrected Method (FCM) realizes that the expression of the total-flux at the w-interface is actually governed by the same transport equation 2.78 applied to the main control-volume containing that interface. Thus, a natural way to evaluate the x-direction total-flux is to use the conservation principle itself, which is rewritten in the form:

$$\begin{aligned} \frac{\partial}{\partial x}(J_x) &= -\frac{\partial(\rho\phi)}{\partial t} - \frac{\partial}{\partial y}(J_y) + S \\ &= (S_x)_{cd} \, . \end{aligned} \tag{2.81}$$

Equation 2.81 is the convection-diffusion equation with source whose solution and characteristics have been discussed extensively in the previous section. It is also assumed that (ρu), Γ, and $(S_x)_{cd}$ are constant throughout the control-volume considered. The left and right boundary conditions are given by ϕ_W and ϕ_P. Then, using equation 2.76, the total-flux in the x-direction at the w-interface can be written in terms of the boundary values ϕ_W and ϕ_P. Similarly, the total-flux expression at the e-interface and at the interfaces at the other coordinate directions can also be expressed in terms of the neighboring values of the dependent variable ϕ in that coordinate direction. In this way, the integrated transport equation (equation 2.80) is transformed into the discretized form.

The distinguishing mark of this approach is that the full conservation equation is not only satisfied at the control-volume over which it is integrated, but is also fully conserved in the determination of the total-fluxes at the interfaces. Thus, the unsteady term, the cross-wise total-fluxes, and the source term have a direct way to influence the total-flux profile in a coordinate direction. The idea behind FCM and its subsequent development is motivated by the failure of the exponential scheme to take into account the multidimensionality and the presence of transient and source terms in the interface total-flux calculation. Since the exponential scheme (and its derivatives, ie: hybrid and Power

Law schemes) is based on the solution of steady, one-dimensional, convection-diffusion without source, the resulting total-flux profile is constant throughout the control-volume considered. What FCM does is to take this constant profile as the baseline profile and add a non-monotonous correction profile to account for the presence of S_{cd}. This approach is appropriately reflected in the name 'Flux Corrected Method'.

2.6.2 Discretization of the x- and y-momentum Equations

The previous modeling concept for the general multi-dimensional convection-diffusion transport will now be applied to obtain the discretized x-momentum equation. The conservative form of the x-momentum equation (equation 2.13) is quoted below for convenience:

$$\frac{\partial(\rho u)}{\partial t} + \frac{\partial}{\partial x}\left((\rho u)u - \Gamma\frac{\partial u}{\partial x}\right) + \frac{\partial}{\partial y}\left((\rho v)u - \Gamma\frac{\partial u}{\partial y}\right) = -\frac{\partial P}{\partial x}\,, \tag{2.82}$$

$$\frac{\partial(\rho u)}{\partial t} + \frac{\partial}{\partial x}(J_{xx}) + \frac{\partial}{\partial y}(J_{yx}) = -\frac{\partial P}{\partial x}\,. \tag{2.83}$$

Integration of equation 2.83 over time and over the two-dimensional control-volume (Figure 2.1) results in the following integral balance of the x-momentum equation:

$$\frac{\left[(\rho u)_p - (\rho u)_p^o\right]\Delta x\Delta y}{\Delta t} +$$

$$f(J^{intg}_{xx-e} - J^{intg}_{xx-w} + J^{intg}_{yx-n} - J^{intg}_{yx-s}) +$$

$$(1-f)(J^{o\ intg}_{xx-e} - J^{o\ intg}_{xx-w} + J^{o\ intg}_{yx-n} - J^{o\ intg}_{yx-s}) =$$

$$P^{intg}_w - P^{intg}_e\,, \tag{2.84}$$

where

$$J^{intg}_{xx-e,w} = \int_s^n J_{xx-e,w}\,dy = J_{xx-e,w}\,\Delta y\,, \tag{2.85}$$

$$J^{intg}_{yx-n,s} = \int_w^e J_{yx-n,s}\,dx = J_{yx-n,s}\,\Delta x\,, \tag{2.86}$$

$$P^{intg}_{e,w} = \int_s^n P_{e,w}\,dy = P_{e,w}\,\Delta y\,. \tag{2.87}$$

Note that the time integration of the pressure term is treated implicitly.

Since mass must also be conserved at each timestep, the integral balance of the continuity equation (equation 2.26) can be rewritten as:

$$f(F_{x-e}^{intg} - F_{x-w}^{intg} + F_{y-n}^{intg} - F_{y-s}^{intg}) +$$

$$(1-f)(F_{x-e}^{o\ intg} - F_{x-w}^{o\ intg} + F_{y-n}^{o\ intg} - F_{y-s}^{o\ intg}) = 0\ . \tag{2.88}$$

By multiplying the above equation with u_P and then substituting the Taylor series expansion for u_P about time t:

$$\begin{aligned} u_P &= u_P^o + \left(\frac{\partial u}{\partial t}\right)_P^o \Delta t + O(\Delta t^2) \\ &= u_P^o + u_{tP}^o \Delta t + O(\Delta t^2) \end{aligned} \tag{2.89}$$

in the previous integrated mass-conservation equation, one obtains:

$$f(F_{x-e}^{intg} - F_{x-w}^{intg} + F_{y-n}^{intg} - F_{y-s}^{intg})u_P +$$

$$(1-f)(F_{x-e}^{o\ intg} - F_{x-w}^{o\ intg} + F_{y-n}^{o\ intg} - F_{y-s}^{o\ intg})u_P^o =$$

$$-(1-f)(F_{x-e}^{o\ intg} - F_{x-w}^{o\ intg} + F_{y-n}^{o\ intg} - F_{y-s}^{o\ intg})u_{tP}^o \Delta t\ . \tag{2.90}$$

Subtracting equation 2.90 from equation 2.84 yields:

$$\frac{(u_P - u_P^o)\rho_P^o \Delta x \Delta y}{\Delta t} +$$

$$\begin{aligned} f[(J_{xx-e}^{intg} - F_{x-e}^{intg}u_P) - (J_{xx-w}^{intg} - F_{x-w}^{intg}u_P) \ + \\ (J_{yx-n}^{intg} - F_{y-n}^{intg}u_P) - (J_{yx-s}^{intg} - F_{y-s}^{intg}u_P)\ ] \ + \\ (1-f)[(J_{xx-e}^{intg} - F_{x-e}^{intg}u_P)^o - (J_{xx-w}^{intg} - F_{x-w}^{intg}u_P)^o \ + \\ (J_{yx-n}^{intg} - F_{y-n}^{intg}u_P)^o - (J_{yx-s}^{intg} - F_{y-s}^{intg}u_P)^o\ ] \ = \end{aligned}$$

$$(P_w^{intg} - P_e^{intg}) +$$

$$(1-f)[(F_{x-e}^{intg} - F_{x-w}^{intg})^o + (F_{y-n}^{intg} - F_{y-s}^{intg})^o]u_{tP}^o \Delta t\ . \tag{2.91}$$

Note that the last term of equation 2.91 vanishes due to mass conservation at the previous timestep. The next step in the discretization process is to express the total-fluxes at the interfaces in terms of the neighboring u values. Considering for example the e- and w-interfaces, the total-fluxes at these interfaces are obtained by solving the x-direction, one-dimensional, convection-diffusion with source over the x-intervals containing those interfaces:

$$\frac{\partial}{\partial x}(J_{xx-e,w}) = S_{xx-e,w} \ , \tag{2.92}$$

and similarly, the total-flux at the n- and s-interfaces are obtained by solving:

$$\frac{\partial}{\partial y}(J_{yx-n,s}) = S_{yx-n,s} \ , \tag{2.93}$$

over the y-intervals containing the n- and s-interfaces. The convention used for the first and second subscripts of the above sources is the same as that used to differentiate the momentum total-fluxes. Although the appropriate choice for $S_{xx-e,w}$ and $S_{yx-n,s}$ should be obvious based on the discussion of the general transport formulation in the previous subsection, let the two convection-diffusion sources represent a general source expression which will be specified in the next chapter. The combined flux at the w-interface can be written as:

$$\begin{aligned}
& J^{intg}_{xx-w} - F^{intg}_{x-w}u_P = combined\ flux\ at\ w-interface \\
&= [J_{xx-w} - F_{x-w}u_P]\Delta y \\
&= [F_{x-w}u_P + \{D_{x-w}A(|P_{ex-w}|) + [\![F_{x-w}, 0]\!]\}(u_W - u_P) + J_{xxs-w} - F_{x-w}u_P]\Delta y \\
&= [\{D_{x-w}A(|P_{ex-w}|) + [\![F_{x-w}, 0]\!]\}(u_W - u_P) + J_{xxs-w}]\Delta y \ ,
\end{aligned} \tag{2.94}$$

where equation 2.76 has been substituted for J_{xx-w}. Referring to Figure 2.2, it should also be obvious that:

$$D_{x-w} = \frac{\mu}{\Delta x_w} \ , \tag{2.95}$$

$$P_{ex-w} = \frac{F_{x-w}}{D_{x-w}} = \frac{F^{intg}_{x-w}}{D^{intg}_{x-w}} = \frac{F_{x-w}\Delta y}{D_{x-w}\Delta y} \ . \tag{2.96}$$

Similarly, the combined flux at the n-interface can be written as:

$$\begin{aligned} & J^{intg}_{yx-n} - F^{intg}_{y-n} u_P = combined\ flux\ at\ n-interface \\ &= [J_{yx-n} - F_{y-n} u_P]\Delta x \\ &= [F_{y-n} u_P + \{D_{y-n} A(|P_{ey-n}|) + [\![-F_{y-n}, 0]\!]\}(u_P - u_N) + J_{yxs-n} - F_{y-n} u_P]\Delta x \\ &= [\{D_n A(|P_{ey-n}|) + [\![-F_{y-n}, 0]\!]\}(u_P - u_N) + J_{yxs-n}]\Delta x \ , \end{aligned} \tag{2.97}$$

where equation 2.75 has been substituted for J_{yx-n}. Also referring to Figure 2.2:

$$D_{y-n} = \frac{\mu}{\Delta y_n} \ , \tag{2.98}$$

$$P_{ey-n} = \frac{F_{y-n}}{D_{y-n}} = \frac{F^{intg}_{y-n}}{D^{intg}_{y-n}} = \frac{F_{y-n}\Delta x}{D_{y-n}\Delta x} \ . \tag{2.99}$$

The combined fluxes at the e- and s-interfaces are obtained in the same way. Substituting into equation 2.91, the final discretized form of the x-momentum equation is obtained as:

$$\begin{aligned} a_P u_P &= a_E u_E + a_W u_W + a_N u_N + a_S u_S + b_u \\ &= \sum a_{nb} u_{nb} + b_u \ , \end{aligned} \tag{2.100}$$

where E, W, N, and S refer to the East, West, North, and South grid points respectively. The coefficients a_E, a_W, a_N, a_S in equation 2.100 contain the convection and diffusion terms and are given by the following relations:

$$\begin{aligned} a_E &= f\{D_e A(|P_e|) + [\![-F_{x-e}, 0]\!]\} &&= f\bar{a}_E \ , \\ a_W &= f\{D_w A(|P_w|) + [\![F_{x-w}, 0]\!]\} &&= f\bar{a}_W \ , \\ a_N &= f\{D_n A(|P_n|) + [\![-F_{y-n}, 0]\!]\} &&= f\bar{a}_N \ , \\ a_S &= f\{D_s A(|P_s|) + [\![F_{y-s}, 0]\!]\} &&= f\bar{a}_S \ . \end{aligned} \tag{2.101}$$

The center coefficient a_P is given by:

$$a_P = (a_E + a_W + a_N + a_S) + a^o_P \ , \tag{2.102}$$

$$a^o_P = \frac{\rho_P \Delta x \Delta y}{\Delta t} \ , \tag{2.103}$$

and is composed of the sum of the neighboring coefficients and the terms due to the unsteady integration a_P^o. Similarly, the source term b_u is given by:

$$b_u = (P_e - P_w)\Delta y + b_{us} + b_u^o \ . \tag{2.104}$$

$$b_{us} = -f[J_{xxs-e} - J_{xxs-w}]\Delta y - f[J_{yxs-n} - J_{yxs-s}]\Delta x \ . \tag{2.105}$$

$$\begin{aligned} b_u^o = {} & a_P^o u_P^o - (1-f)[\bar{a}_E^o(u_P - u_E)^o + \bar{a}_W^o(u_P - u_W)^o + \\ & \bar{a}_N^o(u_P - u_N)^o + \bar{a}_S^o(u_P - u_S)^o] + \\ & (1-f)[J_{xxs-e} - J_{xxs-w}]^o\Delta y + (1-f)[J_{yxs-n} - J_{yxs-s}]^o\Delta x \ . \end{aligned} \tag{2.106}$$

where b_{us} is the collection of the total-flux corrections at the interfaces, and b_u^o is the source term due to the unsteady integration.

Observation of equation 2.102 shows that the neighboring coefficients contain the term $A(|P_e|)$, which is an exponential function given by equation 2.62. Although the exponential expression is based on the exact solution of the one-dimensional convection-diffusion equation considered, it is not recommended for use because (1) exponentials are relatively expensive to compute, and (2) for an NxN two-dimensional grid, the term $A(|P_e|)$ must be computed $2\times N^2$ times. An alternative to computing $A(|P_e|)$ is to use the Power Law expression given by Patankar [5]:

$$A(|P_e|) \approx [\![0, (1 - 0.1|P_e|)^5]\!] \ . \tag{2.107}$$

The above function is a curve fit to the exponential expression and has been shown to be sufficiently accurate for all practical purposes. Graphical comparison between the exponential and Power Law functions can be found in **Appendix A.**

Careful observation of the above final discretized form also shows that Patankar's 'Four Basic Rules' necessary for convergence and for physically realistic solutions [5] are preserved. The total-flux corrections are all collected as an additional source. No change is introduced to the other coefficients. This property makes FCM very attractive for established codes based on the exponential scheme (or its variants).

The previous approach to the discretization of the x-momentum equation is also applied to discretize the y-momentum equation. Again, as in the x-momentum discretization procedure, the expressions for the convection-diffusion sources $Sxy_{e,w}$ and $Syy_{n,s}$ are left in general form at this time. Even though FCM refers to both (1) the method of adding non-monotonous source driven correction to the homogeneous profile obtained from solving the one-dimensional convection-diffusion without source, and (2) the approach using the conservation principle in the determination of the interface total-fluxes, only the latter will be discussed extensively in the next chapter.

2.7 Staggered Grid Arrangement

Recall that the discretization of the momentum equations would require the integration of the pressure gradient, for example $-\frac{\partial P}{\partial x}$ for the x-momentum equation. The resulting contribution to the discretized equation is the pressure drop P_e-P_w. Using a non-staggered grid, a piecewise-linear profile for interface pressure using the two grid points surrounding the interface can lead to an unrealistic 'checker-board' pressure field in the converged solution. A similar difficulty also arises in the discretization of the continuity equation. Patankar [5] has discussed in detail the shortcomings resulting from using this type of grid.

The above difficulty can be resolved by using a staggered grid arrangement. In the staggered grid, the u and v velocities are defined at the control-volume faces rather than at the grid points, whereas the pressure P, the density ρ, and the viscosity μ are defined at the grid points. Different staggered grid arrangements are used for each of the momentum equations. Using the staggered grid arrangement, the pressure gradient can be expressed in terms of the grid point pressures, and the difficulty with the discretized continuity equation can also be avoided. The staggered grid arrangement used for the x-momentum equation is given in Figure 2.8. Note that dotted zero-width control-volumes

are used to enclose the boundary grid points. The use of zero-width control-volumes makes it easier to keep track of the indexing used for the velocity components. From this point on, distinctions will be made among the terms "main control-volume", "staggered x-control-volume", and "staggered y-control-volume".

The discretized momentum equations, each written using its corresponding staggered grid arrangement, are :

$$a_e u_e = \sum a_{nb} u_{nb} + (P_P - P_E)\Delta y + b_{us} + b_u^o \ , \tag{2.108}$$

$$a_n v_n = \sum a_{nb} v_{nb} + (P_P - P_N)\Delta x + b_{vs} + b_v^o \ . \tag{2.109}$$

Since each momentum equation is written based on its own staggered grid arrangement, the coefficients are different for different momentum equations.

The staggered grid arrangement was first used by Harlow and Welch [37] in the MAC method. It also forms the basis of the SIVA procedure of Caretto, Curr, and Spalding [38] and the SIMPLER procedure of Patankar [5] used in the present work.

The use of a staggered grid also necessitates the establishment of a subscript/indexing convention to allow quick and convenient reference to a grid-point or a control-volume face. The x-direction indexing is given in Figure 2.8 where ig is used to denote the grid index and if is used to denote the control-volume face index. The j-index is defined trivially. Thus an i subscript to u means an if subscript, and an i subscript to pressure means an ig subscript. Grid face is then defined as the face which passes through a grid point, and its indexing convention follows the one used for grid point. The grid and control-volume face indexes in the y-direction are defined in the same way.

2.8 SIMPLER Algorithm

Early in this chapter, it was mentioned that one approach to solving the incompressible flow equations is to use an iterative procedure which alternately solves for the

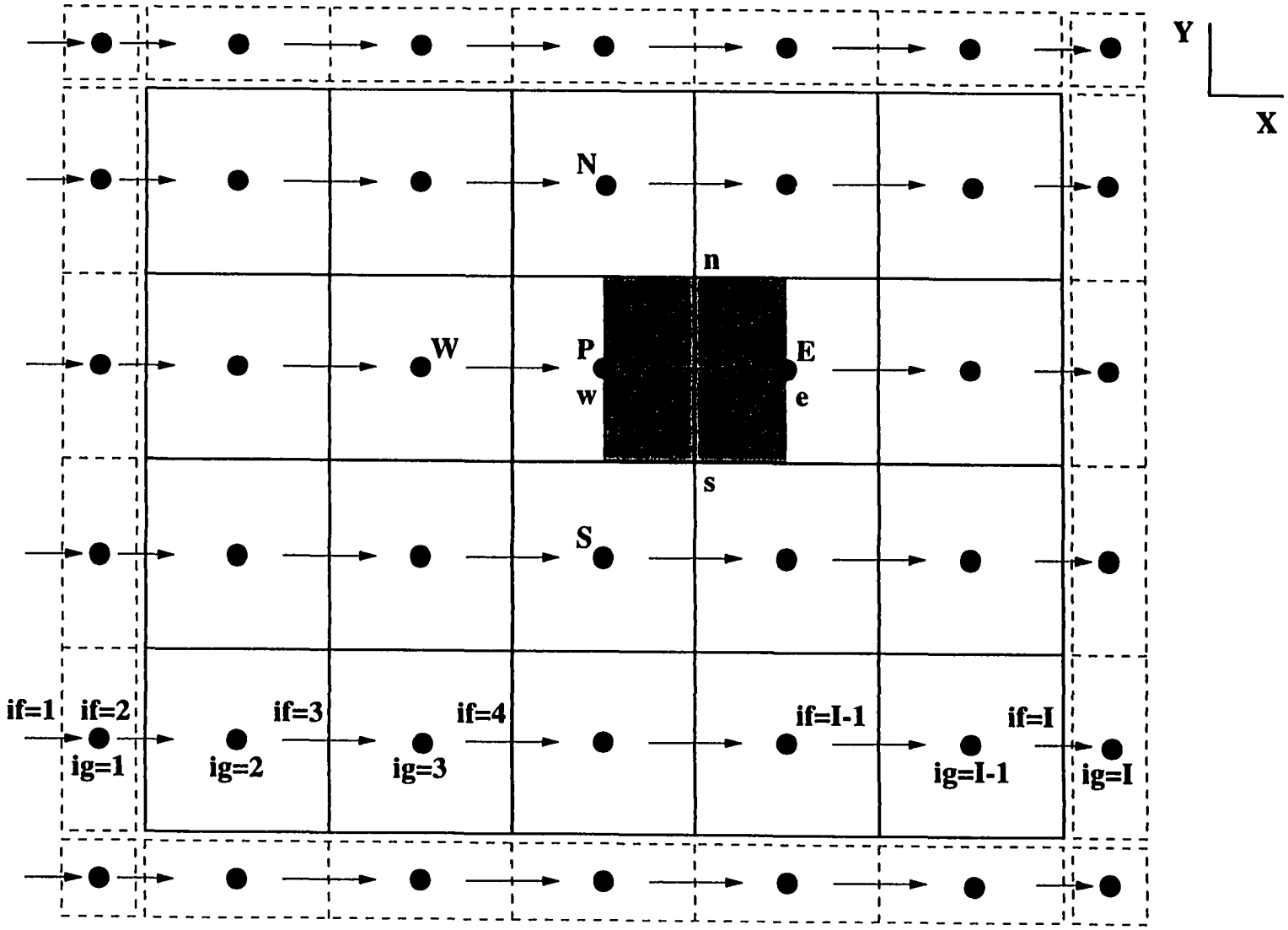

Figure 2.8 Staggered x-control-volume

velocity and pressure fields. Thus, given a velocity field, a procedure must be developed to obtain pressure. In the current work, the well-known SIMPLER algorithm introduced by Patankar [5] is employed to handle the velocity-pressure coupling. In this section, the SIMPLER algorithm is briefly reviewed. Since the FCM extra correction terms are simply additions to the source terms of the discretized momentum equations, no modifications whatsoever are introduced in the SIMPLER algorithm itself.

2.8.1 Pressure Equation

The discretized x-momentum equation (equation 2.108) can be written as:

$$\begin{aligned} u_e &= \left(\frac{\sum a_{nb} u_{nb} + b_{us} + b_u^o}{a_e} \right) + d_e (P_P - P_E) \\ &= \hat{u}_e + d_e (P_P - P_E) \ , \end{aligned} \tag{2.110}$$

where the pseudo-velocity $\hat{u}_e$ is given by:

$$\hat{u}_e = \frac{\sum a_{nb} u_{nb} + b_{us} + b_u^o}{a_e} \ . \tag{2.111}$$

Similarly, the discretized y-momentum equation (equation 2.109) can be written as:

$$v_n = \hat{v}_n + d_n (P_P - P_N) \ . \tag{2.112}$$

The d term is the ratio of the interface area and the center coefficient of the respective momentum equation and is given by:

$$d_e = \frac{\Delta y}{a_e} \ , \tag{2.113}$$

$$d_n = \frac{\Delta x}{a_n} \ . \tag{2.114}$$

Substituting the pseudo-velocities into the integral balance for the continuity equation (equation 2.26) written for the main control volume yields the discretized pressure equation:

$$a_P P_P = a_E P_E + a_W P_W + a_N P_N + a_S P_S + b_P \ , \tag{2.115}$$

where the coefficients are given by:

$$\begin{aligned} a_E &= (\rho d)_e \Delta y \ , \\ a_W &= (\rho d)_w \Delta y \ , \\ a_N &= (\rho d)_s \Delta x \ , \\ a_S &= (\rho d)_n \Delta x \ , \\ a_P &= a_E + a_W + a_N + a_S \ , \end{aligned} \tag{2.116}$$

and the source term is given by:

$$b_P = -[(\rho \hat{u})_e - (\rho \hat{u})_w]\Delta y - [(\rho \hat{u})_n - (\rho \hat{u})_s]\Delta x \ . \tag{2.117}$$

2.8.2 Correction Equations

In order to get a converged solution of the velocity field at a given timestep, the coefficients of the momentum equations are lagged or calculated either by using the velocity field obtained from the previous iteration or from the converged velocity field of the previous timestep in the case of the first iteration within a time-loop. The same principle is also applied to any source term which is a function of the velocity components. However, a different treatment is used for the pressure gradient. The pressure gradient terms are not estimated using the values from the previous iteration, but are determined directly from the velocity field of the previous iteration using the pressure equation derived in the previous subsection. The discretized momentum equations can then be solved for the current iteration to obtain a new velocity field. However, unless convergence has been achieved, this newly computed velocity field may not satisfy the continuity equation since the pressure field calculated from the previous iteration of the velocity field may not have converged yet. Thus a procedure is needed to correct the pressure field. The corrected pressure field can then be used to correct the velocity field

for that iteration. This is accomplished using the pressure-correction equation and the velocity-correction equation derived in the next two subsections.

2.8.3 Velocity Correction

Unless the correct pressure field is employed, the resulting velocity field will not satisfy the continuity equation. Such an imperfect velocity field based on an estimated pressure field P^* is denoted by u^* and v^*. The correct velocity and pressure can then be written as:

$$\begin{aligned} u &= u^* + u' , \\ v &= v^* + v' , \\ P &= P^* + P' , \end{aligned} \tag{2.118}$$

where u' and v' are the velocity corrections and P' is the pressure correction.

Following the procedure given in [5], the velocity-correction equations are given as:

$$\begin{aligned} u_e &= u_e^* + d_e(P'_P - P'_E) , \\ u_w &= u_w^* + d_w(P'_W - P'_P) , \\ v_n &= v_n^* + d_n(P'_P - P'_N) , \\ v_s &= v_s^* + d_s(P'_S - P'_P) . \end{aligned} \tag{2.119}$$

2.8.4 Pressure Correction Equation

Substituting the velocity correction equations (equation 2.119) into the integrated continuity equation (equation 2.26) written for the main control volume yields the discretized pressure correction equation:

$$a_P P'_P = a_E P'_E + a_W P'_W + a_N P'_N + a_S P'_S + b_{P'} , \tag{2.120}$$

where a_E, a_W, a_N, and a_S are given by equation 2.116, and the source term is given by:

$$b_{P'} = -[(\rho u^*)_e - (\rho u^*)_w]\Delta y - [(\rho v^*)_n - (\rho v^*)_s]\Delta x . \tag{2.121}$$

Note that from the above equation, $b_{P'}$ represents a measure of how well the mass conservation at the main control-volume is satisfied at each iteration. Thus, this quantity is often used as the indicator for convergence of the numerical solution. However, this condition is to be used in conjunction with the convergence of the residual of the momentum-conservation and with the residual of the velocity components. It has been observed that for high Reynolds number flow problems, it is possible to see convergence of the mass conservation to an acceptable level while the residuals of the other two criterias are still not satisfied.

2.8.5 Solution Procedure for the Discretized Equations

The governing equations for the flow-field are non-linear. Even though the discretized equations have been cast into a linear form, the coefficients and the source terms are functions of the dependent variables. In the present work the discretized equations are solved independently and sequentially (also known as the 'segregated' approach). For a given timestep and at each iteration, the coefficients and the source terms are lagged using the flow-field obtained from the previous iteration. Iterations are repeated until convergence is achieved for that timestep.

Writing the discretized equations for all the control volumes in the flow domain yields a tridiagonal system of simultaneous algebraic equations. This algebraic system of equations is solved using the Successive Line Over-Relaxation (SLOR) method. The SLOR method proceeds by sweeping the two-dimensional computational space, line by line, in both directions. The TriDiagonal Matrix Algorithm (TDMA) is used for each line sweep. An under-relaxation is used between each TDMA update to prevent the solution from diverging.

2.8.6 SIMPLER Algorithm Summary

The sequence of steps for the unsteady SIMPLER algorithm modified for FCM implementation can be summarized as follows:

1. Start with a given initial flowfield.

2. Calculate the unsteady portion of the center coefficients (for the x-momentum. calculate a_P^o given by equation 2.103).

3. Calculate the unsteady portion of the source terms (for the x-momentum, calculate b_u^o given by equation 2.106).

4. Calculate the total-flux corrections and add to the source of the momentum equations (for the x-momentum, calculate b_{us} given by equation 2.105).

5. Calculate the coefficients for the momentum equations and the pseudo-velocities (equation 2.111 for pseudo $u-$velocity).

6. Using the calculated pseudo-velocities, calculate the source term for the pressure equation (equation 2.117).

7. Calculate the coefficients (equation 2.116) and solve the pressure equation (equation 2.115) to obtain the pressure field.

8. Using the calculated pressure field, solve the momentum equations (equation 2.100 for x-momentum) to get the velocity field.

9. Calculate the source term of the pressure-correction equations (equation 2.121) and solve for the pressure corrections (equation 2.120).

10. Correct the velocities using the velocity-correction equations (equation 2.119).

11. Return to step 4 and repeat until convergence.

12. Start with a new time level.

3 HANDLING THE SOURCE TERM

It was mentioned in the previous chapter that the choices for the sources S_{xx}, S_{yx} for the x-momentum and S_{xy}, S_{yy} for the y-momentum discretization equations should be obvious from the example given in the application of FCM to the transport of the general variable ϕ. Thus, ideally these sources should take the form:

$$\begin{aligned} \frac{\partial}{\partial x}(J_{xx}) &= S_{xx} \\ &= -\frac{\partial P}{\partial x} - \frac{\partial J_{yx}}{\partial y} - \frac{\partial(\rho u)}{\partial t} , \end{aligned} \tag{3.1}$$

$$\begin{aligned} \frac{\partial}{\partial y}(J_{yx}) &= S_{xx} \\ &= -\frac{\partial P}{\partial x} - \frac{\partial J_{xx}}{\partial x} - \frac{\partial(\rho u)}{\partial t} , \end{aligned} \tag{3.2}$$

for the x-momentum, and similarly for the y-momentum:

$$\begin{aligned} \frac{\partial}{\partial x}(J_{xy}) &= S_{xy} \\ &= -\frac{\partial P}{\partial y} - \frac{\partial J_{yy}}{\partial y} - \frac{\partial(\rho v)}{\partial t} , \end{aligned} \tag{3.3}$$

$$\begin{aligned} \frac{\partial}{\partial y}(J_{yy}) &= S_{yy} \\ &= -\frac{\partial P}{\partial y} - \frac{\partial J_{xy}}{\partial x} - \frac{\partial(\rho v)}{\partial t} . \end{aligned} \tag{3.4}$$

The above choices mean that the full conservation equation itself is used to determine the total-fluxes at the interfaces. At this time, reviewing the conventions used in **section 2.3** to make distinctions among the various total-fluxes, is recommended. The total-fluxes J_{xx} and J_{yy} are referred to as the directional total-fluxes for the x-momentum and y-momentum equations respectively, and J_{yx} and J_{xy} are referred to as the non-directional

total-fluxes for the respective momentum equations. Similarly, S_{xx} and S_{yy} are defined as the directional discretized convection-diffusion sources for the x-momentum and y-momentum equations respectively, and S_{yx} and S_{xy} are referred to as the non-directional discretized convection-diffusion sources for the x-momentum and y-momentum equations. The second subscript always refers to the considered momentum equation and the first subscript gives the coordinate direction of the transport of the flux or source considered.

At this point in the development of FCM, a thorough study is initiated to investigate the effects of the various components of the above sources individually before combining them into the appropriate groups. Note that the convection-diffusion sources for the x-momentum discretization concept can be categorized as the following:

Group A Unsteady term present in both S_{xx} and S_{yx}.

Group B Pressure gradient term present in both S_{xx} and S_{yx}.

Group C Derivative of the non-directional total-flux present in S_{xx}.

Group D Derivative of the directional total-flux present in S_{yx}.

The y-momentum convection-diffusion sources are classified in the same way.

The inclusion of the unsteady term is relatively straightforward to implement and will not be specifically investigated in this chapter. Although only limited testings on moderately unsteady problems will be done in the subsequent chapter due to time constraints, it is expected that FCM will perform well for highly unsteady problems. The mechanism to account for the driving unsteady force has been included in the discretized equations. In this chapter, attention will focus on the effects of pressure gradients and derivatives of the total-fluxes on the numerical accuracy of steady problems. In the following sections, the individual and combined effects of all the source components are investigated. For simplicity, only the total-fluxes at the staggered control-volume

faces which make up the inner staggered cells are corrected. The effects of total-flux corrections at the boundary cells will be investigated separately in the next section. The standard well-known laminar steady two-dimensional flow inside a lid-driven square cavity given in Figure 3.1 will be used as the test problem. The Reynolds number is defined by $Re=(\rho U_{lid} L)/\mu$, where ρ is the constant density of the fluid, U_{lid} is the speed of the sliding wall, L is the length of the square enclosure side wall, and μ is the fluid viscosity. The cavity length is chosen to be unity, and a 42x42 uniform grid is used.

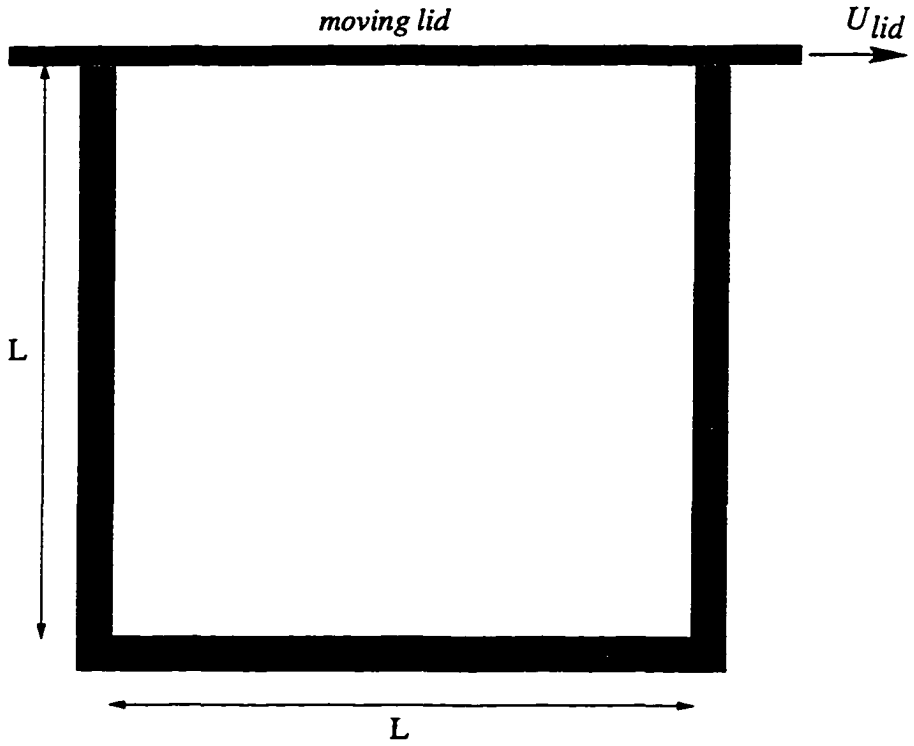

Figure 3.1 Two-dimensional lid-driven cavity.

Furthermore, a moderately high Reynolds number, Re=400, is chosen for this testing purpose. The fine grid solutions obtained using the central-difference scheme will be used as the benchmark solution. Finally, the results obtained using the Power Law scheme are also given for the purpose of comparison.

3.1 Effect of Pressure Gradients (Group B)

In this section, the effects of the pressure gradients as part of the overall sources used in the one-dimensional convection-diffusion process are investigated. The convection-diffusion sources then can be written as:

$$S_{xx} = -\frac{\partial P}{\partial x}, \tag{3.5}$$

$$S_{yx} = -\frac{\partial P}{\partial x}, \tag{3.6}$$

$$S_{xy} = -\frac{\partial P}{\partial y}, \tag{3.7}$$

$$S_{yy} = -\frac{\partial P}{\partial y}. \tag{3.8}$$

Along the vertical centerline (x=0.5), the u-velocity is the dominant component, and along the horizontal centerline (y=0.5), the v-velocity is the dominant component. Therefore, the accuracy with which the formulation can model these dominant velocity components, each in its respective centerline, will be analyzed.

The plots of the velocity components and pressures along the centerlines are given in Figure 3.2 to Figure 3.5. Observations of the u- and v-velocity components along the vertical and horizontal centerlines respectively show that slight overshoots are observed in some regions, while in regions of high flow gradients, the corrected profiles still fall short of the benchmark solutions. The effects of the flux-correction can be seen much more clearly on the pressure profiles along the centerlines. It is quite obvious from Figures 3.4 and 3.5 that the corrected solution can handle sharp turning profiles much better than the original Power Law scheme. Overall, it can be concluded that even though the inclusion of pressure gradients in the convection-diffusion sources does not reproduce the benchmark solution, significant improvement is observed.

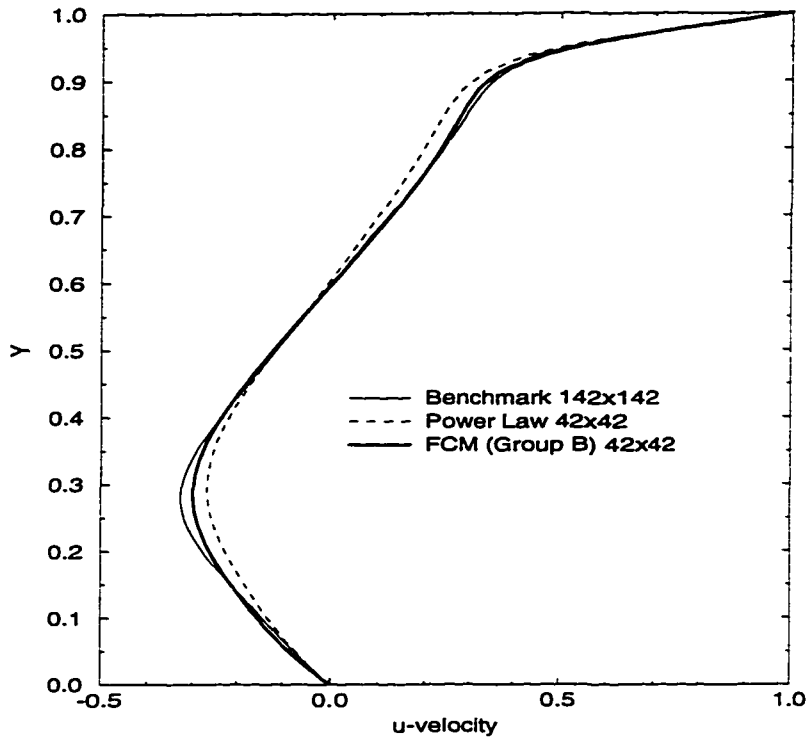

Figure 3.2 Driven Cavity Re=400. Effect of using source **Group B** on the vertical centerline u profile.

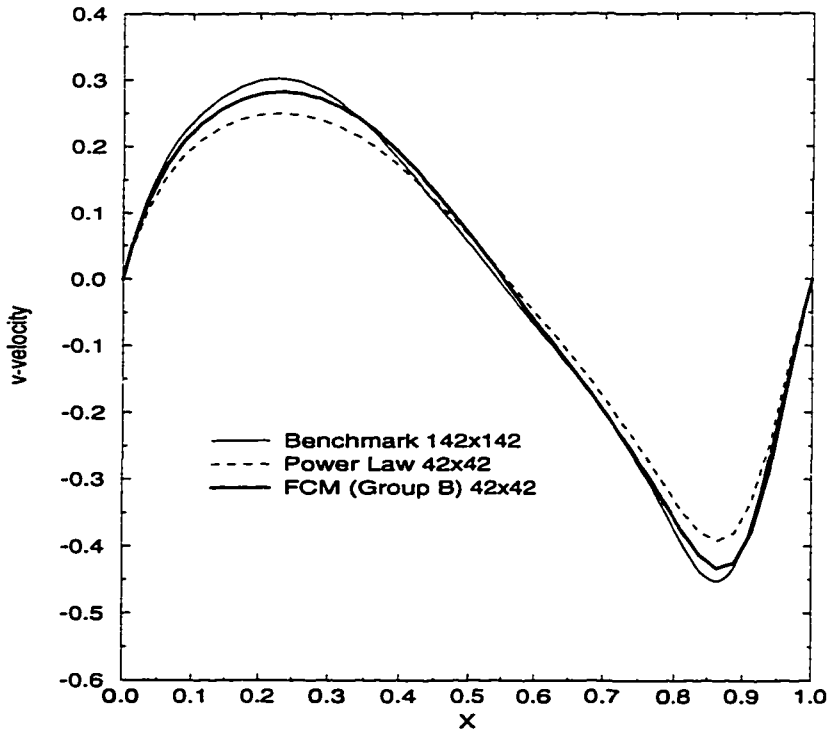

Figure 3.3 Driven Cavity Re=400. Effect of using source **Group B** on the horizontal centerline v profile.

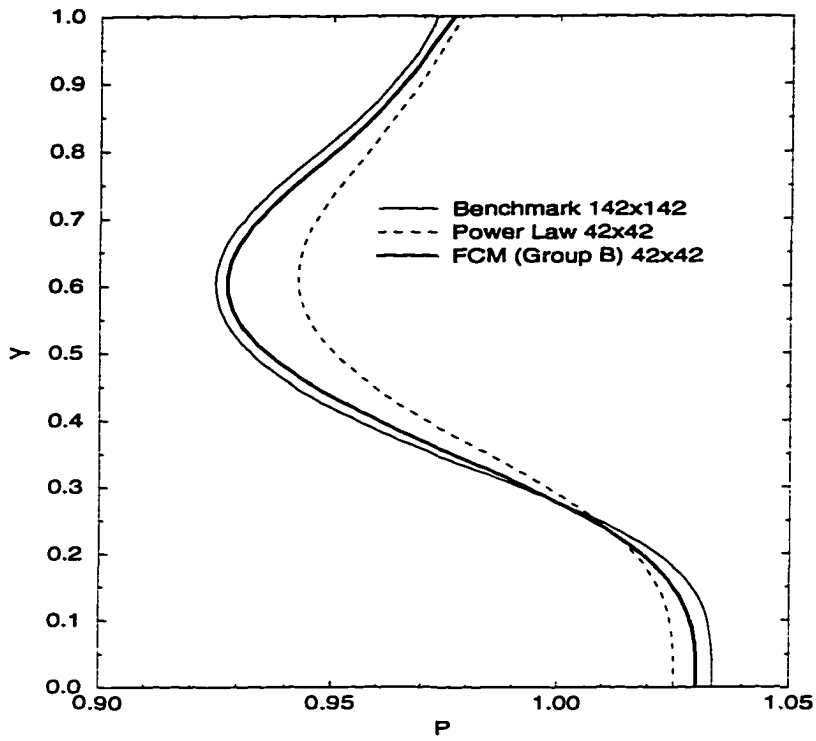

Figure 3.4 Driven Cavity Re=400. Effect of using source **Group B** on the vertical centerline P profile.

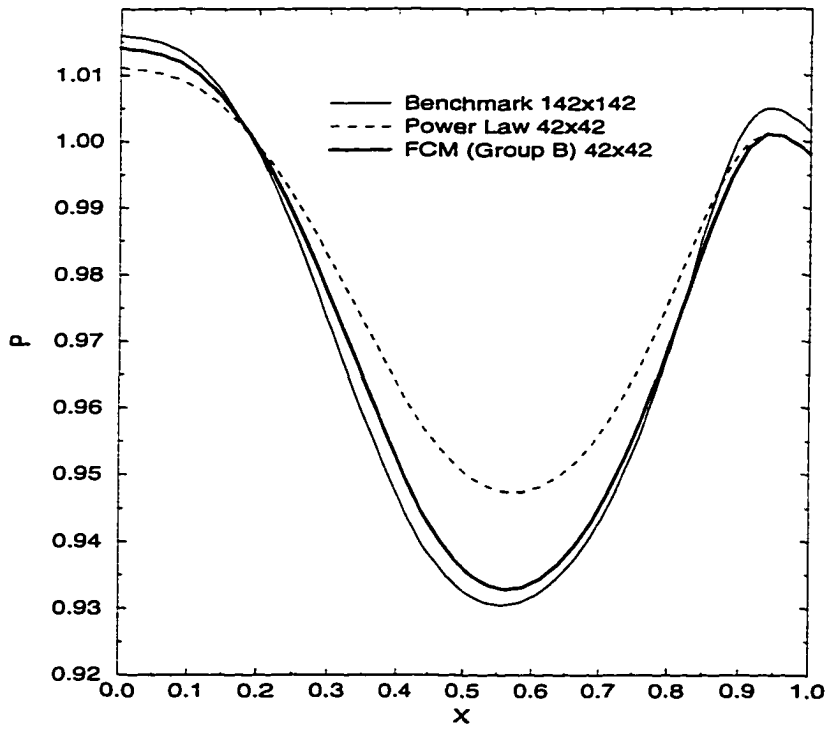

Figure 3.5 Driven Cavity Re=400. Effect of using source **Group B** on the horizontal centerline P profile.

3.2 Effect of the Derivatives of the Non-directional Total-fluxes (Group C)

In the present study, the effects of the derivatives of the non-directional total-fluxes are investigated. The convection-diffusion sources are given by:

$$S_{xx} = -\frac{\partial J_{yx}}{\partial y} , \tag{3.9}$$

$$S_{yx} = 0 , \tag{3.10}$$

$$S_{xy} = 0 , \tag{3.11}$$

$$S_{yy} = -\frac{\partial J_{xy}}{\partial x} . \tag{3.12}$$

As is obvious from the above equations, this means that the non-directional total-fluxes are not corrected at all, and only the effects of the cross-wise transports are used to correct the directional total-fluxes.

The plots of the velocity components along the centerlines are given in Figures 3.6 and 3.7. Only minor improvements on these profiles are observed. For the most part, the corrected profiles follow the baseline Power Law solution. However, it should be noted that there are small improvements observed in the regions of high flow gradients. The pressure profiles given in Figures 3.8 and 3.9 reveal insignificant improvements, as the corrected and baseline profiles are practically similar. It should be concluded that isolated use of the source components considered in this section is not effective for the directional total-flux corrections.

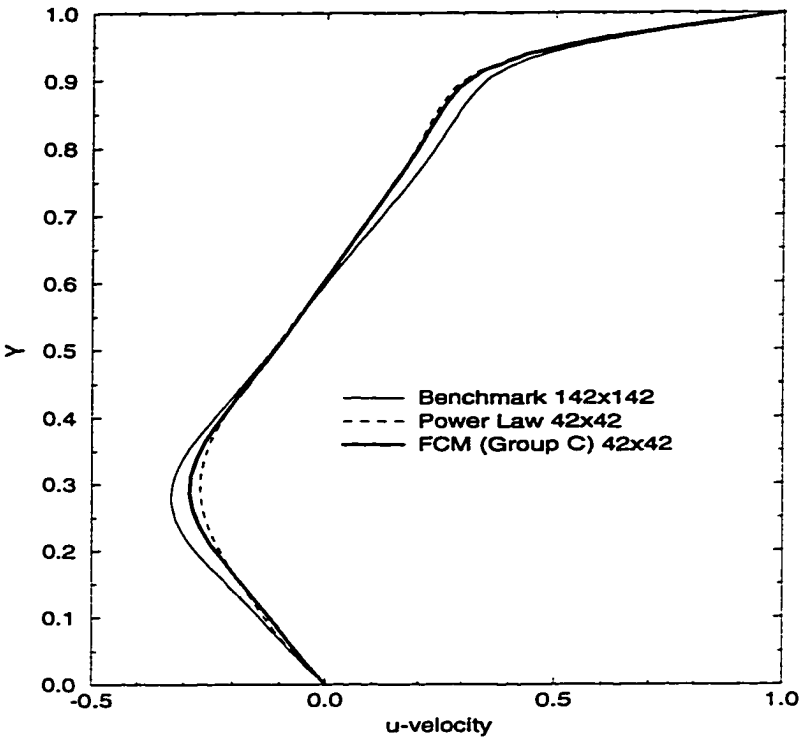

Figure 3.6 Driven Cavity Re=400. Effect of using source **Group C** on the vertical centerline u profile.

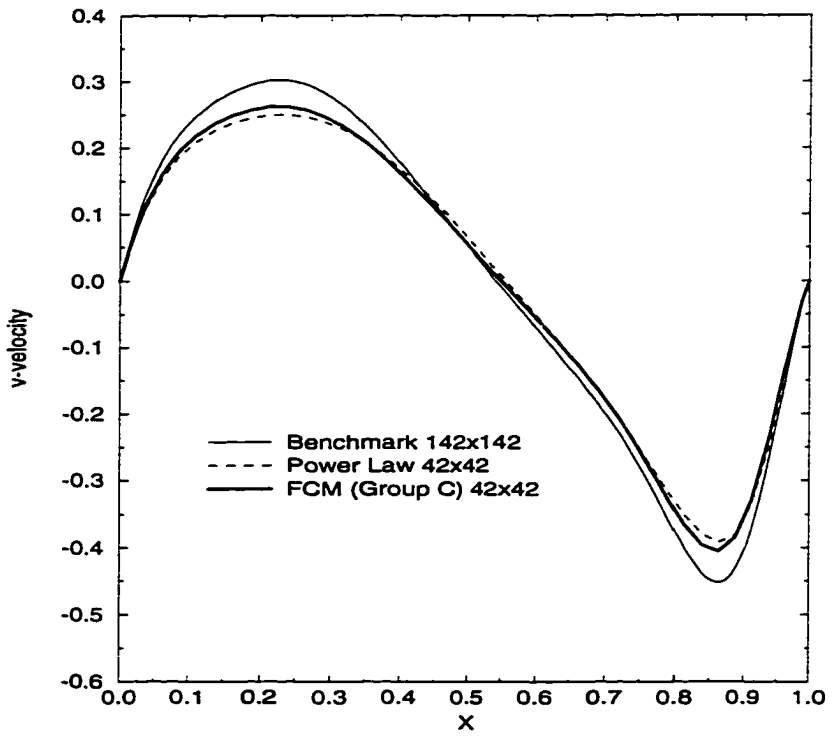

Figure 3.7 Driven Cavity Re=400. Effect of using source **Group C** on the horizontal centerline v profile.

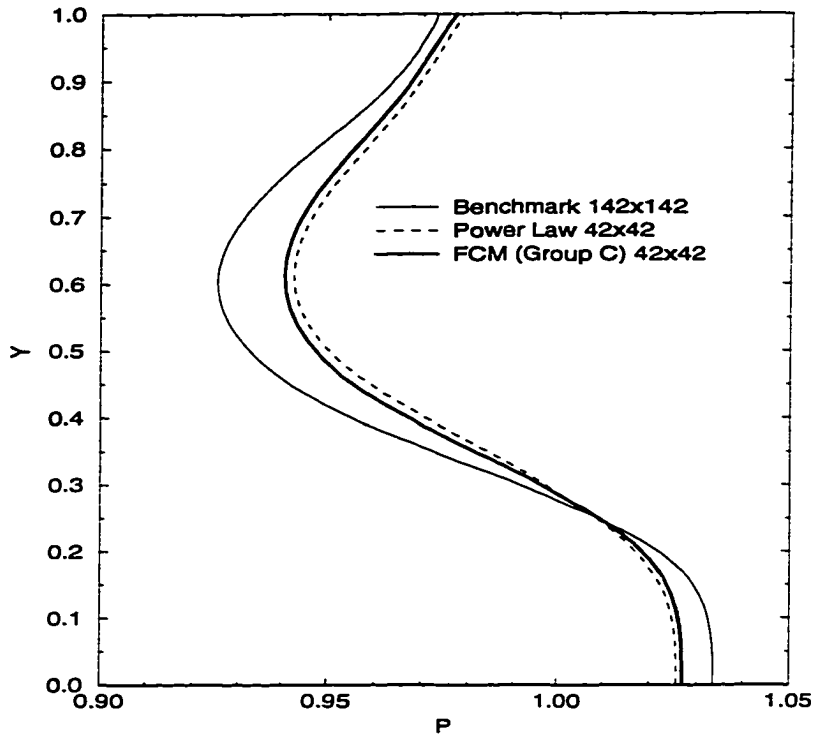

Figure 3.8 Driven Cavity Re=400. Effect of using source **Group C** on the vertical centerline P profile.

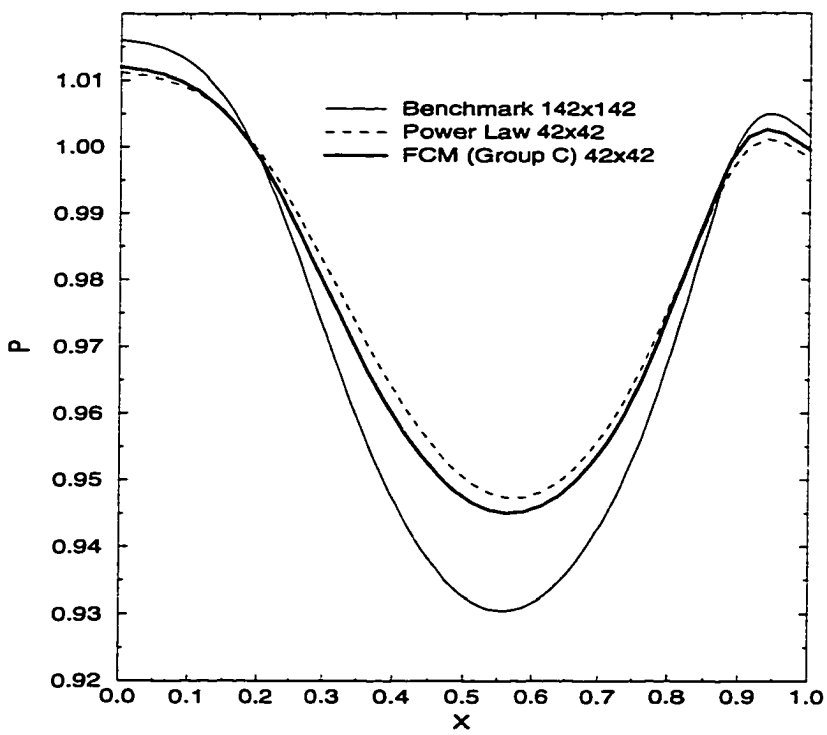

Figure 3.9 Driven Cavity Re=400. Effect of using source **Group C** on the horizontal centerline P profile.

3.3 Effect of the Derivatives of the Directional Total-fluxes (Group D)

The effects of the streamwise transport on the cross-wise convection-diffusion process are considered in this section. The convection-diffusion sources are given by:

$$S_{xx} = 0 , \tag{3.13}$$

$$S_{yx} = -\frac{\partial J_{xx}}{\partial x} , \tag{3.14}$$

$$S_{xy} = -\frac{\partial J_{yy}}{\partial y} , \tag{3.15}$$

$$S_{yy} = 0 . \tag{3.16}$$

The profiles of the velocity components and pressures are given in Figure 3.10 to Figure 3.13. Not surprisingly, improvement characteristics similar to the case considered in the previous section are observed for the velocity components. However, slightly better pressure profiles are obtained in this case. This reinforces the conclusion of the previous section that the exclusive use of the total-flux derivatives in the convection-diffusion sources cannot be expected to give adequate total-flux corrections.

3.4 Combined Effect of the Individual Source Components

The combined effects of the source components discussed individually in the previous three sections are now investigated. Recall that the pressure gradients have the most significant effects on the corrected profiles. The individual influence of the other components are relatively minor. Therefore, the combination which gives the best results must include the pressure gradient terms. The strategy used in the present study is to systematically compare the following possible combinations:

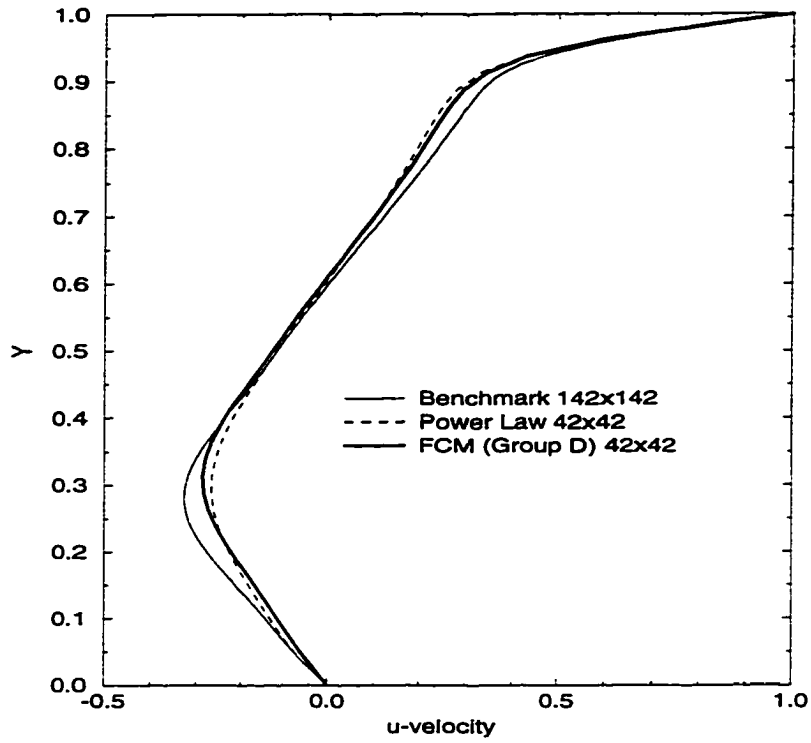

Figure 3.10 Driven Cavity Re=400. Effect of using source **Group D** on the vertical u centerline profile.

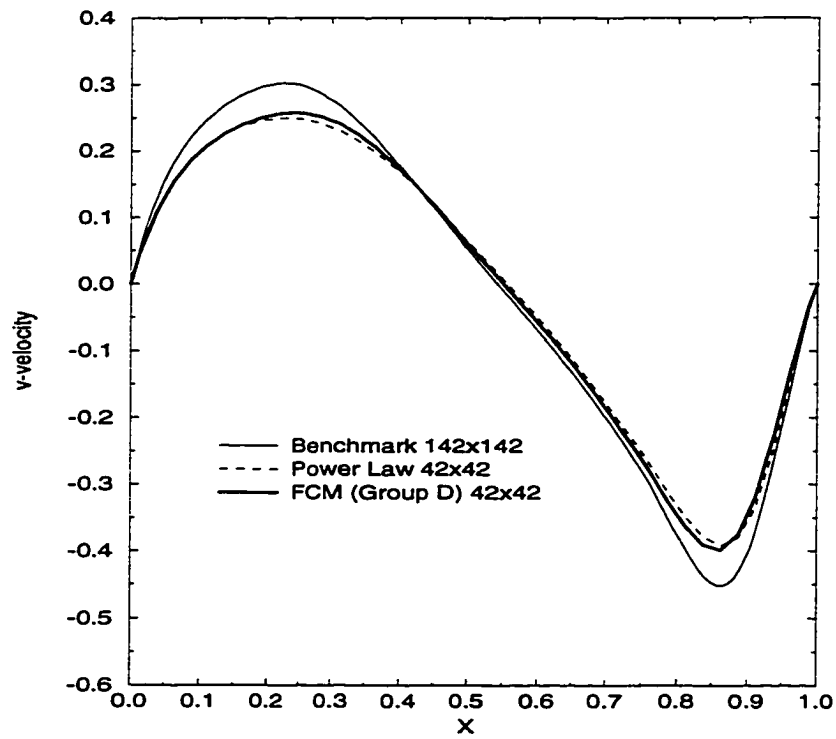

Figure 3.11 Driven Cavity Re=400. Effect of using source **Group D** on the horizontal centerline v profile.

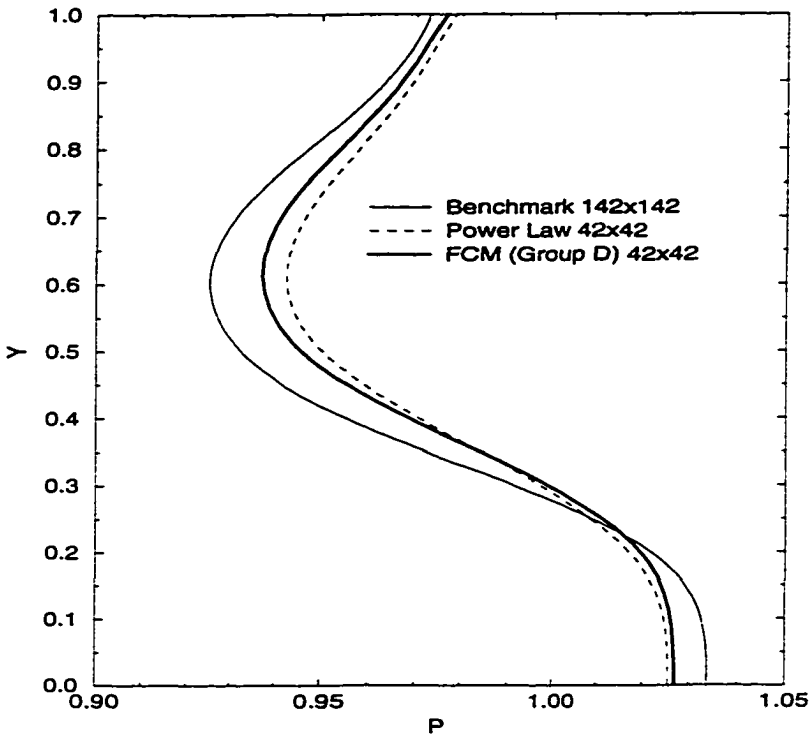

Figure 3.12 Driven Cavity Re=400. Effect of using source **Group D** on the vertical centerline P profile.

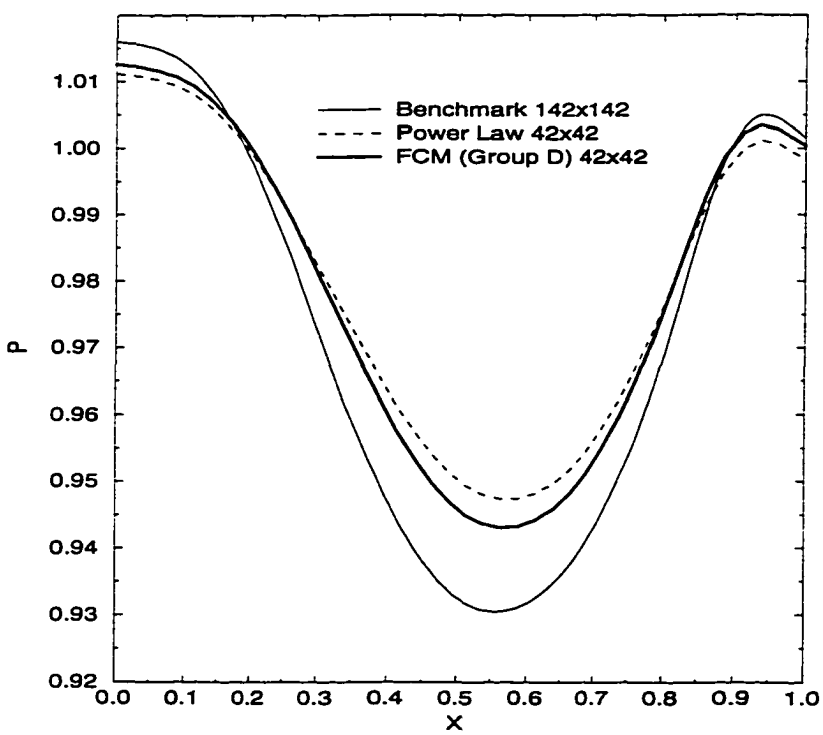

Figure 3.13 Driven Cavity Re=400. Effect of using source **Group D** on the horizontal centerline P profile.

Group B+C Combine pressure gradients and derivatives of the non-directional total-fluxes.

Group B+D Combine pressure gradients and derivatives of the directional total-fluxes.

Group B+C+D Combine pressure gradients and derivatives of the directional and non-directional total-fluxes.

The profiles of u-velocity along the vertical centerline for the three possible combinations are given in Figure 3.14 to Figure 3.16. Despite the logical expectation that the use of all three components should give the best profiles, it is the combination of pressure gradients and derivatives of the non-directional total-fluxes (**Group B+C**) which gives the best solution. As shown in Figure 3.14, the corrected profiles given by this combination literally fall on top of the benchmark solution. The same conclusion is maintained upon comparing the v-velocity components along the horizontal centerline (Figure 3.17 to Figure 3.19) and pressure along the vertical and horizontal centerlines (Figure 3.20 to Figure 3.25). For simplicity, this combination will be referred to as the 'Basic'/'Standard' FCM, or simply as FCM. The convection-diffusion sources for this combination are given by:

$$S_{xx} = -\frac{\partial P}{\partial x} - \frac{\partial J_{yx}}{\partial y}, \tag{3.17}$$

$$S_{yx} = -\frac{\partial P}{\partial x}, \tag{3.18}$$

$$S_{xy} = -\frac{\partial P}{\partial y}, \tag{3.19}$$

$$S_{yy} = -\frac{\partial P}{\partial y} - \frac{\partial J_{xy}}{\partial x}. \tag{3.20}$$

This combination means that the streamwise total-fluxes are fully corrected, while only pressure gradients are used to correct the cross-wise total-fluxes. The combination of

Group B+D, which consists of the pressure gradients and derivatives of the directional total-fluxes, results in slight but non-negligible overshoots and undershoots. Overcorrection is obtained when the three source components are used all together as one source.

It is not immediately clear why the theoretically better combination of all available source components gives the worst results. Not only are there overcorrections, but the slope of the u-velocity at the bottom wall is clearly not correct (Figure 3.16). It is found that this wall slope anomaly disappears as the grid is refined. It is the author's opinion that future work on FCM should include an attempt to further investigate this unexpected behavior.

3.5 Effect of Correction on Boundary Cells

Up to this point, FCM has been applied only to the inner staggered cells. In this section, total-flux corrections are also applied to the staggered control-volume faces which make up the boundary staggered cells. The difficult step in the boundary cell correction procedure is deciding whether or not it is necessary to correct the boundary total-fluxes. A closer look at the formulation of boundary total-fluxes is therefore necessary. For the purpose of convenience, attention will be focused on the left boundary. The total-flux expression at this boundary is given by:

$$J_{xx-ig=1} = (\rho u_2)u_2 - \mu \frac{\partial u}{\partial x}_{ig=1} . \tag{3.21}$$

Using equation 2.75 and eliminating the total-flux correction term, the left boundary total-flux can also be written as:

$$J_{xx-ig=1} = F_{x-if=2}u_2 + \{D_{x-ig=2}A(|P_{e-ig=2}|) + [\![-F_{x-if=2}, 0]\!]\}(u_2 - u_3) . \tag{3.22}$$

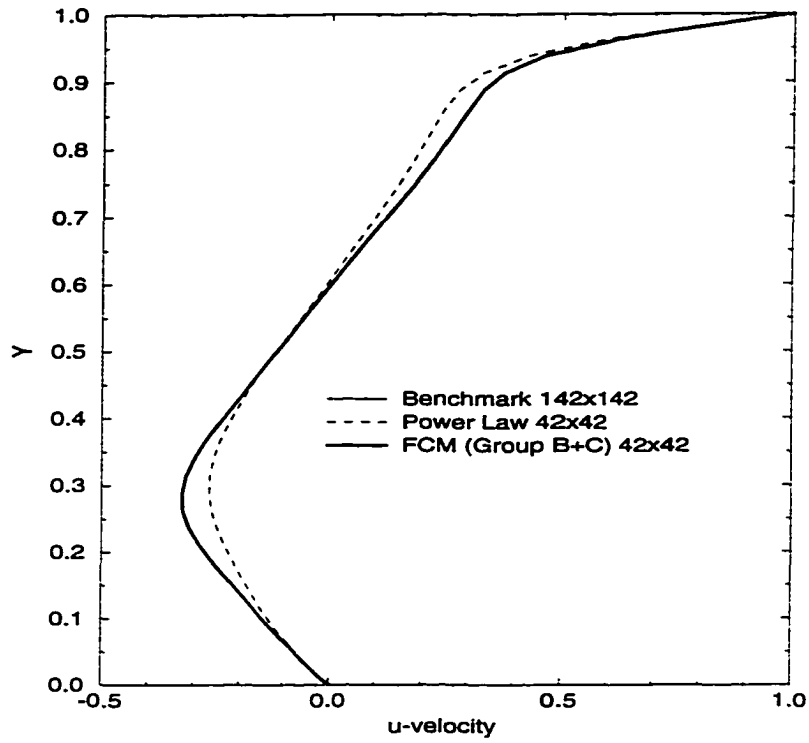

Figure 3.14 Driven Cavity Re=400. Effect of using combined source **Group B+C** on the vertical centerline u profile.

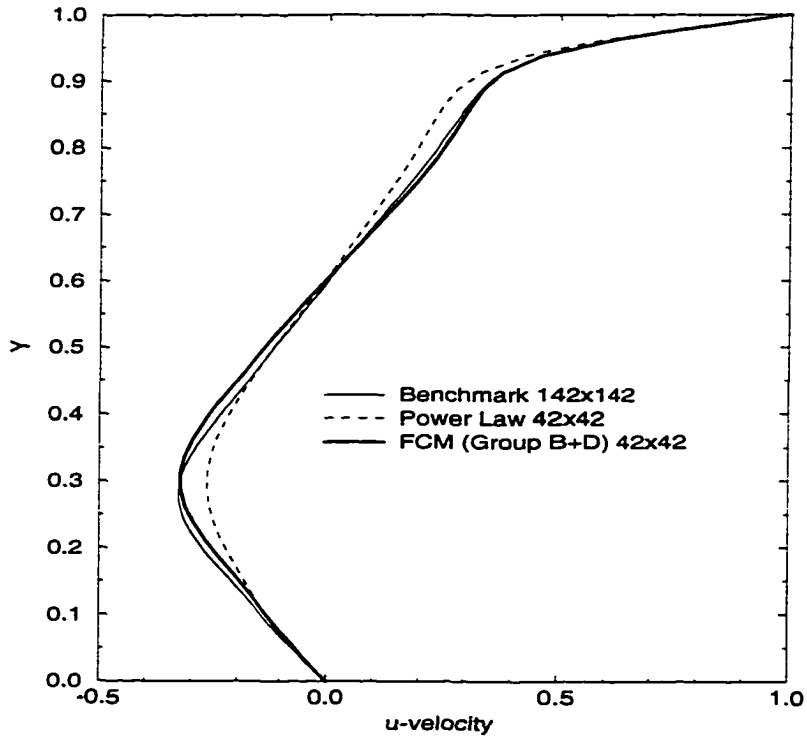

Figure 3.15 Driven Cavity Re=400. Effect of using combined source **Group B+D** on the vertical centerline u profile.

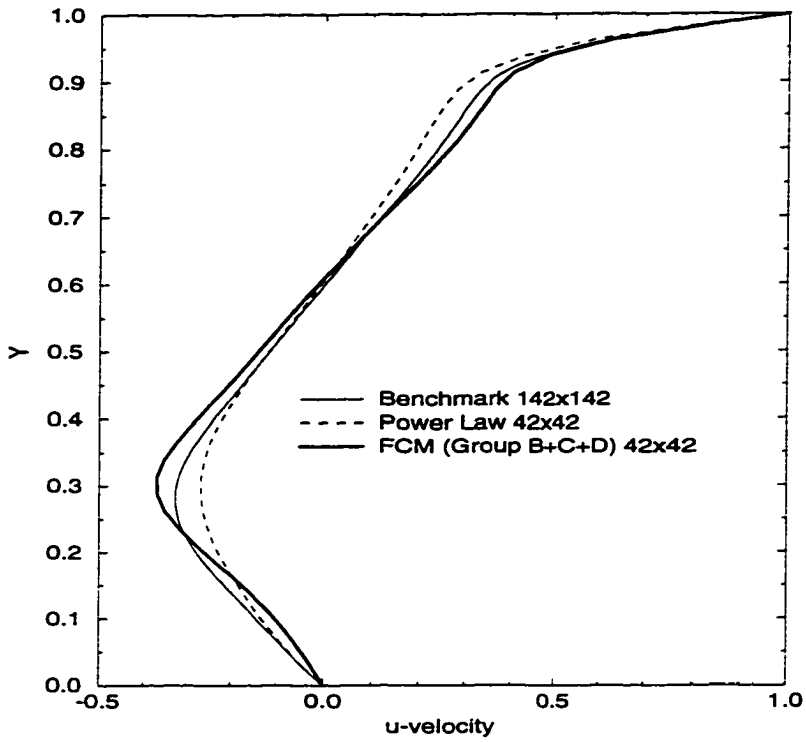

Figure 3.16 Driven Cavity Re=400. Effect of using combined source **Group B+C+D** on the vertical centerline u profile.

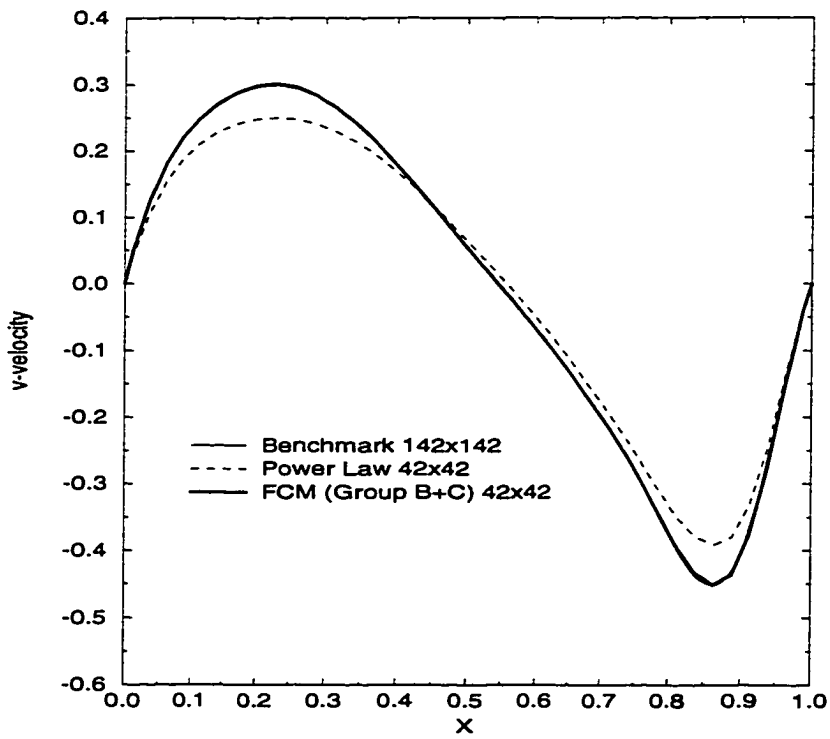

Figure 3.17 Driven Cavity Re=400. Effect of using combined source **Group B+C** on the horizontal centerline v profile.

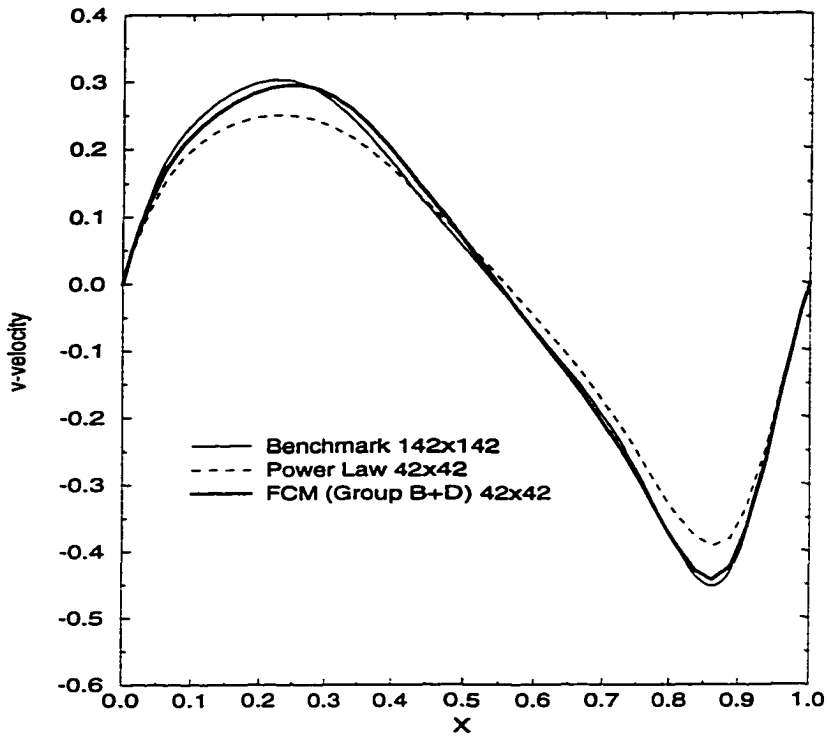

Figure 3.18 Driven Cavity Re=400. Effect of using combined source **Group B+D** on the horizontal centerline v profile.

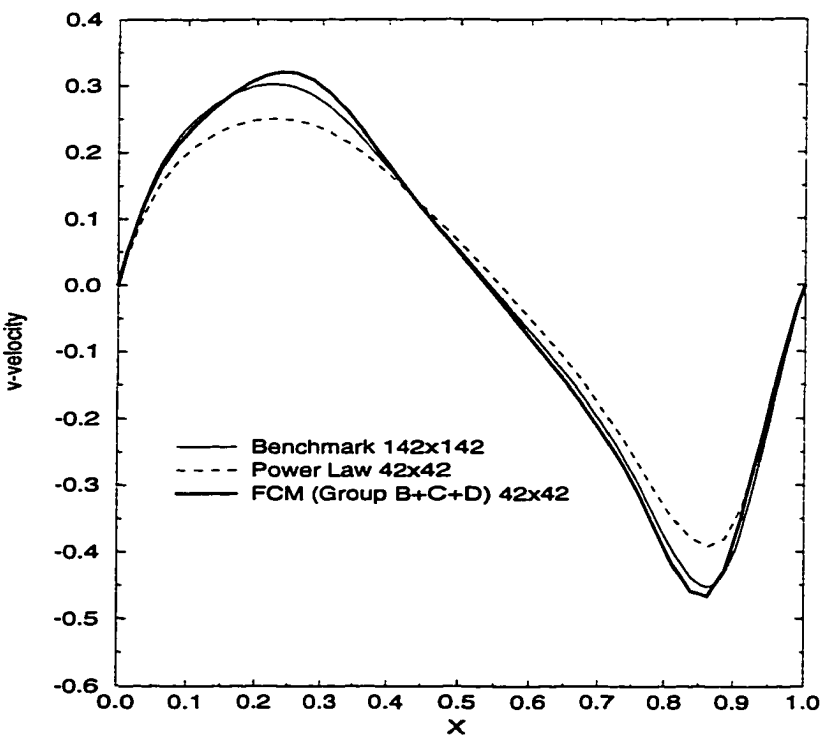

Figure 3.19 Driven Cavity Re=400. Effect of using combined source **Group B+C+D** on the horizontal centerline v profile.

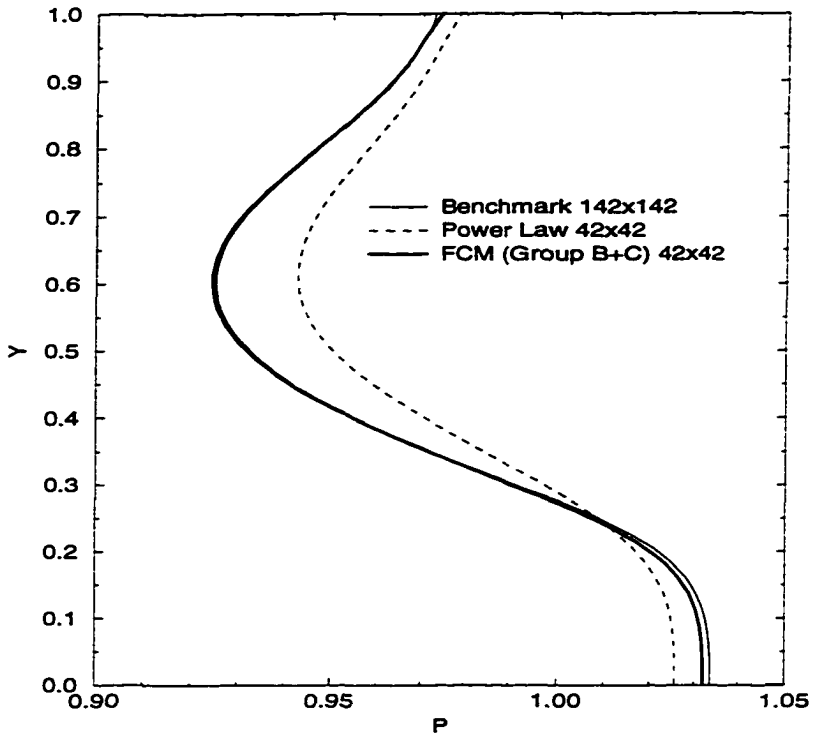

Figure 3.20 Driven Cavity Re=400. Effect of using combined source **Group B+C** on the vertical centerline P profile.

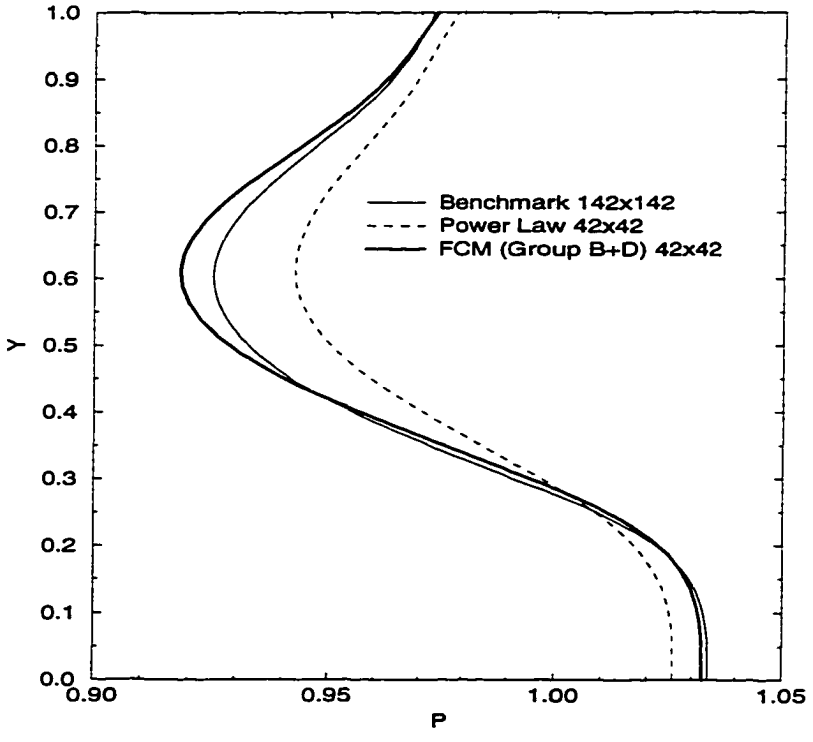

Figure 3.21 Driven Cavity Re=400. Effect of using combined source **Group B+D** on the vertical centerline P profile.

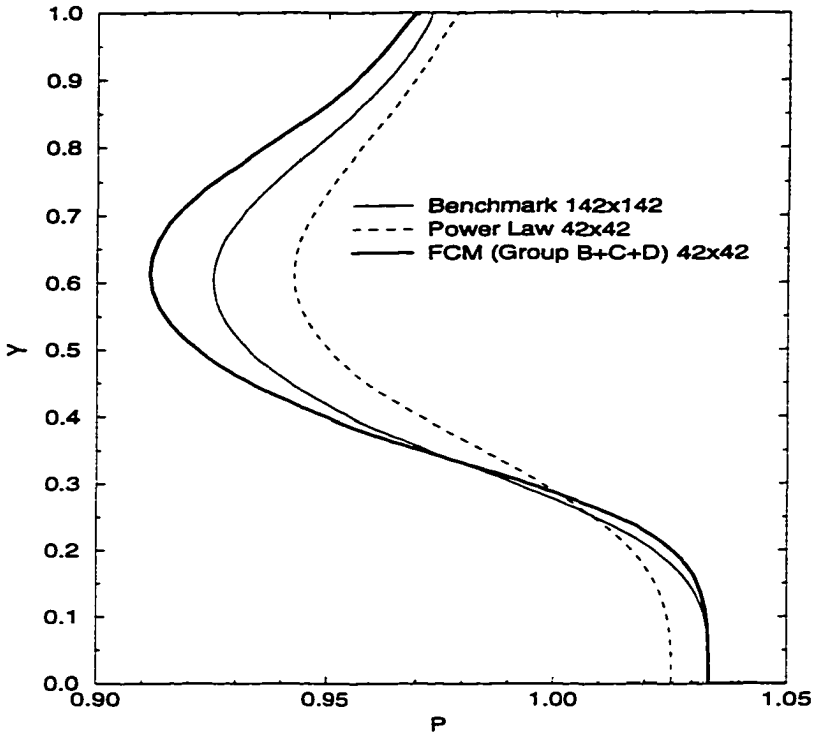

Figure 3.22 Driven Cavity Re=400. Effect of using combined source **Group B+C+D** on the vertical centerline P profile.

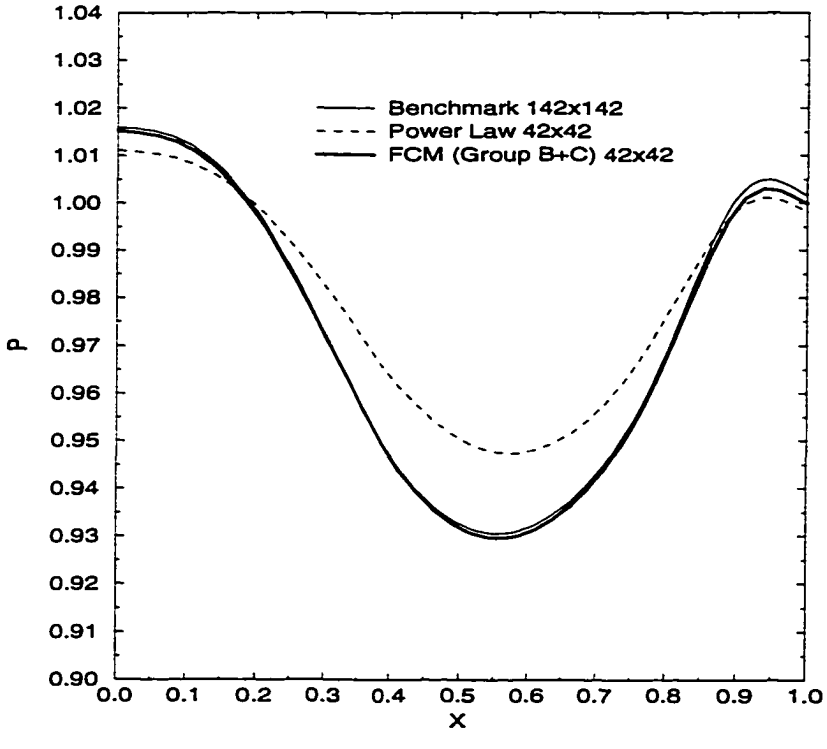

Figure 3.23 Driven Cavity Re=400. Effect of using combined source **Group B+C** on the horizontal centerline P profile.

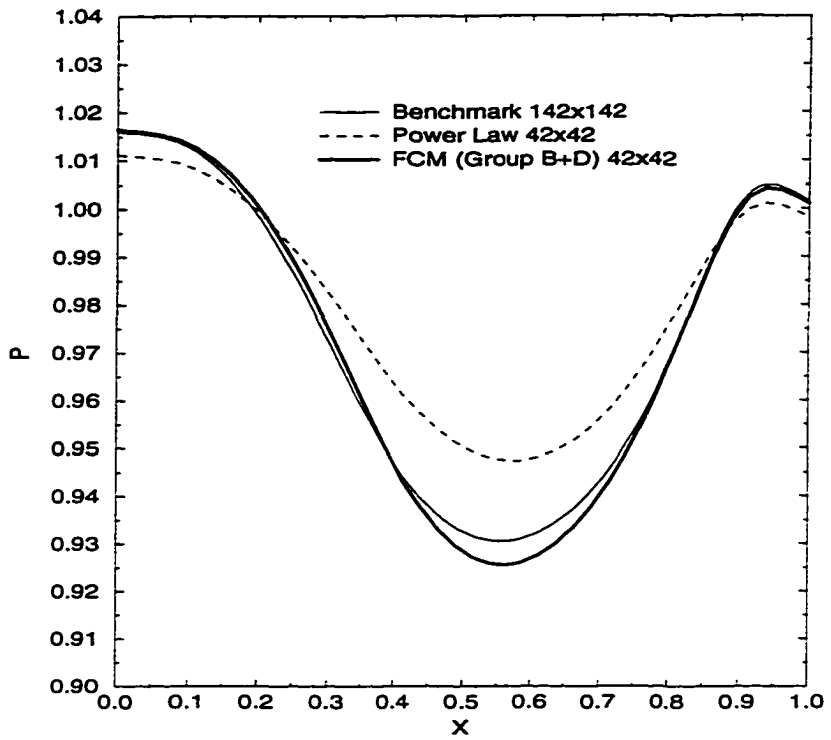

Figure 3.24 Driven Cavity Re=400. Effect of using combined source **Group B+D** on the horizontal centerline P profile.

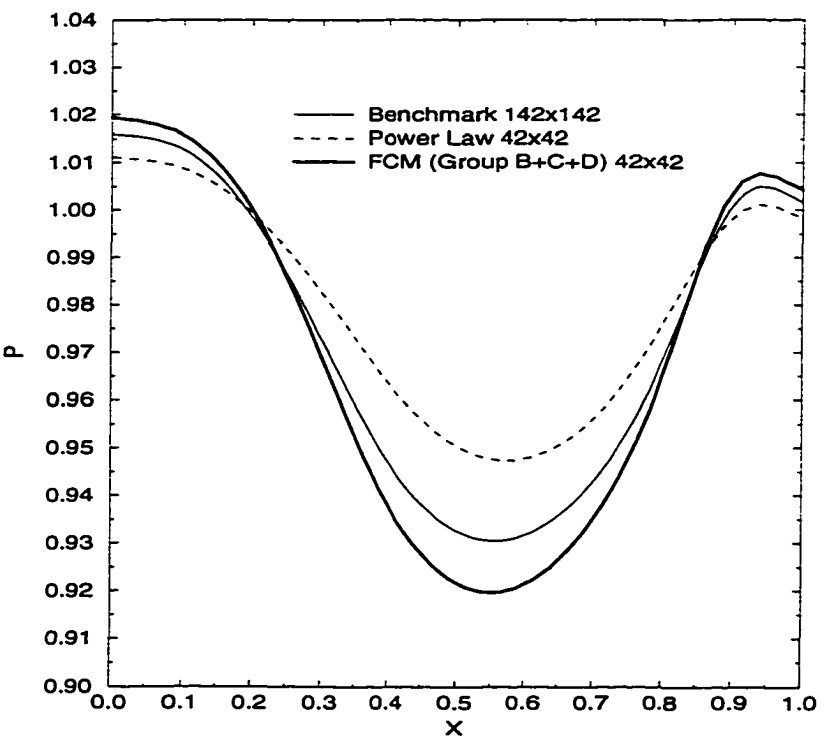

Figure 3.25 Driven Cavity Re=400. Effect of using combined source **Group B+C+D** on the horizontal centerline P profile.

Realizing that $F_{x-if=2}=(\rho u_2)$, the following equality is obtained upon comparing the previous two equations:

$$\mu \frac{\partial u}{\partial x}_{ig=1} = \{D_{x-ig=2} A(|P_{e-ig=2}|) + [\![-F_{x-if=2}, 0]\!]\}(u_3 - u_2) \ . \tag{3.23}$$

The convection term is always known since the normal boundary velocity is either specified or iteratively computed (such as through the application of the mass conservation principle). Therefore, the accuracy of the considered boundary total-flux (equation 3.21) is measured by how well the right-hand side of equation 3.23 approximates the left-hand side of the same equation, which is the diffusion flux at the left boundary. For non-zero convection, it is not possible to judge the accuracy of the approximation. However, it is known that diffusion is less dominant in the presence of strong convection (as in the case of the inlet/outlet boundary). Therefore, it is less relevant to question the accuracy of the approximating diffusion expression. The worst situation occurs for a wall boundary where convection vanishes and diffusion is most dominant. For a wall boundary, the following conditions prevail:

$$F_{x-if=2} = 0 \ , \tag{3.24}$$

$$P_{e-ig=2} = \frac{F_{x-if=2}}{D_{x-ig=2}} = 0 \ , \tag{3.25}$$

$$A(|P_{e-ig=2}|) = 1 \ . \tag{3.26}$$

Applying the above conditions to equation 3.23, the following results are obtained:

$$\begin{aligned} \mu \frac{\partial u}{\partial x}_{ig=1} &= D_{x-ig=2}(u_3 - u_2) \\ &= \frac{\mu}{\Delta x_{ig=2}}(u_3 - u_2) \\ &= \mu \left[\frac{u_3 - u_2}{\Delta x_{ig=2}} \right] \ . \end{aligned} \tag{3.27}$$

Note that for a wall boundary, the diffusion flux is represented by a first-order finite-difference equation. This fact raises questions about whether the high-accuracy nature

of FCM will be downgraded by the low order accuracy of the boundary total fluxes, especially when wall conditions exist. However, applying the total-flux correction to the boundary total-fluxes using the sources which prevail at the boundary main control-volumes results in overshoots and numerical instabilities. It is observed that if convergence can be achieved, these overshoots will eventually disappear with grid refinement. An attempt was also made to apply the correction only to the diffusion flux since the convection is known at the boundary, but only an insignificant reduction in overshoots was observed, while the formulation was still numerically unstable for practical purposes. Clearly, a different approach must be used if the desired goal is to increase the formal order of accuracy of the boundary diffusion fluxes. One such procedure is to use a higher order one-sided finite-difference expression for the boundary diffusion term. However, it should always be remembered that in so doing, it is important to introduce minimum changes in the main procedure. In the case of left wall boundary, it is proposed that the left boundary diffusion be written as:

$$\mu \frac{\partial u}{\partial x}_{ig=1} = \{D_{x-ig=2} A(|P_{e-ig=2}|) + [\![-F_{x-if=2}, 0]\!]\}(u_3 - u_2) + \left[-\mu \frac{u_3 - u_2}{\Delta x_{ig=2}} + \mu \frac{\partial u}{\partial x}_{ig=1}\right], \tag{3.28}$$

where the term $\frac{\partial u}{\partial x}_{ig=1}$ is to be replaced by the chosen one-sided finite-difference expression. The extra terms in the square bracket should be lagged and grouped together as part of the source term in the discretized momentum equation. For non-wall boundary, the extra term is neglected. This proposed procedure has not been implemented during the course of the current work due to the limited time available; however, it is the author's opinion that one of the most important follow-up tasks on the FCM is to investigate whether improved accuracy is observed with the implementation of the above procedure. Thus, in the present work, the corrections have been implemented at the staggered boundary cells, but the original Power Law scheme has been retained for the boundary total-fluxes.

The plots of the velocity components at the centerlines are given in Figures 3.26 and 3.27. In these figures, the profiles obtained using FCM with and without boundary cells corrected are compared against each other. The extension **-nb** will be used to indicate that boundary cell correction is not implemented. Note that a coarse 22x22 uniform grid is used to help show the differences. It is observed that definite improvements are clearly achieved, especially at regions of high flow gradients. If a 32x32 or finer grid is used instead, no difference in the profiles can be observed visually. The effects of boundary correction are most notably observed in the pressure profiles given in Figures 3.28 and 3.29. Excellent agreement between the benchmark solution and FCM_b is observed for most of the x or y range. However, careful observation of the centerline pressure profiles reveals that the slope of the corrected profile at the moving lid is clearly not correct. It will be seen later that this rather significant disagreement is the result of the conventional way the pressure equation is handled at the boundary. This undesirable behavior is one of the motivating factors for reformulating the procedure used to obtain and solve the pressure equation at the boundary in the next chapter. It is also found that with a modest refinement of the grid, the profiles obtained with/without boundary corrections quickly coalesce into one single profile.

3.6 Effect of Linear Source Profile

The total-flux corrections employed by FCM are based on the solution of one-dimensional convection-diffusion with a source. Recall that the source is assumed to be constant (equation 2.36) over the given one-dimensional domain (Figure 2.2). In this section, the effects of a linear source profile are investigated. The centerline profiles are given in Figure 3.30 to Figure 3.33. It can be seen that no improvement over the constant source situation is observed for either the velocity-components or pressure profiles. This confirms the conclusion obtained during the preliminary study of the sensitivity of

the one-dimensional convection-diffusion equation that slight perturbations in the source profile and source level result only in insignificant changes in the total-flux profile.

The important conclusion of this particular study is that the use of a simple constant source is sufficient to obtain the right correction, and further work on FCM should be focused on investigating the other issues suggested in the previous sections.

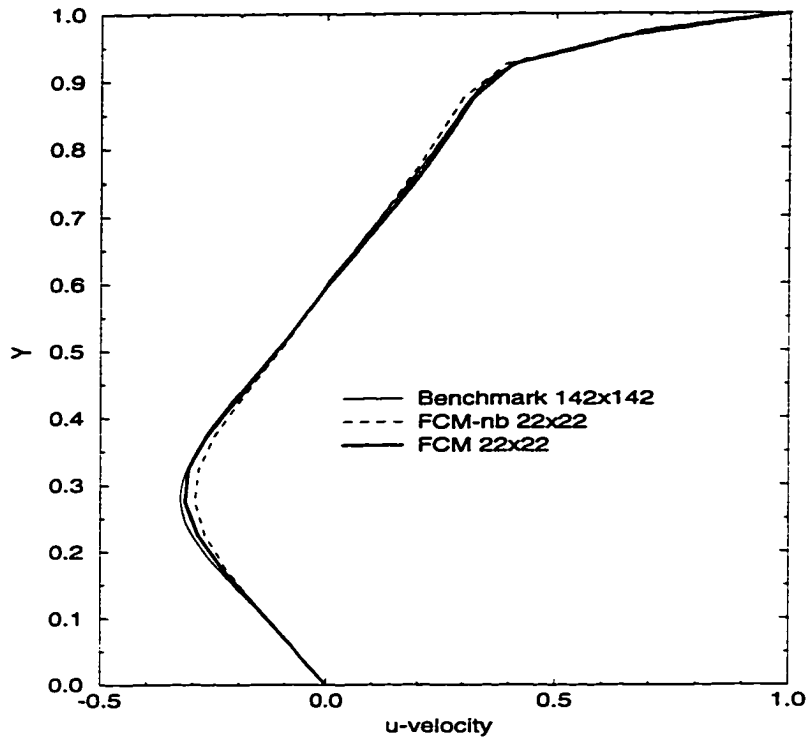

Figure 3.26 Driven Cavity Re=400. Effects of boundary cell corrections on the vertical centerline u profile.

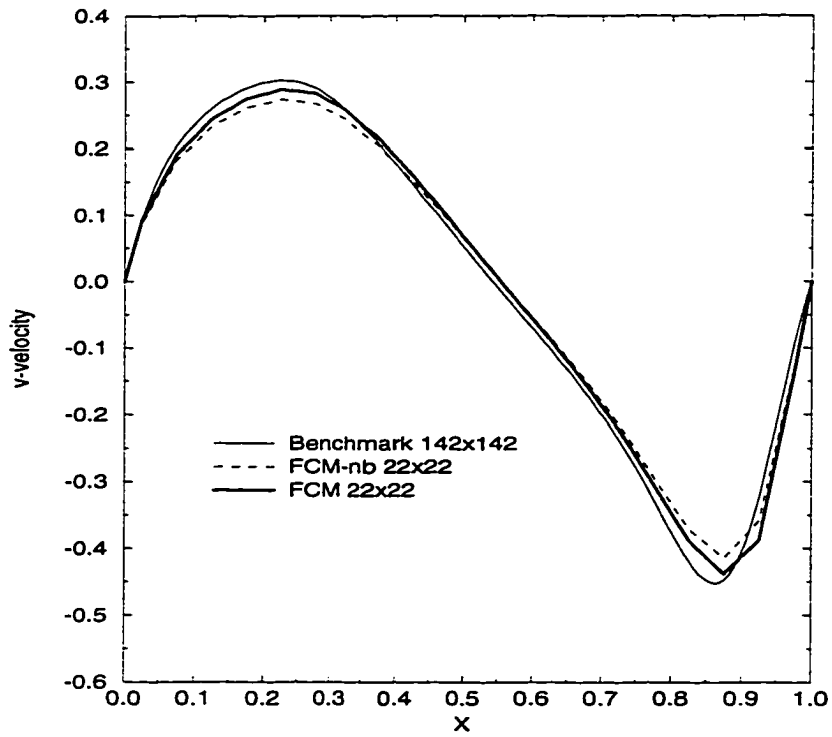

Figure 3.27 Driven Cavity Re=400. Effects of boundary cell corrections on the horizontal centerline v profile.

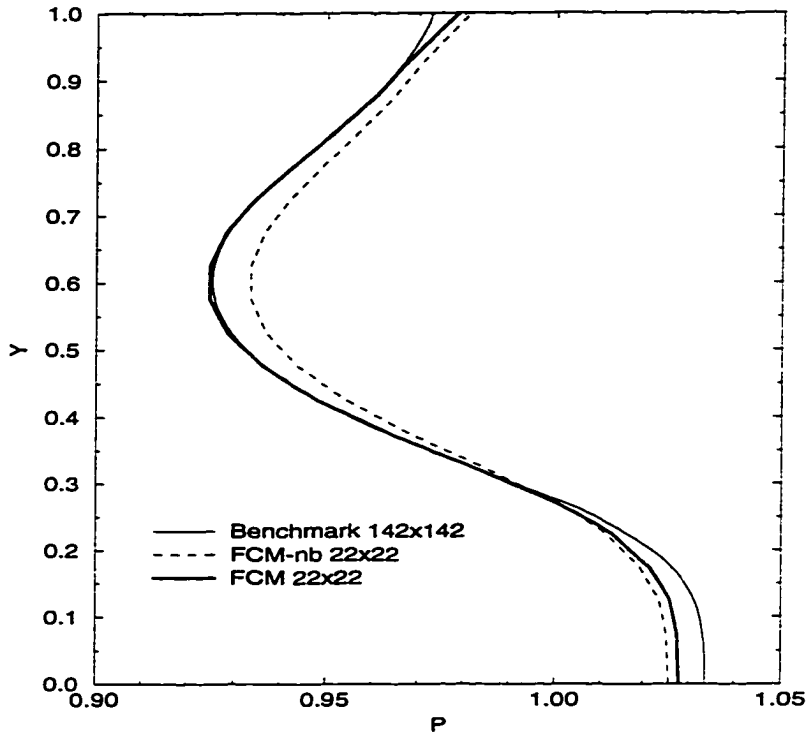

Figure 3.28 Driven Cavity Re=400. Effects of boundary cell corrections on the vertical centerline P profile.

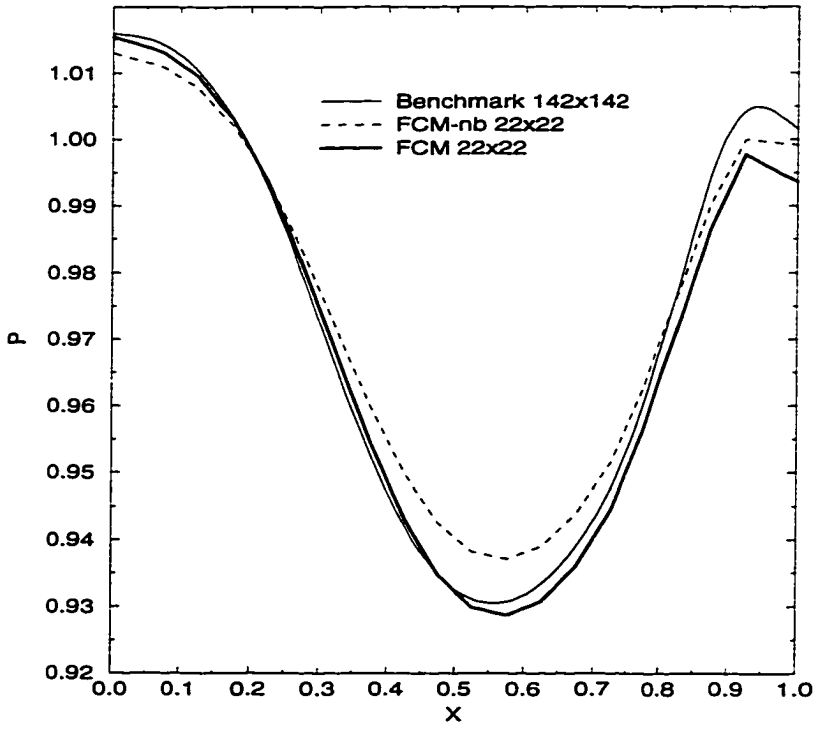

Figure 3.29 Driven Cavity Re=400. Effects of boundary cell corrections on the horizontal centerline P profile.

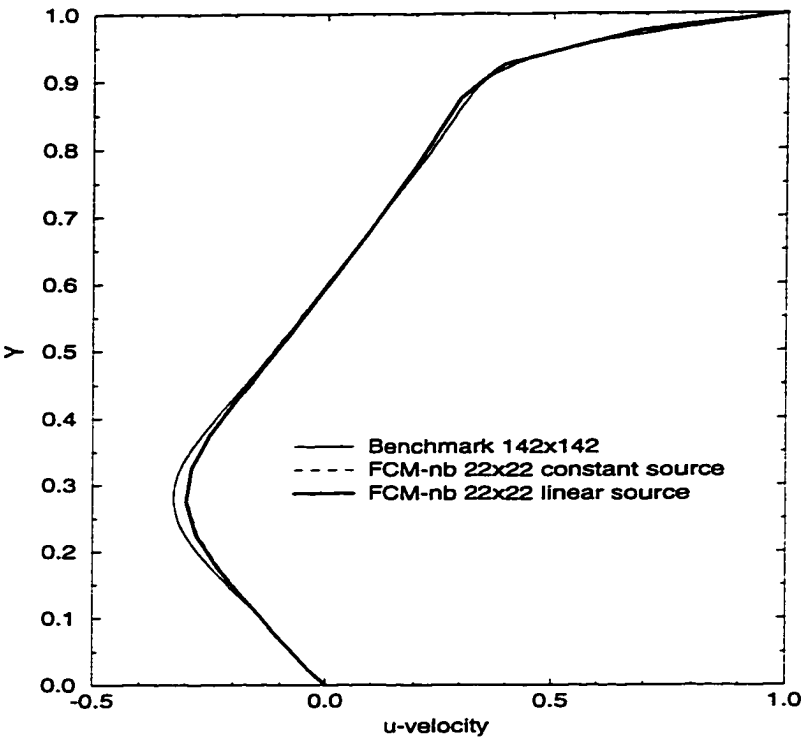

Figure 3.30 Driven Cavity Re=400. Effects of linear source on the vertical centerline u profile.

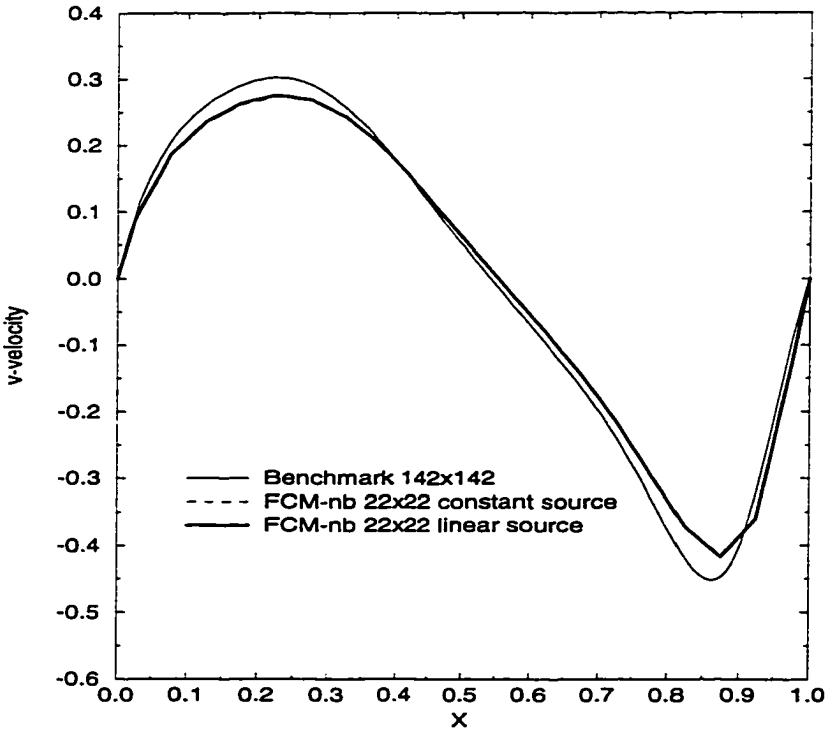

Figure 3.31 Driven Cavity Re=400. Effects of linear source on the horizontal centerline v profile.

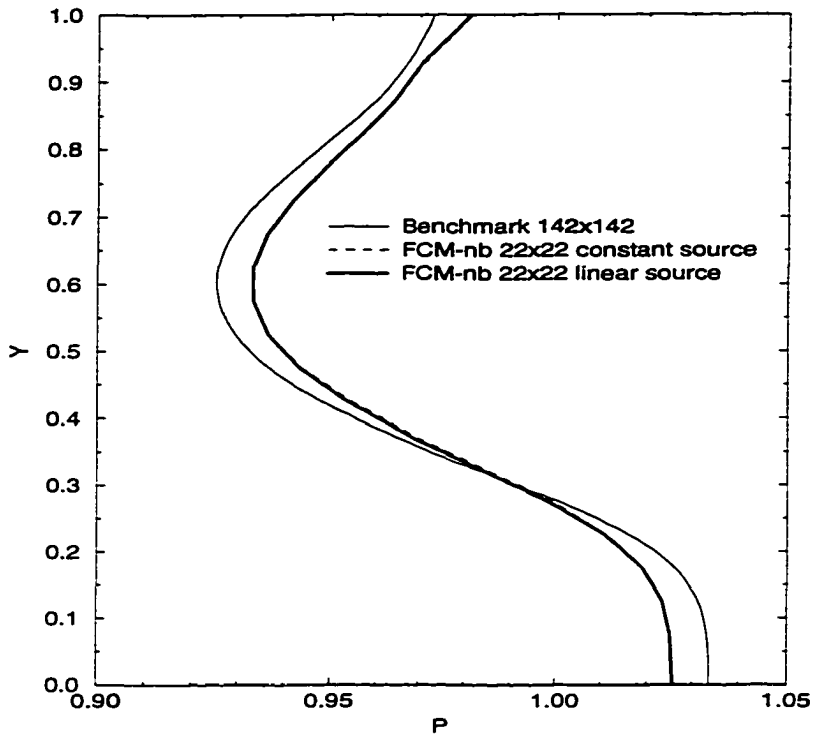

Figure 3.32 Driven Cavity Re=400. Effects of linear source on the vertical centerline P profile.

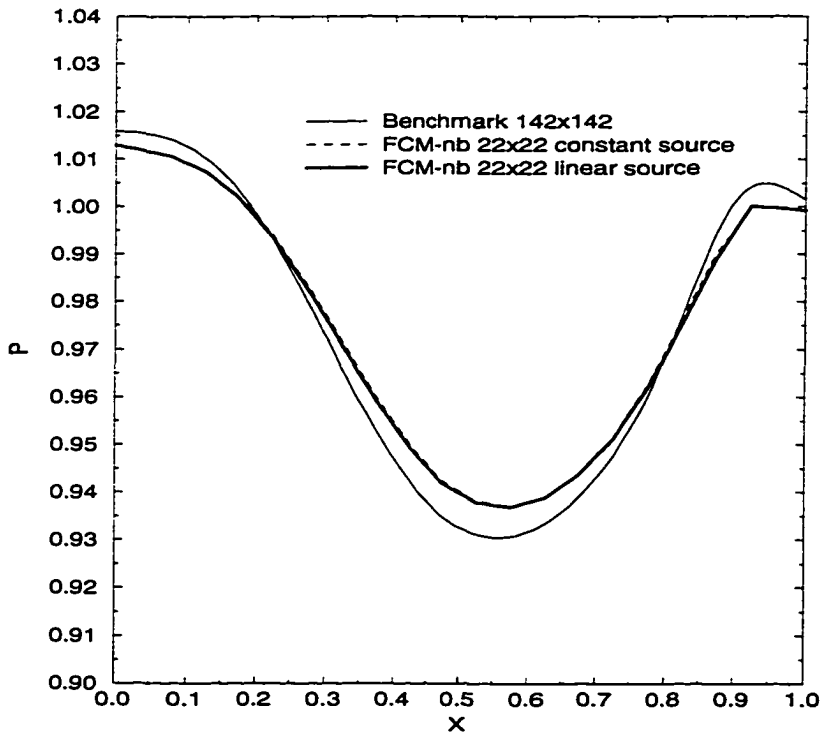

Figure 3.33 Driven Cavity Re=400. Effects of linear source on the horizontal centerline P profile.

4 DEVELOPMENT OF GENERAL BOUNDARY FORMULATION FOR PRESSURE EQUATION

4.1 Background

Recall the staggered control-volume for the x-momentum given in Figure 2.8. A complete portion of this grid at a given y-location is presented in Figure 4.1. Note that dotted control-volumes are used to represent the zero-width boundary control-volumes and that the choice of staggered grid means that u_1=u_2. Assuming that the boundary is not periodic ($u2 \neq u_I$) and the boundary values are prescribed, then (I-3) interior u-values ($u_3,\ldots,u_{I-1}$) are to be solved during the iterative process. Recall from equation 2.110 that integrating the x-momentum equation over the staggered u_i control-volume enables u_i to be written as the sum of the pseudo-velocity $\hat{u}_i$ and a term involving the difference of the pressures at the grid points neighboring u_i, as given by:

$$u_i = \hat{u}_i + d_i(P_{i-1} - P_i) \ , \tag{4.1}$$

where d_i is the area of the face (at which u_i is defined) divided by the center coefficient multiplying u_i. The above relationship involving u and the neighboring pressures needs to be established at every main control-volume face and will form the means by which the pressure equation is formulated.

The choice for the staggered control-volume containing u_3 (or u_{I-1}) is not as straightforward. If the left interface of the left boundary cell is made to pass through grid point ig=2, then the x-momentum equation is not conserved over the whole computational

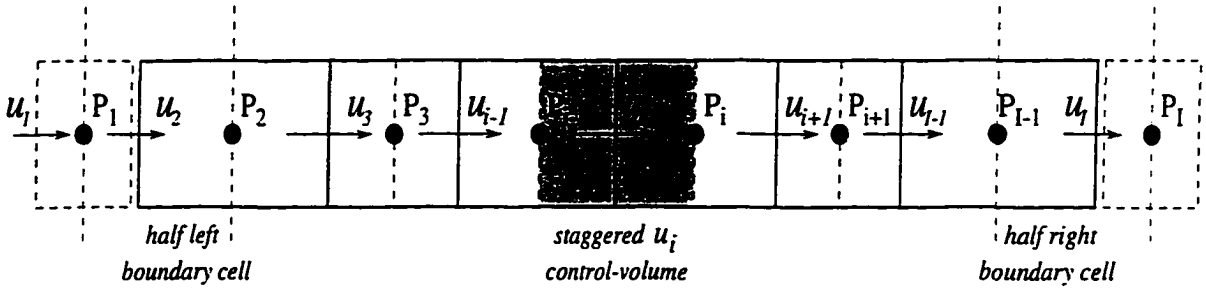

Figure 4.1 X-direction grid with main and staggered control-volumes.

domain. Note that each unknown u-velocity is to be covered by one staggered u-control-volume, thus the choice for the placement of the left interface of the left boundary cell means that half of the left boundary is uncovered by the x-momentum since u_2 is assumed to be known. Conservation of the x-momentum equation over the whole domain can be achieved by letting that left interface pass through grid point ig=1. Thus effectively $1\frac{1}{2}$ control-volume is used for the left boundary. This approach means that P_2 instead of P_1 is to be used with P_3 to represent the pressure difference across the left boundary control-volume so that the required relation involving u_3, P_2, and P_3 can be established. The right boundary staggered control-volume is established in the same manner. Thus, equation 4.1 can be written for i=3, ..., $(i-1)$. This concept of how the staggered boundary control-volume is formulated is also used for the integration of the y-momentum equation over the corresponding staggered grid.

Recall that the pressure equation is obtained by integrating the mass conservation equation over the main control-volume cells. The integrated equation is then discretized by substituting equation 4.1 for the u contained in the x-direction mass-flux expression at the considered main control-volume face. In this way, the dependency of the pressures at the left, inside, and right side of a main control-volume face is established. The dependency in the y-direction is obtained by substituting the counterpart of equation 4.1

(resulting from the integration of the y-momentum equation) for the v contained in the y-direction mass-flux expression. The complete discretization of the pressure equation still requires the establishment of the relationship described in equation 4.1 for i=2 and i=I-1, which are the relations at the left and right boundaries respectively. However, no equation relating u_2, P_1, and P_2 for the left boundary is available, and similarly for the right boundary. One way to work around this problem, as suggested by Patankar [5], is to realize that the assumption of known normal velocities at a given boundary face allows equation 4.1 to be written for that face by setting the pseudo-velocity equal to the known boundary normal velocity and setting the d term, which multiplies the pressure difference term, to zero. In other words, the mass-flux across that boundary face should not be expressed in terms of the pseudo-velocity but in terms of the known prescribed boundary velocity itself. In this way, boundary pressure will not appear in the discretized form of the pressure equation. This is consistent with the known principle that at a given boundary, either the normal velocity or the pressure is specified, but not both simultaneously. Thus, if the normal velocity at a given boundary is known, the computation of the pressure at that boundary becomes a post-processing procedure after convergence of the iterative process is achieved. The same principle also applies for the pressure-correction boundary condition.

Thus, for situations where all the boundary normal velocities are known/prescribed, boundary pressures have no means of influencing the interior pressures. Consequently, there are no means by which a unique pressure field can be established. In the introduction of the SIMPLER algorithm, Patankar points out that the fact that a unique absolute pressure field cannot be established does not pose a problem for the constant density case (no link between density and pressure) as long as an iterative solution procedure is used. The absolute pressure field obtained upon convergence depends on the initial guess used. Adding a constant to a pressure field which satisfies the momentum equation does not change the numerical solution. It is the differences in pressure which

are meaningful. For example, consider a simple channel flow problem given below in Figure 4.2.

At the left boundary, the inlet profile is given. If the inlet profile is not yet fully developed for the Reynolds number considered, then the outlet profile cannot be specified easily since it must first be determined if the channel length is sufficient for the flow at the outlet to be fully developed. However, the mass conservation principle requires that the mass-flow at the outlet be equal to the inlet mass-flow. This principle, together with the u-velocity profile at the immediate upstream of the outlet boundary, can be used to calculate the mass-flow adjusted outlet boundary. Thus, the outflow boundary is continually updated every iteration until convergence is achieved. In this example, no

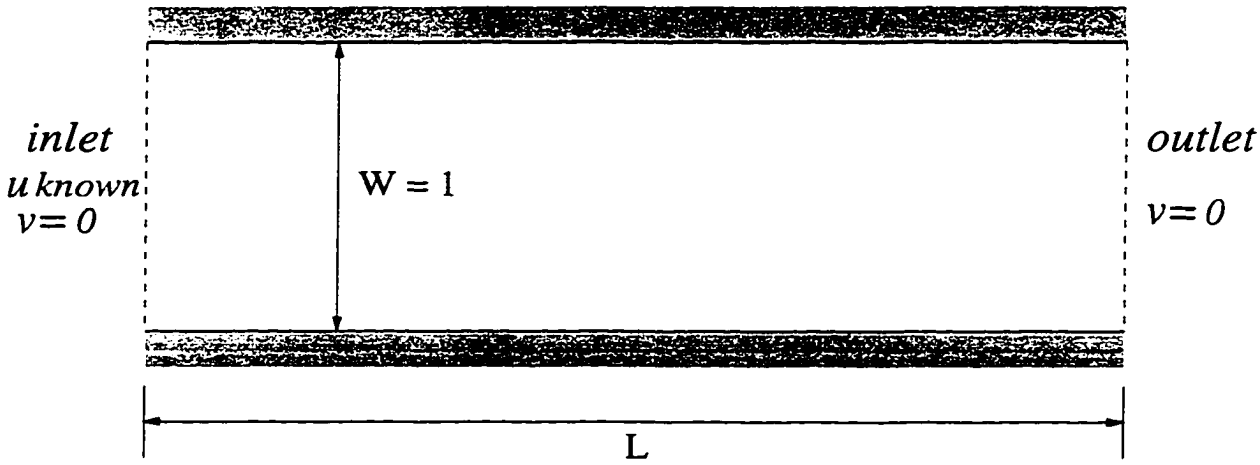

Figure 4.2 Two-dimensional channel flow with prescribed inlet velocity profile.

pressure at either the inlet or the outlet needs to be specified. Boundary pressures can be computed by extrapolation using the interior pressure values. The resulting pressure field will be unique up to a constant. If a pressure value is known at the inlet/outlet or at any other location, then the converged pressure field can be referenced to the known pressure value by adding or subtracting the appropriate constant to the pressure field. This formulation does not provide the means for a pressure value to be specified at a

certain boundary and then allow that reference value to determine the 'level' of the resulting pressure field automatically during the iterative procedure.

4.2 General Pressure Boundary Condition

Although the previous formulation of the boundary conditions for the pressure equation offers a simple and powerful procedure when the boundary normal velocities are known, it is not directly applicable when the pressure rather than the normal velocity is prescribed at the boundaries. Despite the fact that in the majority of fluid flow simulations it is generally possible to specify the normal velocities at the boundary faces (either through the known freestream/wall conditions or through iterative mass balance at an outlet boundary), there exist other flow problems where the pressure at a given boundary is easily defined but the normal velocity at that boundary is either not known or not easily approximated, even iteratively. This class of flow problems spurs the need to modify the existing procedure (discussed in the previous section) so that the resulting algorithm will be able to handle the general case of pressure boundary conditions. In particular, the modified formulation should be able to handle the following three cases:

Case 1 The formulation should be able to handle the trivial case of prescribed boundary normal velocities just as well as the previous formulation.

Case 2 Given the normal velocity at the boundaries and a reference pressure at a boundary segment, the formulation should be able to establish the level of the absolute pressure field correctly, based on the given reference value.

Case 3 Given pressure values at one or more segments of the boundary, the formulation should be able to develop the correct normal velocity profiles at that boundary segment(s) through the iterative process.

The first and second cases serve only as verifications for the modified formulation and do not make it any more useful than the original formulation. The strength of the modified formulation will be demonstrated by an example problem of the third case which the previous formulation is not capable of solving.

4.2.1 Development of General Pressure Boundary Equations

Recall that for the discretization of the x-momentum equation, $1\frac{1}{2}$ boundary cells are used for the left and right boundaries. For the left boundary cell, the reason for not placing the left interface of that cell at grid face ig=2 is that a half boundary cell remains which is not covered by the integration of the x-momentum equation. Also recall that the ability to take into account the influence of the boundary pressure into the discretized pressure equation requires that equation 4.1 be developed for i=2. In other words, the relationship between u_2 and the pressure difference (P_2-P_1) must be derived. A logical approach to formulate this required relationship is to place the left interface of the left boundary cell at grid point ig=2 and integrate the x-momentum equation at the remaining half-left boundary cell to find this needed relationship. In this way, the x-momentum equation is balanced throughout the whole computational domain. Even though the subsequent development focuses only on the left boundary, the same concept is used for the right, bottom, and top boundaries.

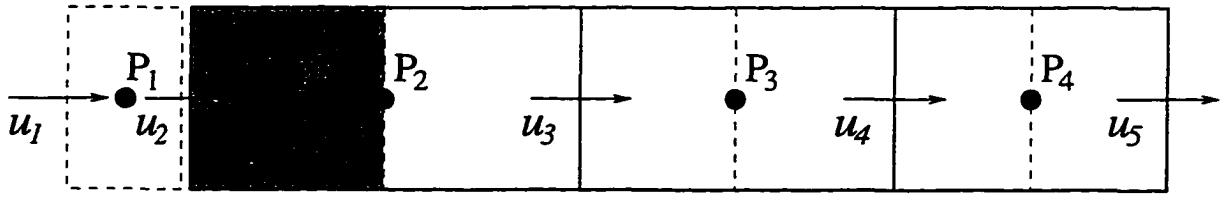

Figure 4.3 X-direction grid with shaded half-left boundary cell.

Consider a portion of the staggered x-momentum grid involving the left boundary given in Figure 4.3. Integration of the x-momentum equation 2.13 over time and over the half left boundary cell gives:

$$\frac{\left[(\rho u)_{pl} - (\rho u)^{o}_{pl}\right] \Delta x \Delta y}{\Delta t} +$$

$$f(J^{intg}_{xx-e} - J^{intg}_{xx-w} + J^{intg}_{yx-n} - J^{intg}_{yx-s}) +$$

$$(1-f)(J^{o\ intg}_{xx-e} - J^{o\ intg}_{xx-w} + J^{o\ intg}_{yx-n} - J^{o\ intg}_{yx-s}) =$$

$$P^{intg}_{1} - P^{intg}_{2} \ , \tag{4.2}$$

where the total-fluxes are evaluated at the appropriate places. The above equation can be rearranged and written as:

$$f J^{intg}_{xx-w} + (P^{intg}_{1} - P^{intg}_{2}) = Sla \ , \tag{4.3}$$

where

$$\begin{aligned} Sla \ = \ & \frac{\left[(\rho u)_{pl} - (\rho u)^{o}_{pl}\right] \Delta x \Delta y}{\Delta t} + \\ & f(J^{intg}_{xx-e} + J^{intg}_{yx-n} - J^{intg}_{yx-s}) \ + \\ & (1-f)(J^{o\ intg}_{xx-e} - J^{o\ intg}_{xx-w} + J^{o\ intg}_{yx-n} - J^{o\ intg}_{yx-s}) \ . \end{aligned} \tag{4.4}$$

It should be obvious that the purpose of equation 4.3 is to develop a relationship involving u_2 and (P_1-P_2). The next step is to develop a procedure to evaluate u_{pl} and the total-fluxes J_{xx-e}, J_{xx-w}, J_{yx-n}, and J_{yx-s}.

Using equation 2.76, the x-momentum x-direction total-flux (J_{xx}) at grid-face ig=2 can be written as:

$$J_{xx-e} = F_{x-ig=2} u_3 + \{D_{x-ig=2} A(|P_{ex-ig=2}|) + [\![F_{x-ig=2}, 0]\!]\}(u_2 - u_3) \ . \tag{4.5}$$

Note that even though the total-flux correction has not been included in the above equation, the on-going development applies equally well to FCM. Also observe that

equation 4.5 can either be written as an expression or evaluated numerically. In the calculation of the West-coefficient of the x-momentum staggered cell ig=3, equation 4.5 is used as an expression, while in the current discussion it is evaluated to find a numerical value for the total-flux J_{xx-e}. The use of the same equation to represent the total-flux at grid-face ig=2 must be observed to ensure the conservation of the x-momentum over the whole computational domain.

Recalling equation 2.14, the x-momentum x-direction total-flux at grid-face ig=1 can be written as:

$$J_{xx-w} = (\rho u_2)u_2 - \mu \frac{\partial u}{\partial x}_{ig=1} . \tag{4.6}$$

If the velocity component u_2 (boundary normal velocity) is known, then the formulation must solve for pressure P_1, and if it is not known, then the boundary pressure P_1 is specified. In general the term $\frac{\partial u}{\partial x}_{ig=1}$ can be written as:

$$\frac{\partial u}{\partial x}_{ig=1} = C_2 u_2 + C_3 u_3 + C_4 u_4 , \tag{4.7}$$

and can be evaluated in a number of different ways:

- First-order forward-difference.
- Second-order three-point unequal-space one-sided forward-difference.
- One-dimensional convection-diffusion without source applied to the main control-volume enclosing grid point ig=2.
- One-dimensional convection-diffusion without source applied to the combination of control-volumes enclosing grid point ig=2 and ig=3.

Before the x-momentum y-direction total flux J_{yx} can be evaluated, it is first necessary to evaluate u_{pl}. As in the case of the evaluation of $\frac{\partial u}{\partial x}_{ig=1}$, there are several different ways to do so, which are:

- First-order linear interpolation using u_2 and u_3.
- Second-order parabolic interpolation using u_2, u_3, and u_4.
- One-dimensional convection-diffusion without source applied to the main control-volume enclosing grid point ig=2.
- One-dimensional convection-diffusion without source applied to the combination of control-volumes enclosing grid point ig=2 and ig=3.

Once u_{pl} has been evaluated for the range of its j-index (j=1,...,J), the non-directional total-flux J_{yx} can be evaluated as:

$$J_{yx-jf} = F_{y-jf}u_{pl-j=jf} + \{D_{jf}A(P_{e-jf}) + [\![-F_{y-jf}, 0]\!]\}(u_{pl-j=jf-1} - u_{pl-j=jf}) \quad (4.8)$$

for jf=2,...,J. Now that all the needed components are in place, the term Sla given in equation 4.4 can be calculated.

Upon substituting equation 4.6 into equation 4.3, the following relation is obtained:

$$F_{x-ig=1}u_2 - \mu(C_2u_2 + C_3u_3 + C_4u_4) + \frac{1}{f}(P_1 - P_2) = \frac{Sla}{f\Delta y} . \quad (4.9)$$

For purposes which will be clear shortly in the discussion, equation 4.9 can also be written in the second form as:

$$(F_{x-ig=1} - \mu C_2)u_2 - \mu(C_3u_3 + C_4u_4) + \frac{1}{f}(P_1 - P_2) = \frac{Sla}{f\Delta y} . \quad (4.10)$$

Isolating u_2 and (P_1-P_2) to one side, the above two equations can be rearranged as:

$$F_{x-ig=1}u_2 + \frac{1}{f}(P_1 - P_2) = \frac{Sla}{f\Delta y} + \mu(C_2u_2 + C_3u_3 + C_4u_4) , \quad (4.11)$$

and

$$(F_{x-ig=1} - \mu C_2)u_2 + \frac{1}{f}(P_1 - P_2) = \frac{Sla}{f\Delta y} + \mu(C_3u_3 + C_4u_4) , \quad (4.12)$$

respectively. Equation 4.11 and equation 4.12 can be cast into an intermediate general form as:

$$a_1 u_2 + \frac{1}{f}(P_1 - P_2) = a_2 \ . \tag{4.13}$$

Finally, the needed relationship described in equation 4.1 for i=2 is found as:

$$u_2 = \xi_w + \eta_w (P_1 - P_2) \ , \tag{4.14}$$

where

$$\xi_w = \frac{a_2}{a_1} \ , \tag{4.15}$$

$$\eta_w = \frac{1}{f a_1} \ . \tag{4.16}$$

Note that upon comparing the above equation to equation 4.1, it is clear that ξ_w and η_w are used to represent $\hat{u}_2$ and d. At this point, it is important to explain why for certain situations it is necessary to use equation 4.10 instead of equation 4.9 (or equation 4.12 instead of equation 4.11). Observe that for the specific situation of Case 1 (prescribed boundary normal velocity and unknown boundary pressure), when the boundary is wall, if equation 4.11 is used, then the term a_1 vanishes since $F_{x-ig=1}$=0. This in turn leads to division by zero in the computation of ξ_w and η_w. For this situation, the use of equation 4.12 avoids the division by zero since the term (μC_2) is generally non-zero. However, it should be noted that in situations where the normal velocity at the boundary is given and non-zero, it is preferable to use equation 4.11 since this means that the term $\frac{\partial u}{\partial x}_{ig=1}$ is not partially but instead completely lagged, a procedure which tends to give better stability characteristics. For **Case 3** (prescribed boundary pressure but unknown boundary normal velocity), equation 4.11 should always be used since the *'yet to be solved'* normal velocity at the boundary is non-zero in general. Equation 4.14 makes it possible to take into account the influence of P_1. The effect of pressure at the right boundary is accounted for in the same way. Integration of the y-momentum

equation over the half bottom and top boundaries allows equations involving the pressure at the bottom and top boundaries to be taken into account in the same manner.

Consider the formulation of the discretized pressure equation at the left boundary main control-volume cell, excluding the left bottom and left upper cells. The left face of this cell is the left boundary of the domain considered. Using the procedure outlined in section 2.8.1, the discretized pressure equation for this cell is obtained as:

$$a_P P_P = a_E P_E + a_W P_W + a_N P_N + a_S P_S + b_P \ , \tag{4.17}$$

where the coefficients are given by:

$$\begin{aligned} a_E &= (\rho d)_e \Delta y \ , \\ a_W &= (\rho \eta)_w \Delta y \ , \\ a_N &= (\rho d)_s \Delta x \ , \\ a_S &= (\rho d)_n \Delta x \ , \\ a_P &= a_E + a_W + a_N + a_S \ , \end{aligned} \tag{4.18}$$

and the source term is given by:

$$b_P = -[(\rho \hat{u})_e - (\rho \xi)_w]\Delta y - [(\rho \hat{u})_n - (\rho \hat{u})_s]\Delta x \ . \tag{4.19}$$

The important thing to note is that the standard form of the discretized pressure equation for the inner cells (equation 2.115) is not changed. Similar equations are obtained for the other boundary and corner cells.

In the following sections, further development of each of the three cases is discussed separately.

4.2.2 Case 1: Prescribed Boundary Normal Velocity with No Reference Pressure

This case is the trivial situation where all the boundary normal velocities are prescribed and no reference pressure is given. It has been pointed out previously that the

original formulation is able to handle this case by using the known boundary normal velocity itself as the pseudo-velocity and setting the d-term to zero in equation 4.1 for i=2. The effect of the boundary pressure is neglected in the computation, and its value is found by extrapolation using the interior values once convergence is achieved. Examples of this class of problems are the confined flow inside a two-dimensional lid-driven cavity, internal flows with prescribed inlet profile(s) (a simple example is the channel flow with specified inlet profile as given in Figure 4.2), and external flows where either the boundary normal velocity or its derivative is given, or the normal velocity can be iterated using the mass-conservation principle.

In the previous section, a general formulation to account for the influence of boundary pressure was developed. However, the boundary pressure is unknown for this type of flow problems. Therefore, an equation relating the pressure at a given boundary to the immediate interior pressure must be developed. For example, at the left boundary, it is the relationship between P_1 and P_2. The purpose of this equation is to close the algebraic system of equations resulting from the formulation of the pressure equation. Recall that the formulation of the discretized pressure equation along the x-direction begins by integrating the continuity equation over the main control-volume cell for i=2, ..., $(I-1)$ and then substituting the flow-rate with a sum of the pseudo-velocity and the pressure difference term. This gives (I-2) equations, and there are I unknown pressures. The relationships between P_1 and P_2 and between P_{I-1} and P_I give the needed two equations to close the system of equations. The following discussion will focus on finding the relation between P_1 and P_2 at the left boundary, and as before, the same procedure is used for the other boundaries as well.

First, the relation involving u_2 and $(P_1 - P_2)$ given in equation 4.14 is repeated below for convenience:

$$u_2 = \xi_w + \eta_w(P_1 - P_2) \; . \tag{4.20}$$

This equation has been used as a means to bring P_1 into the discretized pressure equation. Therefore, trying to find the pressure relationship by substituting the known u_2 into the above equation will cause the system of equations to be indeterminate. It should be observed that during the development of the above equation, the conservation of mass has not been applied to the half left boundary cell. Integration of the continuity equation over this cell gives:

$$F_{x-e}^{intg} - F_{x-w}^{intg} + F_{y-n}^{intg} - F_{y-ss}^{intg} = 0 \ . \tag{4.21}$$

Isolating F_{x-w}^{intg} to one side and then using the definition of F_x, the above equation is rewritten as:

$$\begin{aligned} F_{x-w}^{intg} &= F_{x-e}^{intg} + F_{y-n}^{intg} - F_{y-ss}^{intg} \\ &= F_{x-w}\Delta y \\ &= (\rho u_2)\Delta y \ . \end{aligned} \tag{4.22}$$

Further rearrangement results in:

$$u_2 = \frac{1}{\rho \Delta y}[F_{x-e}^{intg} + F_{y-n}^{intg} - F_{y-s}^{intg}] \ . \tag{4.23}$$

Finally, by realizing that the common factor u_2 present in both equations 4.20 and 4.23 can be eliminated by subtracting one equation from the other, the following relation is obtained:

$$\begin{aligned} P_1 - P_2 &= \frac{1}{\rho \eta_w \Delta y}[F_{x-e}^{intg} + F_{y-n}^{intg} - F_{y-ss}^{intg} - (\rho \xi_w)\Delta y] \\ &= \chi_L \ . \end{aligned} \tag{4.24}$$

It is clear that the use of the above equation and its counterpart for the right boundary does not cause the considered system of equations to be indeterminate due to the incorporation of the mass conservation in the set.

The next step in the procedure is to decide how equation 4.24 should be used in the iterative process. One possibility is to use equation 4.24 to solve for P_1 using the

previously iterated (lagged) value of P_2 at the beginning of each SIMPLER iteration. This predicted P_1 is then used as the Dirichlet boundary condition for the interior pressures. Thus, in a sense, P_1 is solved explicitly. This procedure proves to be unstable in the current formulation. The other possibility is to rearrange equation 4.24 for P_1 and then use it in equation 4.17 to substitute for P_W. Thus, the following equation is obtained:

$$a_P P_P = a_E P_E + a_N P_N + a_S P_S + b_P \ , \tag{4.25}$$

where the coefficients a_E, a_N, and a_S are the same as those given in equation 4.18. The center-coefficient now becomes the summation of only three neighboring coefficients:

$$a_P \ = \ a_E + a_N + a_S \ ,$$

and the source term has an additional term:

$$b_P = -[(\rho\hat{u})_e - (\rho\xi)_w]\Delta y - [(\rho\hat{u})_n - (\rho\hat{u})_s]\Delta x + a_W \chi_L \ , \tag{4.26}$$

where again the coefficient a_W is the same as that given in equation 4.18. Note that the boundary pressure P_W does not appear in the discretized equation. However, this does not mean that the boundary pressure does not influence the interior values. Rather, the effect of P_W is included implicitly in the source term of the discretized equation. After solving the interior pressures, the boundary pressure can then be calculated using equation 4.24. However, before convergence is achieved, it is not necessary to update the boundary pressure at each iteration unless it is needed for the calculations of other non-primary flow variables. The above procedure to implicitly account for the pressure boundary influence has been shown to be quite successful.

The steady two-dimensional lid-driven cavity problem is again used to test the previously discussed formulation. A square cavity of unit length is used, and the moving lid is chosen to be the top boundary. Both the lid velocity and the density are chosen to be unity, and thus the Reynolds number is specified by using the appropriate value of

the diffusion μ. A Reynolds number of 400 is chosen, and the velocity components and pressure are initialized to zero and one respectively. Moreover, the Power Law scheme will be used throughout the verification process of this general boundary pressure formulation. Both 22x22 and 42x42 uniform grids are used, and the results obtained using the original formulation will be plotted against the results obtained using the general formulation.

The plots of the pressure along the vertical centerline (x=0.5) for both grids are given in Figures 4.4 and 4.5. For the purpose of comparison, the results obtained using the 142x142 fine grid and the original formulation are also plotted. It is important to mention that the original formulation uses linear interpolation of the interior pressures to calculate boundary pressures. It is clear from these figures that for most of the y-range, the original and general formulation give practically the same profile. However, close observation at the vicinity of the top boundary reveals that the general formulation gives a more conforming profile to the benchmark solution than the original formulation. This could be an important factor if the normal pressure gradient at the moving lid is to be used in the calculation of other variables of interest. From these figures, it can also be observed that since no reference pressure is specified anywhere in the domain, a floating pressure field is obtained. Adding a constant to this pressure field does not change the numerical solution for the velocity components.

In Figure 4.6, the plot of the velocity components along the vertical centerline is given. No differences between the original and general formulation are observed. Even though the velocity and pressure profiles along the horizontal centerline are not given, the same characteristics are observed.

The mass, x-momentum, and u-velocity convergence histories are given in Figure 4.7 through Figure 4.9. The relaxation factor used is 0.4, and only insignificant differences in the convergence characteristics are observed. This is another important characteristic of the general formulation.

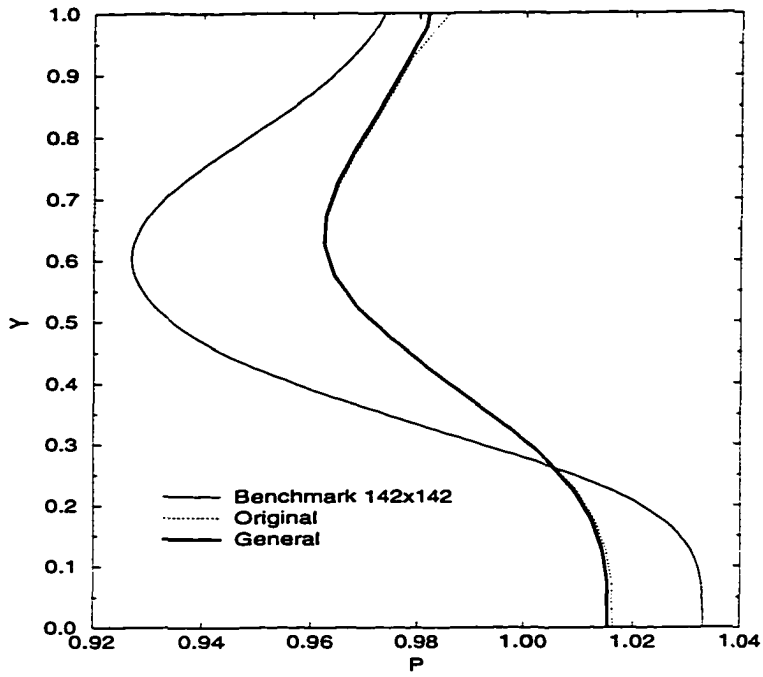

Figure 4.4 Driven Cavity Re=400 using 22x22 grid. Comparison of vertical centerline pressure profile between original and general pressure boundary formulation.

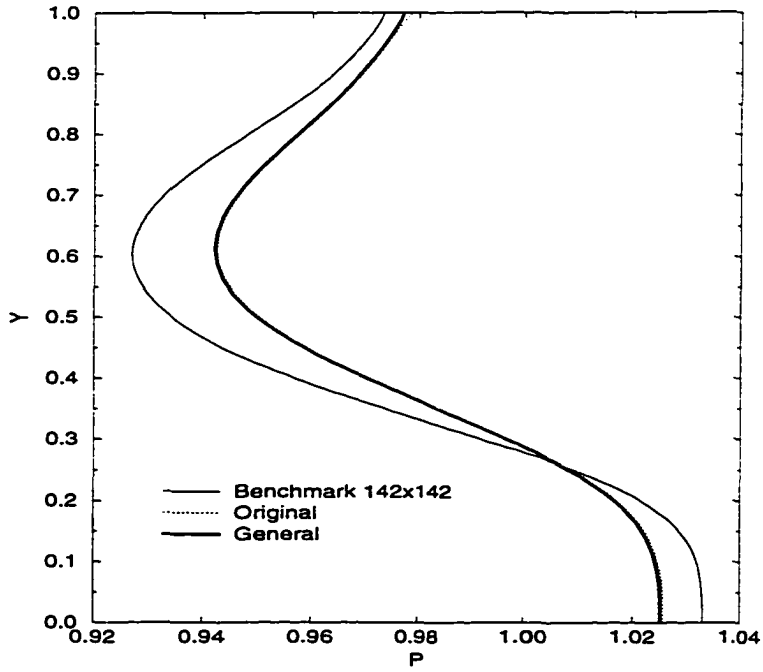

Figure 4.5 Driven Cavity Re=400 using 42x42 grid. Comparison of vertical centerline pressure profile between original and general pressure boundary formulation.

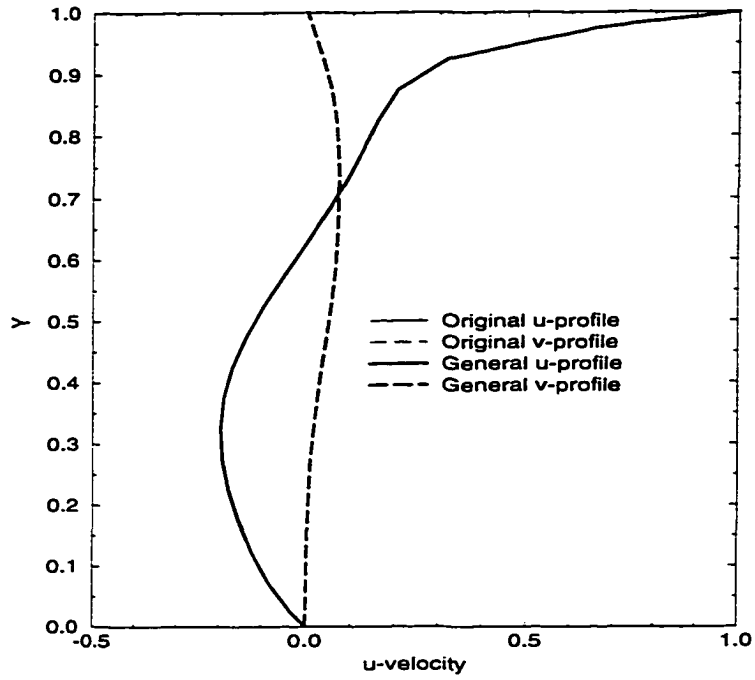

Figure 4.6 Driven Cavity Re=400 using 22x22 grid. Comparison of centerline u and v profiles between original and general pressure boundary formulation.

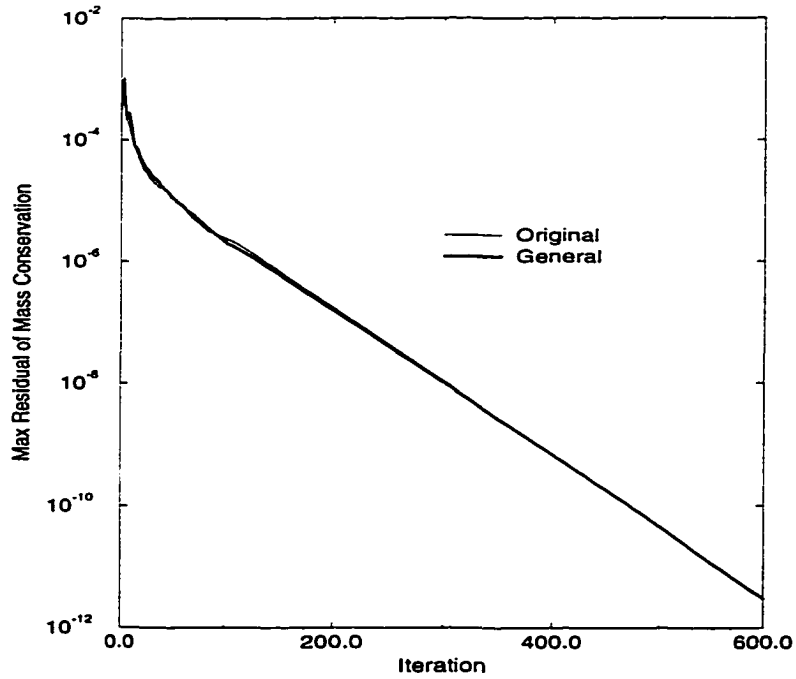

Figure 4.7 Driven Cavity Re=400 using 22x22 grid. Comparison of mass convergence history between original and general pressure boundary formulation.

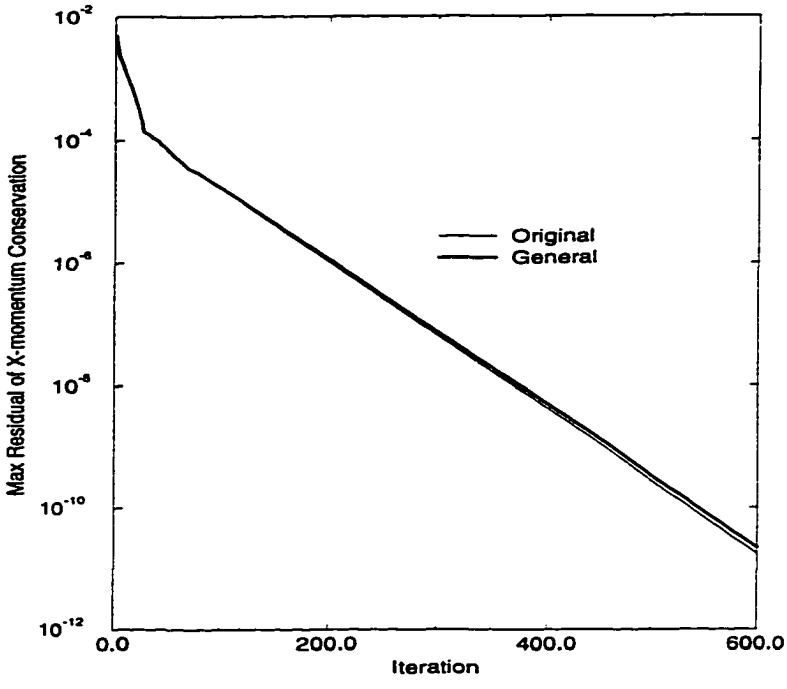

Figure 4.8 Driven Cavity Re=400 using 22x22 grid. Comparison of x-momentum convergence history between original and general pressure boundary formulation.

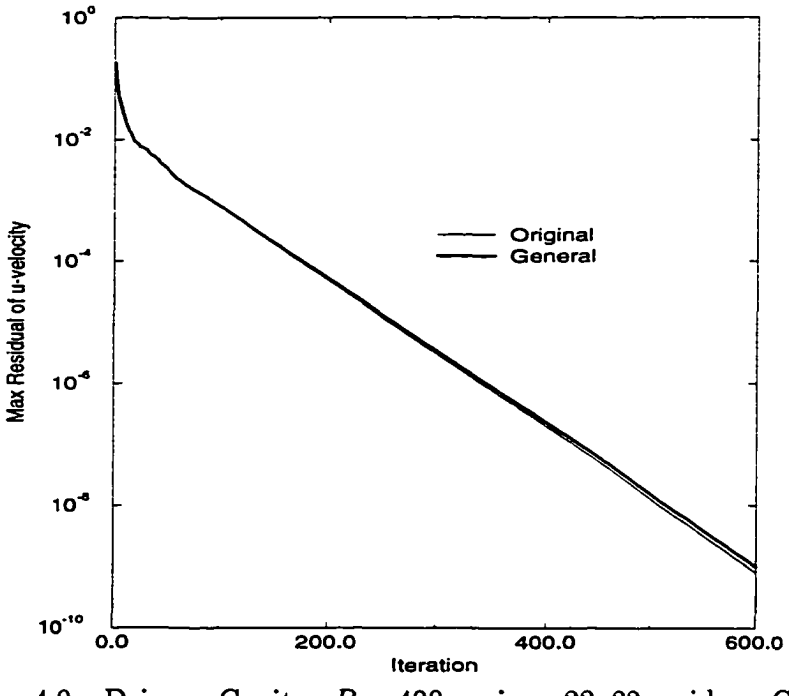

Figure 4.9 Driven Cavity Re=400 using 22x22 grid. Comparison of u-velocity convergence history between original and general pressure boundary formulation.

The most important characteristic of this new formulation is that it is now possible to take into account the effect of the boundary pressure if it is specified. The present situation of prescribed normal-velocity at the boundaries is just a special case for this general formulation.

4.2.3 Case 2: Prescribed Boundary Normal Velocity with Reference Pressure

The procedure for the specified boundary normal velocities but with a given reference pressure at a boundary segment is actually very similar to the procedure used in the previous case. As an example problem, consider the steady two-dimensional flow inside a channel as shown in Figure 4.2. The inlet profile is specified and the u-profile at the outlet boundary is iteratively specified imposing mass conservation. This problem is already adequately specified at this stage. The resulting pressure profile will be uniform at a given x-location, and if the inlet profile is already developed for the considered channel width and Reynolds number, a linear pressure drop will be observed along the x-direction (Poseuille flow). However, a floating pressure field will be obtained since no reference pressure is specified. Now suppose that a uniform pressure is specified at the inlet boundary. Since the left boundary pressure is known, the procedure used in the previous subsection to find the relation between P_1 and P_2 is not needed. It is at the right, bottom, and top boundaries that boundary pressures are implicitly accounted for as outlined in the **Case 1** discussed previously. Upon convergence of the iterative process, the pressure field will no longer float but is fixed at the level dictated by the reference pressure. However, the rate of the pressure drop at a given x-location will still be the same as the situation where no pressure reference is given. Because of its significant similarity with the previous case, this case is not illustrated in this study. Rather, effort will be focused on the subsequent final case where it is the prescribed pressure boundary that is used to drive the flow during the iterative process.

4.2.4 Case 3: Prescribed Boundary Pressure

Consider the channel flow problem discussed in the previous subsection. For the sake of simplicity, assume that a fully developed inlet profile is used. It is important to note that in this problem, it is the prescribed profile of the inlet boundary normal velocity that really drives the interior velocity components to the correct profile. During the iterative process, it is relatively 'easy' for the interior velocity components to adjust to the correct field since the left boundary condition is both known and unchanging. At the outlet boundary, even though the boundary normal velocity is being iteratively solved, a relatively good profile can be specified satisfying mass conservation. Convergence of the pressure field is also relatively straightforward since a good intermediate velocity field will result in a good predicted pressure field (recall that the pressure field is deducted from the velocity field in the SIMPLER algorithm).

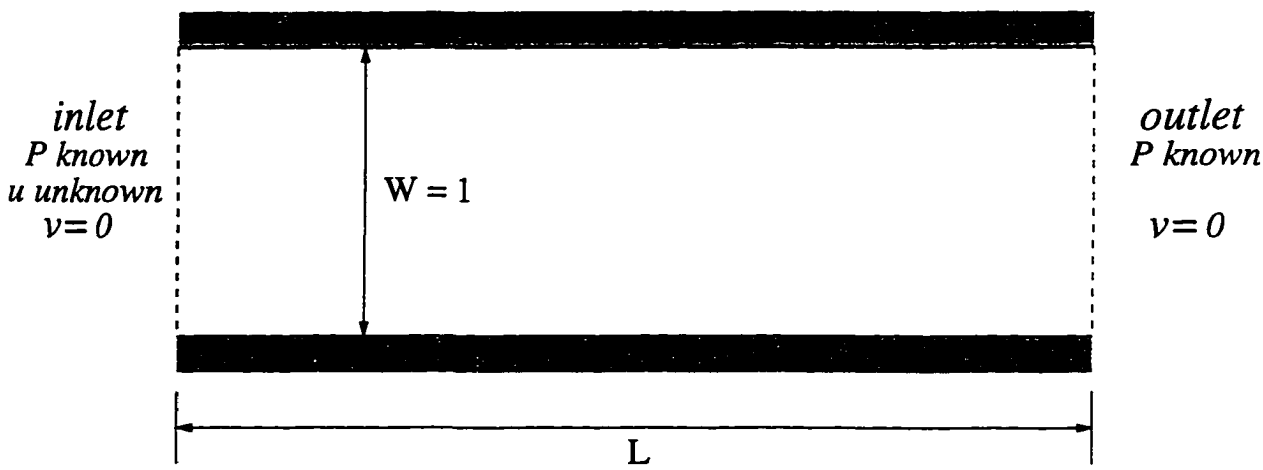

Figure 4.10 Two-dimensional channel flow with prescribed inlet and outlet pressure profiles.

For the same channel configuration, a vastly different situation is encountered if, instead of specifying the inlet u-profile, pressure profile is specified at the inlet and the outlet boundaries (refer to Figure 4.10). This means that the numerical process uses the difference of the inlet and outlet pressure to drive the flow to convergence since the

correct profile of the inlet boundary velocity is not known. The inlet u-profile must now be iteratively deducted from the known pressure boundary, while at the outlet boundary, the predicted profile can be obtained in a similar manner, or the profile at the immediate interior location to the right boundary can be used. Whichever method is chosen to obtain the outlet profile, the outlet profile should then be adjusted to preserve mass conservation. Thus, a much more extensive dependency between pressure and velocity fields exists. During the iterative process, since the normal velocity boundary condition is being iteratively developed, a relatively good intermediate velocity field is no longer available to obtain a good pressure field. In turn, the pressure gradient term in the momentum equations cannot be accurately calculated.

A procedure must now be developed to calculate the boundary normal velocity given the boundary pressure. For this example problem, the left boundary is considered. The first approach is to apply mass conservation to the main control-volume i=2 (refer to Figure 4.3). Integration of the continuity equation over this cell and then solving for u_2 gives an equation identical to equation 4.23:

$$u_2 = \frac{1}{\rho \Delta y}[F^{intg}_{x-e} + F^{intg}_{y-n} - F^{intg}_{y-s}] \,. \tag{4.27}$$

where the only difference is that the domain of integration of equation 4.23 is over the half left boundary cell. Note that the above equation does not involve the pressure difference term at the left boundary. Another alternative is to combine equation 4.27 and equation 4.20 to give:

$$u_2 = \frac{1}{2}\{\xi_w + \frac{1}{\rho \Delta y}[F^{intg}_{x-e} + F^{intg}_{y-n} - F^{intg}_{y-ss}]\} + \frac{\eta_w}{2}(P_1 - P_2) \,, \tag{4.28}$$

where now the left boundary pressure difference is taken into account. It is observed in the current study that the two procedures have virtually identical convergence characteristics. Either of them may be chosen, although the former may be preferable due to its simplicity.

As in the case of solving the boundary pressure in **Case1**, the question now arises as to how to use the equation for u_2 given above in the iterative process. Again, the easiest approach is to solve for u_2 explicitly and then use this predicted u_2 as the boundary condition for the interior values. Moreover, this predicted inlet profile is also used to estimate the amount of massflow and is then used to adjust the massflow at the outlet boundary. An implicit way to calculate u_2 is also possible, in which case the relationship between u_2 and u_3 will be developed from equation 4.27 as:

$$u_2 = u_3 + \frac{1}{\rho \Delta y}[F_{y-n}^{intg} - F_{y-ss}^{intg}] \; . \tag{4.29}$$

The subsequent procedure is similar to the one used for the pressure equation discussed previously. Both the explicit and the implicit procedures for solving u_2 prove to be stable and exhibit the same convergence characteristics.

A channel flow problem with a fully developed inlet profile, known as the Poiseuille flow, is one of the very few flow problems where the exact solution to the Navier-Stokes equations exists. From the available literature [39], it is known that a linear pressure drop (P_x=*const*) will occur throughout the length of the channel with vertical velocity component v=0. The u-velocity is a parabolic function of y and is independent of x. Assuming that the Reynolds number is based on the channel-width W and that the reference velocity u_{ref} is unity, the analytical profile of the u-velocity is given by:

$$u(y) = -\frac{R_e P_x}{2} \, y(1-y) \; . \tag{4.30}$$

For the current test case, the following parameters are used: ρ=1, μ=0.01, W=1, and L=4. The Reynolds number is then calculated to be Re=100. If the value of the u-velocity at the middle of the channel is chosen to be 0.5, then using equation 4.30, the pressure gradient P_x is found to be -0.04. The pressure drop across the channel is easily calculated to be 0.16. The pressure at the inlet is specified to be unity, and the outlet pressure is fixed at 0.84, giving the correct pressure drop. For this case, a 22x22 uniform grid is used.

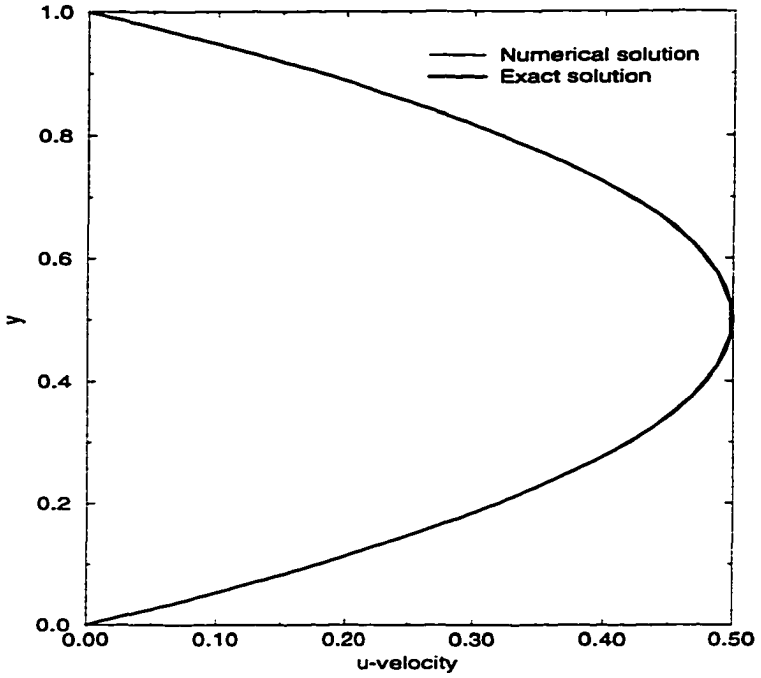

Figure 4.11 Comparison between exact and numerical u-velocity profile for two-dimensional channel flow with Re=100 and channel-width W=1.

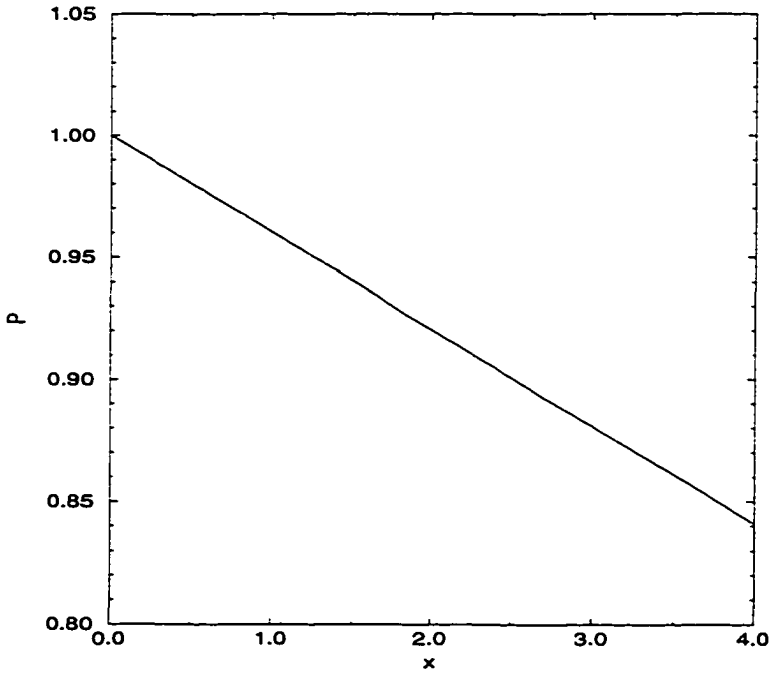

Figure 4.12 Pressure distribution for two-dimensional channel flow with Re=100 and channel-width W=1.

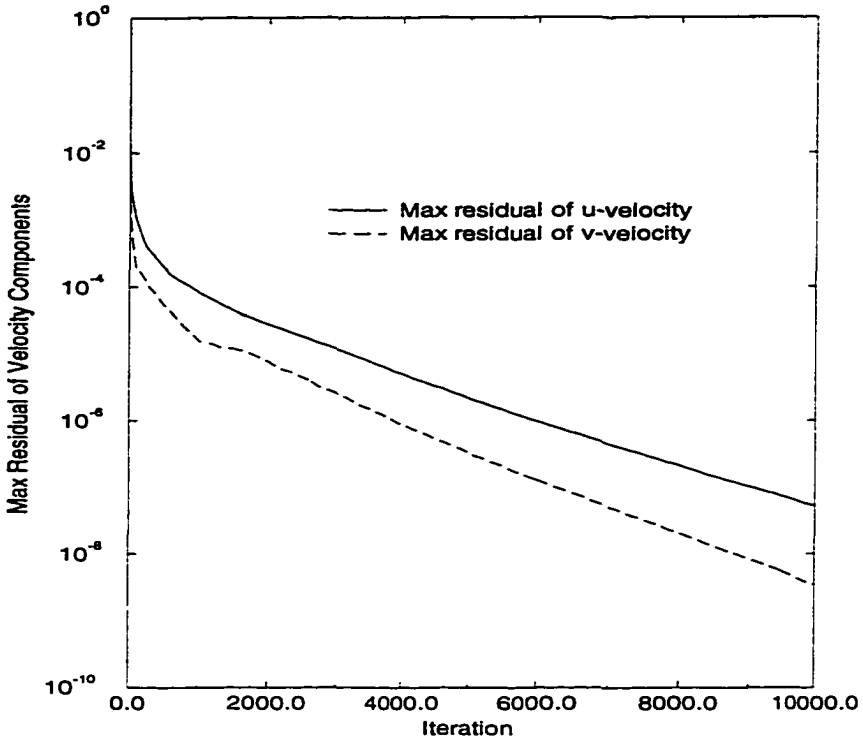

Figure 4.13 Convergence history of velocity components for two-dimensional channel flow with Re=100 and channel-width W=1.

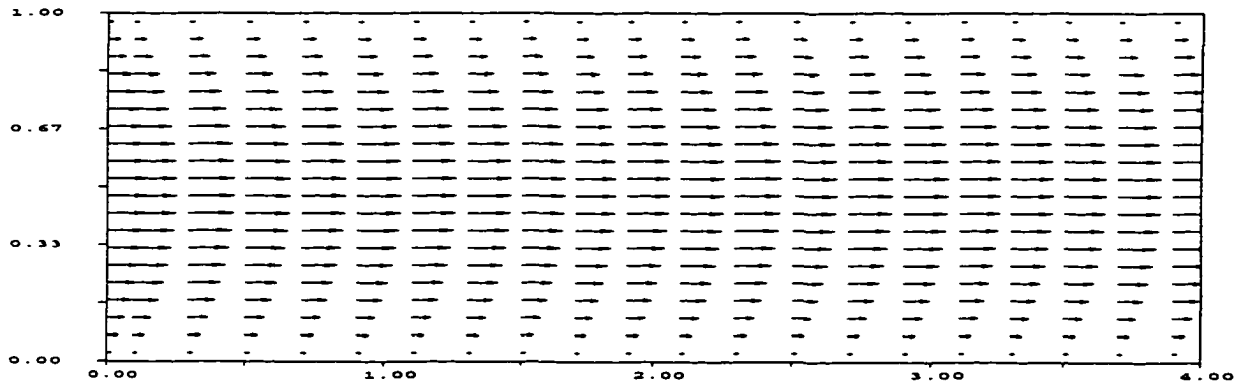

Figure 4.14 Velocity vector plot for two-dimensional channel flow with Re=100 and channel-width W=1.

The plot of the u-velocity profile as a function of y is given in Figure 4.11. An excellent comparison with the exact solution is observed. The plot of the pressure profile along the x-direction is given in Figure 4.12. As expected, the pressure drops very linearly across the length of the channel. Figure 4.13 gives the convergence history of the maximum residual of both velocity components. The profiles of the u-velocity at different x-locations along the channel is given in Figure 4.14.

Thus, it can be concluded that the general formulation developed in this section to account for the influence of boundary pressure has proven to be effective in handling the three types of boundary specifications discussed previously. Most importantly, the general formulation is able to solve the type of flow problems such as **Case C**, where at some given boundary segments, pressure and tangential velocity are specified, and which is simply unsolvable using the original formulation.

4.3 Implementation of General Pressure Boundary in FCM

Even though the current implementation is applied to the Power Law scheme, implementation to the FCM requires no special procedure. Throughout the course of FCM development, both the original and the general pressure boundary formulation have been tested and used. Recall the coarse grid (22x22) pressure profile of FCM with boundary correction for the lid-driven cavity test case (Re=400) given in Figure 3.28. It was mentioned before that the corrected pressure profile at the vertical centerline shows excellent agreement with the benchmark solution. However, significant deviation from the reference solution is observed for the portion of the profile near the lid. It was also observed in Figures 4.4 and 4.5 that the use of the general pressure boundary formulation results in an improved pressure profile near the lid for the case of the Power Law scheme. The vertical centerline pressure profile obtained using this new pressure boundary formulation applied to FCM with the boundary correction is given in Figure 4.15. It can be

seen that at the region near the lid, the new corrected profile conforms very well to the reference solution. However, it can also be observed that a slight decrease in accuracy results from the implementation of the general pressure boundary procedure. As the grid is refined to 32x32, the discrepancies disappear.

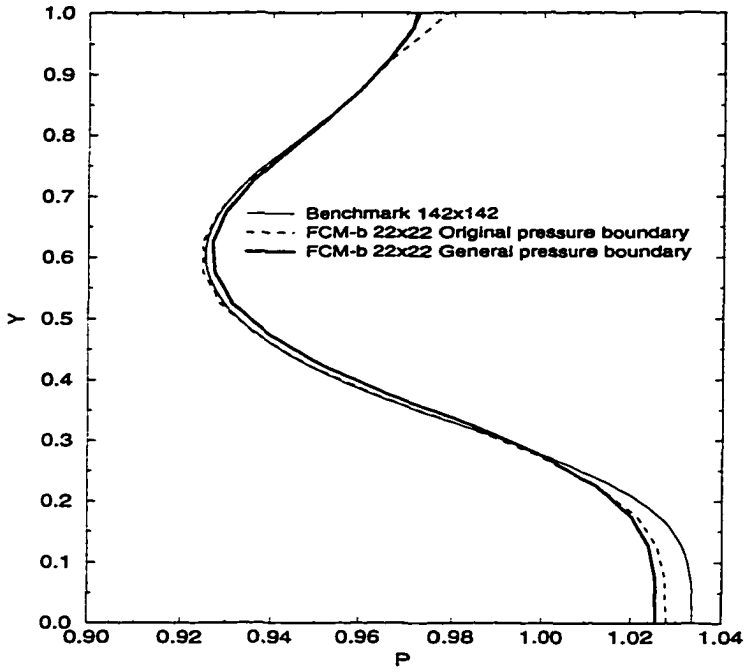

Figure 4.15 Driven Cavity Re=400 using 22x22 grid. Comparison between original and general pressure boundary formulation applied to FCM with boundary cell correction.

5 NUMERICAL VERIFICATION AND TESTING OF THE ALGORITHM

During the development phase in **Chapter 3**, the higher accuracy of FCM was briefly introduced. However, before using FCM to solve practical, real world flow problems, it is first necessary to investigate and establish the basic characteristics of FCM. In particular, it is necessary to investigate whether the FCM approach to flux correction does indeed reduce the numerical diffusion displayed by the Power Law scheme when the flow is significantly skewed to the grid. Secondly, it is important to see how FCM performs in situations where there is a mix of flows aligned and skewed to the grid. These accuracy issues are addressed in the context of the two-dimensional lid-driven cavity and backward facing step flow simulations. Thirdly, it is known that for a given number of grid points, the accuracy of a numerical solution degrades as the grid is stretched. Thus, the sensitivity of FCM to grid stretching needs to be studied and understood as well. The stability, convergence characteristics, and extra CPU time needed for FCM need to be assessed. Next, the capabilities of FCM to accurately simulate time-dependent flow problems must then be verified by solving the impulsively started lid-driven cavity problem. An understanding of these aforementioned properties of FCM is essential in order to be able to apply FCM effectively and efficiently. The simple test problems chosen to carry out these investigations do not, by any measure, consist only of simple flow structures. On the other hand, the flow structures present in these test problems are typical of what will be found in solving complex, real world, industrial type flow

problems.

Over the last decade, the multigrid technique to accelerate the convergence of an iterative numerical scheme for linear and non-linear problems has been widely adopted by the CFD community. The well-known and widely used FAS multigrid technique has been used in conjunction with the segregated SIMPLER algorithm by Zori [40] and has been shown to effectively speed up the convergence of the algorithm. In the current work, the performance of FCM, when used in conjunction with this multigrid technique, is also analyzed.

Having done extensive FCM testing in two-dimensions, a limited testing of FCM for three-dimensional flow situations is then performed on the standard three-dimensional lid-driven cavity.

5.1 Two-dimensional Lid-Driven Cavity Flow

In spite of its idealization, the flow inside a lid-driven cavity has been widely acknowledged as an excellent test case for evaluating numerical schemes. This is due to the presence of large streamline to grid skewness over most of the flow domain (on a rectangular grid). Moreover, the existence of several relatively large recirculating regions, where convection and diffusion are of comparable magnitude, requires that the difference formulation of the latter be at least as accurate as the former. The steady flows inside a two-dimensional lid-driven cavity (Figure 3.1) for a range of low, medium, high, and very high Reynolds numbers (Re=100,400,1000,10000) have been used to investigate the characteristics of FCM and its performance relative to the Power Law, central-difference, and QUICK schemes. Constant property laminar flow is assumed, and the Reynolds number is defined by $Re=(\rho U_{lid} L)/\mu$, where ρ is the density of the fluid, U_{lid} is the speed of the sliding lid, L is the length of the square enclosure side wall, and μ is the fluid viscosity. Fine grid solutions obtained using the central-difference

scheme are used as reference solutions. For Re=100, 1000, and 10000, fine grid solutions obtained using the vorticity-stream function formulation with the multigrid method by Ghia [7] are given as further verifications. Numerical solutions of the QUICK scheme with third-order boundary treatment are taken from published results by Hayase [8].

All calculations are started with a zero velocity field and unit pressure field. For comparison with standard published results, uniformly spaced grids are used unless otherwise noted. Each calculation is terminated when the residual ϵ became smaller than 10^{-9}, where ϵ is defined as the maximum value of the residuals for the mass, x-momentum, y-momentum, and the difference between the values of u- and v-velocities between two successive iterations. It is found that it is not necessary to retain the unsteady terms in the momentum equations (time marching) in order to achieve stable and converged solutions on all grids for the first three Reynolds numbers considered. However, for reasons discussed later in the appropriate subsection, it is necessary to retain the unsteady terms for the very high Re=10000 case.

To facilitate future comparisons with other numerical schemes, tabular forms of FCM solution along the cavity centerlines are given in **Appendix B**.

5.1.1 Calculations for Re=100

The velocity profiles for the u- and v-velocities along the vertical and horizontal centerlines are given in Figures 5.1 and 5.2 respectively. As is obvious, the coarse grid solutions given by Power Law, Central, FCM, and QUICK are all in close agreement with the reference solution. This is expected since in general for low Reynolds number flows, the influence of the flow transport in a coordinate direction is usually too small to significantly affect the transport profiles in the other coordinate directions. Thus, the 'one-dimensional' nature of the Power Law scheme is usually sufficient to model the flow.

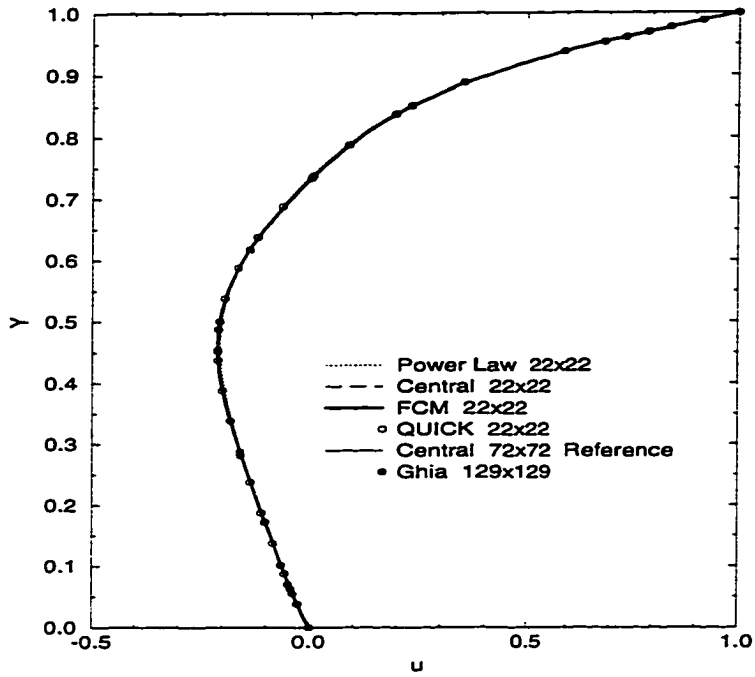

Figure 5.1 Vertical centerline u-velocity profile for Re=100.

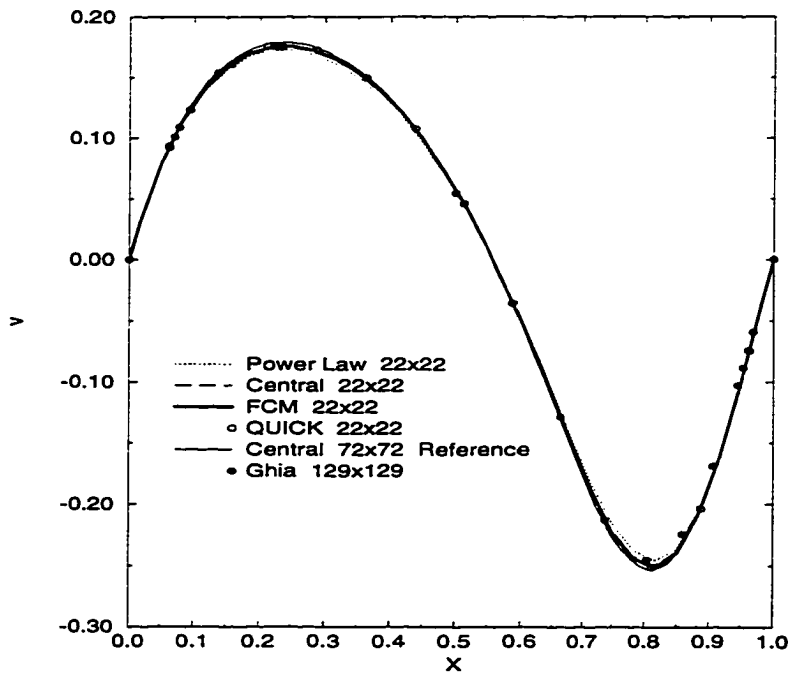

Figure 5.2 Horizontal centerline v-velocity profile for Re=100.

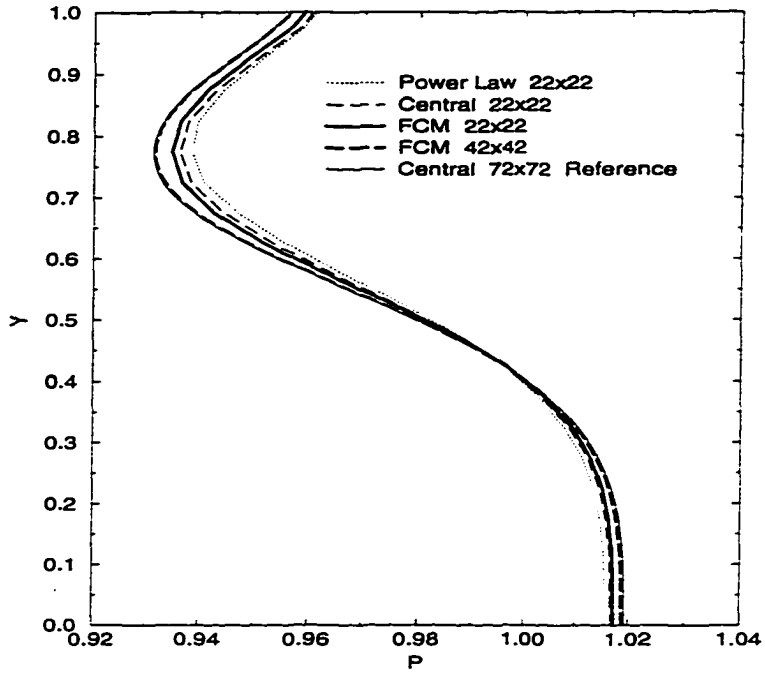

Figure 5.3 Vertical centerline pressure profile for Re=100.

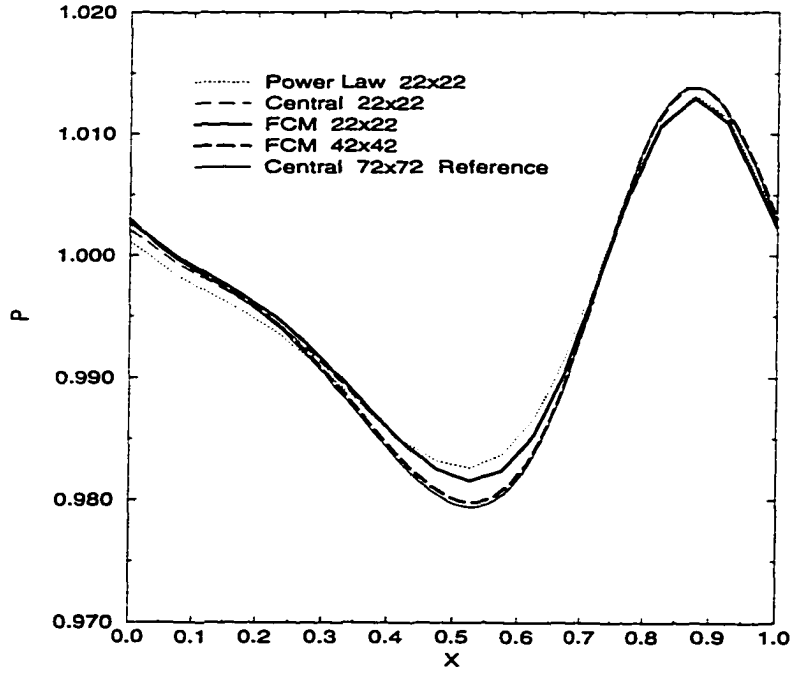

Figure 5.4 Horizontal centerline pressure profile for Re=100.

In spite of its triviality, this flow situation shows that the convection-diffusion source S_{cd} (refer to equations 3.17 to 3.20) is self adjusting. In flow regions where the cross-grid transport influence and source are small, S_{cd} is also small and results in a small total-flux correction, and vice-versa. The variation of pressure along the centerlines is given in Figures 5.3 and 5.4. These plots illustrate that for the same grid, FCM profiles conform better to the reference profiles in the high gradient regions. Note also that the pressure profile in the vicinity of the moving lid conforms well to the reference profile due to the improved boundary pressure formulation developed in **Chapter 4.**

5.1.2 Calculations for Re=400

At Re=400, FCM starts to distinguish itself. Centerline velocity profiles are given in Figures 5.5 through 5.8. From these figures, it is clear that the Power Law scheme is significantly diffusive for high Reynolds number flows. Both the 22x22 and 32x32 coarse grid solutions of that scheme are inadequate to accurately model the centerline profiles. The Power Law solution reaches grid independent solution around the 102x102 grid. On the other hand, a significantly improved solution is obtained using FCM. The solution using a 22x22 grid closely follows the centerline reference solution. Using a 32x32 grid, the FCM solution can no longer be distinguished visually from the reference solution. This is not to say that all the flow properties have been adequately and accurately resolved using this coarse grid. Finer grids are certainly needed to better resolve the two smaller secondary recirculating regions at the bottom corners of the cavity. It is also observed that FCM peforms better than the central-difference scheme. This quality will be consistently observed for higher Reynolds number flows. The highly accurate nature of FCM is also evident from the plots of centerline pressures given in Figures 5.9 and 5.10. A sharp contrast exists between the profiles predicted by FCM, central-difference, and Power Law scheme. The coarse grid FCM solution follows the reference profile very well.

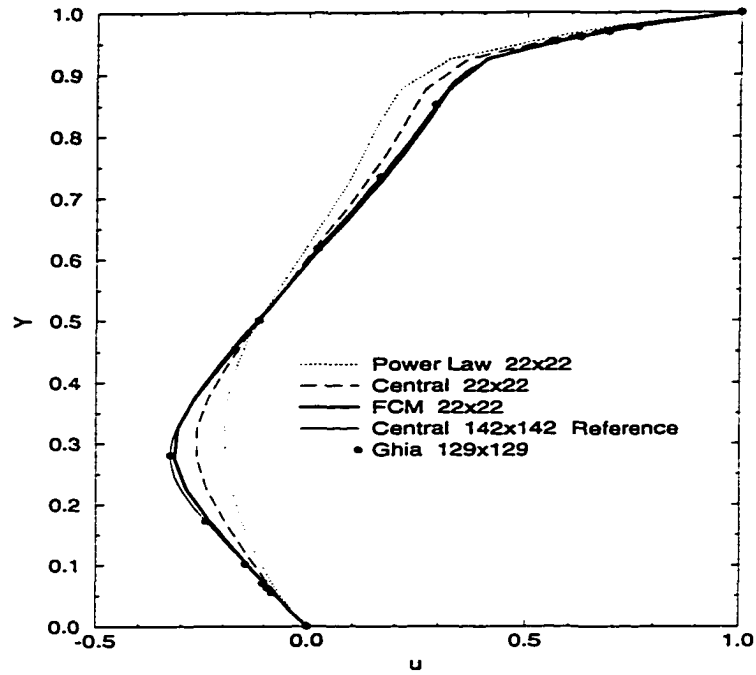

Figure 5.5 Vertical centerline u-velocity profile for Re=400.

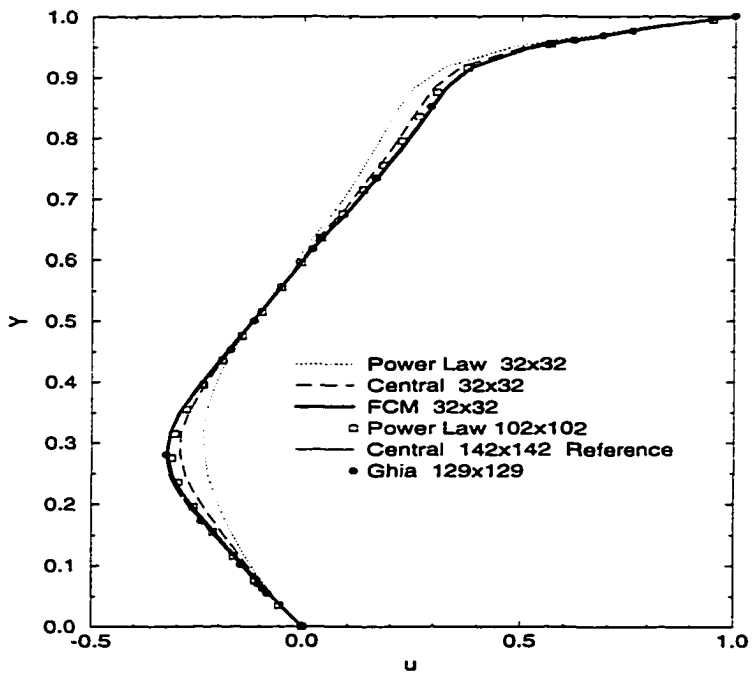

Figure 5.6 Vertical centerline u-velocity profile for Re=400 using finer grid.

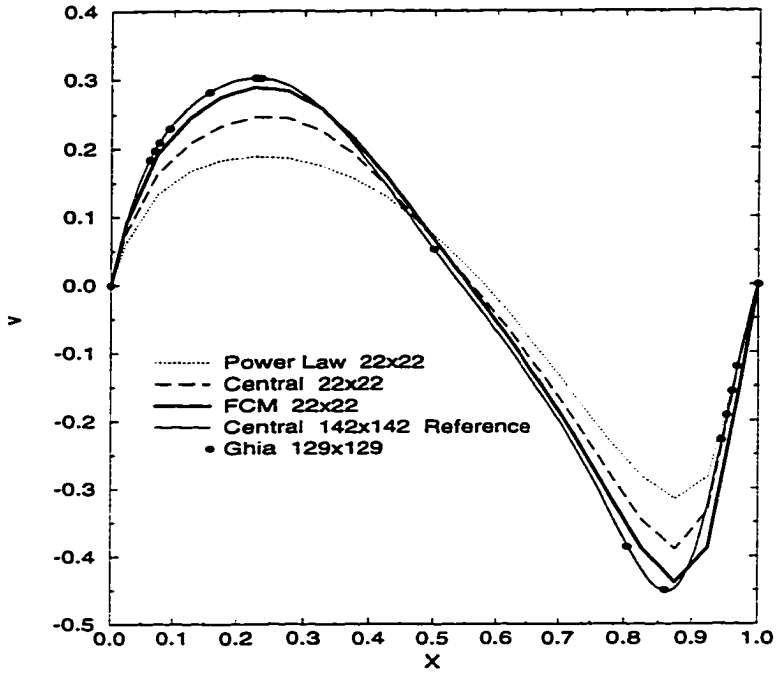

Figure 5.7 Horizontal centerline v-velocity profile for Re=400.

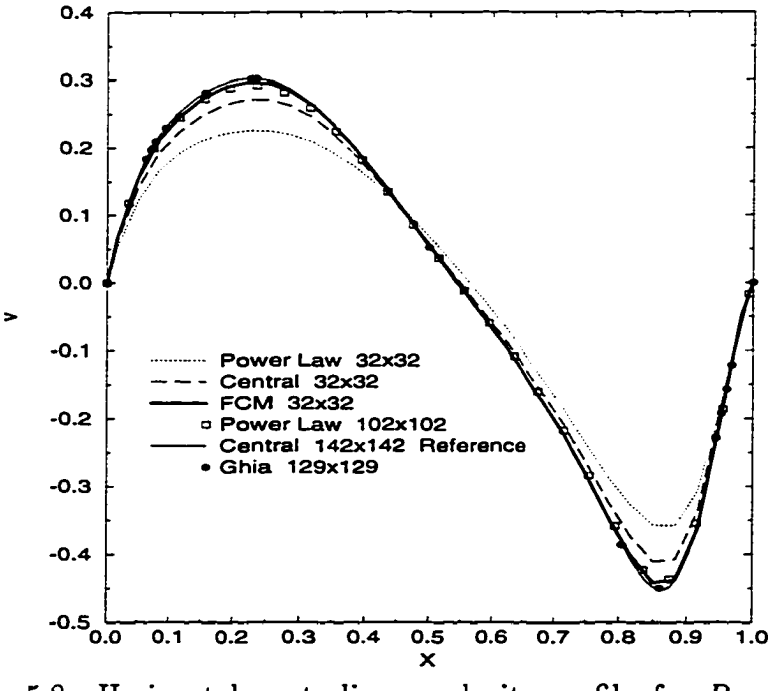

Figure 5.8 Horizontal centerline v-velocity profile for Re=400 using finer grid.

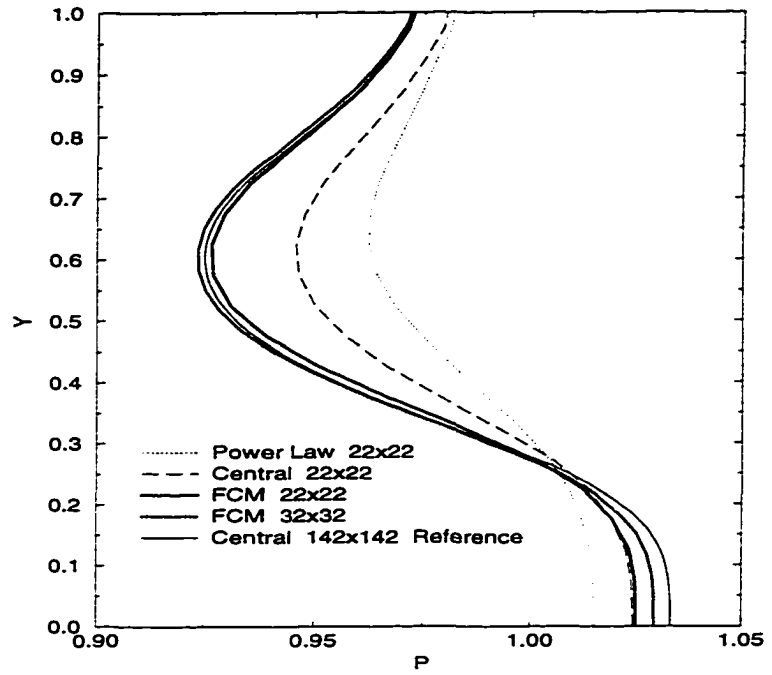

Figure 5.9 Vertical centerline pressure profile for Re=400.

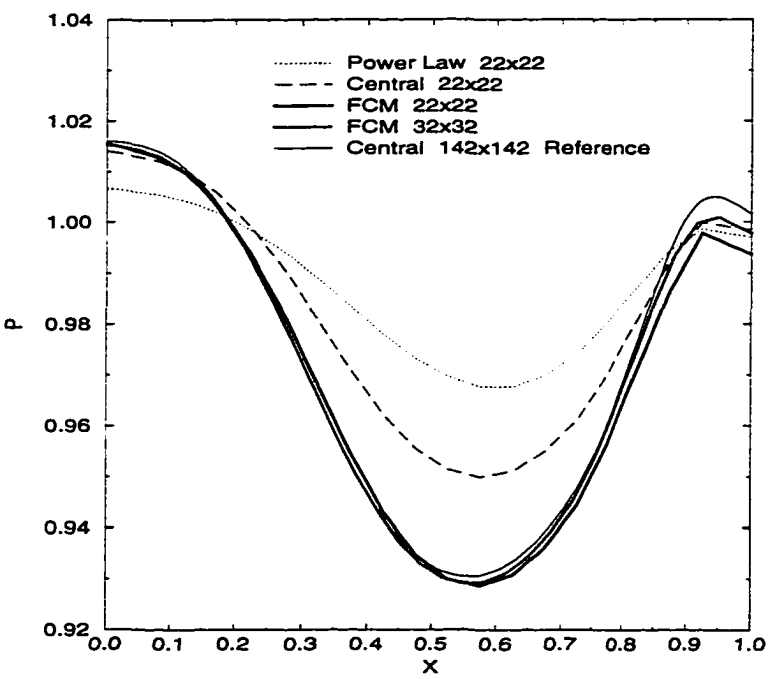

Figure 5.10 Horizontal centerline pressure profile for Re=400.

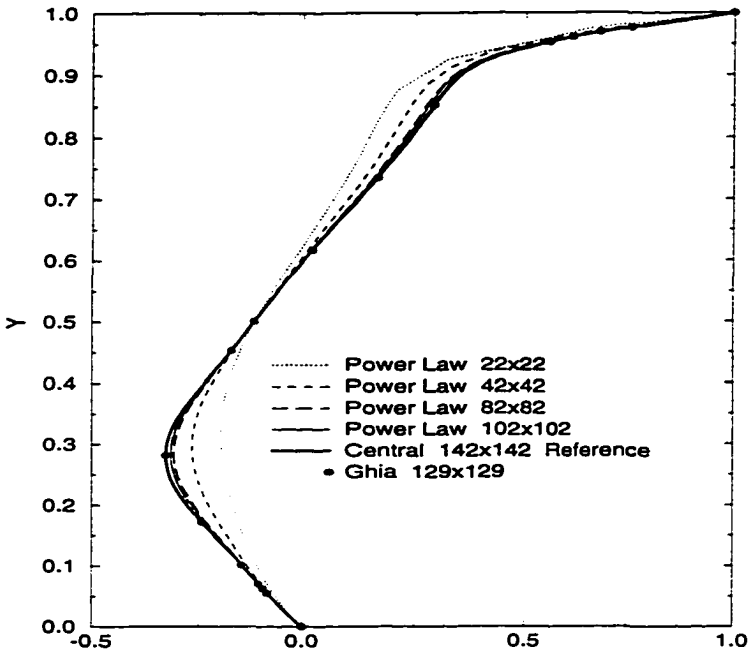

Figure 5.11 Power Law grid independent study for Re=400.

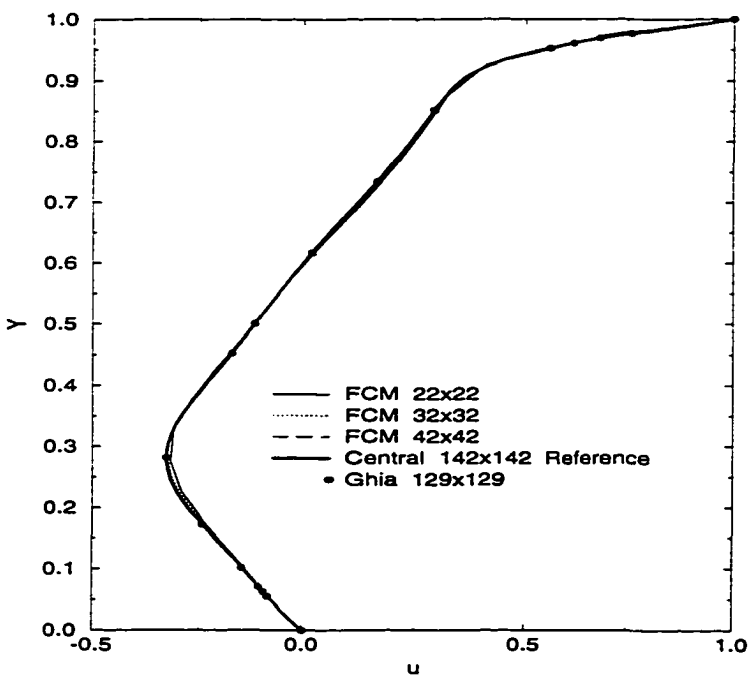

Figure 5.12 FCM grid independent study for Re=400.

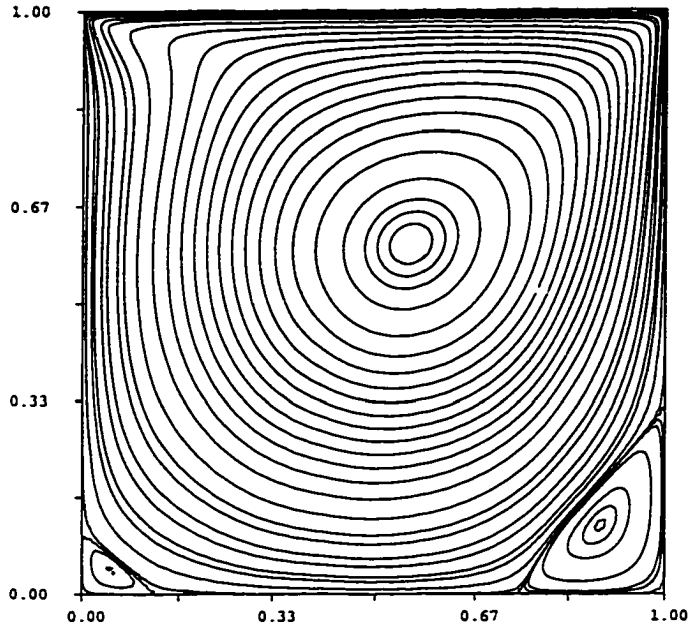

Figure 5.13 Streamline contours using 102x102 grid and Power Law scheme for Re=400.

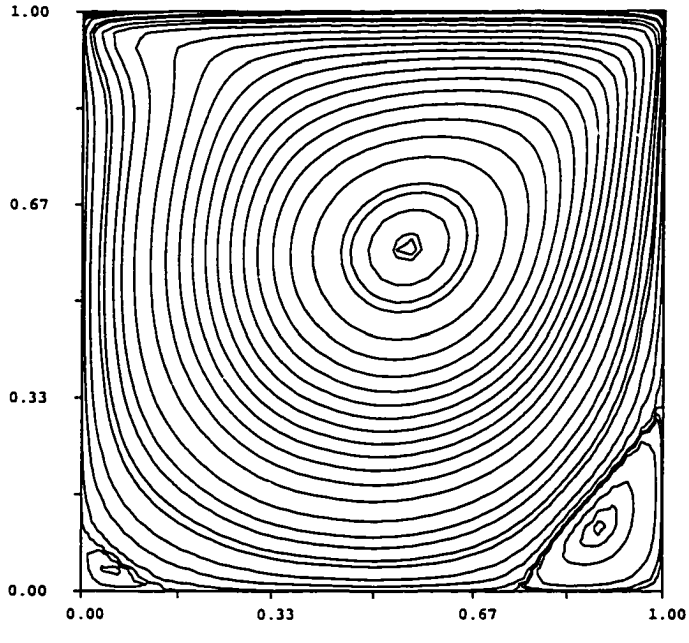

Figure 5.14 Streamline contours using 32x32 grid and FCM for Re=400.

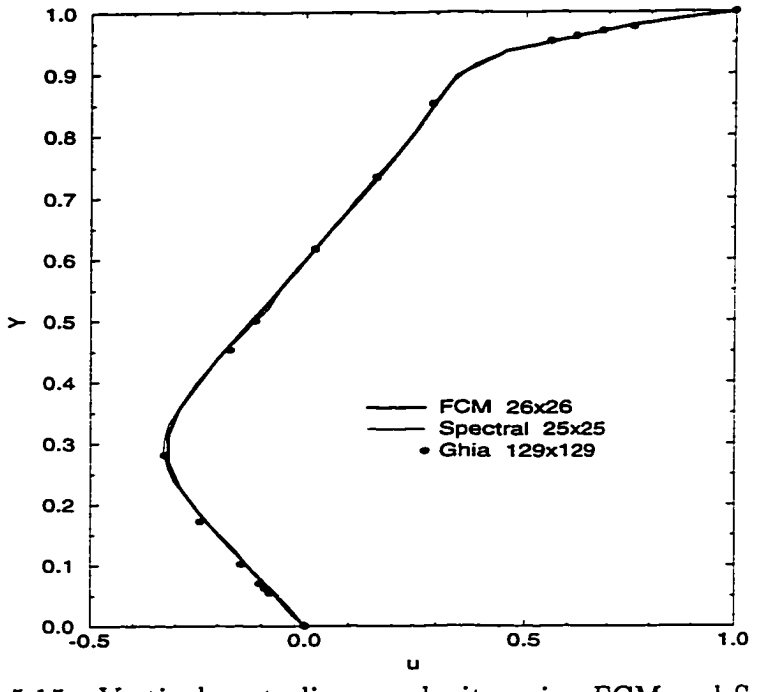

Figure 5.15 Vertical centerline u-velocity using FCM and Spectral method for Re=400.

As shown in these plots, the unacceptably diffusive nature of the Power Law scheme for high speed recirculating flow confirms the conclusions by the previous researchers, most clearly stated by Leonard [2].

The grid-independent study for both the Power Law scheme and FCM are given in Figures 5.11 and 5.12. It is clear that the Power Law scheme requires considerable grid refinement in order to match the reference centerline u-velocity. Even after using a 102x102 grid, the discrepancy from the reference solution can still be observed. On the other hand, FCM very closely approximates the grid-independent centerline profile by using only a 22x22 grid.

The comparison of the streamline contours between the fine 102x102 Power Law and 32x32 FCM solutions are given in Figures 5.13 and 5.14 respectively. Close observation reveals that the location of the center of the primary and secondary vortices, and the size and shape of those vortices, are in very good agreement with each other.

The comparison between FCM and the very accurate Spectral method obtained by

Ku et al. [41] is given in Figure 5.15. Both solutions are in excellent agreement with each other.

5.1.3 Calculations for Re=1000

A rather extensive study is focused on this high Reynolds number case due to the presence of significant cross transport and source term (i.e. pressure gradient) throughout the domain of the flow. The centerline profiles for Re=1000 are given in Figures 5.16 through 5.19. It is obvious from these figures that the Power Law scheme is more diffusive for higher Reynolds number flows. The coarse grid solutions (22x22 and 42x42) of this scheme are far from acceptable. Not until the 162x162 grid is used is the reference solution modeled somewhat closely. Clearly, neglecting the effects of cross transport and source term results in unacceptably large numerical diffusion. Although, in many cases, it is theoretically possible to refine the grid to further reduce the numerical diffusion, economical considerations often prevent the use of such a strategy. The 22x22 coarse grid solutions of both FCM and QUICK are able to capture most of the reference profile except at the high gradient regions. Using a 42x42 grid, FCM is able to conform to the reference profile well. As observed previously, FCM also gives better accuracy than the central-difference scheme for this high Reynolds number case. The solution using a 22x22 grid central-difference scheme does not converge due to the numerical instability associated with this scheme. The streamline contours for the fine 162x162 grid Power Law and 42x42 grid FCM are given in Figures 5.20 and 5.21 respectively. Again, a very good agreement in the location, size, and shape of the primary and secondary vortices is observed. The next two figures (5.22 and 5.23) attempt a direct comparison between FCM and QUICK. Both the 52x52 grid FCM solution and the 82x82 grid QUICK solution exhibit good agreement with the reference solution. Both schemes show that they can follow sharp profile variations with relatively coarse grids.

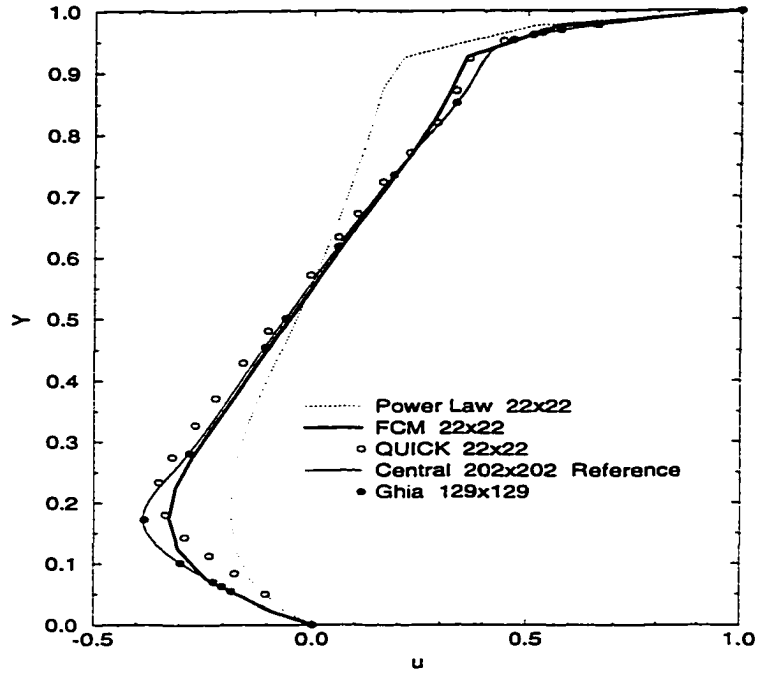

Figure 5.16 Vertical centerline u-velocity profile for Re=1000.

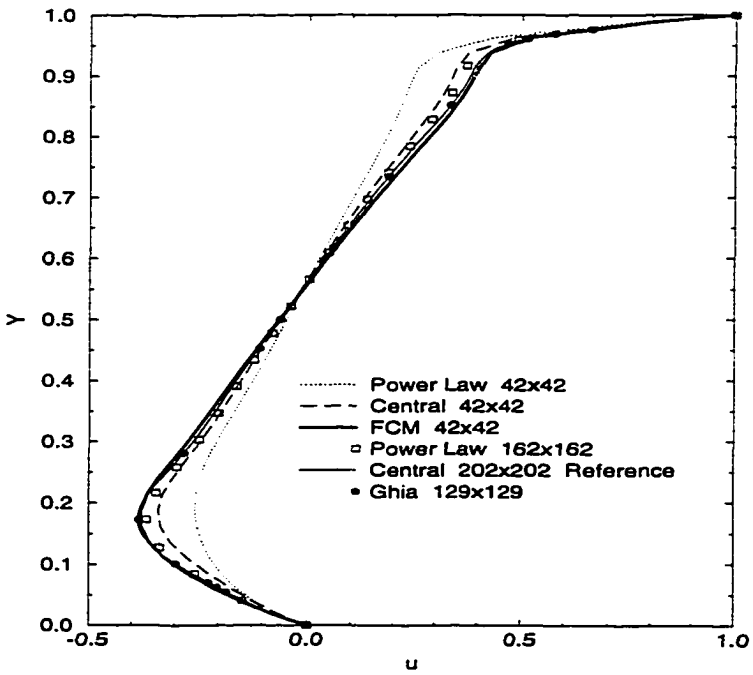

Figure 5.17 Vertical centerline u-velocity profile for Re=1000.

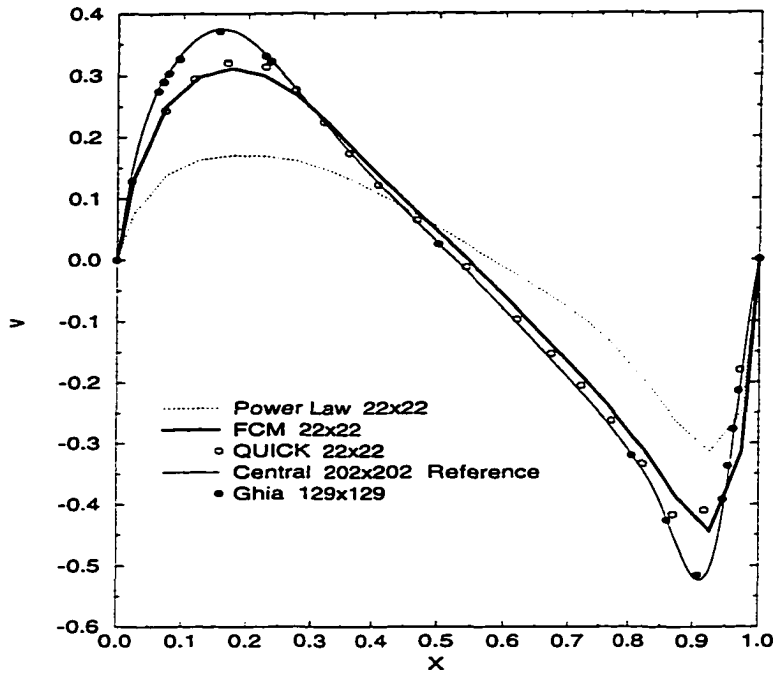

Figure 5.18 Horizontal centerline v-velocity profile for Re=1000.

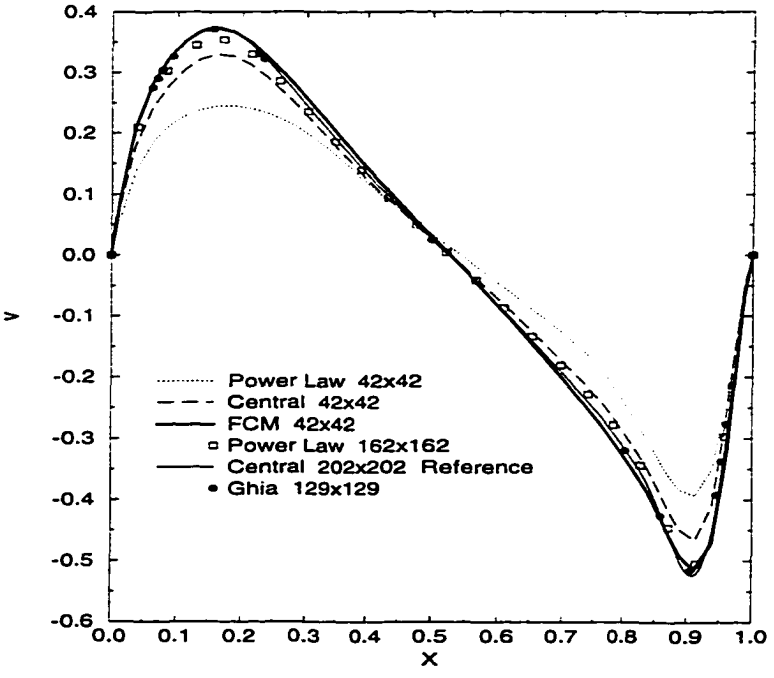

Figure 5.19 Horizontal centerline v-velocity profile for Re=1000.

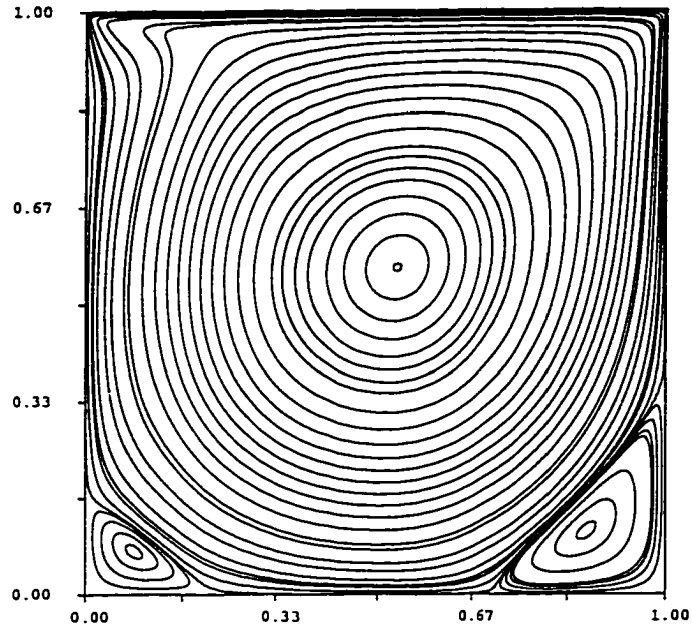

Figure 5.20 Streamline contours using 162x162 grid and Power Law scheme for Re=1000.

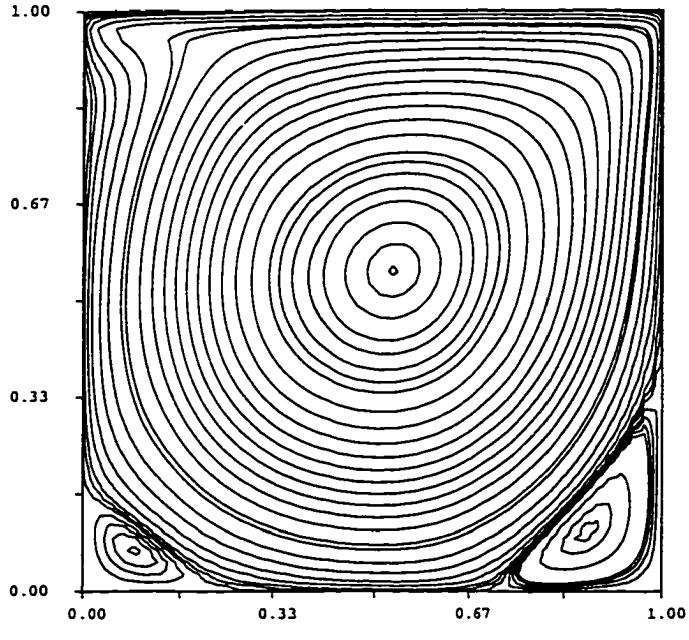

Figure 5.21 Streamline contours using 42x42 grid and FCM for Re=1000.

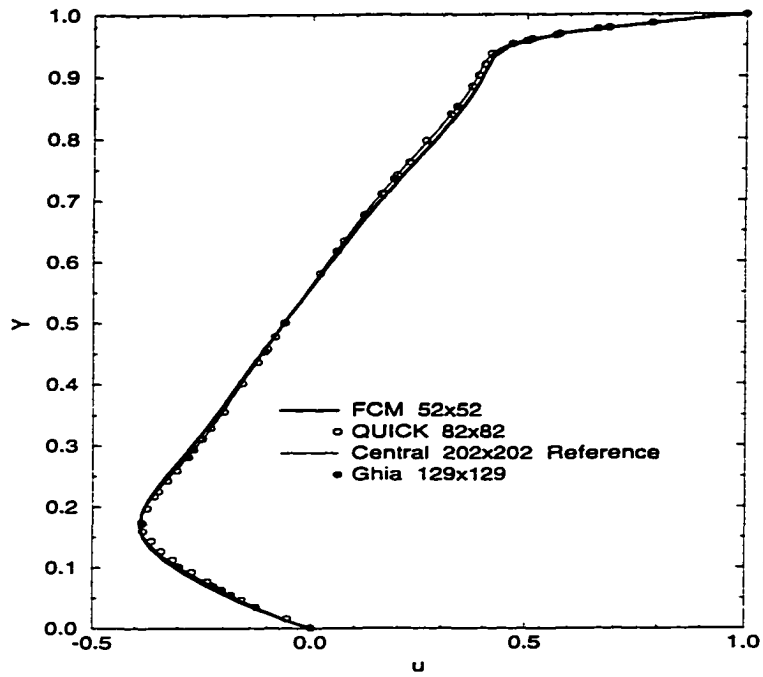

Figure 5.22 FCM and QUICK vertical centerline u-velocity profiles for Re=1000.

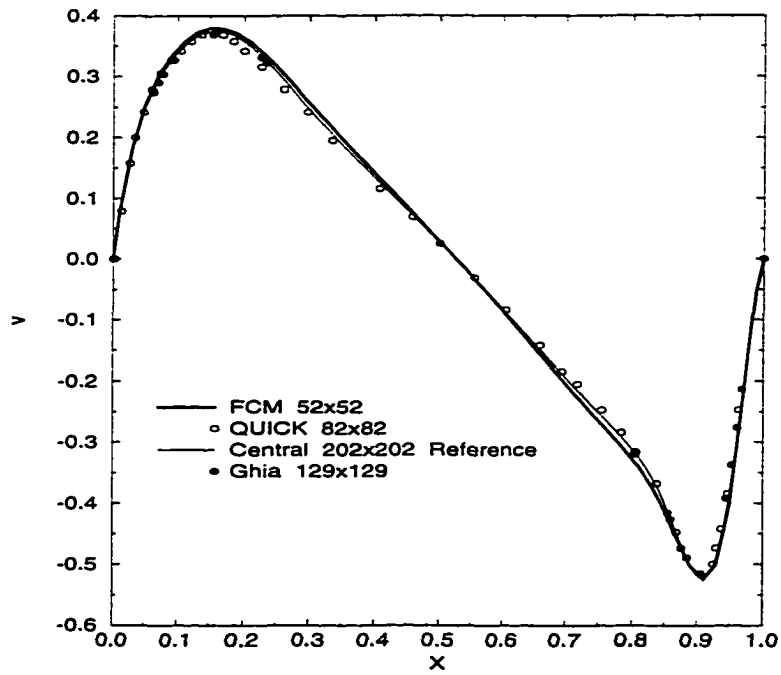

Figure 5.23 FCM and QUICK horizontal centerline v-velocity profiles for Re=1000.

It should be noted from Figure 5.16 that while the 22x22 grid FCM u-centerline profile is able to follow the reference solution at the lower wall region, the QUICK solution for the same grid resolution shows a significant deviation. However, this should not be used as a measure for determining the better scheme. Further study is warranted before a conclusion can be reached.

After showing that the coarse grid solution of FCM can model the reference solution well, it is important to show the consistency of the fine grid solution of FCM. Figures 5.24 and 5.25 show that the 162x162 grid solution of the Power Law scheme is not in close agreement with the reference solution in regions of high flow gradients. Again, this reaffirms the conclusion of previous researchers about the limitations of the Power Law scheme for multi-dimensional problems involving high Reynolds number flows which are oblique or skewed with respect to the grid. Fine grid solutions of FCM and central-difference show excellent agreement with each other and with Ghia's solution.

Figures 5.26 through 5.28 show the grid-independent study for the Power Law, central-difference, and FCM. It can be observed visually that the grid-independent vertical centerline profile for the Power Law scheme barely starts at the 162x162 grid. The central-difference scheme requires a grid slightly finer than 82x82, and FCM needs a 52x52 grid. Close observation shows that the 42x42 grid FCM solution already gives acceptable agreement for practical purposes.

The inability of the Power Law scheme to follow the reference profile on a point-to-point basis even using a fine 162x162 grid (Figure 5.26) prompted the effort to employ an even finer grid to see whether the Power Law scheme is indeed able to do so with further grid refinement. For this purpose, a four stage V-cycle FAS multigrid using a 322x322 grid is used, and the resulting centerline u-velocity plot is given in Figure 5.29. It is concluded from this result that while the Power Law solutions can always follow the reference profile satisfactorily, the excessively fine grid needed renders it impractical for many flow problems.

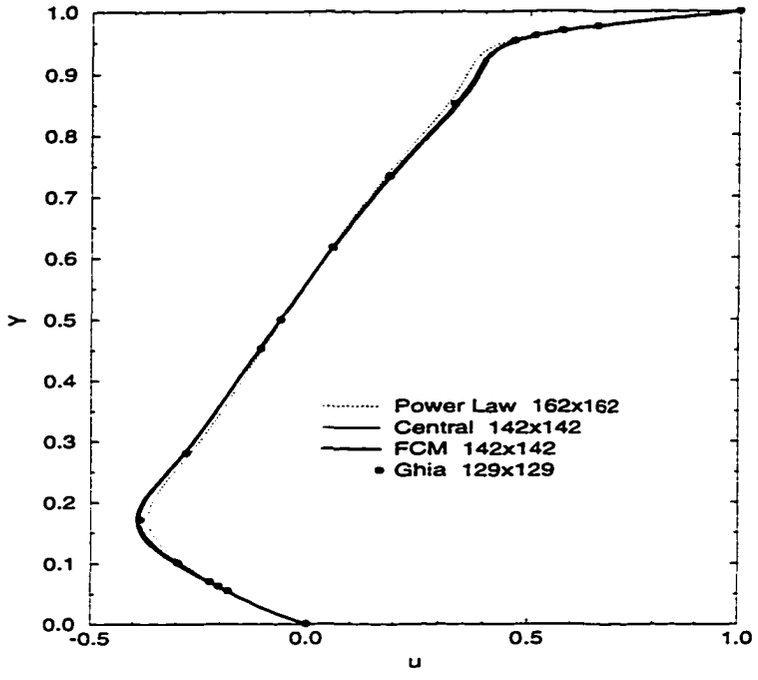

Figure 5.24 Fine grid vertical centerline u-velocity profile for Re=1000.

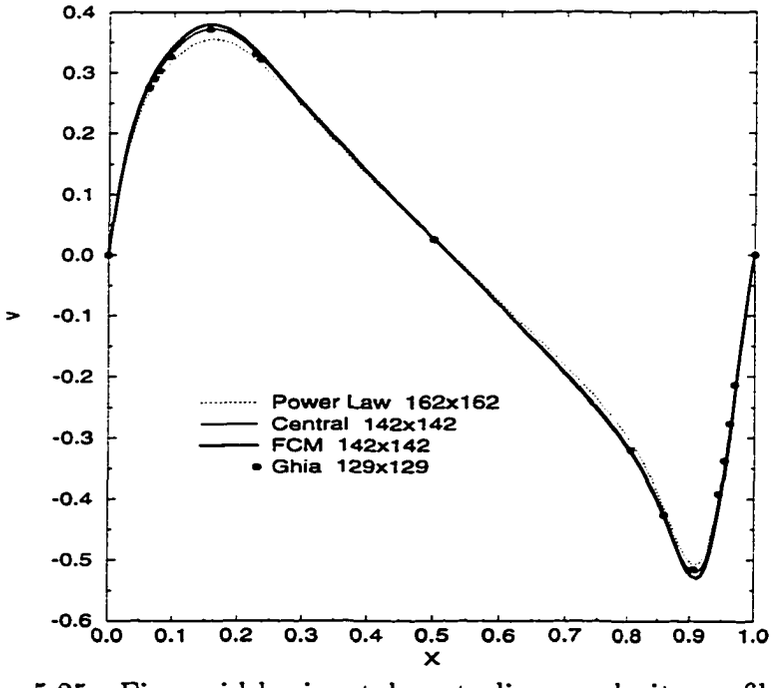

Figure 5.25 Fine grid horizontal centerline v-velocity profile for Re=1000.

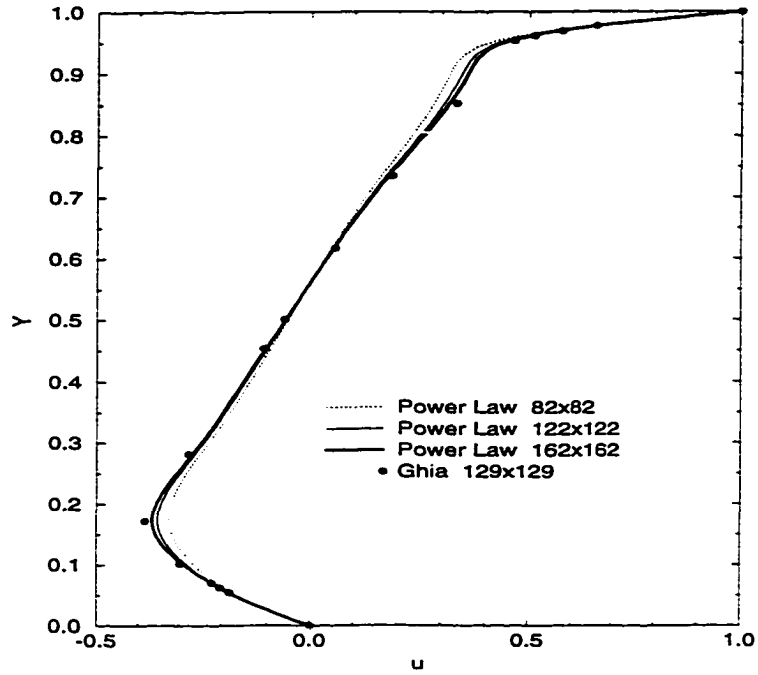

Figure 5.26 Power Law grid independent study using vertical centerline u-velocity profile for Re=1000.

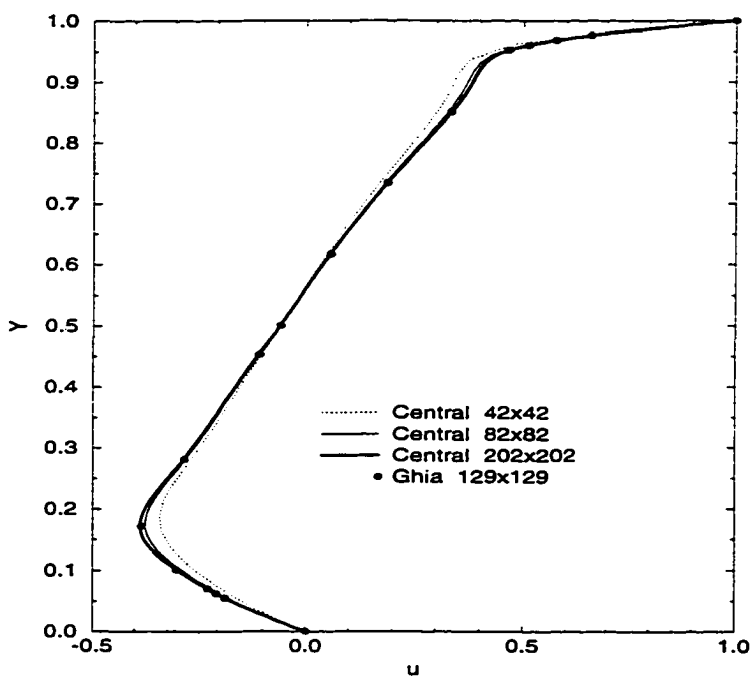

Figure 5.27 Central-difference grid independent study using vertical centerline u-velocity profile for Re=1000.

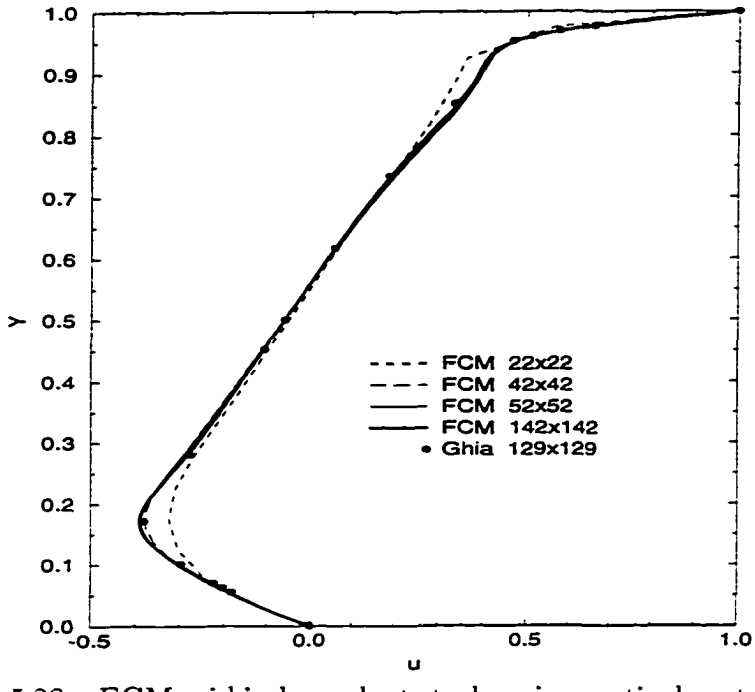

Figure 5.28 FCM grid independent study using vertical centerline u-velocity profile for Re=1000.

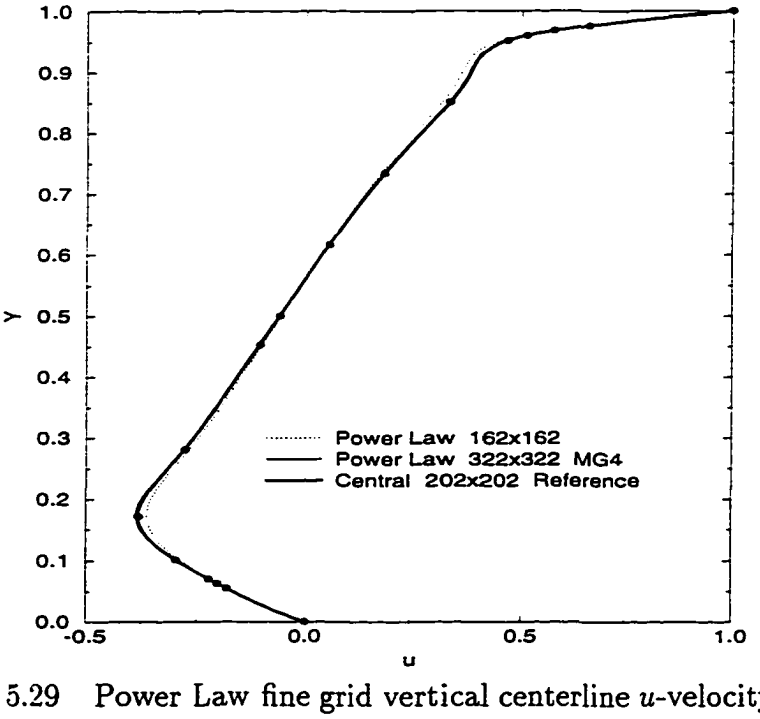

Figure 5.29 Power Law fine grid vertical centerline u-velocity profile for Re=1000.

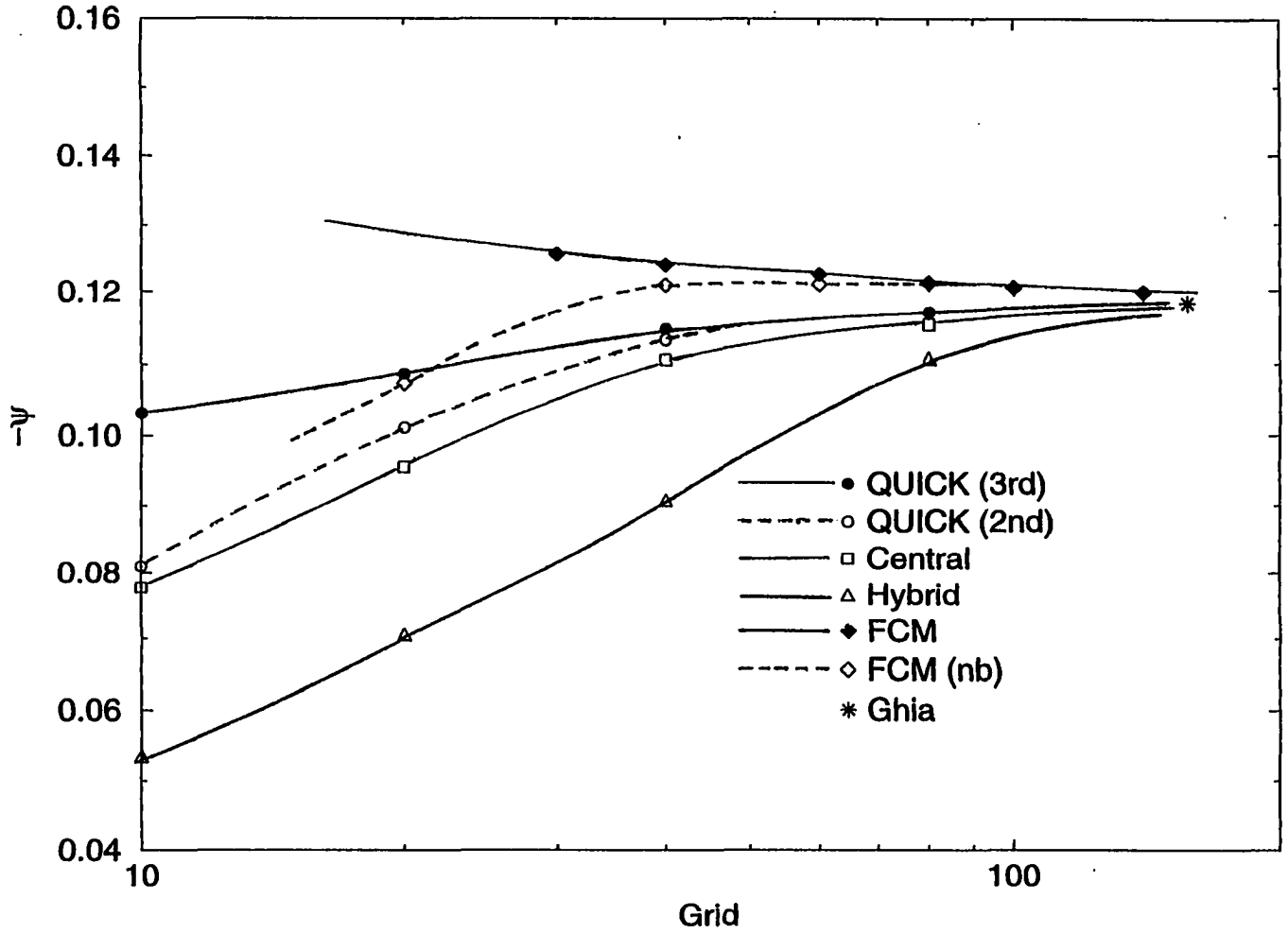

Figure 5.30 Streamfunction at cavity center for Re=1000.

An exploration of the relative accuracy of the schemes considered is carried out for this high Re=1000 case. Figure 5.30 shows the value of the streamfunction, ξ_c, at the center of the primary vortex plotted as a function of grid refinement. The value of ξ_c is commonly used as a sensitivity measure of the accuracy of the numerical schemes being evaluated. For a given grid refinement, these results quantify the extent to which a higher order scheme outperforms a lower order one. For example, a 20x20 grid with QUICK or FCM is roughly equivalent to a 40x40 grid with the central-difference scheme and an 80x80 grid with the hybrid scheme. It can also be observed in this plot that the effects of boundary cell correction on FCM do make a difference when the grid is coarse. This difference quickly disappears with moderate grid refinement. Finally, it should be understood that this rather simple form of performance evaluation should not be used as an indicator to pick the better scheme between FCM and QUICK. A much more extensive study using a more advanced method (i.e. the Richardson method, originally proposed by Richardson [42, 43] and also described by Roache [44]) must be done before any further conclusion can be justifiably drawn.

5.1.4 Calculations for Re=10000

The flow inside a lid-driven cavity at a very high Reynolds number proves to be a difficult test problem to investigate. At this very high Reynolds number, very complex flow interactions, which quite possibly are highly unsteady, are taking place. Moreover, there have been many uncertainties and inconsistencies among the numerical findings of various researchers in determining the limit Reynolds number at which the onset of turbulence occurs. However, it has been the general agreement, as clearly stated by Huser [45], that the transition to turbulence is characterized by the development of small eddies at the vicinity of the two lower corners (and also at the upper left corner), and the laminar mean velocity of the main vortex becomes unstable. The interaction of these eddying motions with the mean shear eventually leads to turbulence.

Due to hardware limitations, early studies on the onset of turbulence for the cavity flow were done on the basis of an analysis using the steady-state Navier-Stokes equations and a relatively coarse grid. Bye [46] determined a range of transition Re between 400 and 600. Kumagai [47] roughly estimated transition to occur at even lower Re. Both authors used the formation of an inflectional velocity profile indicating reverse flow as the criterion for the onset of an unsteady regime. However, Kumagai strongly cautioned against the accuracy of such data obtained from steady-state calculations. More recent work by Ghia [7] using a very fine 257x257 grid with the central-difference scheme coupled with a multigrid technique shows that it is possible to obtain a converged steady state solution for Re=10000. Hayase [8] has also been able to get steady-state solutions using QUICK with an 82x82 grid. Ghia's and Hayase's findings suggests that the flow inside the lid-driven cavity at Re=10000 converges to a steady-state solution. Following this line of thought, the ability of the Power Law scheme and FCM to simulate this high Reynolds number flow in a steady mode is investigated. Ghia's calculations are utilized as a reference solution.

The centerline velocity profiles are given in Figures 5.31 and 5.32. Again, it is evident that the Power Law scheme is far too diffusive to accurately predict this high convection recirculating flow. Even the 322x322 multigrid solution of the Power Law scheme is far from adequate in following the reference solution. On the other hand, the coarse grid solution of FCM and QUICK are able to follow Ghia's fine grid solution closely. However, it should be understood that at this high Reynolds number, stability and convergence of the numerical scheme become more important issues. Hayase reported that it is necessary to retain the unsteady terms in the momentum equation in order to achieve stable, converged solutions on grids finer than 40x40 at this Reynolds number. Although FCM does not need this transient marching procedure, much slower convergence and oscillations of the residuals are observed, in particular with the use of finer grids.

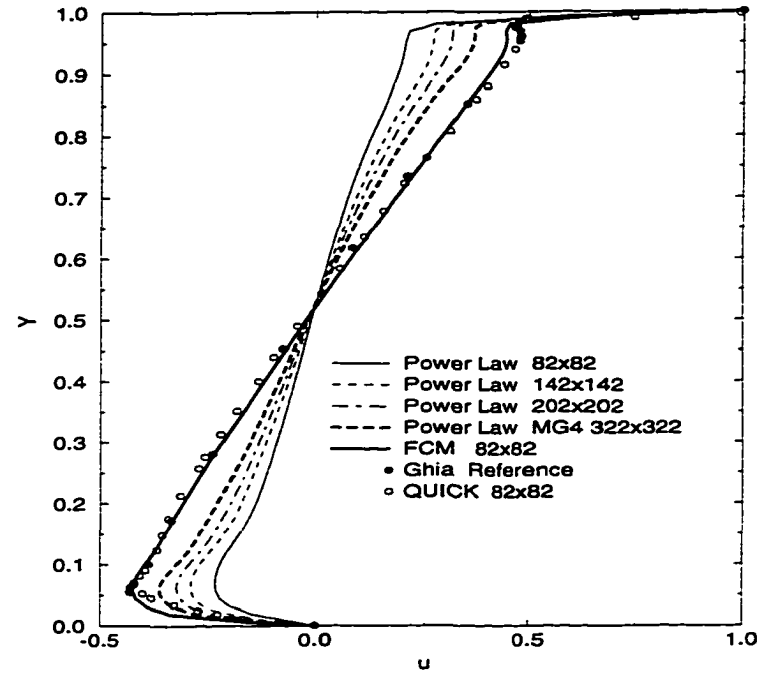

Figure 5.31 Vertical centerline u-velocity profile for Re=10000.

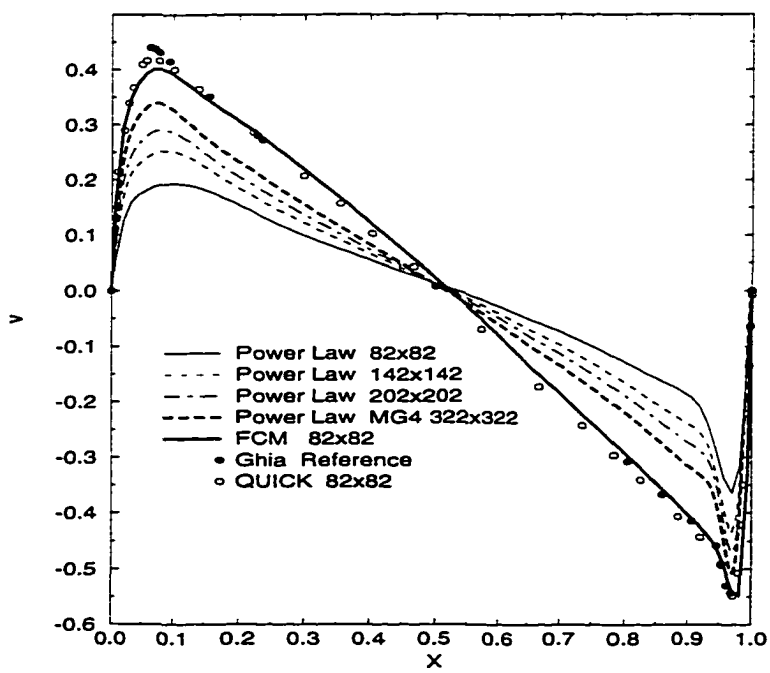

Figure 5.32 Horizontal centerline v-velocity profile for Re=10000.

These oscillations of the residuals suggest the possibility that the lid-driven cavity flow at Re=10000 is indeed unsteady. In fact, it was understood that from the period of the formation of the corner eddies which leads to transition, the flow structure is highly unsteady and thus can no longer be simulated using steady numerical calculations. The fact that it is possible to obtain steady-state convergence suggests that the grid resolution used is not sufficient to resolve the transient physics of the flow, especially at the corner regions. In this case, the use of the numerical scheme in steady mode will result in a fortuitous steady-state solution. The steady-state fine grid Power Law and Ghia central-difference solutions and the coarse grid FCM solution obtained in Figures 5.31 and 5.32 are incorrect but converged solutions. It is very likely that this behavior was also observed by Hayase in his calculations. If the numerical scheme is used in the unsteady mode, good converged iteration will be obtained at each timestep and a steady-state solution will be obtained after sufficient time has elapsed.

Theoretically, it is always possible to refine the grid sufficiently to reach the limit where the numerical scheme is able to pick up the transient physics of the problem. At this grid resolution, the use of the numerical scheme in the steady mode will result in very slow convergence and eventual stalling of the residuals after only a few order drop in the magnitude of the residuals. On the other hand, in using the unsteady calculations. satisfactory convergence will be obtained at each timestep, and the transient nature will be captured in real time.

A higher order numerical scheme will be able to pick up the unsteady nature of the flow using a relatively coarser grid, and this leads to residual oscillations when an attempt is made to simulate transient behavior using steady calculations. It is therefore clear why steady-state convergence is not obtained using a 322x322 multigrid FCM in steady mode. A four order drop in the magnitude of the residual (Equation 5.1) is observed before residual oscillation starts.

This finding prompted a further study of this particular test problem using FCM in

an unsteady mode. A very fine 322x322 grid is used, and the flow solution obtained from the previously mentioned steady multigrid run with the same grid resolution is used as the initial solution for the unsteady calculations. The main reason for not using the unsteady impulsively started lid-driven cavity with static initial velocities at time t=0 is the limitation on computer resources available for transient study at this level of grid resolution. It is assumed that if the flow is steady, the unsteady calculations will converge to a steady-state solution, and the stability problems observed in the steady-state calculations are due to the numerical formulation of the scheme. On the contrary, if the problem is unsteady, the unsteady run should be able to pick up the transient nature of the flow.

From the multigrid run using a 322x322 grid given in Figure 5.46, it is known that the cavity problem for Re=1000 is steady. Using this steady-state multigrid solution as the initial condition, an unsteady run for this problem is also performed for comparison purposes and to verify that the unsteady run at this Reynolds number will not change the flow solution from the steady run (used as initial condition) at all.

The plots of the velocity components as a function of time for both Re=1000 and 10000 at four locations of the cavity ((x,y)=(0.5,0.5),(0.25,0.5),(0.75,0.5),(0.5,0.25)) are given in plots a, b, c, and d respectively of Figure 5.33 and 5.34. From these plots, semi-random behavior of the velocity component as a function of time for Re=10000 is observed, while monotone solutions are observed for Re=1000. The u- and v-velocities for Re=1000 are translated appropriately to provide clear comparison with the solutions for Re=10000. In this study, graphical unsteady simulations of the streamlines for both Reynolds numbers are also made, using a movie package. Observations using this movie package show that the primary vortex is indeed unsteady with small transient variations. The highly transient behavior of the flow is observed at the two lower wall corners and upper left corner.

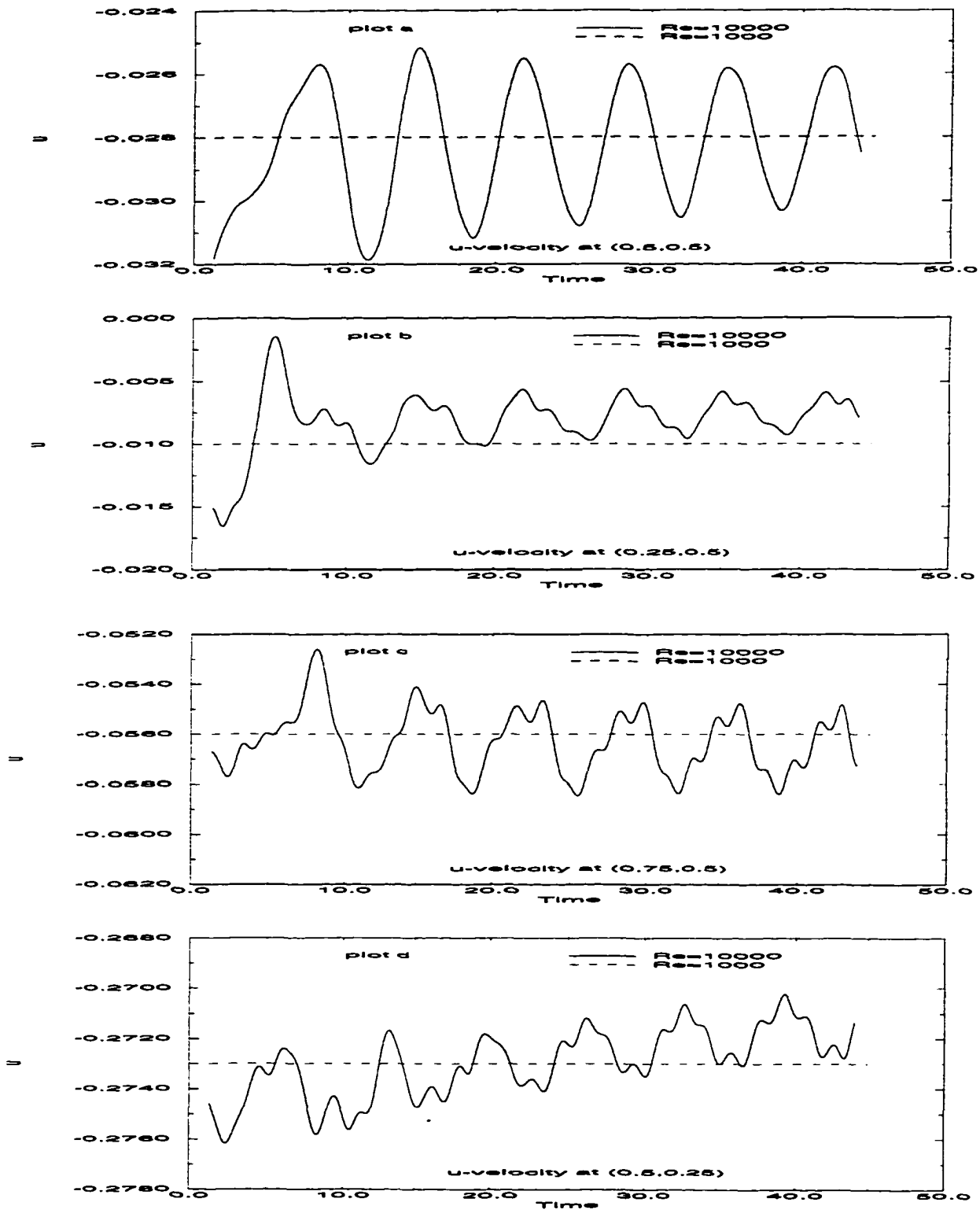

Figure 5.33 Time history of the u-velocity at four specific locations inside the cavity for Re=10000 and Re=1000 computed using FCM with 322x322 grid.

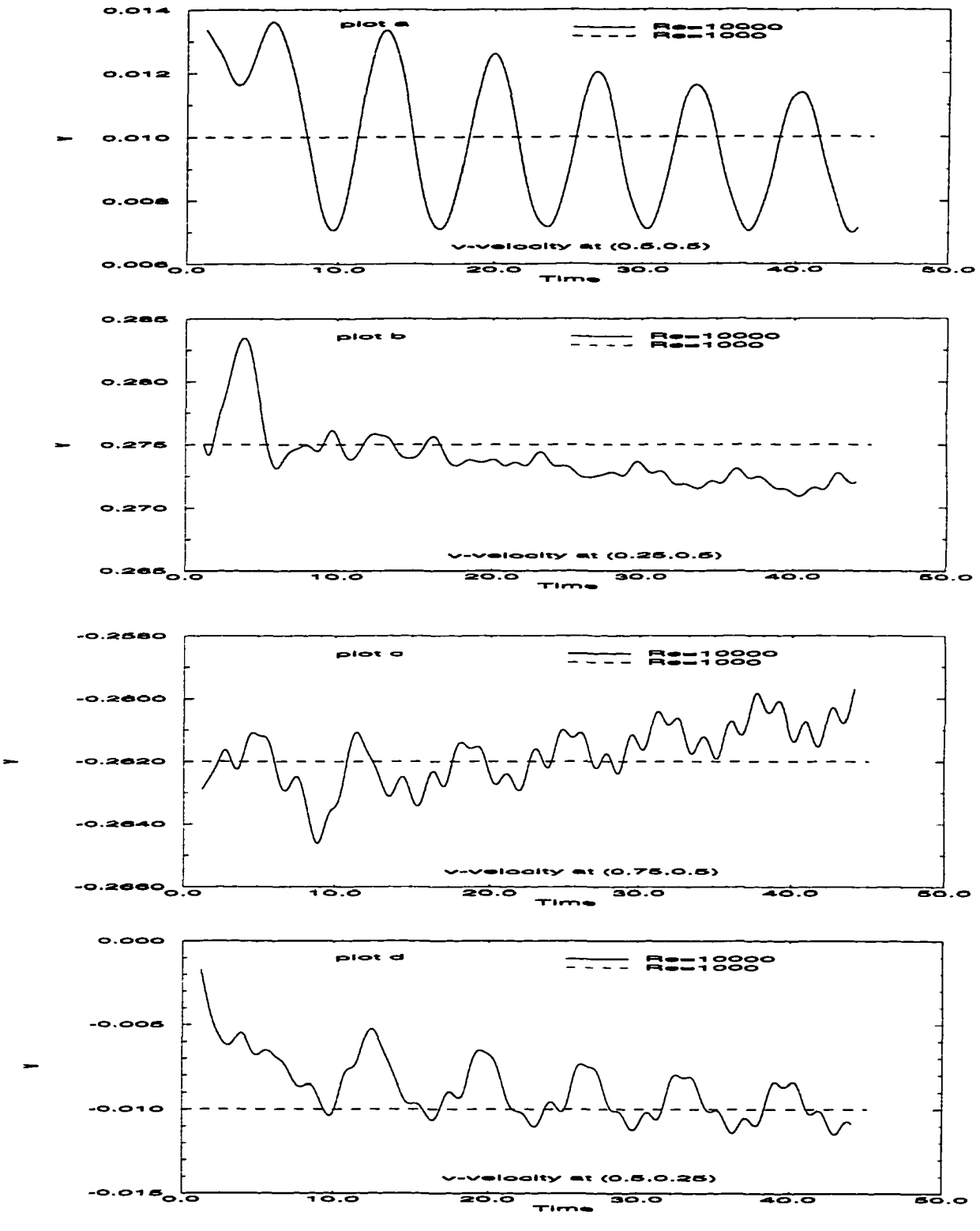

Figure 5.34 Time history of the v-velocity at four specific locations inside the cavity for Re=10000 and Re=1000 computed using FCM with 322x322 grid.

In the lower left wall corner, it is observed that three secondary vortices continuously develop, gain and loose strength, and burst to facilitate the formation of the other vortices. This is in clear agreement with the work of Huser mentioned previously which is based on the unsteady flow calculation at Re roughly equal to 10000. This finding is also consistent with the experimental results obtained by Koseff et al. [48] who observed the onset of turbulence at $Re \approx 6000$.

5.2 Grid Stretching

In solving practical flow problems, due to the limitations on the number of grid points which can be afforded, it is always desirable to cluster grid points in regions with high flow gradients (i.e. in the boundary layer region near the wall) and coarsen the grid at other regions. It is well-known that mesh coarsening also degrades the numerical solutions by introducing undershoots and/or overshoots in certain regions of the flow. Therefore, it is very important to know the limit at which a particular numerical scheme can tolerate local grid stretching without causing unacceptably large error in the numerical solution. In Figures 5.35 through 5.37, three different stretchings (moderate, high, and extreme) are tested on the lid-driven cavity flow for Re=400. It is important to mention here that a sufficient number of grid points required to conform point-to-point (in the unstretched mode) with the reference solution must be used to conduct a meaningful study. From previous exercises, it is known that for this Reynolds number, the use of a 122x122 grid ensures a grid-independent solution. For each grid, the centerline u-velocity profile obtained using Power Law and FCM are compared against the unstretched fine grid reference solution obtained using the central-difference scheme.

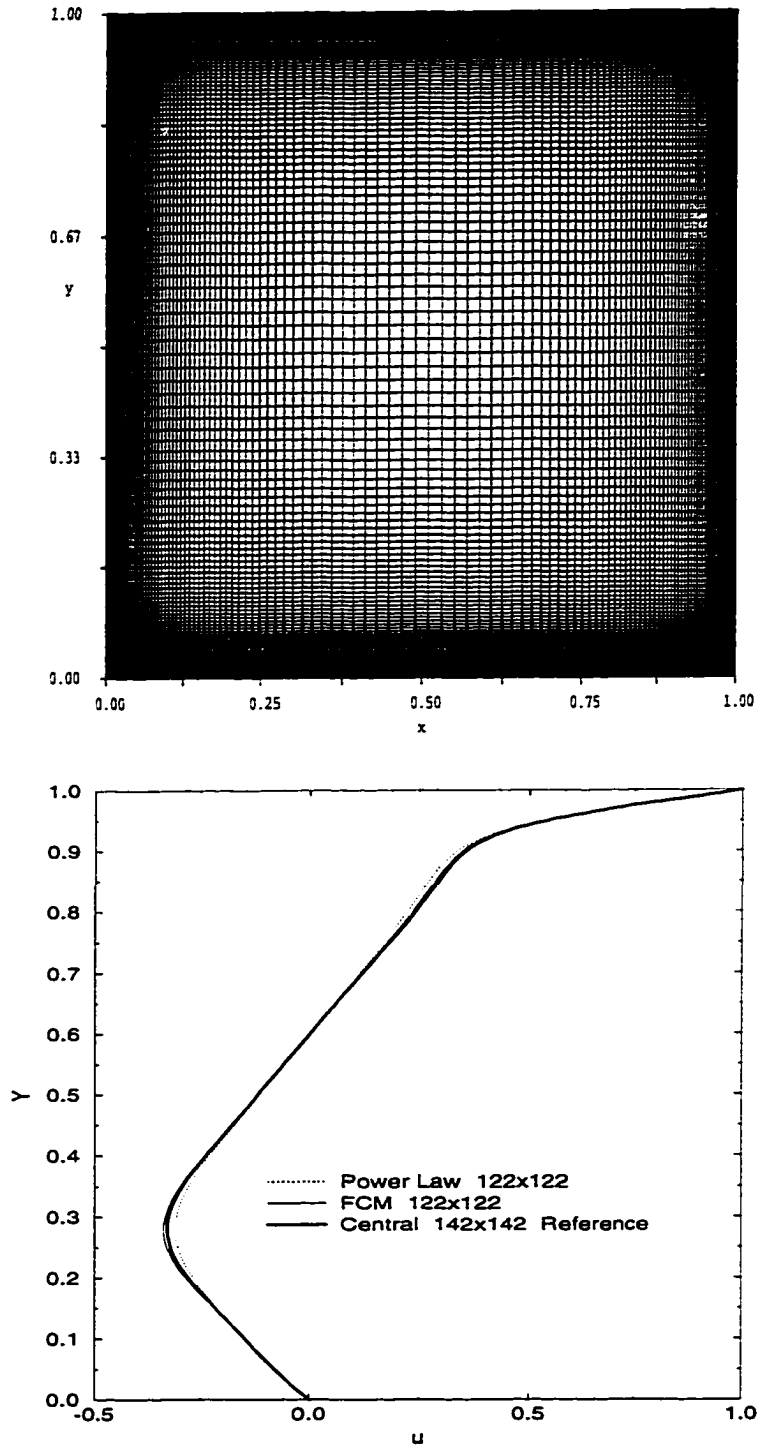

Figure 5.35 Effects of moderate grid stretching on vertical centerline u-velocity profile for $Re = 400$.

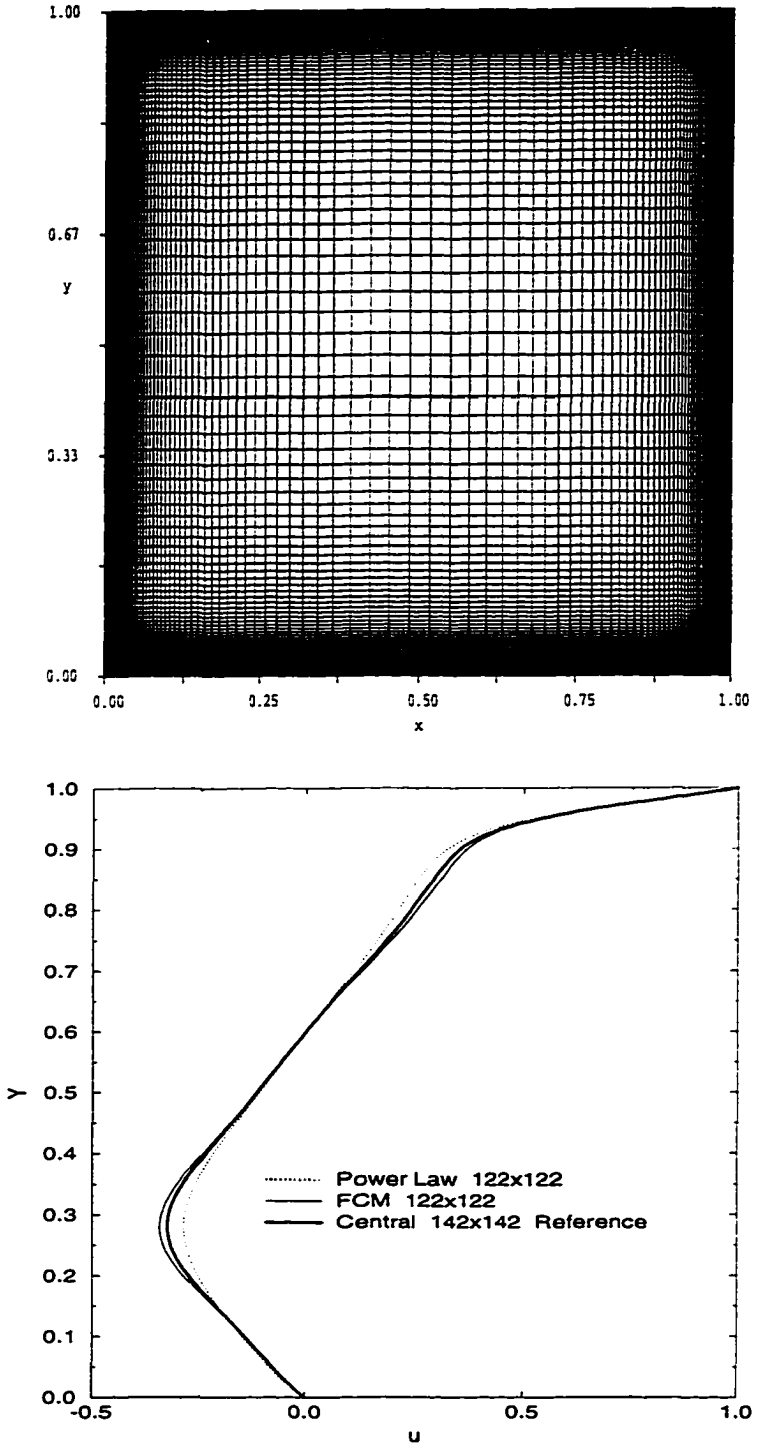

Figure 5.36 Effects of high grid stretching on vertical centerline u-velocity profile for $Re = 400$.

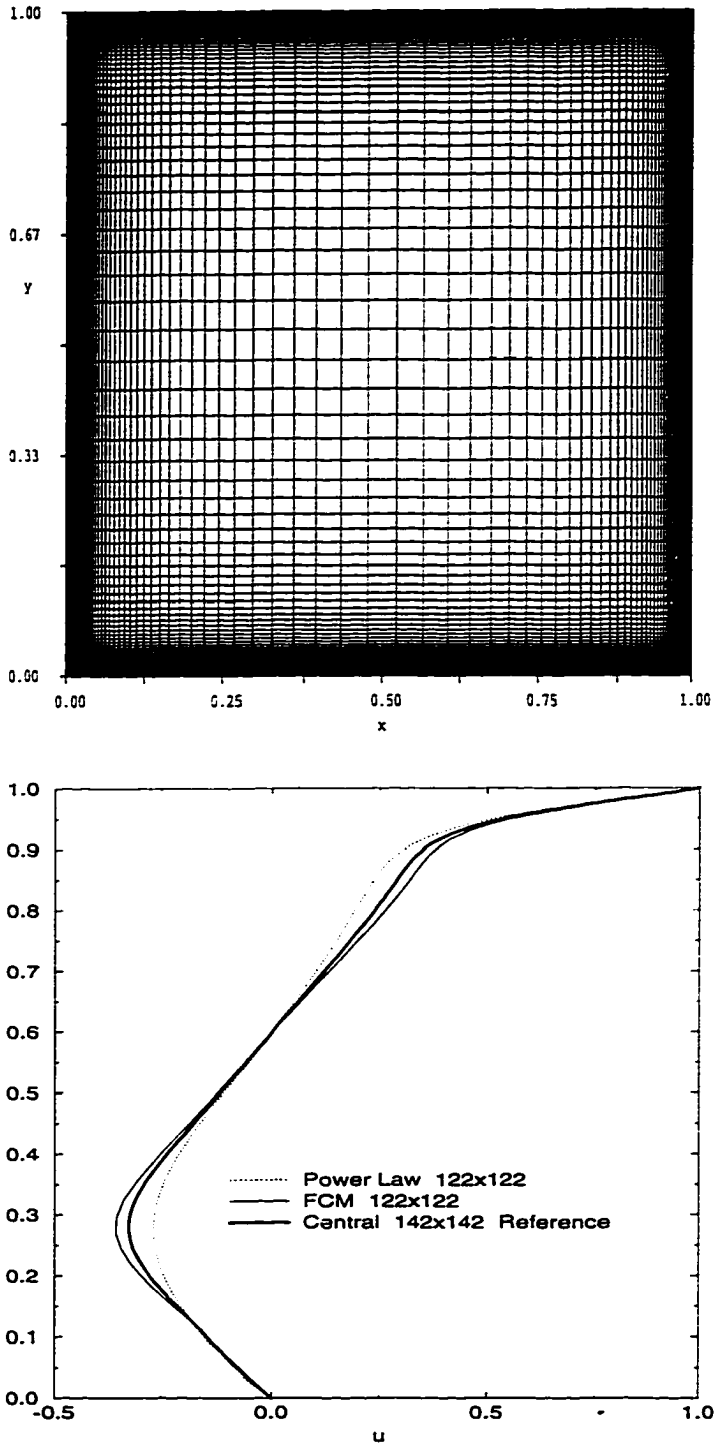

Figure 5.37 Effects of extreme grid stretching on vertical centerline u-velocity profile for $Re = 400$.

Observation of the moderate stretching (Figure 5.35) shows that FCM produces an almost negligible overshoot at the high gradient (which now has a lower grid density) region while the errors produced by the Power Law scheme have become very apparent in more than one region. An even more important conclusion can be obtained by looking at the results produced by the high and extreme stretching (Figure 5.36 and 5.37). It is observed that while FCM solutions now display more profound overshoot error in both the lower and upper high gradient regions, the errors produced by the Power Law scheme are comparatively larger. It should also be noted that in the regions of the lower wall boundary, the Power Law solution also displays slightly incorrect slope, not observed in the FCM solution. It is therefore concluded that FCM behaves better than the Power Law scheme when local grid stretching is used. However, regardless of which numerical scheme is used, the use of grid stretching must always be done with caution and care.

5.3 Convergence Characteristics and CPU Requirement

Having addressed the important issues of accuracy and stretching in the previous subsections, it is now necessary to investigate the convergence characteristics of FCM as compared with its parent method (i.e. Power Law). Recall that the main idea behind FCM is to correct the flux computation at an interface by using the governing conservation law itself applied to a control-volume enclosing that interface. Thus, for an interface in a given direction, the cross transport, the unsteady term, and the original source present in the considered conservation equation are combined into one single source used in the one-dimensional convection-diffusion equation. Therefore, the total-flux profile at an interface consists of a homogeneous profile and a correction profile due to that source. Hence, an FCM iteration is basically a Power Law iteration plus iteration on the added correction source. Consequently, FCM is expected to inherit all the stable convergence properties of the first-order Power Law scheme, including the 'Four Stable

Convergence Rules' established by Patankar [5]. The plots of the mass, x-momentum, and u-velocity convergence for an Re=400 lid-driven cavity problem using a 42x42 grid are given in plots a, b, and c respectively of Figure 5.38. It is observed that FCM displays similar convergence trends as the Power Law scheme. The fact that FCM has a lower convergence rate can be rationalized as the extra effort needed to iterate on the extra correction sources. It is also obvious that the FCM convergence stalls at a few orders of magnitude higher than Power Law convergence and produces more noise at those stalled levels. This behavior, while generally best avoided, should not be of any concern here. Close observation reveals that at least a ten order drop in magnitude is achieved for any of the convergence criteria considered, which is much more than enough for all purposes. This stalling and subsequent oscillatory behavior are again attributed to the presence and the iteration of the extra correction sources, which are highly non-linear. It should be the goal of future work to investigate whether special procedures to evaluate the correction terms will eventually reduce, if not eliminate, the stalling behavior and noise.

Figure 5.39 gives the convergence history for Re=1000 using a 62x62 grid and a 102x102 grid. The same convergence trend between FCM and Power Law is again observed. For the 62x62 grid, it is observed that after a three or four order drop in magnitude of the residuals, FCM has a noticeably lower convergence rate than the Power Law scheme. However, it has been the common practice in CFD (as is evident in the published literature) that under usual circumstances, it is very rarely necessary to converge to a residual value of 10^{-10} or 10^{-12} during the iterative process. A five or six order drop in magnitude of the residuals is usually sufficient to consider the solution converged.

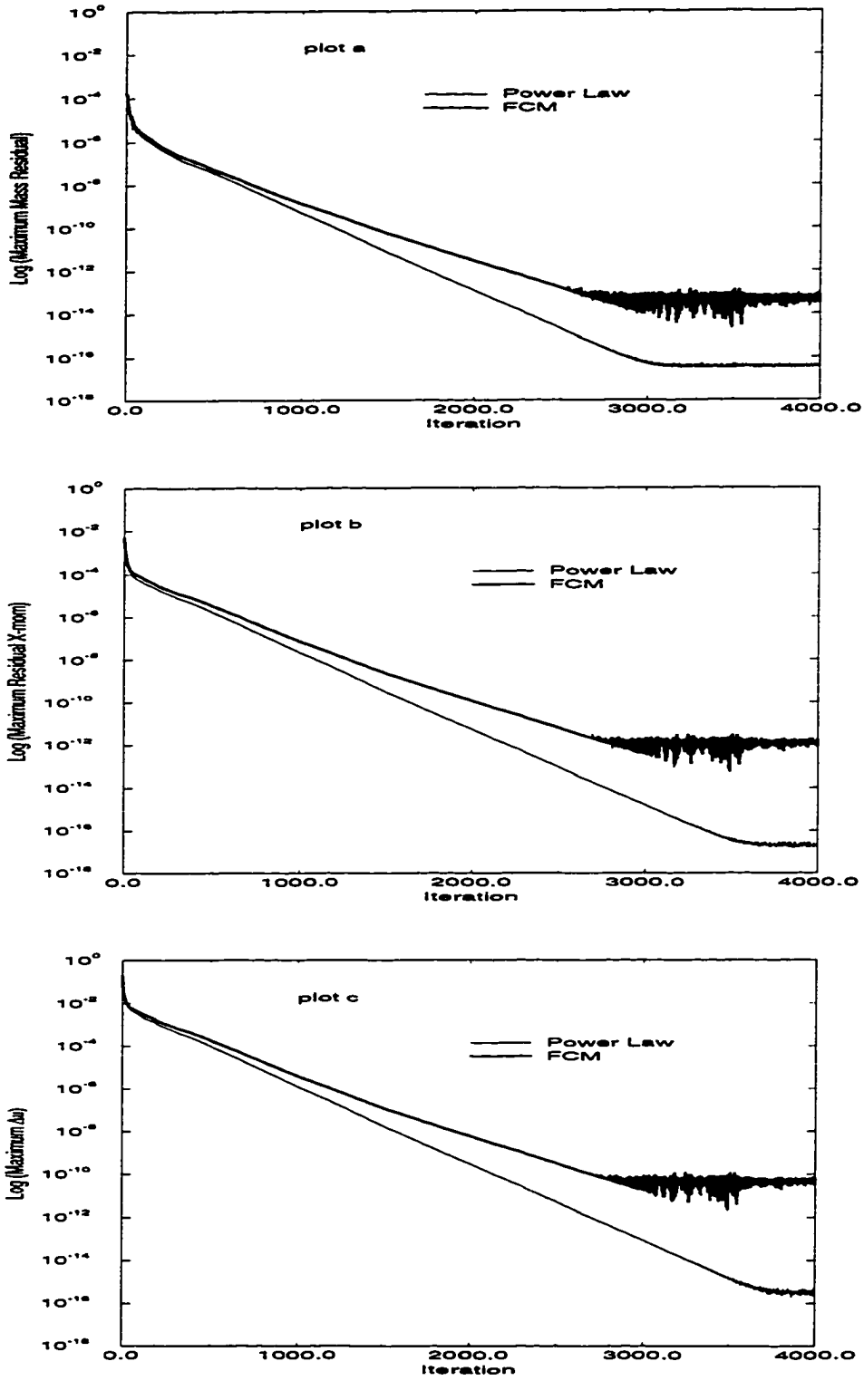

Figure 5.38 Convergence of the residuals for Re=400.

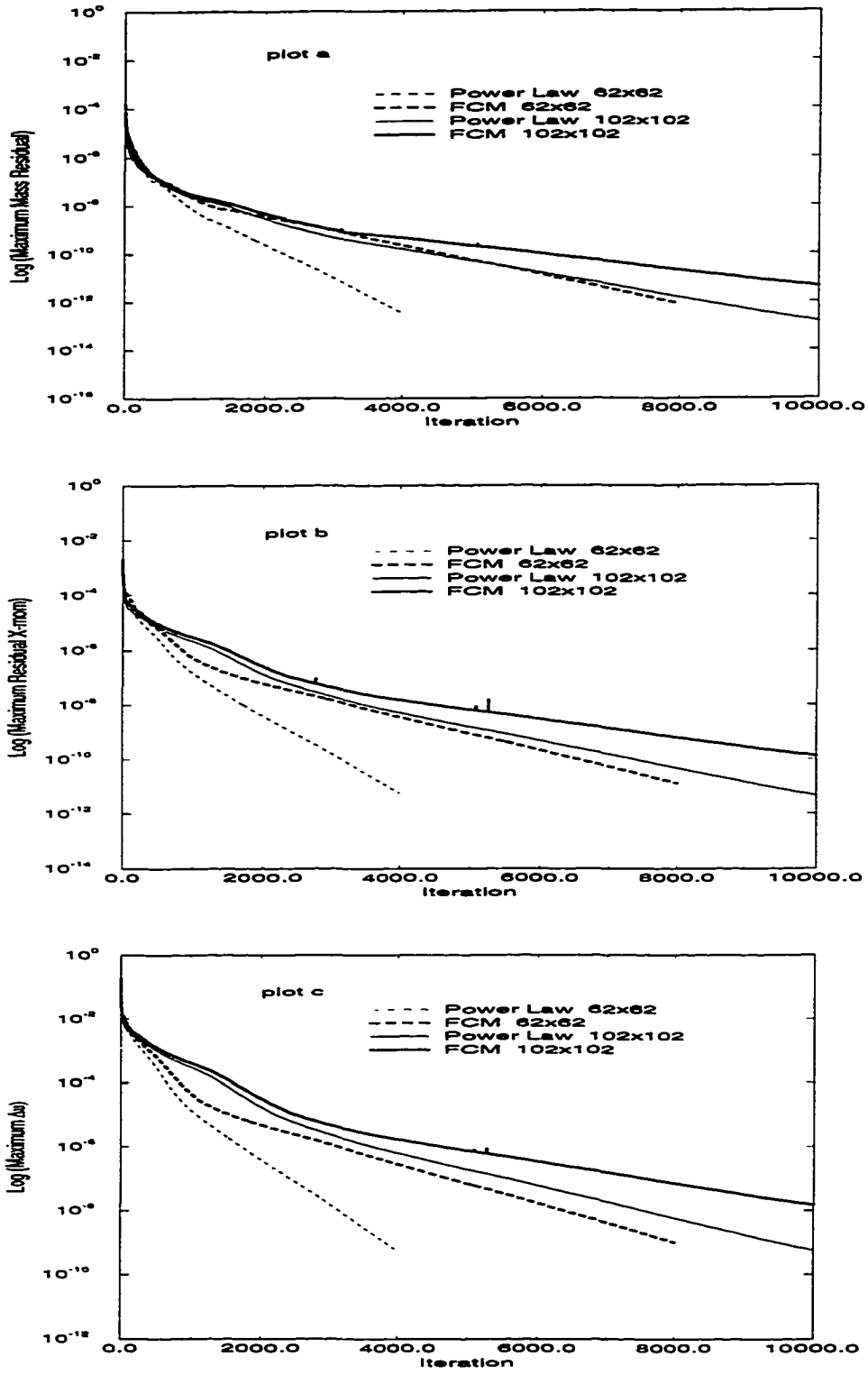

Figure 5.39 Convergence of the residuals for Re=1000.

More importantly, from the same plots, it should be noted that as the grid is refined to 102x102, the difference in the convergence rate between FCM and the Power Law scheme diminishes substantially.

The fact that FCM becomes more efficient with grid refinement is also demonstrated in Figure 5.40. In this figure, the ratio of the CPU time requirement of FCM to that of the Power Law scheme (to converge to a given residual) for three different Reynolds numbers is plotted as a function of the number of grid points. As expected, for a given grid size and Reynolds number, FCM requires more CPU time than the Power Law scheme to converge to the same residual. This CPU time increase is attributed to two factors. First, the increase is due to the extra time needed by FCM to converge. Thus, it is inherent in the scheme's formulation. This contribution can be measured by looking at the extra number of iterations needed, as given previously in Figures 5.38 and 5.39. Secondly, the increase in time is also due to the time needed for the extra computation of the source correction within each iteration. While it is not generally possible to reduce the first contribution without introducing major changes in the scheme's formulation, it is indeed quite possible to reduce the second contribution by using better and more efficient coding techniques. Throughout the development phase of FCM, clarity and ease of debugging are given precedence over efficiency during the code development. In fact, the expensive-to-compute total-fluxes which will be used in the FCM sources are recalculated in order to allow testing of different schemes. These total-fluxes should have been available from the computation of the influence coefficients. Thus, it is indeed possible to reduce the CPU time requirement of FCM per-iteration by writing the code used in this study more efficiently. In fact, this step must be done once sufficient maturity is accomplished in the development of FCM. Nevertheless, the plot in Figure 5.40 still gives a qualitative idea of the CPU time requirement of FCM.

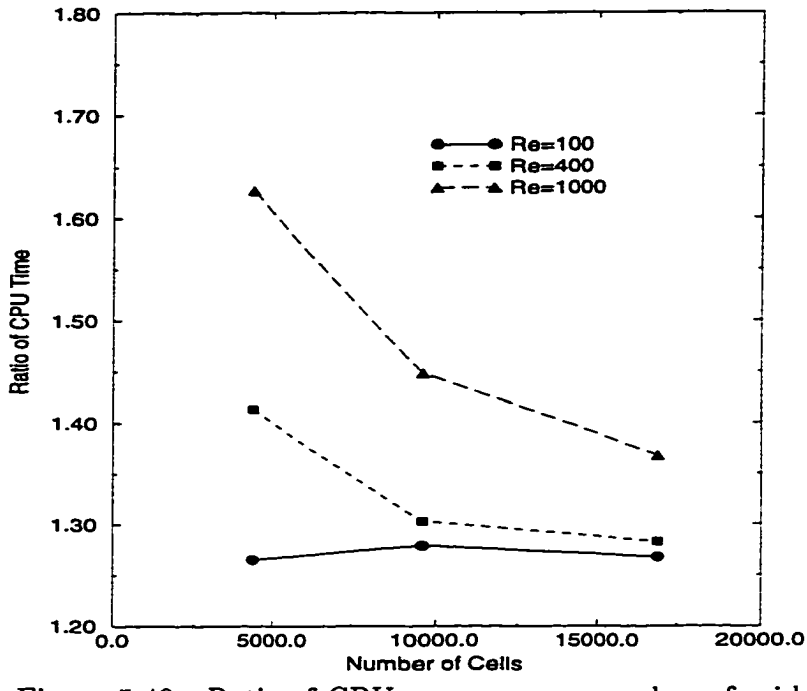

Figure 5.40 Ratio of CPU usage versus number of grid points.

5.4 Unsteady Impulsively Started Lid-Driven Cavity

Under most conditions of practical interest, the component grid Peclet number in the main flow direction is likely to be much larger than one. This means that EDS-based schemes (i.e. Power Law, hybrid, exponential) are operating as first-order upwinding for convection with physical diffusion neglected. As is well known, first-order upwinding is extremely diffusive for transient problems. That is why EDS-based schemes are not usually used for unsteady flow calculations. Thus, it is important to investigate whether FCM shares this particular shortcoming with the Power Law scheme, its parent.

For this purpose, the unsteady flow inside the impulsively started lid-driven cavity at Re=1000 is used as the test problem. This flow situation is not mildly unsteady; in contrast, it is highly transient in the initial period when the primary vortex is developing, gaining strength, translating downward toward the bottom wall, bouncing back, and eventually settling in a steady-state. The Crank-Nicholson time integration scheme with Δt=0.2 and 30 subiterations per time-step is used in this study.

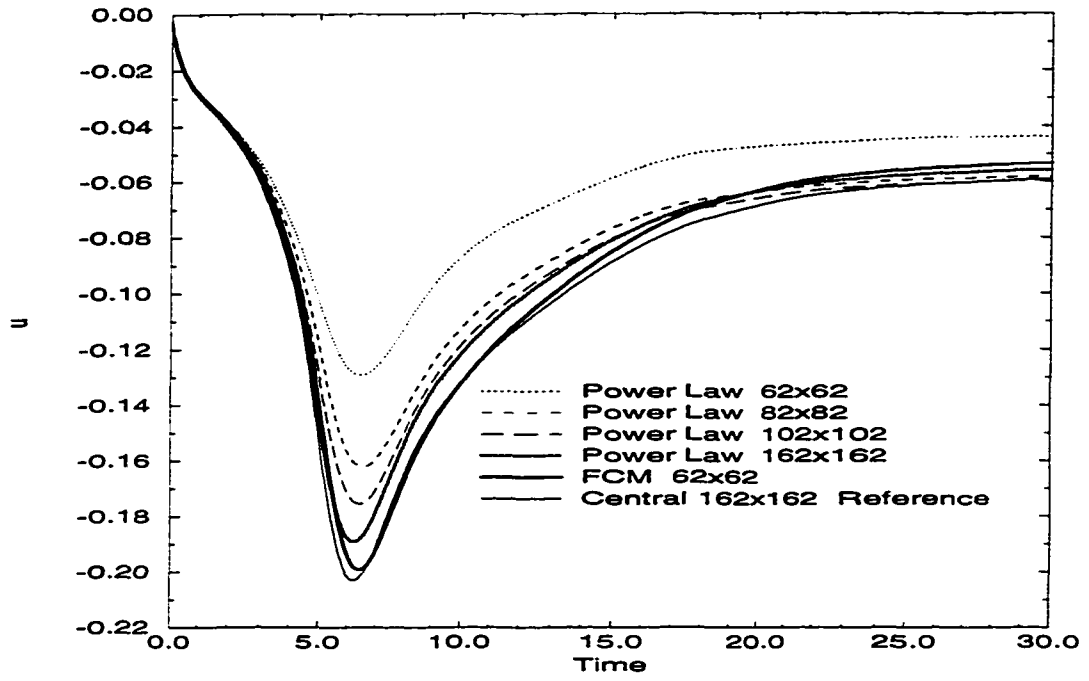

Figure 5.41 Time history of center u-velocity for Re=1000.

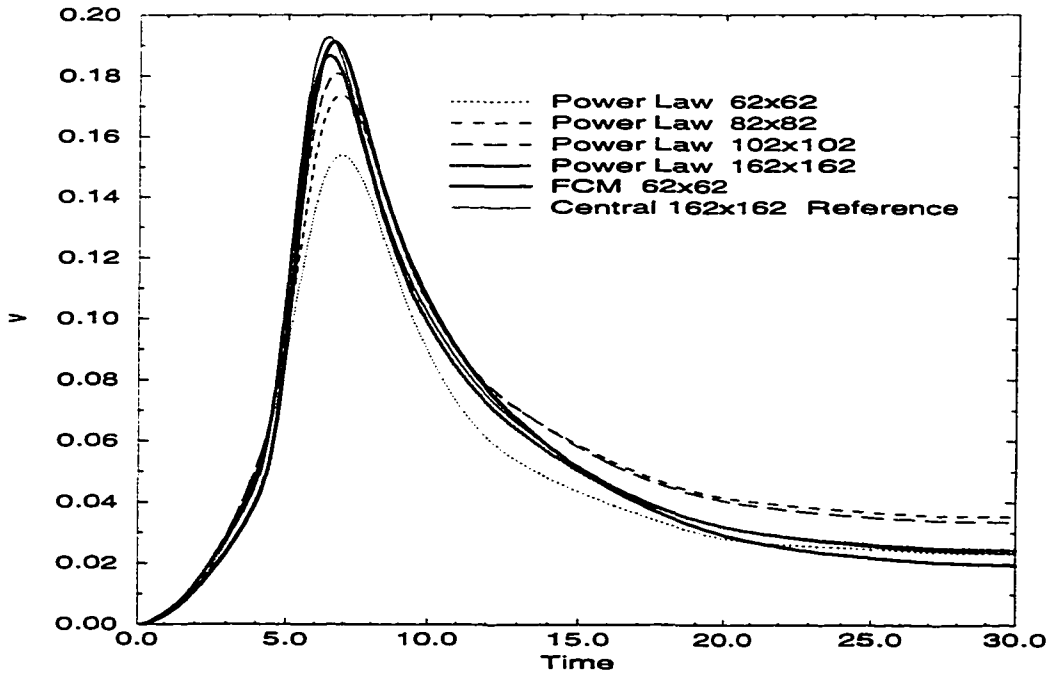

Figure 5.42 Time history of center v-velocity for Re=1000.

The plots of the u- and v-velocities at the center of the cavity versus time are given in Figure 5.41 and 5.42 respectively. It is observed that the Power Law scheme is indeed very diffusive for the transient problem. The Power Law solution obtained using a 62x62 grid is far from adequate in following the reference solution. Even the 162x162 Power Law solution cannot quite follow the high transient gradient between t=5 and t=8. On the other hand, the 62x62 FCM solution is able to closely follow the fine grid reference solution even until steady-state is reached. It is also found during this study that increasing the time-step to 0.4 introduces very minimal changes to the FCM solution. This finding shows that the overall conservation idea used by FCM not only improves steady-state accuracy, but also significantly enhances transient accuracy.

5.5 MultiGrid Technique on FCM

Over the last decade, the multigrid technique, which has been popular for accelerating the convergence of an iterative numerical scheme for linear equations, has started to gain wide acceptance for non-linear problems with the introduction of the FAS (Full Approximation Storage) technique developed by Brandt [49, 50, 51]. When its potential was realized, this technique was quickly adopted by many CFD practitioners to accelerate the convergence of numerical schemes for Navier-Stokes equations, which are highly non-linear. The multigrid technique used in conjunction with a relaxation scheme (i.e. the Gauss-Seidel scheme) accelerates the convergence by realizing that the relaxation sweep on a given grid is effective only in eliminating the error components whose wavelength is comparable to the size of the mesh. The smooth error components which posses longer wavelengths with respect to a mesh can only be efficiently removed by using a coarser mesh. Hence, after two or three iterations on a given fine mesh, the multigrid method switches to a coarser mesh (usually constructed by combining four control-volumes in two-dimensions) where the error components with longer wavelengths can be rapidly

annihilated. Thus, the multigrid method involves a procedure for transferring the flow properties from finer to coarser mesh (restriction) and communicates the error removal from coarser to finer mesh (prolongation). Another aspect of the multigrid technique is the strategy for cycling through the grid; the simplest and most common is the V-cycle. One V-cycle iteration constitutes stepping down from the finest to the coarsest grid by doing a few relaxation sweeps at each grid, converging the iterative scheme to an acceptable level at the coarsest grid, and then stepping up and transferring the error information successively by doing another few relaxation sweeps at each grid level until the finest grid is reached. The details of the FAS technique are readily available from the literature, as are the different types of restriction and prolongation processes. This work closely follows the special application of the FAS technique for the segregated SIMPLER algorithm developed by Zori [40], and a four stage V-cycle multigrid sweep is employed in this study.

The CPU times needed by the single grid and FAS-SIMPLER multigrid using both the Power Law scheme and FCM for the lid-driven cavity problem at Re=1000 using a 98x98 grid are given in plot *a* of Figure 5.43. The residual used in this analysis is defined by:

$$Rsdl = \left[\frac{\Sigma(Rx^2 + Ry^2)}{Number\ of\ grid\ points}\right]^{\frac{1}{2}}, \tag{5.1}$$

where Rx and Ry are residuals of the x- and y-momentum conservations. All computations are performed using the DEC 3000 AXP workstations. It is observed that the FAS-SIMPLER technique for Power Law and FCM has the same convergence behavior. This is consistent with the single grid convergence characteristics of FCM relative to the Power Law scheme. Using a 66x66 grid and the same Reynolds number, the effect of different relaxation parameters on the multigrid convergence is given in plot *b* of Figure 5.43. It is obvious that the value of the relaxation parameter used does influence the rate of convergence of the multigrid iteration.

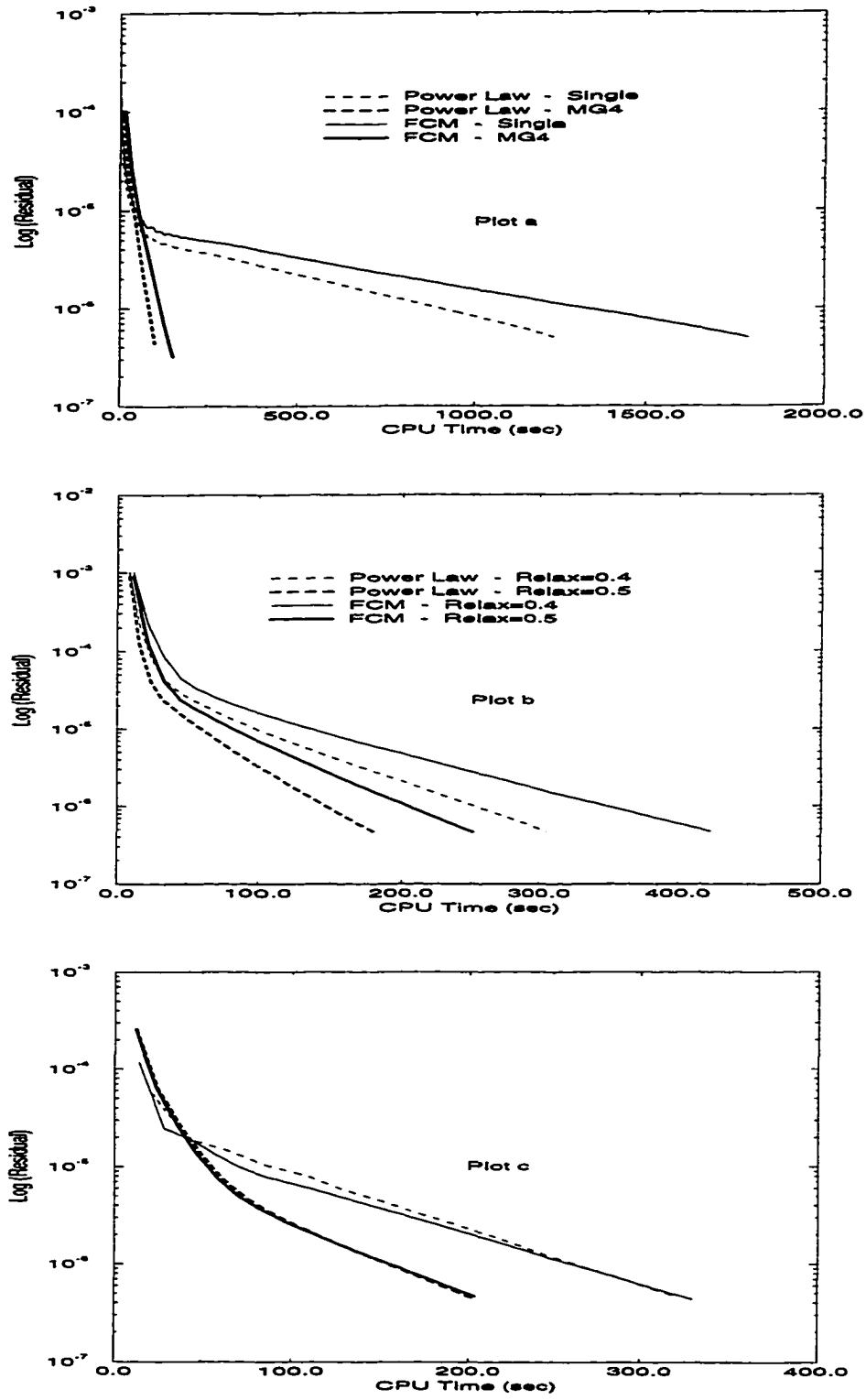

Figure 5.43 Multigrid convergence for Re=400.

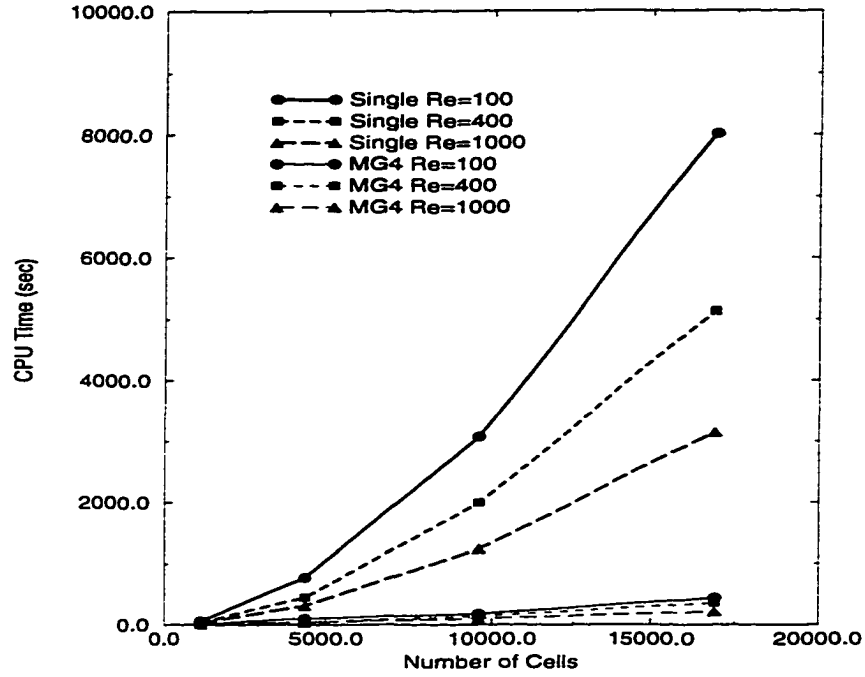

Figure 5.44 Single grid and multigrid convergence using Power Law.

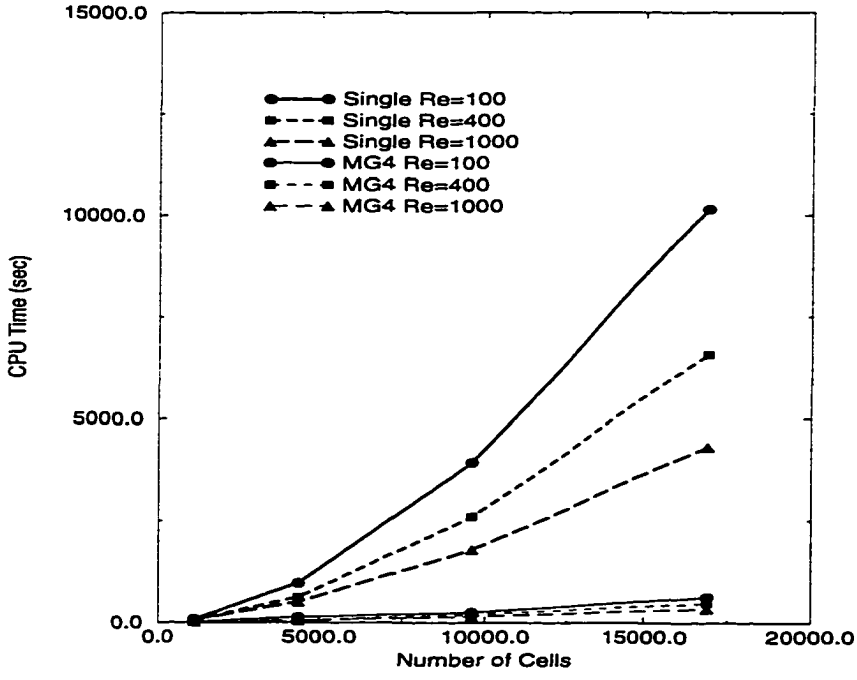

Figure 5.45 Single grid and multigrid convergence using FCM.

Finally, the effect of the different choices of the number of sweeps at each grid level during one V-cycle iteration is given in plot *c* of Figure 5.43 for Re=400 using a 98x98 grid. It should be noted that the choice of the number of relaxation sweeps during the restriction and prolongation in a V-cycle iteration also influences the multigrid convergence behavior. Unfortunately, there is no clear guideline to determine what the optimum number of sweeps are. This is very much dependent on the Reynolds number, mesh size, and type of problem itself. However, it is observed through experimentation that only a few sweeps are generally needed during the restriction to a coarser grid, but significantly more iteration is needed during the prolongation to a finer grid. At the coarsest grid, a sufficient number of iterations must be performed to ensure sufficient convergence at this level.

A more systematic study of the FAS-SIMPLER behavior for the Power Law and FCM is summarized in Table 5.1. Calculations are made for a Reynolds number of 100, 400, and 1000 at four different grid sizes of 34x34, 66x66, 98x98, and 130x130. Calculations are terminated when the residual (defined by Equation 5.1) reaches a value less than or equal to 5.0×10^{-7}. It is observed that multigrid efficiency improves with increasing grid-density. Consistent behavior between Power Law and FCM is also observed. Figures 5.44 and 5.45 show that the CPU time required for convergence, for both Power Law and FCM, increases almost linearly for the multigrid and almost quadratically for the single grid.

Finally, the performance of the FAS-SIMPLER for very high grid density is investigated. Figure 5.46 shows the convergence behavior for the cavity problem at Re=1000 using a 322x322 grid. It is obvious from this plot that a problem of this size is hardly affordable using a single grid. This particular study also shows that lid-driven cavity flow for Re=1000 is truly steady. Convergence using Power Law and FCM to 10^{-11} residual is achieved. On the same graph, the multigrid convergence for the Power Law scheme at Re=10000 using the same grid is also plotted. However, the FCM solutions at this

Reynolds number are not obtained since the residual stalls and oscillates at about 10^{-6} level due to the transient characteristics of the problem. It is the steady converged and non-converged solutions (for Re=1000 and 10000 respectively) obtained using multigrid technique in this study which are used as the initial solutions for the FCM unsteady run given in Figures 5.33 and 5.34.

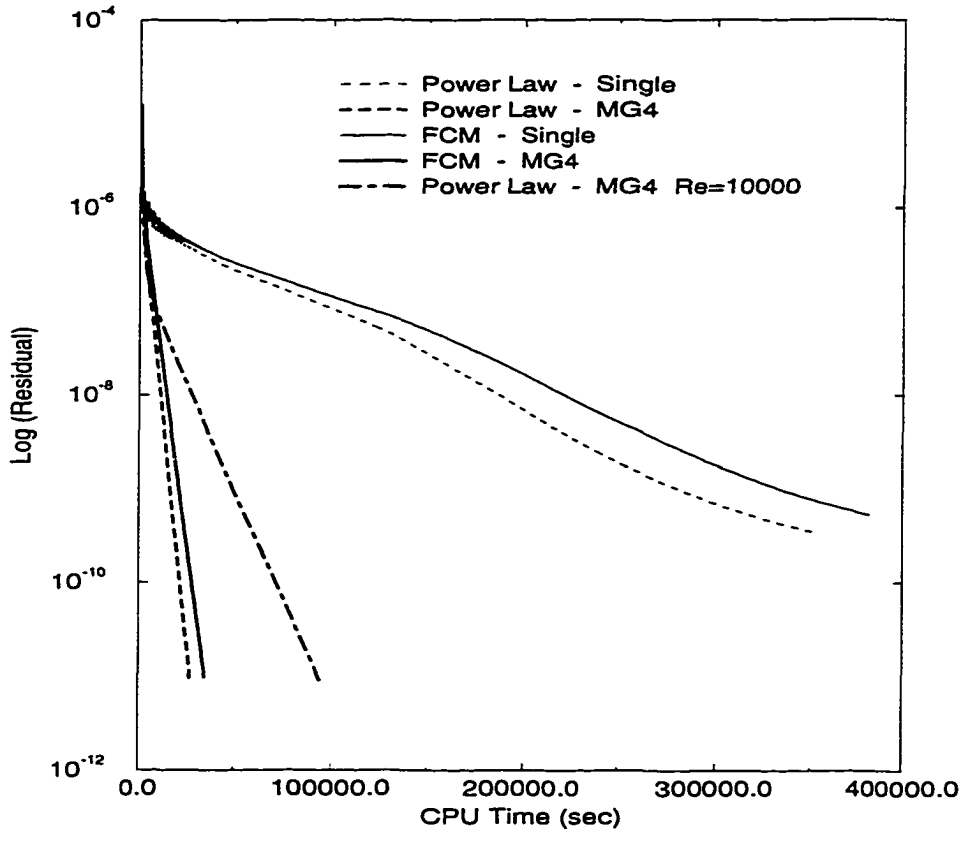

Figure 5.46 322x322 single grid and multigrid convergence for Re=1000.

Table 5.1 Multigrid performance of the Power Law scheme and FCM.

34x34						
	PL			FCM		
Re	SG	MG4	Speedup	SG	MG4	Speedup
100	57.1	20.1	2.8	78.3	29.8	2.6
400	39.0	8.8	4.4	64.0	12.6	5.1
1000	28.5	9.6	3.0	73.6	15.9	4.6
66x66						
	PL			FCM		
Re	SG	MG4	Speedup	SG	MG4	Speedup
100	767.7	97.6	7.9	971.0	129.7	7.5
400	441.1	39.6	11.1	623.3	49.4	12.6
1000	310.0	36.5	8.5	504.4	54.5	9.3
98x98						
	PL			FCM		
Re	SG	MG4	Speedup	SG	MG4	Speedup
100	3072.0	179.3	17.1	3929.4	251.0	15.7
400	1994.6	141.7	14.1	2599.7	202.0	12.9
1000	1235.8	101.1	12.2	1789.5	153.0	11.7
130x130						
	PL			FCM		
Re	SG	MG4	Speedup	SG	MG4	Speedup
100	8008.7	437.9	18.3	10156.8	624.5	16.3
400	5128.0	359.4	14.3	6577.5	479.5	13.7
1000	3149.0	212.9	14.8	4308.6	341.7	12.6

5.6 Three-dimensional Lid-Driven Cavity Flow

A limited testing on the three-dimensional flow inside a cubic cavity was also conducted in the present study. Referring to Figure 3.1, the third-dimension is given perpendicular to the page. It is obvious from the geometry that, for the Reynolds number case where there is a steady-state solution, the flow is symmetric about the half span of the cavity length in the third-dimension. For this present study, the two Reynolds number cases Re=400 and Re=1000 are considered, and uniform grids in all three directions are used. The fine 82x82x82 grid Power Law solution will be used as the reference solutions.

The vertical centerline u-velocity profile at the symmetry plane for Re=400 is given in Figure 5.47. It is observed from this figure that the 22x22x22 grid FCM solution falls right on top of the 42x42x42 grid Power Law solution. The reference Power Law solution is followed very closely by using the 32x32x32 grid FCM solution. The superior peformance of FCM is even more obvious for the higher Re=1000 case, as shown in Figure 5.48. In this figure, the 22x22x22 grid FCM solution follows the reference solution closer than the 42x42x42 grid Power Law solution. Using a 32x32x32 grid, the FCM solution is able to match the reference solution very closely.

The effectiveness of FCM for fluid flow simulations can be appreciated better when solving three-dimensional flow problems. In solving two-dimensional problems, the increase in the CPU time to obtain convergence, as a result of doubling the number of grid points in each coordinate direction, is significant but is much smaller than the CPU time increase resulting from doubling the grid on three-dimensional problems.

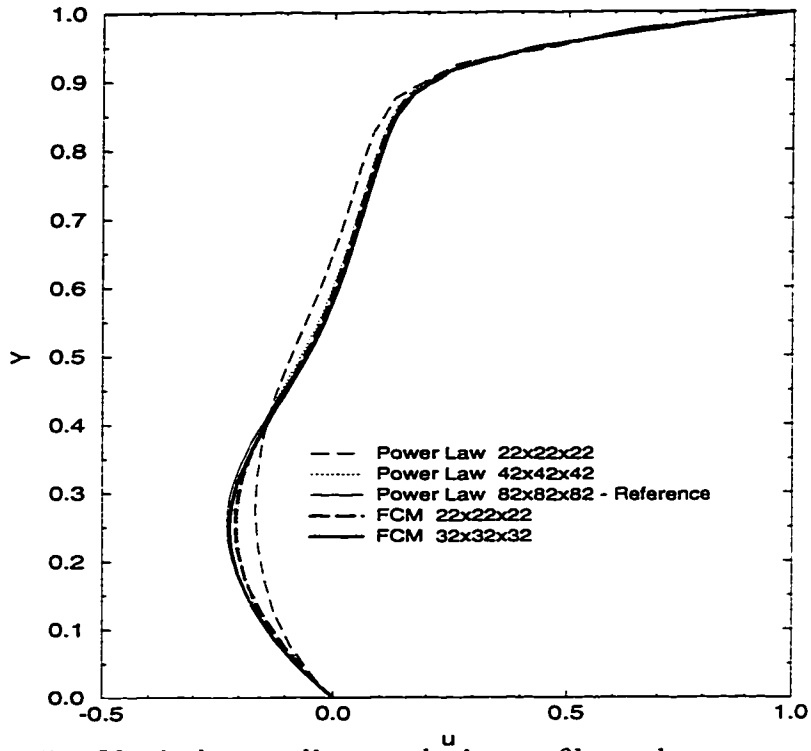

Figure 5.47 Vertical centerline u-velocity profile at the symmetry plane for the 3-D cavity problem for Re=400.

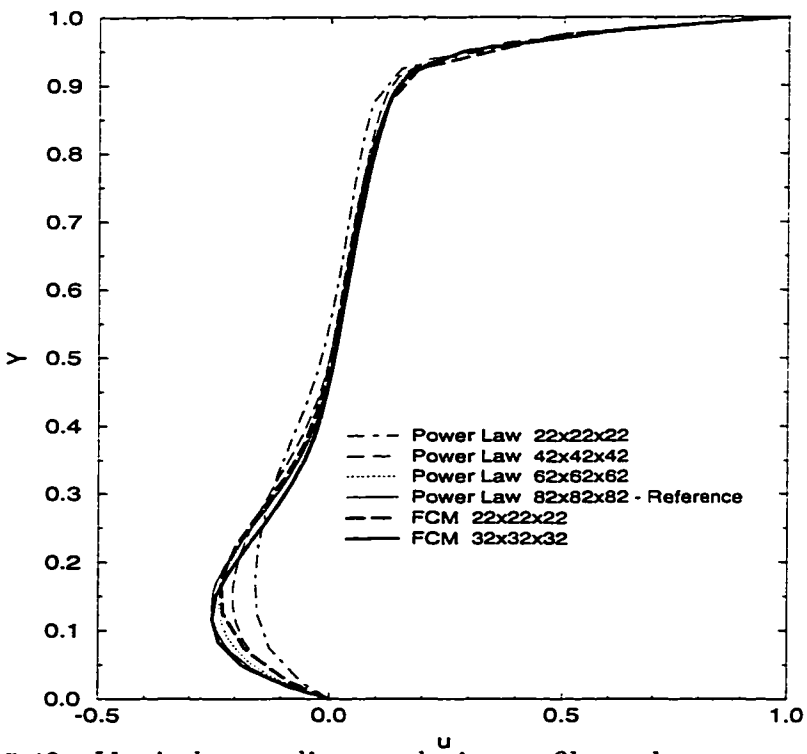

Figure 5.48 Vertical centerline u-velocity profile at the symmetry plane for the 3-D cavity problem for Re=1000.

5.7 Flow Over a Backward-Facing Step

The simulation of a viscous incompressible flow over a two-dimensional backward-facing step has been well recognized as another excellent test problem for evaluating various schemes. This particular flow problem represents a simplification of the well-known internal flow over a sudden expansion found in many important industrial applications. A special characteristic of this flow is the interaction between two different flow structures, which are the primary reverse flow just behind the step and the shear layer emanating from the step edge. It has been verified, both experimentally and numerically, that for a given expansion ratio and assumed inlet profile, the reattachment point of that separated region is dependent only on the Reynolds number. The schematic diagram of this flow problem is given in Figure 5.49. The expansion ratio is defined as:

$$\eta = \frac{H}{h}\,, \tag{5.2}$$

where h is the inlet height, H is the channel height, and $S = H - h$ is the step height. The length of the channel is L, and the three possible recirculating regions are also denoted in this figure, whose corresponding sizes and locations are given by the variable x's. The Reynolds number is given by:

$$Re = \frac{U_{avg}(2h)}{\nu}\,, \tag{5.3}$$

where U_{avg} is the average inlet velocity and ν is the kinematic viscosity of the fluid.

Over the past two decades, both experimental and numerical investigations have been performed on this problem. The most notable experimental investigation is the Laser-Doppler measurements of Armaly et al. [52] which investigated in detail the characteristics of this flow for a Reynolds number range of $70 \leq Re \leq 8000$, covering the laminar, transitional, and turbulent flows. In that paper, Armaly reported that for a certain range of Reynolds numbers, there are two other possible secondary recirculating regions (II and III) of vastly different strength besides the primary recirculating region just

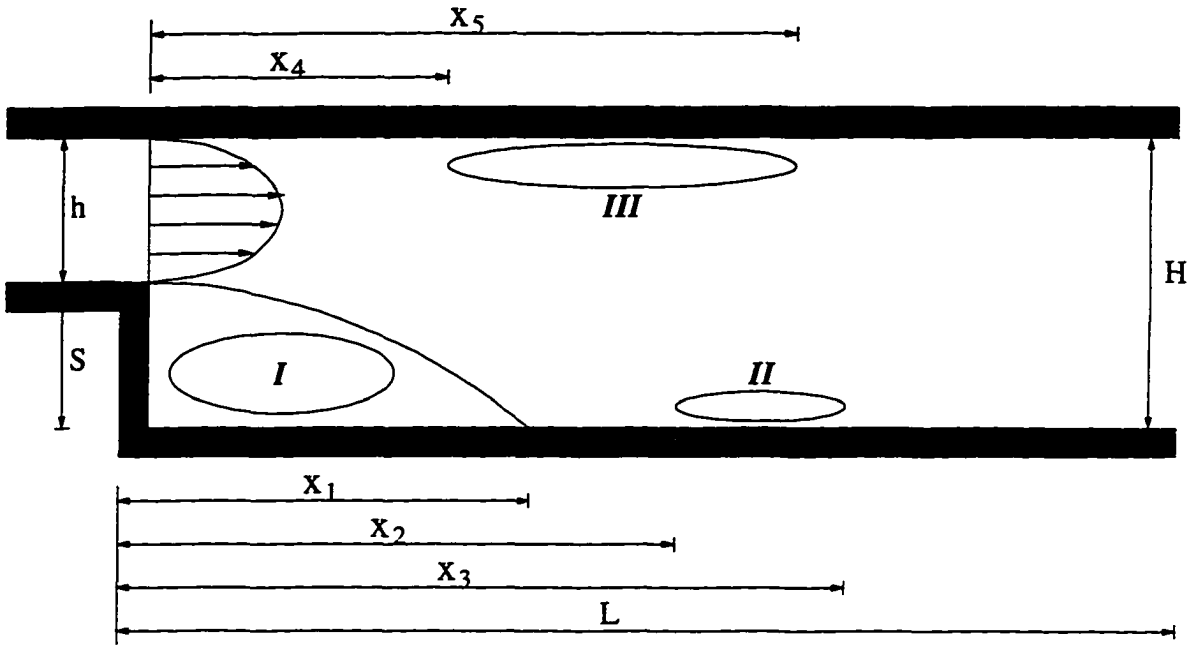

Figure 5.49 Two-dimensional backward-facing step.

behind the step (I). The dependence of the size and location of these separated flow structures on the Reynolds number is summarized by Armaly in Figure 5.50. It should be mentioned here that while Armaly's experiment is always referred to as *'two-dimensional'*, the experimental apparatus itself is a three-dimensional channel with an 18:1 ratio of spanwise width to channel height. Therefore, it is important to note that three-dimensional effects are present to some extent. Moreover, an expansion ratio of 1.94 is used instead of 2.0, giving slightly unsymmetric step and inlet heights. From the shape of the curve fit of the reattachment length x_1 versus Reynolds number given in Figure 5.50, Armaly approximated the laminar range (Re<1200), the transitional range (1200<Re<6600), and the turbulent range (Re>6600) of the flow. The laminar regime is characterized by a reattachment length that increases with the Reynolds number. The increase, however, is not linear, as suggested for reattachment length variations for flows in an axisymmetric sudden pipe expansion. Starting at Re>400, a secondary recirculating region (**III**) at the nonstep wall is observed. This separated region is of

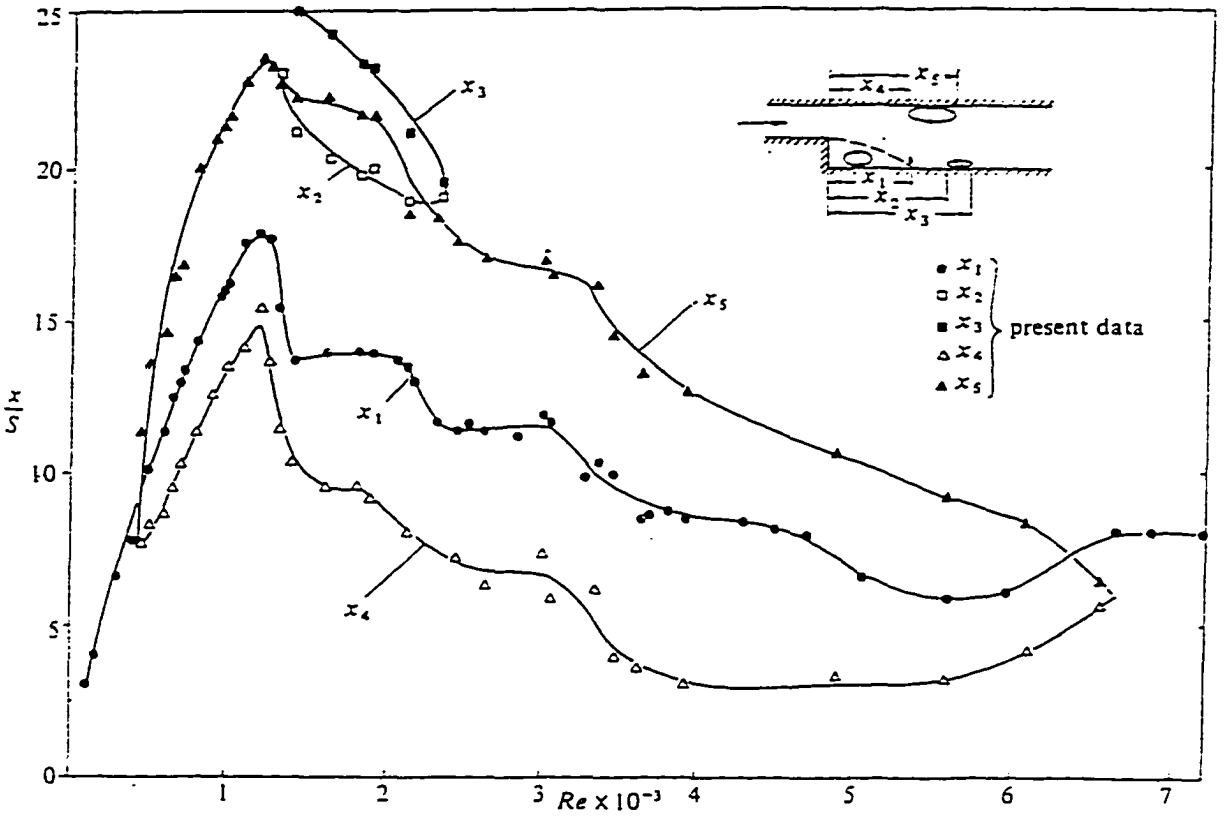

Figure 5.50 Experimental results for size and location of the recirculating regions (taken from Armaly et al.).

lower strength and continues to be present until the start of the turbulent regime. The transitional regime is characterized by first a sharp decrease in that reattachment length, followed by a continued gradual but irregular decrease to a minimum value at a Reynolds number of approximately 5500, and then an increase to a constant level which characterizes the turbulent flow regime. It is early in this transition regime that Armaly reported another secondary recirculating region (**II**) at the step wall, just downstream of the primary vortex. This separated region is very thin and decreases in strength rapidly as the Reynolds number increases and finally disappears for Re>2300. The turbulent regime is characterized by a fairly constant primary reattachment length. Recalling the data in Figure 5.50, it is seen that there is a one-to-one relationship between reattachment

length x_1 and the Reynolds number, with a large positive increasing slope, pointing to the sensitivity of x_1 to Re. This makes the laminar backward-facing step flow an excellent standard problem for testing the accuracy of numerical methods. The closeness of the predicted primary separation length to experimental values can then be used as a measuring stick to study the methods investigated. Moreover, the large body of available literature on the numerical solution of this problem provides helpful comparisons for the particular scheme studied.

In the present study, the performance of FCM for the backward-facing step flow for Re=100,200,400,600, and 800 is investigated. For all the computations peformed in this work, a step height of 0.5 is chosen, and thus for a given expansion ratio η, the inlet height h can be calculated. The average inlet velocity is fixed to be unity, and subsequently the kinematic viscosity ν can be calculated for a given Reynolds number. A parabolic horizontal velocity is specified at the inlet and is given by:

$$u = c(y - y_{lwr})(y - y_{upr}) \ , \tag{5.4}$$

where the value of c is determined through the matching of the integration of the above equation along the specified inlet to the integration of the chosen average velocity along the same inlet. The assumption of parabolic inlet velocity is supported by both experimental and numerical work done by Armaly et al. [52] and Kaiktsis et al. [53] respectively. Armaly mentioned that the measurements of the profile of the inlet velocity spanwise along the channel width is two-dimensional to within 1%. He also reported that for the laminar range, the profile is 'close' to that of a fully developed channel flow with a slight deviation from a parabolic profile. Three-dimensional numerical simulations of Kaiktsis, which are modeled after Armaly's experiment, also show that experiments with the parabolic profile imposed at different upstream locations result in negligible differences in the flow-field, unless the Reynolds number is very low ($Re \leq 200$). For $Re \leq 200$, the value of the primary separation distance is overpredicted by about 10% if the inflow

boundary is taken exactly at the step expansion. The channel length is chosen to be 40 step height units, which for the range of Reynolds number considered, is more than sufficient for the downstream flow to develop into a parabolic channel profile. This is also verified by the work of Kim and Moin [54] which used only a 30 step height channel length employing both Neumann and Dirichlet boundary conditions. The massflow adjusted boundary condition is used at the outlet, and is updated after each iteration. For comparison purposes, the numerical solutions obtained by Armaly [52], Kim and Moin [54], and Gartling [55] are given together with the Power Law and FCM computations. The definition of the Reynolds numbers used by the abovementioned researchers are consistent with the definition used in the present work. Moreover, they all use the same value of expansion ratio ($\eta = 2.0$), except the computations of Armaly and Kaiktsis which use $\eta = 1.94$, modeling Armaly's experimental setup. It will shortly be shown numerically that this slight difference in the expansion ratio produces negligible differences in the computed primary reattachment length. It is also important to mention that they all use a parabolic inlet profile at the step expansion.

The dependence of the primary reattachment length, x_1, on the Reynolds number for the laminar regime, computed using FCM, is given in Figure 5.51. The same data is also given in **Appendix C** in tabular form. The number of grid points in the streamwise x-direction is fixed at 102, but the number of grid points in the y-direction, across the channel height, is varied as 22, 42, and 82. It is observed that the use of 22 grid points in the y-direction is sufficient to predict the separation length up to $Re = 600$, but 42 grid points are needed to achieve grid-independent solution at $Re = 800$. It is also observed from this figure that changing the expansion ratio to 1.94 causes negligible changes in the dependence of the separation length on the Reynolds number.

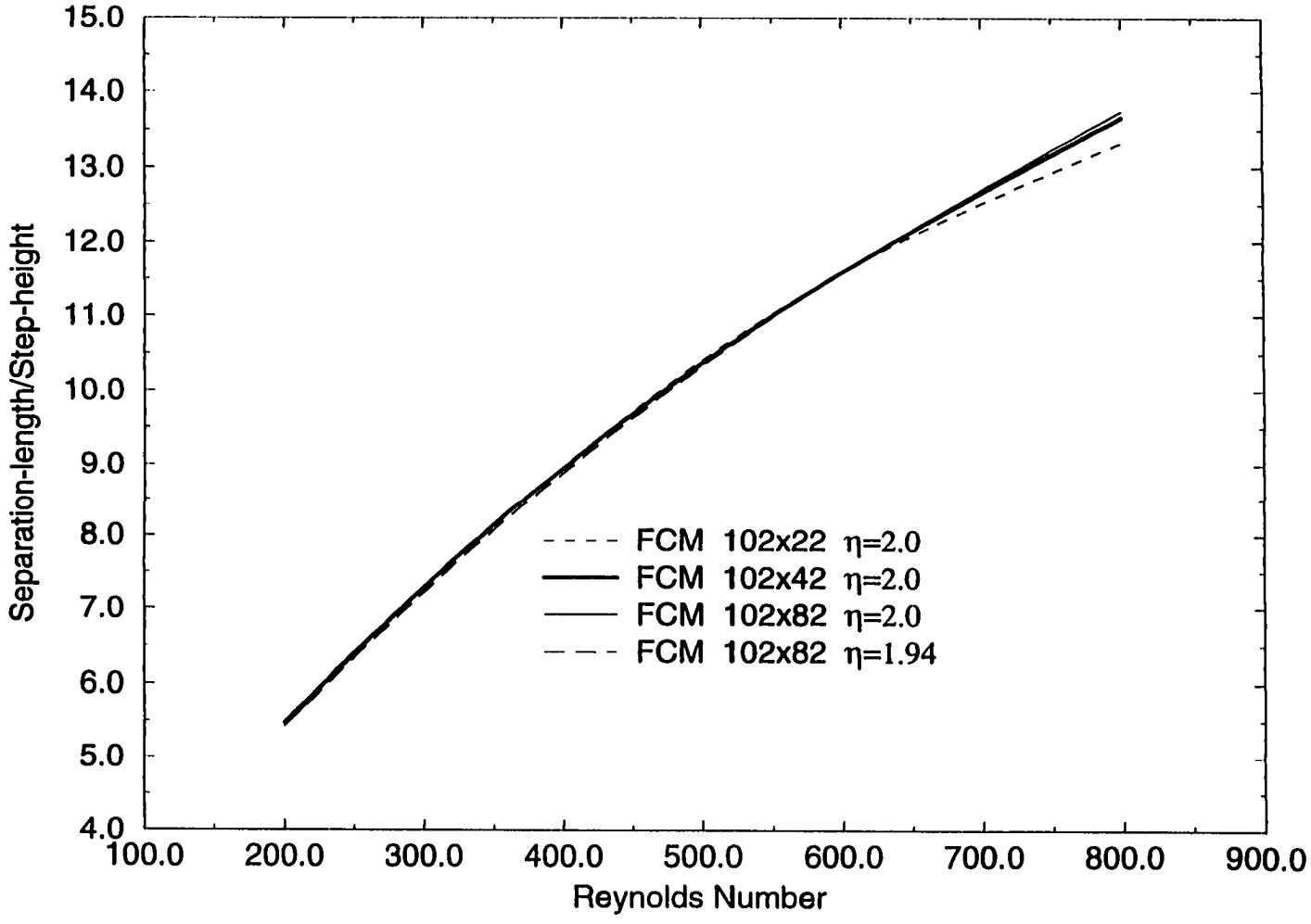

Figure 5.51 Primary separation length versus Reynolds number. FCM grid independent study.

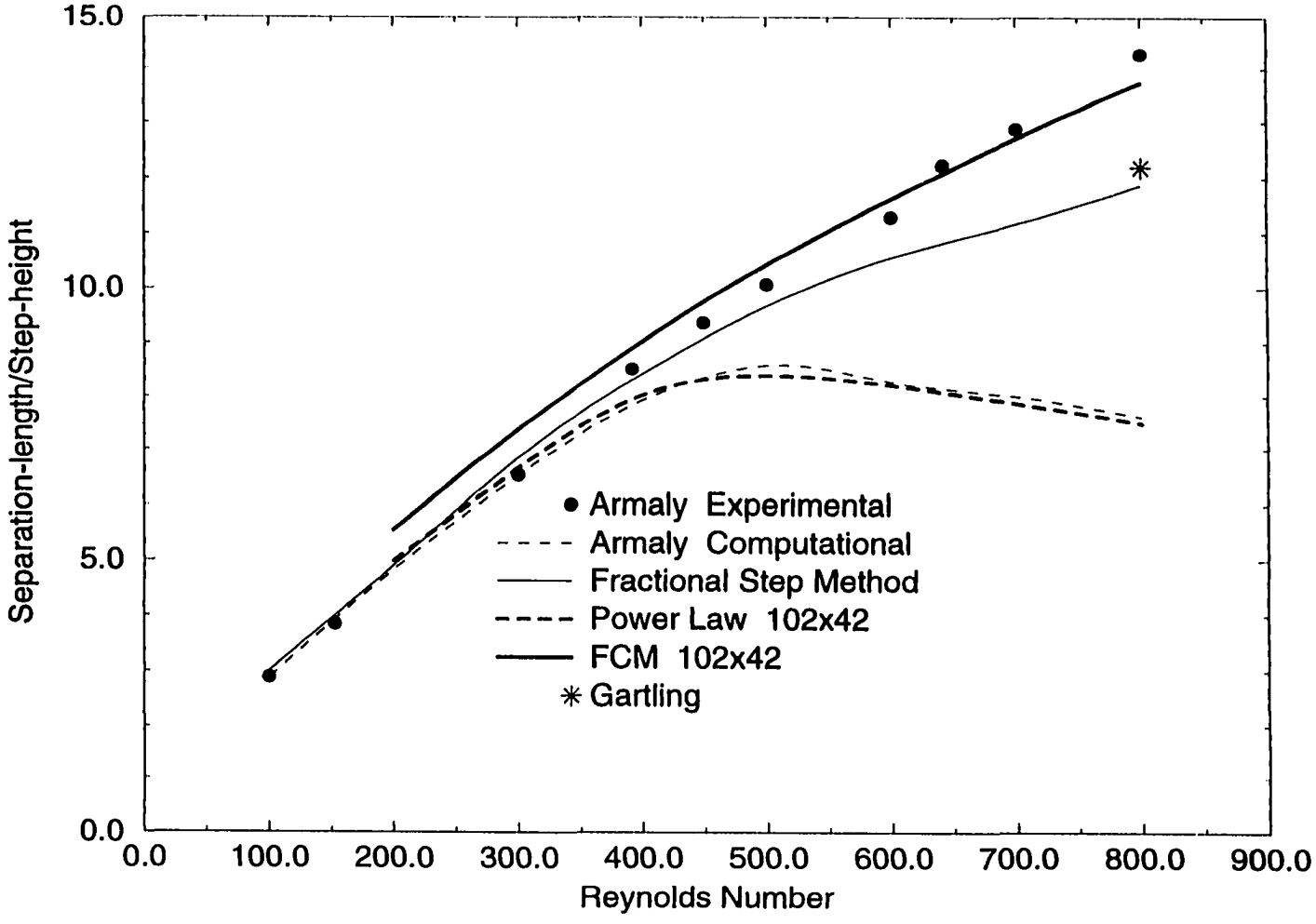

Figure 5.52 Primary separation length versus Reynolds number. Experimental and numerical results.

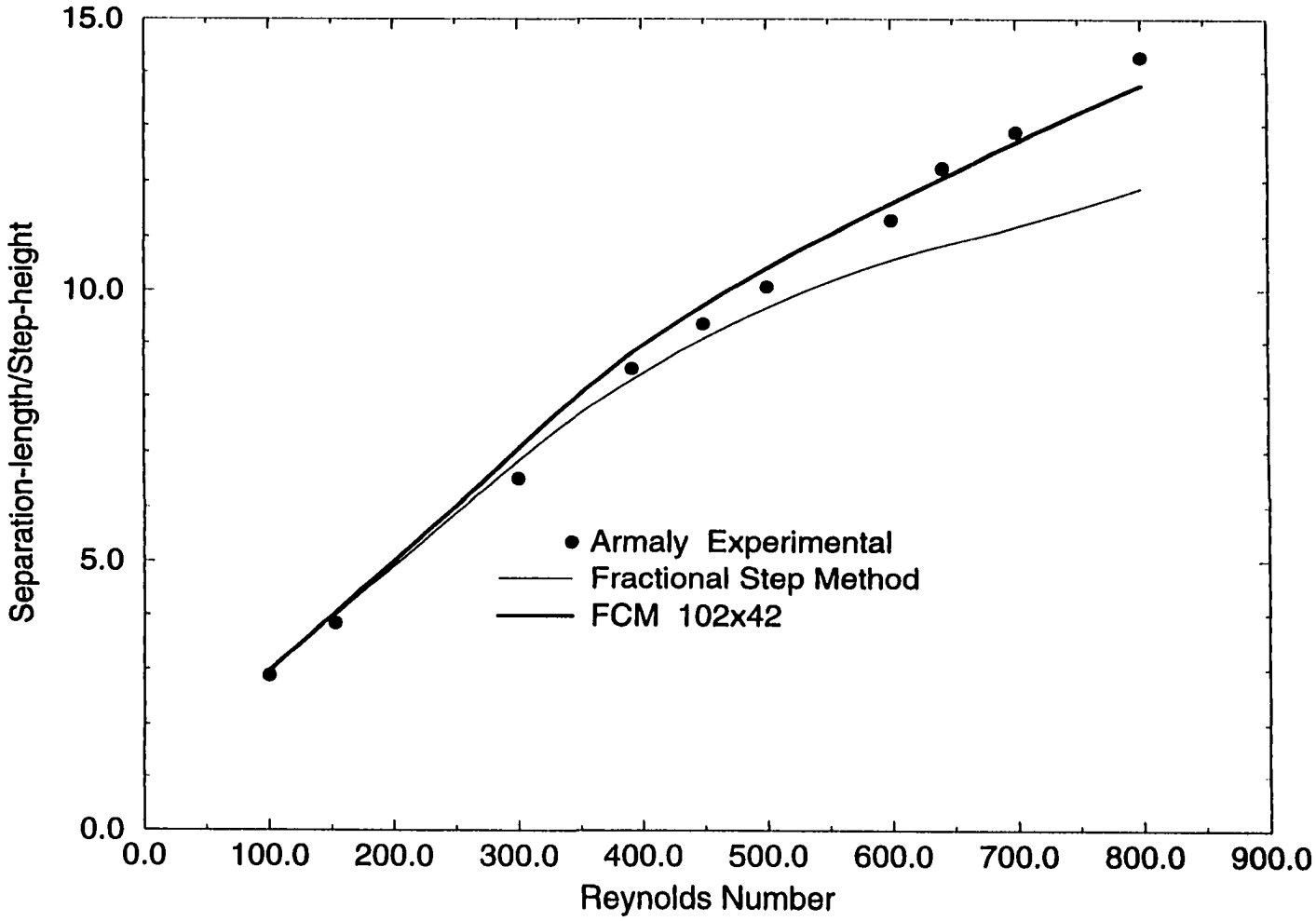

Figure 5.53 Primary separation length versus Reynolds number. Experimental and corrected numerical results.

Figure 5.52 provides a comparison of the FCM solution to the experimental and numerical results obtained by the researchers mentioned previously. Armaly's numerical results are obtained by employing the TEACH computer code, which is basically an exponential-based scheme. Therefore, very close agreement with the Power Law computation is observed throughout the range of the Reynolds number investigated. It is observed that exponential-based schemes can predict the separation length closely only for a low Reynolds number $Re \leq 400$, but the solution quickly deteriorates at higher Reynolds numbers. The predicted separation length is even shorter than the values predicted for the lower Re case. The computation of Kim and Moin uses a second-order accurate finite-difference fractional-step method, and good agreement with experimental results is observed. The steady computation by Gartling for Re=800 is performed by using the code **NACHOS II** [56], which is based on a Galerkin finite-element formulation. It is also verified by using the **FIDAP** [57] program, which is based on the finite-element method as well. It is of particular importance to mention that Gartling's result is also verified by Gresho et al. [58] using four different numerical methods to verify both the accuracy and stability of the backward-facing step flow at $Re = 800$. These four methods, each with its brief description, are given below:

1. A high-order finite-element method solving the unsteady equations by time-marching using the **NACHOS II** code. A quiescent initial condition is used as the initial startup solution. This is the same code used by Gartling in his steady computation.

2. A high-order finite-element method solving the steady equations and the associated linear-stability problem. This code is commonly known as the **ENTWIFE** [59] package, a mixed finite-element approach using nine-node quadrilateral elements with biquadratic interpolation for velocities and discontinuous piecewise-linear interpolation for pressures. This element type is known as one of the best two-dimensional elements.

3. A second-order finite-difference method solving the unsteady equations in stream-function form by time-marching.

4. A spectral-element method solving the unsteady equations by time-marching. The simulation package used is the **NEKTON** [60] code v2.8. **NEKTON** employs a Uzawa spectral element method similar to that developed by Patera [61]. In brief, the spectral element method is a high-order finite-element method where each element has N^D velocity nodes and $(N-2)^D$ pressure nodes, where N is the element order and D is the dimensionality. For a given number of elements, NEKTON is capable of increasing the accuracy of the solution by using a higher element order.

In the case of the unsteady run, Gresho et al. allowed the simulations to run until t=400 to ensure a converged steady-state solution. They also carried out significant grid refinement studies to validate their results. It can clearly be observed from Figure 5.52 that FCM gives an excellent match with the experimental solution, especially for $Re \geq 400$. For $Re \leq 200$, FCM gives a slightly longer separation distance than the experimental values. Recall that in the verification of FCM using the two-dimensional lid-driven cavity problem, FCM performs very well for both the low and high Re case. Thus, it is suspected that the slight overpredictions observed in Figure 5.52 are caused by external means, quite possibly the inlet profile specification. The placement of the outlet boundary as a possible cause is ruled out since rigorous work of other researchers has demonstrated that even shorter channel length has been shown to be sufficient to negate the effects of the outflow boundary condition for this particular Reynolds number. However, the work of Kaiktsis mentioned previously, reported that if the parabolic profile is taken exactly at the step expansion, the value of the primary separation distance is overpredicted by about 10% for $Re \leq 200$. This correction for the low Reynolds number region ($Re \leq 200$) is implemented, and the resulting FCM solution is given in Figure 5.53.

It can now be observed that for all the laminar ranges considered in this backward-facing step simulation, FCM results are in excellent agreement with the experimental results. The underpredicted separation length at Re=800, observed for all the numerical schemes considered in this study, is not likely to be due to the numerical diffusion, but rather is caused by the fact that at this Reynolds number, the three-dimensional effects are sufficiently strong to alter the two-dimensionality of the flow inside the 'three-dimensional channel' used by Armaly et al. in their experimental study. The three-dimensionality of the flow at Re=800 is also shown by Armaly by plotting the spanwise velocity distribution.

It is important to mention here that the FCM solutions presented in this study are obtained by solving the steady flow equations except for the Re=800 case. It was noted that during the steady run at this Reynolds number, the residuals start to oscillate after a four or five order drop in magnitude. Prolonged running of the simulation shows that the oscillations are stable at the original levels. The flow solution reveals that several vortices have developed in the channel, and that these vortices change strength and location along the channel. Recall that this residual oscillation has also been observed before in the lid-driven cavity problem at Re=10000, and in that case, it is shown that the physical problem investigated is not steady. However, in his paper, Gartling [55] was able to obtain a converged solution using steady computation by successively solving the problem at lower Re and extrapolating the converged solution using zeroth-order continuation to higher Re. Certainly, an explanation needs to be developed.

It has been a long held view of the CFD community that the backward-facing step flow at Re=800 does have a steady-state solution. However, the challenges to the existence of the steady-state solution at this Re are not new and have been addressed by A. Tomboulides with M. Israeli and G. Karniadakis as co-authors during the Second Mini Symposium on Outflow Boundary Conditions held at Stanford University in July 1991. The goal of this symposium was to present and discuss four benchmark problems for

testing various outflow boundary conditions, one of them being the backward-facing step flow. Using the 'exponentially accurate for smooth solutions' spectral-element method. Tomboulides showed and stated emphatically that the flow at Re=800 was, in fact, not steady but rather time-dependent, with both eddies (top and bottom) oscillating about their alleged steady-state. The follow-up paper [53], by basically the same group of researchers with Kaiktsis as the primary author, pronounced again that the flow cannot be steady at Re=800 and that it has undergone its first bifurcation at $Re \approx 700$. To clarify understanding of this backward-facing step flow at Re=800, at the conclusion of the minisymposium, Gartling was charged with the task of investigating this problem via the unsteady flow equations starting from rest, since it was thought that the a priori steady assumption made by Gartling was the reason why a steady solution was obtained. This task resulted in the paper by Gresho et al. mentioned previously which uses a finite-element, finite-difference, and very accurate spectral-element method (almost identical to the method used by Kaiktsis) both in steady and unsteady modes. It has been verified in this paper that the backward-facing step flow at Re=800 does indeed asymptote to steady-state for a sufficiently refined grid and sufficiently elapsed time. Using the simulation with the spectral-element **NEKTON** code, Gresho showed that when the resolution is increased beyond a certain point, the numerical solution develops toward an asymptotically steady flow by a monotonous decay of the transient behavior. However, as the resolution is decreased, the numerical solution becomes less stable and develops bounded chaotic behavior, as observed by Kaiktsis et al. The fact that the flow is highly transient in its initial development and will indeed approach steady state is also verified by the unsteady FCM run starting from rest. Figure 5.54 to Figure 5.56 give the streamline plots in the transient development and its corresponding decay using FCM at various times. It is shown in these figures that the initial development of the flow is characterized by continuous shedding of small eddies by the developing primary vortex just behind the step. Moreover, as the primary core flow from the inlet expands and

bends down toward the bottom wall, it starts to generate the secondary vortex at the upper wall, which is then convected downstream and regenerated again at a location further downstream at the upper wall. Moreover, as the primary core flow hits the bottom wall and is reflected, another secondary vortex generation takes place at the bottom wall. This vortex is also regenerated and convected downstream but eventually looses strength and disappears as the flow starts to stabilize toward its steady-state condition. The vortex shedding activities start to diminish at $t \approx 200$, and the flow slowly approaches steady-state.

Of particular interest is the behavior of the unsteady Power Law scheme for this particular problem. Figure 5.57 gives the development of the flow until steady-state is reached. It is observed that no vortex shedding is detected, and the primary and secondary vortices slowly and monotonically develop to their steady-state sizes. This is not surprising. It has been discussed extensively in the previous chapters that the extent of the numerical diffusion of the Power Law scheme prevents accurate prediction of high Reynolds number flow, both steady and unsteady, where there are regions in which the flow is significantly skewed to the grid.

It can therefore be concluded that great care must be used in undertaking CFD analysis. It is very important to know the capabilities of the numerical scheme used and then to allocate a proper number of grid points to ensure that the transient physics of the flow are properly resolved. The fact that FCM fails to converge in the steady mode for the backward-facing step flow at Re=800, using a 102x42 grid, suggests that at that grid resolution, FCM is able to simulate the initial transient nature of the problem but is unable to let the transient structures diminish due to the fact that the time-dependent term is not taken into account in the steady simulation.

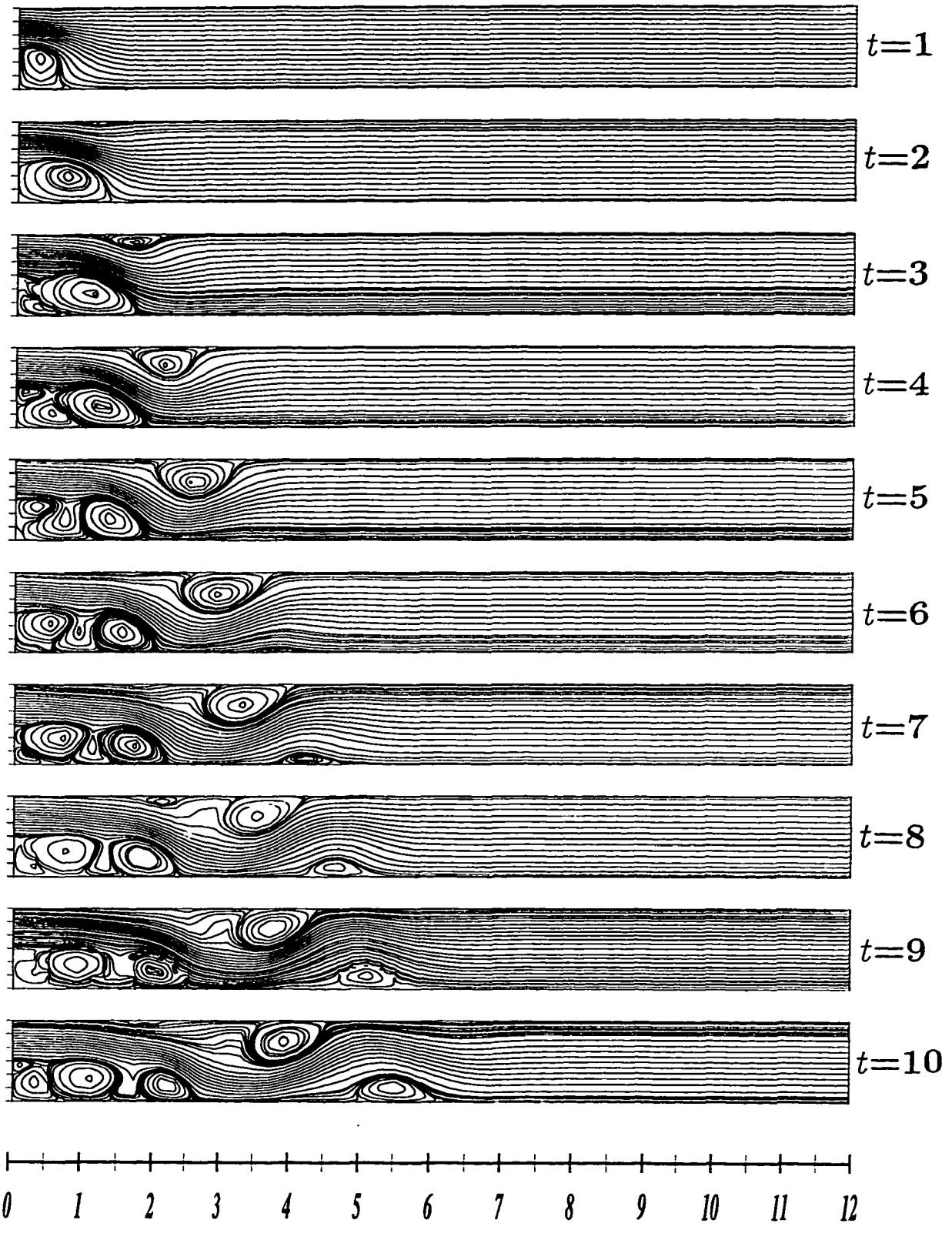

Figure 5.54 FCM unsteady development *part 1* for Re=800.

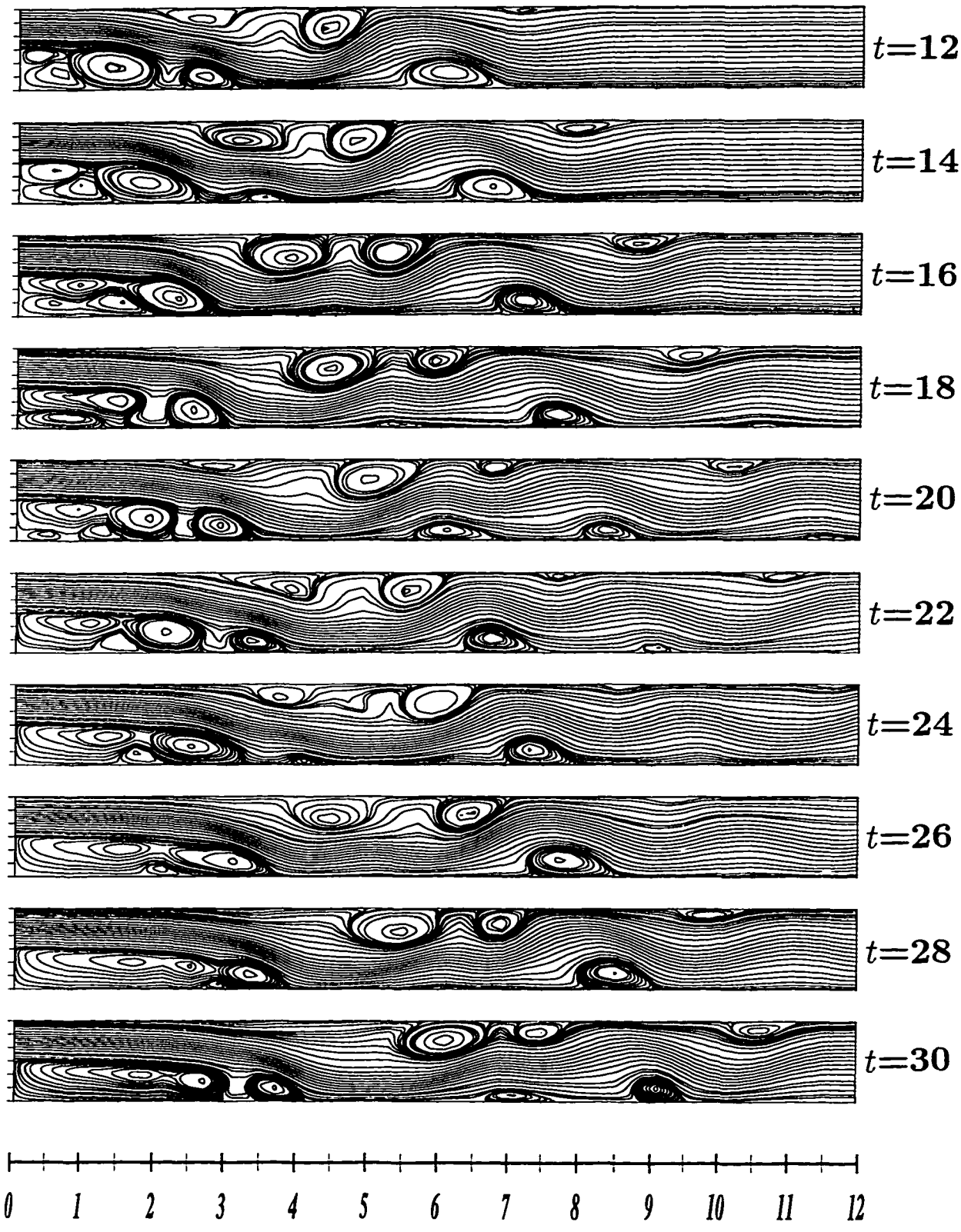

Figure 5.55 FCM unsteady development *part 2* for Re=800.

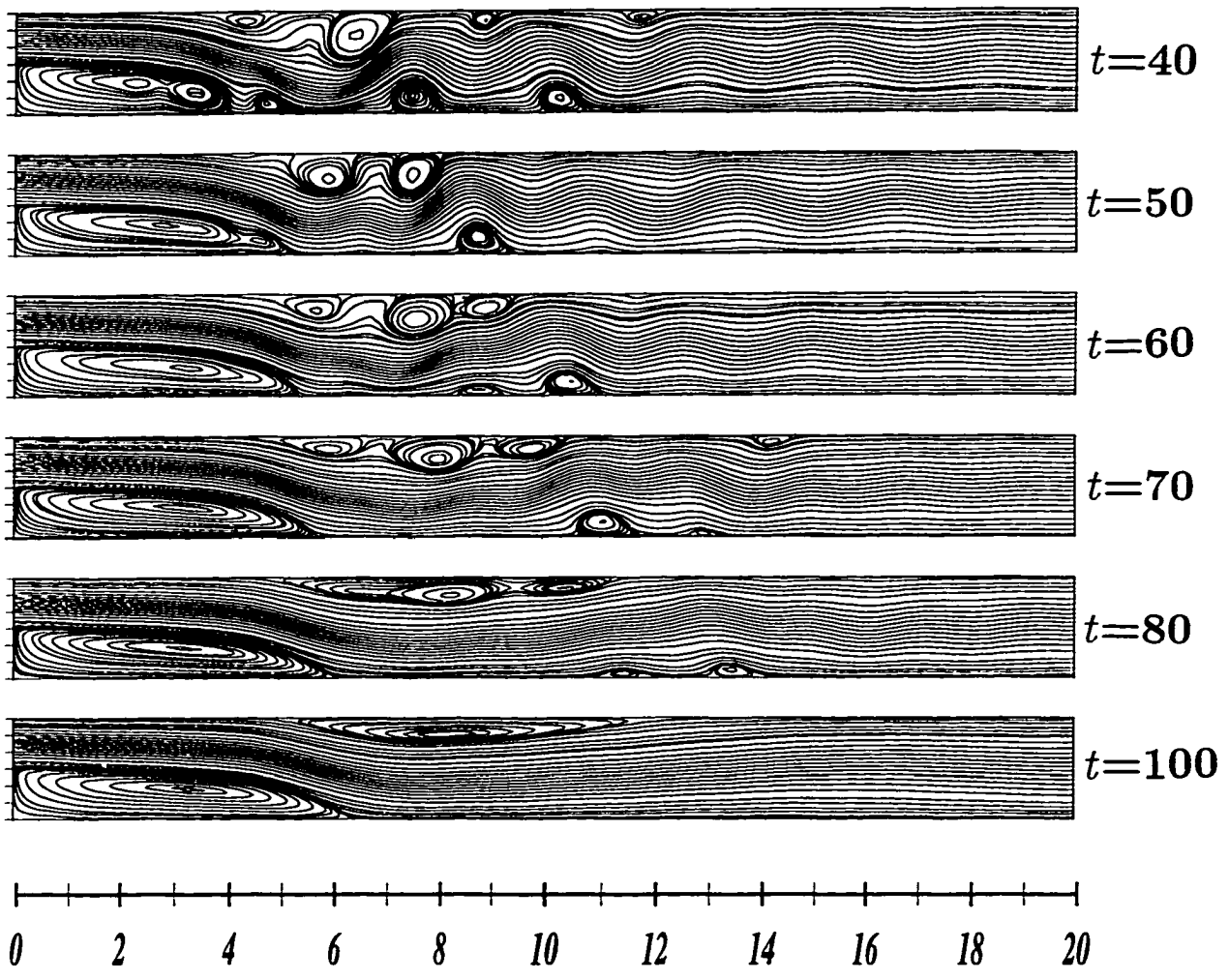

Figure 5.56 FCM unsteady development *part 3* for Re=800.

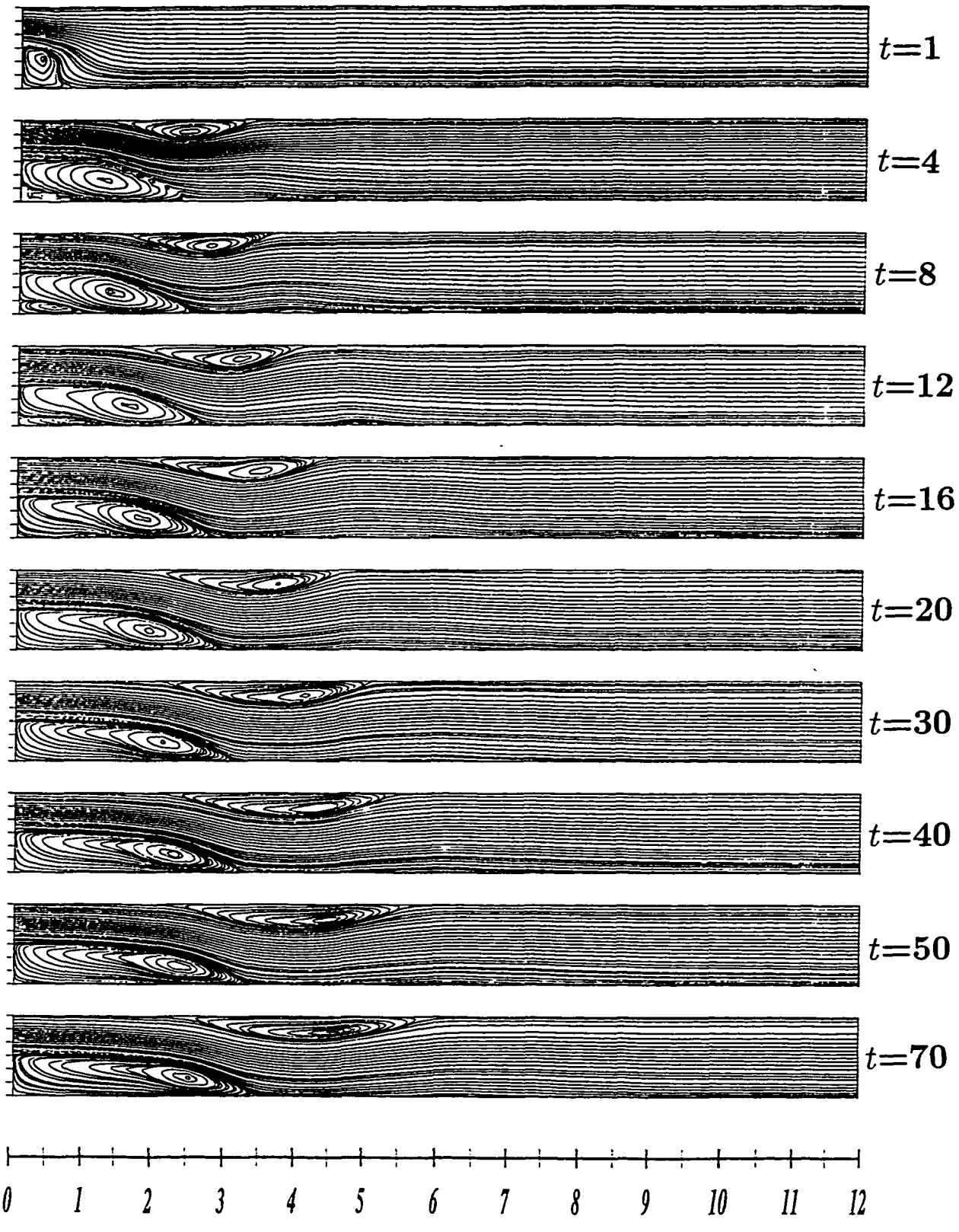

Figure 5.57 Power Law unsteady development for Re=800.

Theoretically, it is always possible to refine the grid sufficiently so that the Power Law scheme is able to adequately resolve the flow physics. But as is shown in Figure 5.29, the cost is undoubtedly beyond what can be afforded.

Finally, the comparison of the final steady-state solution of the Power Law scheme and FCM is given in Figure 5.58. The cross-channel profiles at locations $x = 7$ and $x = 15$ are given in Figure 5.59 and 5.60. In these figures, the results from Gartling [55] and the Power Law and FCM solutions obtained in the current study are plotted together for comparison. It is obvious from Figure 5.59 that the cross-channel profile should not be used as a benchmark measure for the backward-facing step problem since the profile is very sensitive to the reattachment length and will be grossly different even if the numerical schemes compared predict relatively small differences in the reattachment length.

5.8 Numerical Determination of the Accuracy of the Scheme

In the previous sections, the accuracy of the FCM solution has been verified by using the lid-driven cavity and the backward-facing step test problems. Relative performance of FCM has been shown qualitatively by comparing the FCM solution to other numerical solutions obtained using the Power Law scheme, the central-difference scheme, and the QUICK scheme. However, quantitative measures of the accuracy of FCM have not yet been presented. In this section, a simple method of testing the accuracy of numerical schemes which yields measurable parameters is introduced.

To reduce the number of parameters in the study, the lid-driven cavity flow is chosen over the backward-facing step flow, since the latter requires the specification of the outflow boundary conditions. Moreover, besides having a smaller geometry (which is economical in the grid refinement process), the cavity flow also has more 'convenient'

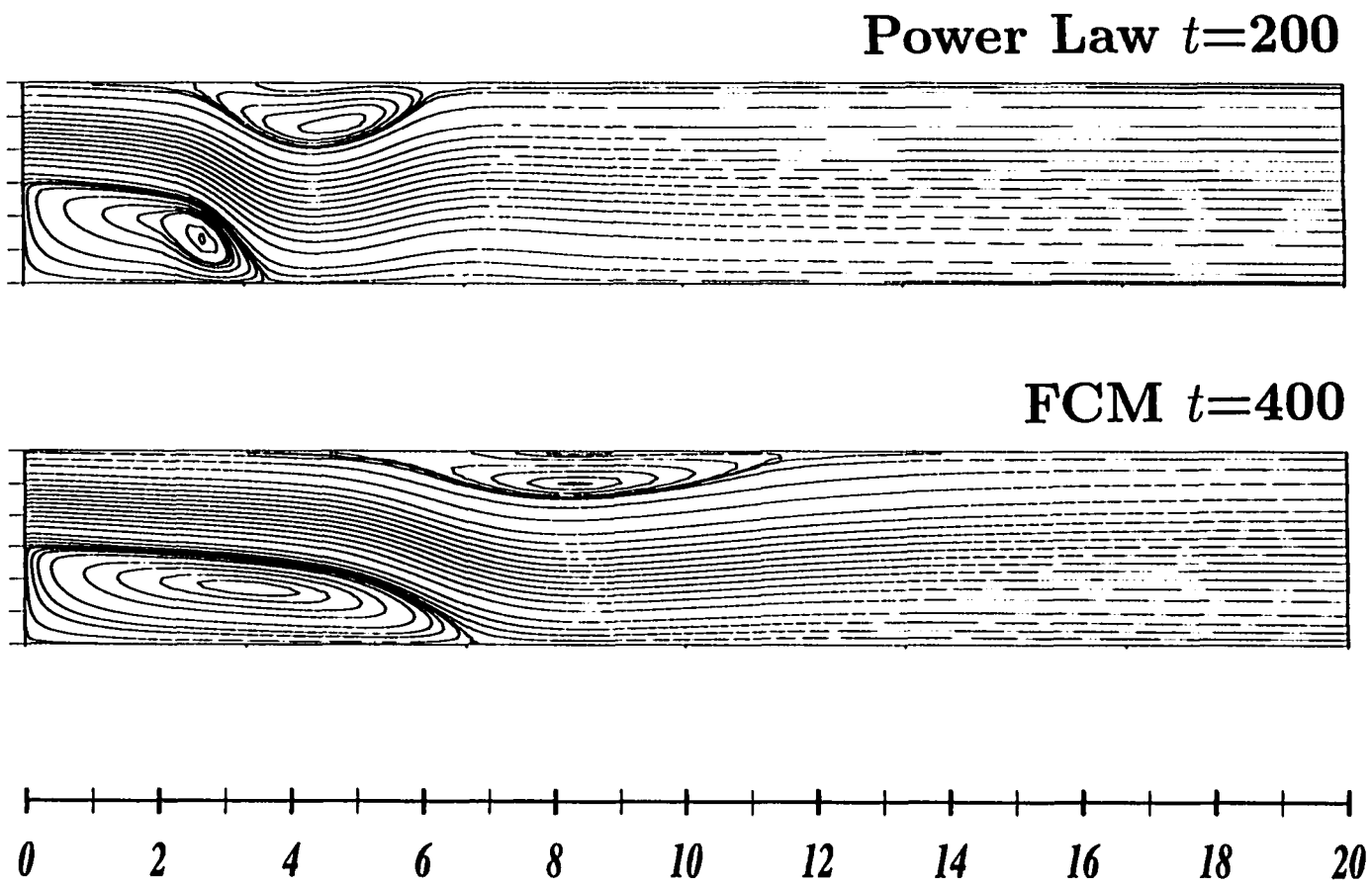

Figure 5.58 Power Law and FCM steady-state solutions for Re=800.

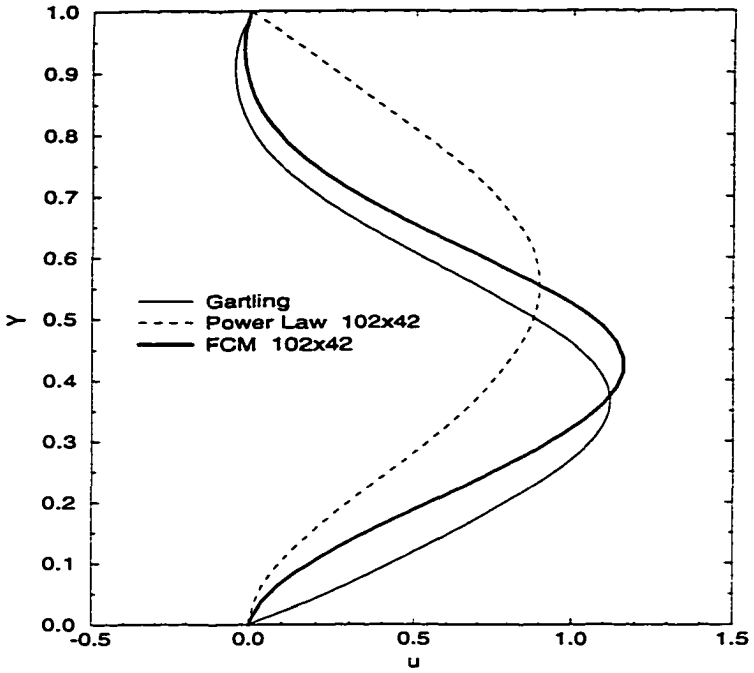

Figure 5.59 Cross channel profile at x=7.

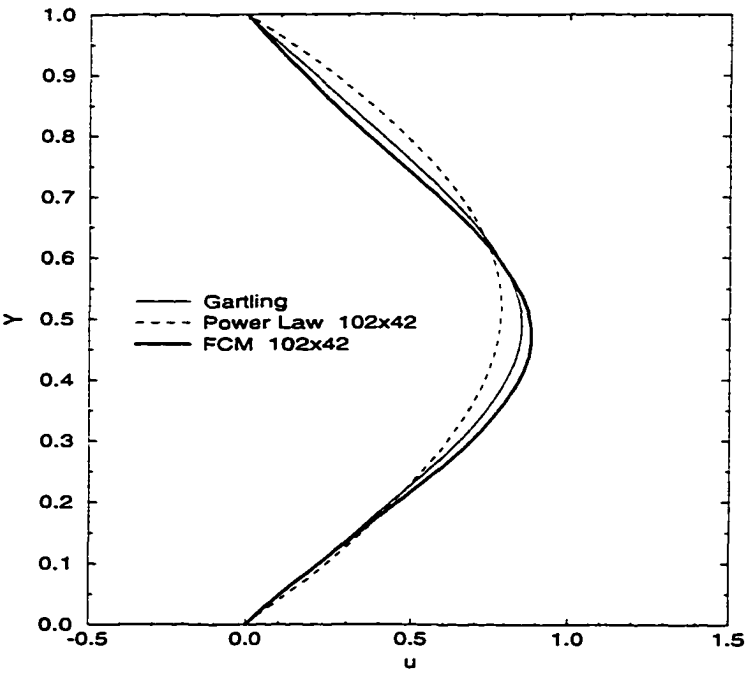

Figure 5.60 Cross channel profile at x=15.

flow profiles which can be directly compared. This order-checking method is outlined as follows:

- Identify the computed flow quantities or profiles (referred to as the flow variables) which will be compared to the benchmark solutions. For the present study using the chosen test flow problem (cavity flow at Re=400), the profiles of the u- and/or v-velocities along the vertical and horizontal lines respectively can be conveniently chosen for this purpose. The more sensitive the chosen quantity to grid refinement, the better it will serve the study.

- Compute the benchmark solutions of the chosen flow variables. Use the highest number of grid points which can be practically afforded. It is observed that the finer the grid used to obtain the benchmark solutions, the wider the applicable range of the results of the study. In this study, a 322x322 grid is used, and converged solutions with residuals up to 10^{-14} are obtained using the multigrid method discussed previously.

- The next step is to compute a series of solutions using progressively finer grids. However, it is first necessary to decide whether to refine the grid in one or in all coordinate directions simultaneously. In practice, it is usually desirable to study how the solutions behave as one grid direction is refined and the other grid directions are kept constant at the resolution of the benchmark resolutions in the corresponding grid directions. For example, in this study, if the u-velocity is chosen, then it is necessary to use 322 grid points in the x-direction and progressively refine the grid in the y-direction (22, 42, 62, 82, and 102), since the u-profile is most sensitive to Δy variations. In a similar way, the same procedure is used if the v-velocity is chosen, only now the grid in the x-direction is refined while the grid in the y-direction is kept at the benchmark resolution.

- After the coarser grid flow variables have been computed for all the grid resolutions desired, the error of the chosen flow variable for a given grid resolution is computed.

$$error = \int |\phi_b - \phi_c| \, ds \ , \tag{5.5}$$

where ϕ_b is the benchmark value and ϕ_c is the coarser grid value. The limit of integration can be determined easily, and ds represents either dx or dy. For example, the error of the u-velocity for a given Δy for all the grid resolutions considered can be computed.

- It is a common practice in CFD to address the accuracy of a numerical scheme in the form:

$$error \approx c \, \Delta^N \ , \tag{5.6}$$

where c is the leading order constant, Δ is the grid spacing, and N is what is usually referred to as the order of the scheme. Writing the above equation in logarithmic form results in:

$$log_{10}(error) = log_{10}(c) + N \, log_{10}(\Delta) \ . \tag{5.7}$$

It is now obvious that by plotting the logarithmic of the error versus the logarithmic of the grid spacing, and then applying a linear regression over the given data, the value of c and N can easily be determined.

The quantitative performance of Power Law, central-difference, and FCM obtained using this simple order-checking method is given in Figure 5.61. In this figure, the u-velocity along the vertical centerline is used as the flow variable. Computations using u-velocity along the other vertical lines or using v-velocity along the other horizontal lines give similar qualitative and quantitative results. It is observed in this figure that tremendous improvement in the leading order term of Equation 5.7 is achieved by FCM. It can be roughly seen from this figure that a 322x22 grid FCM has approximately the

same error level as a 322x42 grid central-difference and an approximately 322x82 grid Power Law scheme. From the slopes of the linear fit lines, it is also obvious that modest improvement in the value of the scheme order N is also achieved by FCM, improved from $N \approx 1.5$ of the Power Law scheme to $N \approx 2.0$ of the central-difference scheme.

It should be obvious from Equation 5.7 that both the values of c and N are equally important in formulating/devising a high accuracy scheme. In the present study, the leading order term is vastly improved, but only modest improvement is observed on the parameter N. In the finite-difference method, the improvement on the value of N is commonly achieved by using more grid points (larger approximating stencil) in a coordinate direction. However, this approach often reduces the diagonal dominance of the iteration matrix, thus resulting in a less stable numerical scheme. On the other hand, it should be recalled that in the formulation of FCM developed in this study, no extended cell is used to approximate the values of the dependent variable and its derivative at an interface. Instead, the two neighboring values directly adjacent to that interface, giving a compact stencil scheme, are used. The corrections are all included in the source, preserving the desirable stability characteristics of the Power Law scheme. Although it is theoretically possible to use a larger approximating cell in the FCM formulation, the complexity and additional computation and CPU time needed to determine the upwind cell may not justify the added accuracy.

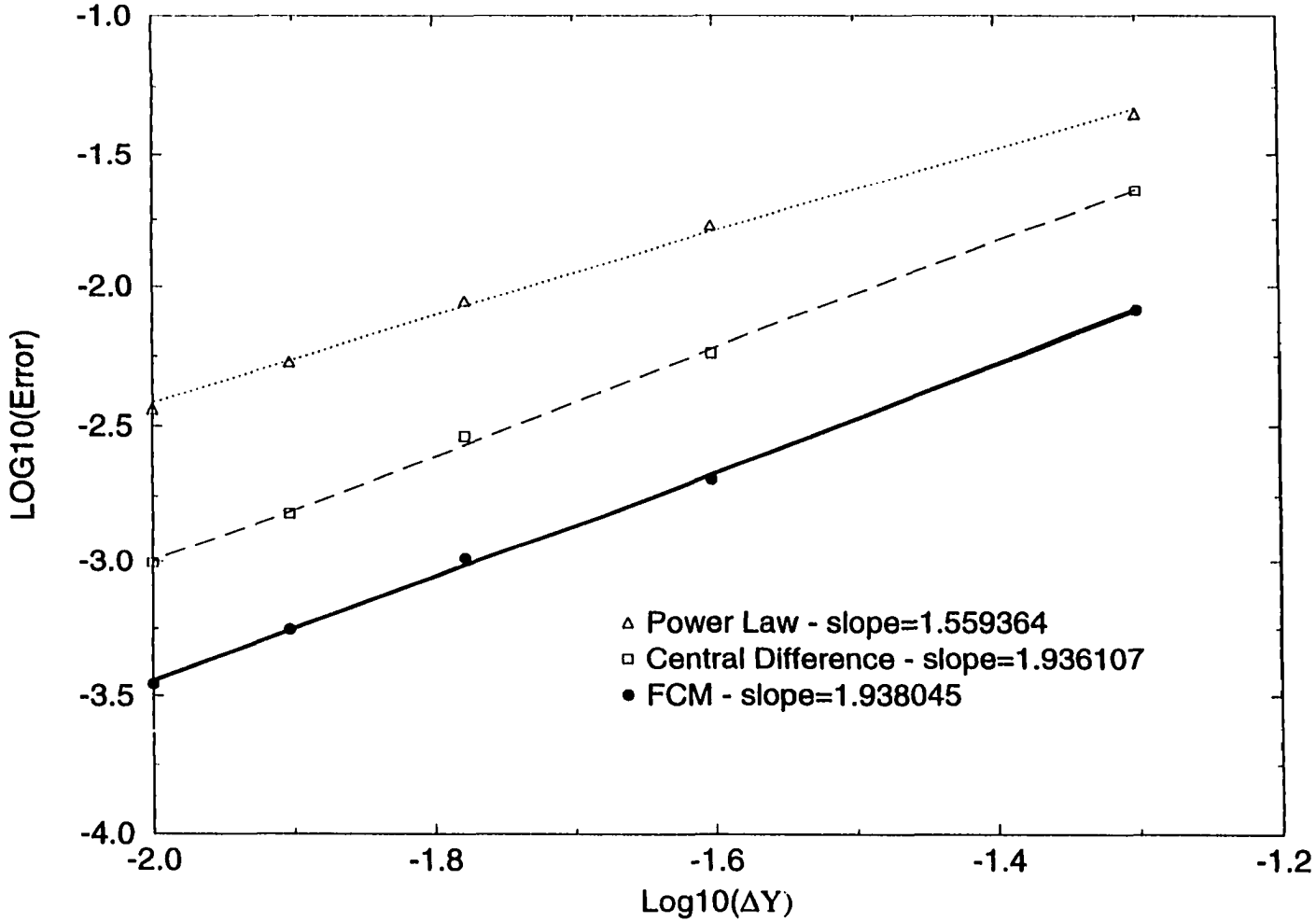

Figure 5.61 Numerical order of accuracy using lid-driven cavity for Re=400.

6 CONCLUSIONS AND RECOMMENDATIONS

In this study, a new approach to the modeling of the multi-dimensional convection-diffusion equation with a source has been developed and tested. The most important strategy of this formulation is the realization that the profile of the dependent flow variable at the interface of a discretized control-volume cell is governed by the governing conservation equation itself across the cell considered. This has led to the effort to rewrite the governing time-dependent multi-dimensional conservation equation with a source as a one dimensional convection-diffusion problem with the other directional transports and the original source lumped together as one constant convection-diffusion source. This results in a non-homogeneous ODE with constant coefficients, whose analytical solution can be directly determined. In the case of zero source, whether imposed or incidental, the resulting profile reduces to the one obtained by using the well-known Power Law scheme, which solves the one-dimensional convection-diffusion equation without a source. For this reason, the new scheme is referred to as the 'Flux Corrected Method' (FCM), since it is basically the Power Law scheme plus a flux correction due to the source. It is also important to note that the resulting formulation conserves the governing conservation equation not only at the control-volume cells where the governing equation is integrated, but also across the cells containing each of the sides of the former cells.

The new formulation has been applied in solving the steady/unsteady incompressible Navier-Stokes equations in conjunction with the SIMPLER algorithm to handle the velocity-pressure coupling in the momentum equations. It is important to note that FCM treats the multidimensionality and the source at the equation level, rather than

by using an improved algebraic profile or any other type of polynomial fit. Since the multidimensionality and the effects of the pressure gradients are directly accounted for, FCM performs very well in recirculating flow regions where more than one component of the grid Peclet number is large.

The test problems chosen to validate the high accuracy nature of FCM are the well-known two-dimensional lid-driven cavity flow and the two-dimensional laminar backward-facing step flow. These are two of the most important benchmark problems used by the CFD community to test the relative accuracy of newly developed numerical schemes. These test problems, though simple in geometry, consist of complex flow structures and do not lack important interaction between the various flow structures present. Indeed, the high Reynolds number cases of these problems are highly transient and unsteady. Systematic study conducted in the present work results in the following conclusions about the characteristics of FCM.

- FCM is very accurate for simulating both steady and unsteady flows, especially when there are recirculating flow regions.

- Since the profile corrections are generated through source addition, FCM retains the basic stable convergence characteristics of the Power Law scheme.

- FCM uses compact stencil in the discretization process. No upwind direction checking is needed (as is required by the QUICK or the second-order upwinding schemes).

- When local grid stretching is used, FCM solutions show less deviation to the reference solution compared to the Power Law scheme.

- Significant additional computation required by FCM can be avoided by reusing the already computed momentum coefficients. However, this approach is not imple-

mented in the current work since a very general code is needed to test the various possibilities in the development process.

- FCM conveniently provides the ability to take into account the user's applied sources in the profile approximation. An example of this concept is the simulation of a helicopter rotor by momentum source as developed by Rajagopalan [33].

- Since FCM corrections are only source additions to the Power Law approach, the conversion of a Power Law based code (or exponential-based code in general) to FCM is minimal.

- Finally, it has also been shown that no modification to the FAS multigrid algorithm is necessary in order to implement FCM over the Power Law scheme. Moreover, it is also verified that the multigrid convergence characteristics of the Power Law scheme are retained by FCM. The use of a high accuracy scheme in combination with the convergence acceleration technique should open the possibility to investigate difficult flow problems which were not considered affordable in the past.

Upon the completion of this study, FCM has been proven to be a highly viable technique for accurate modeling of complex flow structures. The improvement achieved by using FCM over the Power Law scheme is phenomenal. Upon comparing FCM results with the published results in the literature, FCM solutions are also quite competitive compared to the well-known, very accurate, spectral method.

During the course of this study, a procedure for the general pressure boundary condition has been developed and implemented. This formulation enables the specification of either normal velocity or pressure at a given boundary. If normal velocity is specified, then the effect of the boundary pressure is not neglected in the discretization of the pressure and pressure correction equations of the SIMPLER algorithm, as is previously

suggested by Patankar [5]. An improved pressure profile is observed using this new formulation.

Lastly, the recommendations for possible areas of future research or improvements to the current formulation are discussed.

- It is felt that the most important follow up of the current FCM development is the implementation of a higher order diffusion approximation for the case of a wall boundary. Recall that it has been shown that only first order diffusion is used for the wall boundary.

- Recall that during the development phase outlined in **Chapter 3**, the inclusion of the derivatives of the directional total-fluxes on the non-directional sources results in the wrong profile near the bottom wall boundary of the cavity problem. It is felt that in-depth investigation into the cause of this problem needs to be properly conducted to obtain a more thorough understanding of FCM.

- The extension of FCM to the compressible flow regimes is the most obvious next step in FCM's continued development. FCM has proven to be able to accurately predict smooth flow solutions, but its ability, and the subsequent modifications necessary, to capture shocks sharply needs to be developed.

- Finally, the development and testing of FCM for an unstructured grid needs to be undertaken to facilitate the ability to solve problems with complex flow geometries.

APPENDIX A POWER LAW APPROXIMATION OF EXPONENTIAL SCHEME

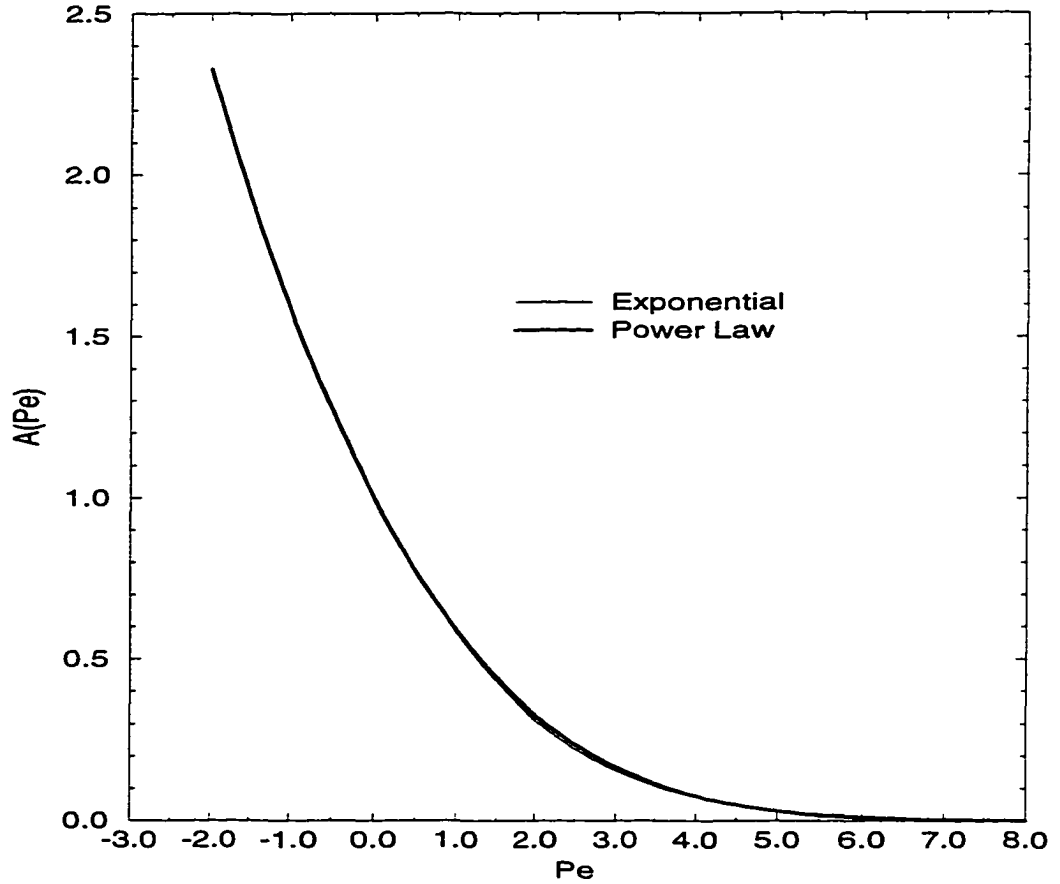

Figure A.1 Power Law approximation of the exact exponential expression $A(P_e) = \frac{P_e}{e^{P_e}-1}$.

APPENDIX B TABULATED VELOCITY COMPONENTS AND PRESSURE DATA FOR THE LID-DRIVEN CAVITY PROBLEM.

Table B.1 Vertical centerline data for Re=100 using 22x22 uniform grid.

y	u	v	P
0.00000	0.0000000	0.0000000	1.0180210
0.02500	-0.0178111	-0.0002172	1.0179880
0.07500	-0.0474099	-0.0010208	1.0179210
0.12500	-0.0737896	-0.0024016	1.0176800
0.17500	-0.0988038	-0.0039293	1.0170740
0.22500	-0.1234368	-0.0049613	1.0158510
0.27500	-0.1477521	-0.0046647	1.0136760
0.32500	-0.1707626	-0.0020876	1.0101380
0.37500	-0.1903584	0.0036873	1.0048060
0.42500	-0.2034496	0.0133019	0.9973474
0.47500	-0.2064611	0.0268254	0.9877180
0.52500	-0.1961882	0.0434871	0.9763519
0.57500	-0.1707808	0.0615647	0.9642477
0.62500	-0.1303739	0.0785336	0.9528331
0.67500	-0.0768143	0.0914681	0.9436080
0.72500	-0.0121221	0.0975285	0.9377182
0.77500	0.0645082	0.0943425	0.9356783
0.82500	0.1614371	0.0804079	0.9373727
0.87500	0.3002032	0.0562730	0.9422647
0.92500	0.5148413	0.0273274	0.9495290
0.97500	0.8253244	0.0063725	0.9599386
1.00000	1.0000000	0.0000000	0.9651434

Table B.2 Horizontal centerline data for Re=100 using 22x22 uniform grid.

x	u	v	P
0.00000	0.0000000	0.0000000	1.0027080
0.02500	-0.0032818	0.0440317	1.0017690
0.07500	-0.0141496	0.1044568	0.9998927
0.12500	-0.0317645	0.1421590	0.9984159
0.17500	-0.0529650	0.1625950	0.9969093
0.22500	-0.0756702	0.1702666	0.9950841
0.27500	-0.0987018	0.1681499	0.9928250
0.32500	-0.1214953	0.1577441	0.9901760
0.37500	-0.1438095	0.1394516	0.9873290
0.42500	-0.1654714	0.1130491	0.9846179
0.47500	-0.1861514	0.0781311	0.9825082
0.52500	-0.2051478	0.0345275	0.9815617
0.57500	-0.2211635	-0.0172371	0.9823562
0.62500	-0.2320836	-0.0753552	0.9853398
0.67500	-0.2348273	-0.1359555	0.9906047
0.72500	-0.2254905	-0.1921685	0.9976107
0.77500	-0.2002279	-0.2334624	1.0049980
0.82500	-0.1574538	-0.2463454	1.0107530
0.87500	-0.1014880	-0.2183866	1.0129580
0.92500	-0.0457588	-0.1471145	1.0109220
0.97500	-0.0101336	-0.0485372	1.0052200
1.00000	0.0000000	0.0000000	1.0023690

Table B.3 Vertical centerline data for Re=400 using 22x22 uniform grid.

y	u	v	P
0.000	0.0000000	0.0000000	1.0279190
0.025	-0.0381836	0.0002779	1.0277650
0.075	-0.1059856	-0.0000208	1.0274560
0.125	-0.1723487	-0.0013406	1.0258120
0.175	-0.2371903	-0.0017492	1.0213920
0.225	-0.2903185	0.0005044	1.0126730
0.275	-0.3171575	0.0057177	0.9990591
0.325	-0.3095288	0.0130599	0.9818367
0.375	-0.2707848	0.0210541	0.9638636
0.425	-0.2131353	0.0281960	0.9480892
0.475	-0.1496527	0.0339585	0.9361970
0.525	-0.0870682	0.0391320	0.9285030
0.575	-0.0257478	0.0447746	0.9247572
0.625	0.0359312	0.0511268	0.9247087
0.675	0.0985410	0.0575414	0.9280936
0.725	0.1608353	0.0628155	0.9344189
0.775	0.2198497	0.0654592	0.9427978
0.825	0.2720213	0.0638666	0.9519188
0.875	0.3189528	0.0556337	0.9602806
0.925	0.4060228	0.0365846	0.9670174
0.975	0.7049478	0.0118538	0.9747910
1.000	1.0000000	0.0000000	0.9786778

Table B.4 Horizontal centerline data for Re=400 using 22x22 uniform grid.

x	u	v	P
0.00000	0.0000000	0.0000000	1.0155550
0.02500	-0.0002003	0.0919057	1.0147480
0.07500	-0.0049376	0.1917139	1.0131340
0.12500	-0.0167932	0.2444882	1.0095820
0.17500	-0.0318632	0.2751068	1.0031770
0.22500	-0.0465665	0.2887528	0.9937059
0.27500	-0.0591347	0.2830520	0.9815885
0.32500	-0.0688676	0.2572737	0.9680101
0.37500	-0.0758213	0.2142023	0.9546536
0.42500	-0.0807782	0.1592602	0.9431825
0.47500	-0.0849830	0.0985303	0.9347702
0.52500	-0.0896744	0.0365258	0.9299298
0.57500	-0.0958184	-0.0249129	0.9286614
0.62500	-0.1043649	-0.0863245	0.9307344
0.67500	-0.1168304	-0.1503393	0.9359629
0.72500	-0.1351546	-0.2216295	0.9443925
0.77500	-0.1586383	-0.3037077	0.9563157
0.82500	-0.1778412	-0.3877972	0.9713490
0.87500	-0.1730214	-0.4385418	0.9864475
0.92500	-0.1255179	-0.3872504	0.9977758
0.97500	-0.0447104	-0.1403085	0.9949989
1.00000	0.0000000	0.0000000	0.9936104

Table B.5 Vertical centerline data for Re=400 using 32x32 uniform grid.

y	u	v	P
0.00000	0.0000000	0.0000000	1.0309010
0.01670	-0.0256169	-0.0000802	1.0308500
0.05000	-0.0716648	-0.0007945	1.0307470
0.08330	-0.1158605	-0.0025272	1.0303050
0.11700	-0.1604731	-0.0047494	1.0291760
0.15000	-0.2059144	-0.0065002	1.0268960
0.18300	-0.2499028	-0.0068766	1.0229190
0.21700	-0.2877441	-0.0053483	1.0167420
0.25000	-0.3139037	-0.0018528	1.0081310
0.28300	-0.3241154	0.0032433	0.9973251
0.31700	-0.3170063	0.0092614	0.9850740
0.35000	-0.2945187	0.0154029	0.9724363
0.38300	-0.2609898	0.0209970	0.9604534
0.41700	-0.2214091	0.0257180	0.9498776
0.45000	-0.1797914	0.0296457	0.9410875
0.48300	-0.1384202	0.0331311	0.9341724
0.51700	-0.0980104	0.0365752	0.9290747
0.55000	-0.0583259	0.0402602	0.9256999
0.58300	-0.0187899	0.0442895	0.9239676
0.61700	0.0211134	0.0486027	0.9238176
0.65000	0.0616418	0.0530156	0.9251875
0.68300	0.1027314	0.0572512	0.9279831
0.71700	0.1439677	0.0609549	0.9320518
0.75000	0.1845873	0.0637073	0.9371581
0.78300	0.2235360	0.0650397	0.9429696
0.81700	0.2596831	0.0644276	0.9490634
0.85000	0.2927410	0.0611555	0.9549638
0.88300	0.3273154	0.0539346	0.9602405
0.91700	0.3856654	0.0408535	0.9646893
0.95000	0.5256302	0.0220666	0.9684694
0.98300	0.8138445	0.0057749	0.9726886
1.00000	1.0000000	0.0000000	0.9747981

Table B.6 Horizontal centerline data for Re=400 using 32x32 uniform grid.

x	u	v	P
0.00000	0.0000000	0.0000000	1.0153290
0.01670	-0.0002328	0.0666630	1.0150050
0.05000	-0.0027659	0.1555721	1.0143590
0.08330	-0.0094523	0.2115584	1.0129640
0.11700	-0.0194682	0.2473590	1.0104330
0.15000	-0.0311024	0.2718103	1.0065630
0.18300	-0.0429077	0.2882116	1.0012430
0.21700	-0.0539708	0.2963574	0.9944778
0.25000	-0.0637639	0.2951173	0.9864407
0.28300	-0.0720024	0.2838957	0.9774914
0.31700	-0.0786091	0.2631000	0.9681384
0.35000	-0.0837150	0.2340958	0.9589573
0.38300	-0.0876318	0.1988931	0.9504925
0.41700	-0.0907821	0.1596935	0.9431770
0.45000	-0.0936091	0.1184460	0.9372934
0.48300	-0.0965030	0.0765578	0.9329803
0.51700	-0.0997683	0.0348173	0.9302668
0.55000	-0.1036386	-0.0065195	0.9291146
0.58300	-0.1083307	-0.0475957	0.9294534
0.61700	-0.1141241	-0.0888885	0.9312115
0.65000	-0.1214405	-0.1312731	0.9343361
0.68300	-0.1308636	-0.1761813	0.9388233
0.71700	-0.1429332	-0.2256002	0.9447547
0.75000	-0.1574474	-0.2812827	0.9523078
0.78300	-0.1721548	-0.3423703	0.9616363
0.81700	-0.1815157	-0.4015506	0.9725044
0.85000	-0.1771682	-0.4419312	0.9838217
0.88300	-0.1513448	-0.4377209	0.9936235
0.91700	-0.1030019	-0.3616910	0.9997078
0.95000	-0.0461101	-0.2100489	1.0009460
0.98300	-0.0092517	-0.0494946	0.9987935
1.00000	0.0000000	0.0000000	0.9977171

Table B.7 Vertical centerline data for Re=1000 using 42x42 uniform grid.

y	u	v	P
0.00000	0.0000000	0.0000000	1.0328450
0.01250	-0.0549809	0.0021139	1.0327150
0.03750	-0.1448317	0.0065170	1.0324530
0.06250	-0.2183069	0.0102051	1.0311600
0.08750	-0.2812200	0.0127047	1.0282530
0.11200	-0.3335491	0.0150277	1.0232920
0.13700	-0.3706359	0.0175656	1.0161330
0.16200	-0.3891102	0.0201354	1.0070770
0.18700	-0.3892540	0.0224558	0.9967902
0.21200	-0.3745435	0.0243361	0.9860745
0.23700	-0.3502097	0.0257324	0.9756156
0.26200	-0.3214890	0.0267691	0.9658396
0.28700	-0.2921489	0.0276923	0.9569112
0.31300	-0.2639225	0.0287586	0.9488284
0.33800	-0.2369515	0.0301297	0.9415328
0.36300	-0.2106758	0.0318405	0.9349789
0.38800	-0.1845300	0.0338384	0.9291538
0.41300	-0.1582099	0.0360441	0.9240690
0.43800	-0.1316384	0.0383908	0.9197443
0.46300	-0.1048400	0.0408354	0.9161975
0.48800	-0.0778480	0.0433518	0.9134404
0.51300	-0.0506651	0.0459199	0.9114787
0.53800	-0.0232593	0.0485178	0.9103136
0.56300	0.0044248	0.0511169	0.9099425
0.58800	0.0324529	0.0536812	0.9103583
0.61300	0.0609069	0.0561667	0.9115472
0.63800	0.0898826	0.0585213	0.9134906
0.66300	0.1194846	0.0606850	0.9161645
0.68800	0.1498220	0.0625918	0.9195385
0.71300	0.1809916	0.0641664	0.9235735
0.73800	0.2130299	0.0653165	0.9282183
0.76300	0.2458239	0.0659190	0.9334026
0.78800	0.2789916	0.0658070	0.9390260
0.81300	0.3117743	0.0647655	0.9449444
0.83800	0.3429897	0.0625465	0.9509571
0.86300	0.3710719	0.0589004	0.9568020

Table B.7 (Continued)

y	u	v	P
0.88800	0.3942664	0.0535976	0.9621654
0.91300	0.4121196	0.0462833	0.9667186
0.93800	0.4360341	0.0358373	0.9702259
0.96300	0.5251966	0.0208158	0.9727685
0.98800	0.7935566	0.0060095	0.9752674
1.00000	1.0000000	0.0000000	0.9765169

Table B.8 Horizontal centerline data for Re=1000 using 42x42 uniform grid.

x	u	v	P
0.00000	0.0000000	0.0000000	1.0149050
0.01250	0.0011035	0.0945037	1.0146190
0.03750	0.0008077	0.2180738	1.0140450
0.06250	-0.0042845	0.2894401	1.0122200
0.08750	-0.0124349	0.3331716	1.0088580
0.11200	-0.0212252	0.3622885	1.0039240
0.13700	-0.0294433	0.3791057	0.9975091
0.16200	-0.0366464	0.3835181	0.9898854
0.18700	-0.0426841	0.3763971	0.9814653
0.21200	-0.0475789	0.3597453	0.9727093
0.23700	-0.0514954	0.3361899	0.9640356
0.26200	-0.0546870	0.3084290	0.9557613
0.28700	-0.0574219	0.2787285	0.9480842
0.31300	-0.0599179	0.2486013	0.9411019
0.33800	-0.0623105	0.2187726	0.9348484
0.36300	-0.0646632	0.1893928	0.9293301
0.38800	-0.0669987	0.1603352	0.9245488
0.41300	-0.0693307	0.1314243	0.9205106
0.43800	-0.0716810	0.1025380	0.9172254
0.46300	-0.0740826	0.0736152	0.9147031
0.48800	-0.0765745	0.0446253	0.9129503
0.51300	-0.0791947	0.0155402	0.9119688
0.53800	-0.0819751	-0.0136791	0.9117546
0.56300	-0.0849382	-0.0430843	0.9123007
0.58800	-0.0880942	-0.0727431	0.9135974
0.61300	-0.0914354	-0.1027230	0.9156304
0.63800	-0.0949299	-0.1330728	0.9183802
0.66300	-0.0985159	-0.1638001	0.9218205
0.68800	-0.1021010	-0.1948453	0.9259154
0.71300	-0.1055786	-0.2260654	0.9306155
0.73800	-0.1088885	-0.2572772	0.9358541
0.76300	-0.1121587	-0.2884821	0.9415500
0.78800	-0.1159065	-0.3204606	0.9476308
0.81300	-0.1210468	-0.3557111	0.9540891
0.83800	-0.1280727	-0.3985166	0.9610540
0.86300	-0.1350944	-0.4509825	0.9687469

Table B.8 (Continued)

x	u	v	P
0.88800	-0.1363141	-0.5038100	0.9771279
0.91300	-0.1236297	-0.5288066	0.9854186
0.93800	-0.0915289	-0.4806987	0.9921272
0.96300	-0.0443061	-0.3112456	0.9955448
0.98800	-0.0091635	-0.0584320	0.9944511
1.00000	0.0000000	0.0000000	0.9939042

Table B.9 Vertical centerline data for Re=1000 using 52x52 uniform grid.

y	u	v	P
0.00000	0.0000000	0.0000000	1.0340410
0.01000	-0.0445122	0.0012285	1.0339870
0.03000	-0.1197817	0.0040121	1.0338800
0.05000	-0.1833551	0.0065628	1.0332340
0.07000	-0.2390521	0.0081538	1.0317230
0.09000	-0.2892542	0.0093628	1.0290480
0.11000	-0.3326855	0.0108000	1.0249720
0.13000	-0.3660751	0.0126209	1.0194090
0.15000	-0.3867465	0.0146689	1.0124930
0.17000	-0.3939331	0.0167030	1.0045630
0.19000	-0.3888899	0.0185147	0.9960735
0.21000	-0.3743616	0.0199774	0.9874799
0.23000	-0.3537490	0.0210707	0.9791407
0.25000	-0.3302418	0.0218779	0.9712745
0.27000	-0.3061847	0.0225501	0.9639713
0.29000	-0.2828543	0.0232502	0.9572345
0.31000	-0.2606229	0.0241025	0.9510288
0.33000	-0.2393198	0.0251701	0.9453139
0.35000	-0.2185801	0.0264595	0.9400622
0.37000	-0.1980676	0.0279425	0.9352616
0.39000	-0.1775623	0.0295781	0.9309123
0.41000	-0.1569581	0.0313276	0.9270207
0.43000	-0.1362245	0.0331612	0.9235956
0.45000	-0.1153661	0.0350582	0.9206450
0.47000	-0.0943952	0.0370049	0.9181751
0.49000	-0.0733169	0.0389908	0.9161898
0.51000	-0.0521245	0.0410064	0.9146912
0.53000	-0.0308003	0.0430412	0.9136798
0.55000	-0.0093175	0.0450821	0.9131544
0.57000	0.0123559	0.0471138	0.9131127
0.59000	0.0342567	0.0491178	0.9135499
0.61000	0.0564285	0.0510729	0.9144592
0.63000	0.0789215	0.0529548	0.9158318
0.65000	0.1017917	0.0547365	0.9176569
0.67000	0.1251019	0.0563884	0.9199212
0.69000	0.1489187	0.0578783	0.9226090

Table B.9 (Continued)

y	u	v	P
0.71000	0.1733059	0.0591705	0.9257010
0.73000	0.1983091	0.0602236	0.9291735
0.75000	0.2239282	0.0609865	0.9329965
0.77000	0.2500774	0.0613937	0.9371306
0.79000	0.2765384	0.0613606	0.9415225
0.81000	0.3029149	0.0607815	0.9461001
0.83000	0.3286046	0.0595323	0.9507675
0.85000	0.3527975	0.0574797	0.9554017
0.87000	0.3745135	0.0544925	0.9598534
0.89000	0.3927595	0.0504384	0.9639533
0.91000	0.4074288	0.0450944	0.9675296
0.93000	0.4236495	0.0378552	0.9704514
0.95000	0.4647213	0.0276047	0.9727102
0.97000	0.5859711	0.0144652	0.9744555
0.99000	0.8410379	0.0036850	0.9761706
1.00000	1.0000000	0.0000000	0.9770282

Table B.10 Horizontal centerline data for Re=1000 using 52x52 uniform grid.

x	u	v	P
0.00000	0.0000000	0.0000000	1.0150740
0.01000	0.0008403	0.0764502	1.0149480
0.03000	0.0013722	0.1867891	1.0146980
0.05000	-0.0010019	0.2587516	1.0137160
0.07000	-0.0062053	0.3052269	1.0117980
0.09000	-0.0127845	0.3378219	1.0088760
0.11000	-0.0195479	0.3616321	1.0049330
0.13000	-0.0258984	0.3773649	1.0000160
0.15000	-0.0315931	0.3846575	0.9942573
0.17000	-0.0365399	0.3836203	0.9878627
0.19000	-0.0407302	0.3750768	0.9810810
0.21000	-0.0442245	0.3603787	0.9741629
0.23000	-0.0471364	0.3411417	0.9673276
0.25000	-0.0496086	0.3189800	0.9607428
0.27000	-0.0517836	0.2952805	0.9545196
0.29000	-0.0537800	0.2710586	0.9487198
0.31000	-0.0556808	0.2469245	0.9433699
0.33000	-0.0575343	0.2231441	0.9384766
0.35000	-0.0593633	0.1997524	0.9340385
0.37000	-0.0611774	0.1766696	0.9300537
0.39000	-0.0629828	0.1537857	0.9265224
0.41000	-0.0647879	0.1310067	0.9234480
0.43000	-0.0666060	0.1082688	0.9208349
0.45000	-0.0684539	0.0855343	0.9186879
0.47000	-0.0703506	0.0627810	0.9170110
0.49000	-0.0723153	0.0399924	0.9158064
0.51000	-0.0743652	0.0171507	0.9150746
0.53000	-0.0765150	-0.0057655	0.9148141
0.55000	-0.0787757	-0.0287825	0.9150218
0.57000	-0.0811541	-0.0519321	0.9156937
0.59000	-0.0836511	-0.0752494	0.9168242
0.61000	-0.0862605	-0.0987681	0.9184059
0.63000	-0.0889669	-0.1225161	0.9204298
0.65000	-0.0917430	-0.1465071	0.9228845
0.67000	-0.0945489	-0.1707321	0.9257558
0.69000	-0.0973323	-0.1951497	0.9290253

Table B.10 (Continued)

x	u	v	P
0.71000	-0.1000356	-0.2196816	0.9326697
0.73000	-0.1026142	-0.2442282	0.9366591
0.75000	-0.1050778	-0.2687304	0.9409576
0.77000	-0.1075596	-0.2933268	0.9455277
0.79000	-0.1103974	-0.3186539	0.9503422
0.81000	-0.1141455	-0.3462413	0.9554086
0.83000	-0.1193311	-0.3786328	0.9608006
0.85000	-0.1257654	-0.4183246	0.9666703
0.87000	-0.1315699	-0.4645720	0.9731808
0.89000	-0.1327308	-0.5088196	0.9803089
0.91000	-0.1240903	-0.5319376	0.9876057
0.93000	-0.1018262	-0.5061572	0.9941225
0.95000	-0.0669293	-0.4041102	0.9985862
0.97000	-0.0294477	-0.2271433	1.0000670
0.99000	-0.0060134	-0.0532790	0.9992161
1.00000	0.0000000	0.0000000	0.9987908

APPENDIX C TABULATED SEPARATION LENGTHS AND LOCATIONS FOR THE LAMINAR BACKWARD-FACING STEP FLOW.

Table C.1 Separation lengths and locations using FCM with 102x22 uniform grid.

Re	x_1	x_4	x_5	$x_5 - x_4$
100	1.638824	-	-	-
200	2.711866	-	-	-
400	4.485030	4.560689	4.875242	0.314553
600	5.792293	4.764441	8.141794	3.377353
800	6.663812	5.265106	10.509930	5.244822

Table C.2 Separation lengths and locations using FCM with 102x42 uniform grid.

Re	x_1	x_4	x_5	$x_5 - x_4$
100	1.638824	-	-	-
200	2.737238	-	-	-
400	4.474053	4.476390	5.305324	0.828934
600	5.793182	4.901751	8.621470	3.719719
800	6.832433	5.578107	11.504930	5.926824

Table C.3 Separation lengths and locations using FCM with 102x82 uniform grid.

Re	x_1	x_4	x_5	$x_5 - x_4$
100	1.638824	-	-	-
200	2.744578	-	-	-
400	4.469681	4.530076	5.356200	0.826124
600	5.796251	4.976115	8.726549	3.750434
800	6.874557	5.709461	11.756830	6.047369

Table C.4 Separation lengths and locations using Power Law with 102x42 uniform grid.

Re	x_1	x_4	x_5	$x_5 - x_4$
100	1.428865	-	-	-
200	2.458813	-	-	-
400	3.926286	3.429865	4.473994	1.044129
600	4.065937	3.108677	6.209945	3.101268
800	3.678668	2.653364	6.169191	3.515827

BIBLIOGRAPHY

[1] Raithby G.D. Skew upstream differencing schemes for problems involving fluid flow. *Computer Methods in Applied Mechanics and Engineering*, 9:153–164, 1976.

[2] Leonard B. P. and Drummond J. E. Why you should not use 'hybrid', 'Power-Law' or related exponential schemes for convective modeling - There are much better alternatives. *International Journal for Numerical Methods in Fluids*, 20:421–442, 1995.

[3] Roache P.J. *Computational Fluid Dynamics.* Hermosa, Albuquerque, NM, 1972.

[4] Leonard B.P. A stable and accurate convective modeling procedure based on quadratic upstream interpolation. *Computer Methods in Applied Mechanics and Engineering*, 19:59–98, 1979.

[5] Patankar S.V. *Numerical Heat Transfer and Fluid Flow.* Hemisphere Publishing Corporation, New York, 1980.

[6] Khosla P.K. and Rubin S.G. A diagonally dominant second-order accurate implicit scheme. *Journal of Computational Fluids*, 2:207–209, 1974.

[7] Ghia U., Ghia K.N., and Shin C.T. High *Re* solutions for incompressible flow using the Navier-Stokes equations and a multigrid method. *Journal of Computational Physics*, 48:387–411, 1982.

[8] Hayase T., Humphrey J.A.C., and Greif R. A consistently formulated QUICK scheme for fast and stable convergence using finite-volume iterative calculation procedures. *Journal of Computational Physics*, 98:108–118, 1992.

[9] Harten A., Engquist B., Osher S., and Chakravarthy S.R. Uniformly high order accurate essentially non-oscillatory schemes, III. *Journal of Computational Physics*, 71:231–303, 1987.

[10] Gentry R.A., Martin R.E., and Daly B.J. An Eulerian differencing method for unsteady compressible flow problems. *Journal of Computational Physics*, 1:87–118, 1966.

[11] Price H.S., Varga R.S., and Warrent J.E. Applications of oscillation matrices to diffusion-correction equations. *Journal of Mathematics and Physics*, 45:301–311, 1966.

[12] Atias M., Wolfshtein M., and Israeli M. Efficiency of Navier-Stokes solver. *AIAA Journal*, 15:263–265, 1977.

[13] Wilkes N.S. and Thompson C.P. An evaluation of higher-order upwind differencing for elliptic flow problems. *Numerical Methods in Laminar and Turbulent Flows*, 248-257, 1983.

[14] Shyy W. and Correa S.M. A systematic comparison of several numerical schemes for complex flow calculations. *AIAA 85-0440*, 1985.

[15] Vanka S.P. Second-order upwind differencing in a recirculating flow. *AIAA Journal*, 25:1435–1441, 1987.

[16] Shyy W., Thakur S., and Wright J. Second-order upwind and central difference schemes for recirculating flow computation. *AIAA Journal*, 30:923–932, 1992.

[17] Leschziner M.A. Practical evaluation of three finite-difference schemes for the computation of steady-state recirculating flows. *Computational Methods in Applied Mechanics Engineering*, 23:293–312, 1980.

[18] Han T., Humphrey J.A.C., and Launder B.E. A comparison of hybrid and quadratic upstream differencing in high Reynolds number elliptic flows. *Computational Methods in Applied Mechanics Engineering*, 29:81–95, 1981.

[19] Pollard A. and Siu A.L.W. The calculation of some laminar flows using various discretization schemes. *Computational Methods in Applied Mechanics Engineering*, 35:293–313, 1982.

[20] Freitas C.J., Street R.L., Findikakis A.N., and Koseff J.R. Numerical simulation of three-dimensional flow in a cavity. *International Journal of Numerical Methods in Fluids*, 5:561–575, 1985.

[21] Perng C.Y. and Street R.L. Three-dimensional unsteady flow simulations: Alternative strategies for a volume-averaged calculation. *International Journal of Numerical Methods in Fluids*, 9:341–362, 1989.

[22] Leonard B.P. *Proceedings of the 5th International Conference on Numerical Methods in Laminar and Turbulent Flows.* Edited by C. Taylor et al. Pineridge Press, Swansea, UK, 35, 1987.

[23] Leonard B.P. and Mokhtari S. ULTRA-SHARP solution of the Smith-Hutton problem. *International Journal of Numerical Methods in Heat and Fluid Flow*, 2:407–427, 1992.

[24] Leonard B.P. and Mokhtari S. Beyond first-order upwinding: The ULTRA-SHARP alternative for non-oscillatory steady state simulation of convection. *International Journal of Numerical Methods in Engineering*, 30:729–766, 1990.

[25] Allen D.N. deG. and Southwell R.V. Relaxation methods applied to determine the motion, in two-dimensions, of a viscous fluid past a fixed cylinder. *Journal of Mechanics and Applied Maths*, 8:129–145, 1955.

[26] Spalding D.B. A novel finite-difference formulation for differential expressions involving both first and second derivatives. *International Journal of Numerical Methods in Engineering*, 4:551–559, 1972.

[27] Gosman A.D. and Pun W.M. Calculation of recirculation flows. *Heat Transfer Section Report HTS/72/2*, 1974.

[28] Huang P.G., Launder B.E., and Leschziner M.A. Discretization of nonlinear convection processes: A broad range comparison of four schemes. *Computer Methods in Applied Mechanics and Engineering*, 48:1–24, 1985.

[29] Patel M.K. and Markatos N.C. An evaluation of eight discretization schemes for two-dimensional convection-diffusion equations. *International Journal for Numerical Methods in Fluids*, 6:129–154, 1986.

[30] Wong H. H. and Raithby G.D. Improved finite-difference methods based on a critical evaluation of the approximating errors. *Numerical Heat Transfer*, 2:131, 1979.

[31] Varejao L.M.C. *Flux-Spline Method for Heat, Mass, and Momentum Transfer.* PhD thesis, Department of Mechanical Engineering, University of Minnesota, 1979.

[32] Karki K., Mongia H., and Patankar S.V. Solution of three-dimensional flow problems using a flux-spline method. *Proceedings of the 27th Aerospace Sciences Meeting AIAA 89-0687*, Reno, Nevada, January 9-12, 1989.

[33] Rajagopalan R.G. and Fanucci J.B. Finite-difference model for vertical axis wind rotors. *Journal of Propulsion and Power*, 1(6):432–436, 1985.

[34] Chorin A.J. A numerical method for solving incompressible viscous flow problems. *Journal of Computational Physics*, 2:12–26, 1967.

[35] Kwak D., Chang J.L.C., Shanks S.P., and Chakravarthy S.R. A three-dimensional incompressible Navier-Stokes flow solver using primitive variables. *AIAA Journal*. 24:390–396, 1986.

[36] Merkle C.L. and Athavale M. Time-accurate unsteady incompressible flow algorithm based on artificial compressibility. *AIAA 87-1137*, 1987.

[37] Harlow F.H. and Welch J.E. Numerical calculation of time-dependent viscous incompressible flow with free surface. *Physics of Fluids*, 18:2182–2184, 1965.

[38] Caretto L.S., Curr R.M., and Spalding D.B. Two numerical methods for three-dimensional boundary layers. *Computer Methods in Applied Mechanics and Engineering*, 1:39, 1972.

[39] Karamcheti K. *Principles of Ideal-Fluid Aerodynamics*. Huntington, New York, NY, 1980.

[40] Zori L.A. and Rajagopalan R.G. The FAS multigrid method for the segregated solution of the SIMPLER algorithm. *Proceedings of the 6th International Symposium on CFD*, 3:1509–1514, Lake Tahoe, Nevada, 1995.

[41] Ku H.C., Hirsh R.S., and Taylor T.D. A pseudospectral method for solution of the three-dimensional incompressible Navier-Stokes equations. *Journal of Computational Physics*, 70:439–462, 1987.

[42] Richardson L.F. The approximate arithmetical solution by finite-differences of physical problems. *Philosophical Transactions of the Royal Society of London Serial A*, 210:307–357, 1911.

[43] Richardson L.F. and Gaunt J.A. The deferred approach to the limit. *Philosophical Transactions of the Royal Society of London Serial A*, 226:299–361, 1927.

[44] Roache P.J. Perspective: A method for uniform reporting of uniform refinement studies. *Journal of Fluids Engineering*, 116:405–413, 1994.

[45] Huser A. and Biringen S. Calculation of two-dimensional shear-driven cavity flows at high Reynolds number. *International Journal of Numerical Methods in Fluids*, 14:1087–1109, 1992.

[46] Bye J.A.T. Numerical solutions of the steady state vorticity equation in rectangular basins. *Journal of Fluid Mechanics*, 26:577–598, 1966.

[47] Kumagai M. A numerical study of wind-driven circulation in rectangular cavities. *Journal of Computational Physics*, 47:130–145, 1982.

[48] Koseff J.R. and Street R.L. Visualization studies of a shear-driven three-dimensional recirculating flow. *Transactions of the ASME*, 106:22, 1984.

[49] Brandt A. Multi-level adaptive solutions to boundary-value problems. *Mathematics of Computation*, 31(138):333–390, 1977.

[50] Brandt A. Guide to multigrid development. *Lecture Notes in Mathematics*, 960:220–312, 1982.

[51] Brandt A. Multigrid techniques: 1984 guide with applications to fluid dynamics. *Computational Fluid Dynamics Lecture Notes 194-04*, von-Karman Institute, 1984.

[52] Armaly B.F., Durst F., and Pereira J.C.F. Experimental and theoretical investigation of backward-facing step flow. *Journal of Fluid Mechanics*, 127:473–496, 1983.

[53] Kaiktsis L., Karniadakis G.EM., and Orszag S.A. Onset of three-dimensionality, equilibria, and early transition in flow over a backward-facing step. *Journal of Fluid Mechanics*, 231:501–528, 1991.

[54] Kim J. and Moin P. Application of fractional-step method to incompressible Navier-Stokes equations. *Journal of Computational Physics*, 59:308–323, 1985.

[55] Gartling D.K. A test problem for outflow boundary conditions - flow over a backward-facing step. *International Journal for Numerical Methods in Fluids*, 11:953–967, 1990.

[56] Gartling D.K. NACHOS II - a finite-element code for incompressible flow problems. *Sandia National Laboratories Report, SAND86-1817*, Albuquerque, NM, 1987.

[57] *FIDAP Theoretical Manual, Version 4.5.* Fluid Dynamics International, Evanston, IL, 1988.

[58] Gresho P.M., Gartling D.K., Torczynski J.R., Garratt T.J., Spence A., and Goodrich J.W. Is the steady viscous incompressible two-dimensional flow over a backward-facing step at *Re*=800 stable ? *International Journal for Numerical Methods in Fluids*, 17:501–541, 1993.

[59] Winters K.H. *ENTWIFE User Manual (Release 1), Harwell Report AERE-R 11577.* 1985.

[60] *NEKTON User's Guide, Version 2.7.* Nektonics Inc. Cambridge, MA, 1991.

[61] Patera A.T. A spectral element method for fluid dynamics: Laminar flow in a channel expansion. *Journal of Computational Physics*, 54:468–488, 1984.